ADVANCED MODELLING OF POROUS SCREENS IN AERODYNAMIC DIFFUSERS USING VARIABLE RESISTANCE FACTORS

by

Jacobus Johannes Janse van Rensburg
M. Dip. Tech. (Mech), Pr. Tech. Eng., MSAIMechE

Dissertation submitted in fulfilment of the requirements for the degree

Magister Technologiae
in the discipline
Mechanical Engineering
in the
Faculty of Engineering and Technology
at the
Vaal University of Technology

Supervisor: Dr. M.P. van Staden
Co-Supervisor: Mr. G.G. Jacobs
Vanderbijlpark
South Africa
December 2004

Dedicated to my wife Murchille

Acknowledgements

- First and foremost, I would like to thank my study leaders Dr. M. P. van Staden and Mr. G. G. Jacobs for their guidance, support and assistance throughout the duration of this study.
- I also want to thank Mr. J. Nel and Mr. S. Bolatti for their assistance during the design, testing and commissioning phase of the project.
- Furthermore, I would like to thank Prof. B. Skews (of Wits University) for his assistance and guidance.
- I would also like to thank Dr. J. Hoffmann and Mr. C. Viljoen for their assistance in the editing of the thesis.
- For financial support I would like to acknowledge The Vaal University of Technology, The National Research Foundation (NRF) and Eskom TSI, specifically Mr. D. Gibson.
- Especially, I want to thank my girls. Firstly to my wife Murchille for her continued support throughout the completion of this study, even through completing her own studies. Without her loving support and patience, I would not have been able to complete this work. To my little girl Jamie who so patiently sat by my side while completing this work. I will make this up to you, I promise. The two of you are the energy that keeps me going. I love you so much.
- Finally and most importantly, I want to thank my Heavenly Father for the ability that he has granted me in his vast wisdom and grace. It is only through His grace that I can achieve anything and for this I honour and thank Him. To Him be the glory and honour, forever and ever.

Abstract

Strict emission legislation has forced industry in general to seriously consider the negative impact it has on the environment, specifically concerning emissions from burning fossil fuel into the atmosphere. In cases where emission levels exceed the allowable limit, companies are forced to operate at lower operating conditions and these load losses can result in a significant loss of revenue. This has forced companies to improve their ash filtering capabilities by optimising electrostatic precipitation systems.

One of the main factors impacting on the efficiency of such a system is the distribution of the flow across the collection plates. The design of the inlet diffuser plays a major role in the ultimate distribution of the flow through the precipitator. Porous screens are positioned in the diffuser in order to distribute the flow across the total flow area with the aim to achieve a uniform distribution of the flow.

CFD is widely used in industry to simulate the flow through precipitators in order to optimise the flow distribution and thus increase the efficiency of the system. It was found however that the current methods used to simulate these screens in CFD models were not well researched and employed fixed resistance values that could not reliably compensate for changes in the resistance coefficient due to a change in the angle of incidence.

This study investigates advanced numerical methods for the simulation of porous screens in applications where the angle of incidence changes continuously across the face of the screen. New methods are introduced where the resistance of the screen is calculated as a function of the changing angle of incidence. The methods currently used are also investigated and compared with results from the new methods.

Extensive experimental work was required to supply empirical data for the validation of the numerical methods that are proposed. For this reason, the first part of this study focused on the design construction and commissioning of a low speed wind tunnel. Results are presented and discussed for flow profiles through wide-angle diffusers at

different angles and also for a number of different screens positioned in the centre of the diffuser.

This study also investigates the sensitivity of a CFD simulation code to factors such as numerical discretisation schemes, turbulence models and solution relaxation specifically for wide-angle diffusers. These factors were tested for diffusers at different angles and included tests on open diffusers and also with screens positioned inside the diffuser.

It was concluded that the current methods used are not adequate to capture the true flow profiles for a range of different screen geometries. Although the proposed models did improve on the limitations of the current methods, it was found that the applicability of these models is still limited and that further research would be required to develop numerical methods that are valid for a wide range of applications.

☆ ☆ ☆ ☆ ☆ ☆ ☆ ☆ ☆ ☆

Table of Contents

List of Figures

List of Tables

List of Symbols

Symbols	Description	SI Unit
a	Horisontal hole size for calculation of FAR	m
A_T	Total flow area	m^2
A_F	Free flow area	m^2
b	Vertical hole size for calculation of FAR	m
B	Barometric pressure	(mbar)
C	Speed of sound	m/s
C_1	User defined variable defining the inertial loss term in the porous medium resistance calculation by Star-CD	-
C_2	User defined variable defining the viscous loss term in the porous medium resistance calculation by Fluent Inc.	-
C_D	Non dimensional drag	-
C_P	Pressure coefficient	-
C_L	Lift coefficient	-
D	Diameter	m
D_H	For Reynolds number D refers to hydraulic diameter	m
dP/ΔP	Pressure drop	Pa
Eu	Euler number	-
f	Pipe friction factor	-
g	Gravitational acceleration	m/s^2
K	Resistance coefficient	-
K_i	Permeability	-
K_o	Oblique resistance coefficient	-
K_p	Perpendicular resistance coefficient	-
K_v	Variable resistance coefficient	-
k-ε	A group of eddy viscosity turbulence models assuming that the turbulent Reynolds stresses and scalar fluxes are linked to the ensemble averaged flow properties in analogous fashion to their laminar flow counterparts, all comprising transport equations for the turbulent kinetic energy k and its	-

	dissipation rate ε (Star-CD, 2001:2-1, 2-3).	
L	Length	m
L_d	Relative length of diffuser	m
m	Mass flow rate	kg/s
Ma	Mach number	-
η	Kolmogoroff scale	-
P_s	Relative duct static pressure	Pa
P_v	Dynamic pressure	Pa
Q	Uncertainty	-
r	Radius	m
R	Gas constant	kJ/kg.K
Re	Reynolds number	-
Re_L	Reynolds number based on the magnitude of the velocity fluctuations and the integral scale	-
S	Momentum Source term in the Navier Stokes Equation	N/m^3
S_u	Momentum Source term in the Navier Stokes Equation for the variable u	N/m^3
S_i	Momentum Source term in the Navier Stokes Equation in the direction i	N/m^3
t	Thickness of porous medium/screen	m
T	Temperature	°C/K
u	Superficial velocity magnitude	m/s
U	Characteristic velocity through a porous medium/momentum sink region	m/s
v	Normal velocity component	m/s
v'^2	Fluctuations of normal velocity component	$(m/s)^2$
v_a	Approach velocity	m/s
v	Velocity of flow	m/s
v	Vertical lattice size for calculation of FAR	m
v_f	Free stream velocity	m/s
v_m	Mean (average) velocity	m/s
v_{peak}	Peak velocity	m/s
v^2-f	Turbulence model where the wall normal component, v^2,	-

	and its source term f, are retained as variables in addition to the traditional k and ε (energy dissipation) parameters of the k-ε eddy viscosity models (Laurence et. al. p. 2).	
w	Horisontal lattice size for calculation of FAR	m
x	A variable in a function where the chain rule is required to determine the partial differential equation of the variable.	-
y	A function where the chain rule is required to determine the partial differential equation of a variable x.	-
y+	Dimensionless distance from wall	-

List of Greek Symbols

Symbols		SI Unit
α	User defined variable defining the viscous loss term in the porous medium resistance calculation by Star-CD	-
α_p	Perpendicular resistance coefficient	-
α_y	Transversal resistance coefficient in the y direction	-
α_z	Transversal resistance coefficient in the z direction	-
β	User defined variable defining the inertial loss term in the porous medium resistance calculation by Star-CD	-
Δ	Differential	-
ε	Turbulent dissipation rate	-
ξ	Mutually orthogonal orthotropic directions	-
γ	Specific heat ratio	-
ρ	Gas density	kg/m^3
Γ	Diffusivity of the quantity u in the Navier Stokes Equation (The unit is related to the quantity u)	-
μ	Dynamic viscosity	$N.s/m^2$
Θ	Flow exit angle	°
Φ	Angle of incidence	°
μm	Micro meter	μm
ω	Inclusive angle of diffuser	°

List of Abbreviations

Abbreviation	Description
AMG	Algebraic Multigrid Solver
CAPCO	Chief air Pollution Control Officer
CD	Central Differencing discretisation scheme
CG	Conjugate Gradient Solver
CSIR	Council for Scientific and Industrial Research
CFD	Computational Fluid Dynamics
DNS	Direct Numerical Simulations
ESP	Electrostatic Precipitator
FAR	Free Area Ratio
FFS	Fabric Filter System
HGL	Hydraulic Gradient Line
LES	Large Eddie Simulations
MARS	Monotone Advection and Reconstruction Scheme (discretization scheme)
NACA	National Advisory Committee for Aeronautics
PISO	Pressure Implicit with Splitting of Operators
QUICK	Quadratic upwind interpolation for convection and kinetics
RANS	Reynolds Averaged Navier-Stokes Equations
RNG	Renormalisation group (form of the k-ε turbulence model)
SGS	Sub Grid Scale
SIMPLE	Semi Implicit Method for Pressure Linked Equations
UD	Upwind differencing discretisation scheme
UDF	User Defined Function

CHAPTER 1: INTRODUCTION

1.1 Background

Since the industrial revolution of the early twentieth century, industries were built globally at an astounding rate with little regard for the environmental impact that this development would have. In the past few decades in South Africa, strict emission legislation by the Chief Air Pollution Control Officer (CAPCO) has however forced industry to seriously consider the negative impact it has on the environment, specifically concerning the emissions from burning fossil fuel into the atmosphere, i.e. NOx gases and ash particles. In cases where emission levels exceed the allowable limit, companies are forced to operate at lower operating conditions and these load losses can result in a significant loss of revenue. This has resulted in companies improving their ash filtering ability by either installing more effective precipitation systems, which include Electrostatic Precipitators (ESP's), Fabric Filter Systems (FFS's) and Cyclone precipitation systems, or by improving the current installation. Eskom (The South African electricity supply company) has been investigating the option of improving their ESP systems rather than replacing these systems with more efficient Fabric Filter Systems at a considerable cost. With seventy three percent of Eskom's coal fired power stations equipped with ESP's (Schmitz and Pretorius, 2004), the total cost of replacing all these systems would be too expensive. For this reason, it is essential to investigate the economical viability of improving the efficiency of such systems.

Due to space restrictions and cost limitations, long transitional ducts upstream of ESP's are not practical in the design of modern power plants and therefore wide-angle transition pieces are commonly used in the flow path (as shown in Figure 1). These transition ducts result in poor flow distribution, i.e. separation of the flow in diffusers and high localised velocities. Coupled to the high abrasiveness of ash suspended in the gas, high velocities can cause severe erosion of the internal structures, e.g. boiler tubes or precipitation plates. Raask (1969) states that the rate of metal loss is proportional to the impact velocity to the power of 2.5. Tilly (1979:300) states: "The consensus of opinion is that the erosion of ductile materials involves an exponent of 2.3 to 2.4". It can therefore be seen that a reduction in localised high velocities can significantly reduce erosion rates. Gibson (2002) has shown that expanded metal

screens have proven to be a cost effective and simple solution to reduce high velocities and thus minimise the occurrence of tube failures resulting from fly-ash erosion in boilers.

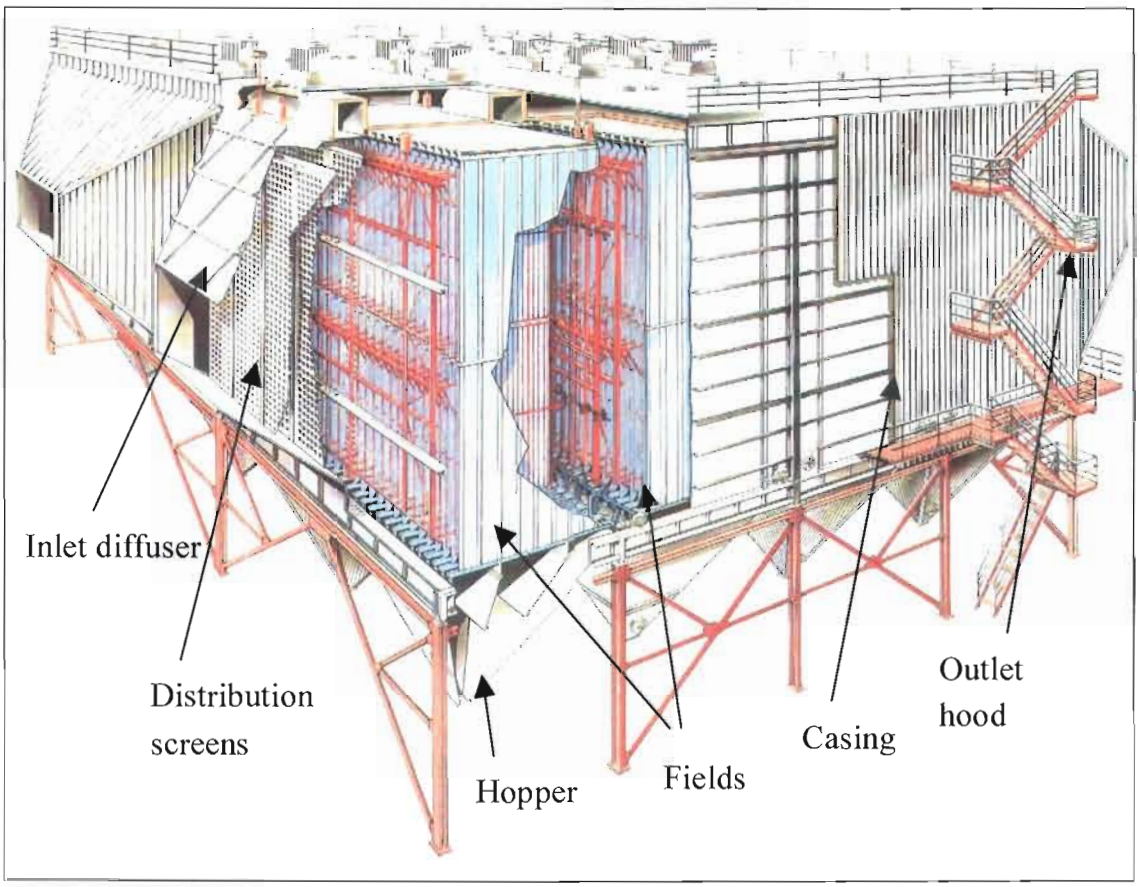

Figure 1: A typical ESP system with wide-angle inlet diffuser (adapted from Apparatebau Rothemühle, 1999)

This study however focuses on another use of perforated screens in ESP's, which is to improve the inlet flow distribution and thus increase the system efficiency. Due to the nature of most industrial systems, aerodynamic efficiency plays a significant role in the overall plant or system performance. It was found that by improving system aerodynamics, the overall plant efficiency can be improved considerably (Gibson, 1992:1-10). The aerodynamic efficiency of an ESP could be defined as the ability of the design to distribute the inlet flow evenly across the collection plates thus reducing the overall velocities through the system, which increases the treatment time and reduces the probability of particle re-entrainment. To better understand this, it is important to understand the mechanism of an ESP as shown in Figure 2.

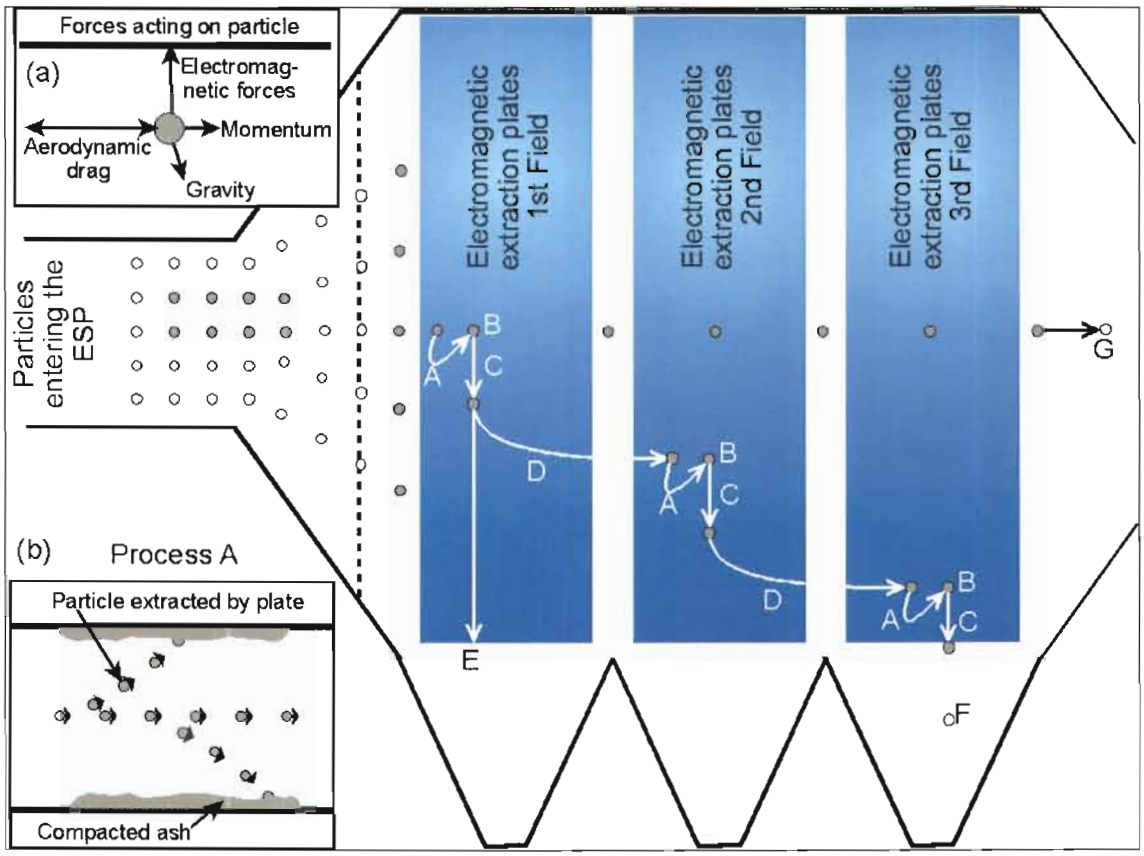

Figure 2: The mechanism of an ESP

Insert (a) shows the forces that are acting upon the particles. These forces include:

- The aerodynamic drag, which is a function of the physical shape, surface roughness and relative velocity of the particle, i.e. the velocity of the particle in relation to the velocity of the gas. This force can be in many different directions depending on the trajectory and mass of the particle.
- The momentum of the particle, which is defined by the mass and the velocity of the particle.
- Gravity force, which is only a function of the mass.
- The electrostatic forces as the particle enters the 1st field. The magnitude of this force is a function of the difference in electromagnetic loading (potential difference) between the collection plate and the particle.

As the particles pass through the ESP, the following processes occur:

A: Electromagnetic forces from the collection plates acting on the particles.

B: Rapping of the plates.

C: After rapping, the compacted ash drops into the ash hoppers at point E.

D: Repeated re-entrainment of smaller particles up to point F.

G: Some particles are never extracted from the flow and passes straight through the ESP to be exhausted into the atmosphere. The aim with the optimisation of an ESP is to reduce these particles thus increasing the filtration ability.

When flow enters a diffuser, flow separation will occur when the walls of the diffuser are diverging with a total inclusive angle (see Figure 3c) greater than approximately 16° (Schubauer & Spangenberg, 1948:1-4). A large angle diffuser is therefore defined as any diffuser with an inclusive angle larger 16°. Since most ESP's are fitted with a diffuser between 60° and 120° inclusive angle, this separation will result in high localised velocities through the ESP and a lower filtration efficiency. It was found that screens, when correctly applied, can be used to minimise flow separation in diffusers resulting in reduced turbulence downstream of the diffuser (Schubauer & Spangenberg, 1948:2). This property of porous screens is called the "filling effect" as the resistance created by the screen would have the tendency to spread the flow in the diffuser minimising flow separation and thus causing the flow to fill the total area of the diffuser. For these reasons, porous screens are fitted in the diffuser before entry into the ESP as shown in Figure 1.

It can therefore be concluded that the optimisation of the flow distribution through an ESP would have the following benefits:

- A reduction in peak velocities through the ESP, which increases the treatment time and reduces the probability of particle re-entrainment.
- A more uniform flow distribution, which distributes the suspended particles more evenly across the total plate area thus reducing the particle ash concentration on the centre plates.
- A reduction in forced outages and thus huge financial benefit.

1.2 Introduction

Most of the ESP's currently running were designed before 1960 with the technology available at that time resulting in systems that operate at low efficiencies. By implementing the latest design techniques on older systems, the efficiency of these older systems can be improved considerably, which subsequently increases the life span of such older systems while still complying with current emission standards and

the requirement for low running costs. One such design technique is the use of Computational Fluid Dynamics (CFD) to investigate fluid dynamic phenomena (such as heat transfer, multiple phase flow and transient flow) in aerodynamic systems. Due to the expensive and tedious nature of traditional optimisation methods such as field-testing and physical models, CFD is fast replacing these methods as a design tool in the optimisation of flow systems. The use of CFD for the modelling of screens is a recent development and subsequently information on this topic is limited.

When modelling a porous screen in a diffuser using CFD, it is impractical to model such screens in detail due to the large number of numerical cells that would be required. Chapter 3 of this study is dedicated to investigating the influence of numerical cell refinement on the accuracy of the pressure differential across the screen. In short, it can be stated that it is not practically and economically viable to run models of such size as computers with this capability are extremely expensive and the excessive running time required to obtain a satisfactory solution would make such modelling impractical. A more practical way to model these screens is by using porous baffles or porous media. The conventional approach was to model screens in the flow field as porous baffles, which are cells with zero thickness of which the flow resistance is calculated by the following equation (Star-CD v3.15 Methodology manual, 2001:8-3):

$$\Delta P = -\rho(\alpha v + \beta)v \qquad \textbf{(1.1)}$$

Where: ΔP = *Pressure differential across the porous baffle (Pa)*

ρ = *Density of the fluid (kg/m^3)*

α = *User defined variable (kg/m^4)*

β = *User defined variable (kg/m^3.s)*

v = *Perpendicular superficial approach velocity (m/s)*

This equation applies the resistance only to the normal component, i.e. normal to the baffle surface (Star-CD v3.15 Methodology manual, 2001:8-3). It is also assumed that the screen is of zero thickness while the thickness of screens used in practice range from approximately 2 to 10mm (with a hole size of approximately 40 to 200mm). These assumptions result in the resistance across a screen in a diverging diffuser being calculated incorrectly as shown in Figure 3a. The normal component of the inlet velocity decreases as the angle Φ increases, thus resulting in a lower pressure drop being implemented (in Star-CD) at a lower normal component regardless of the

magnitude of the velocity. In practice however, larger approach angles result in smaller FAR and higher flow resistance. The actual flow resistance is shown in Figure 3b. The thickness of the screen is responsible for the increase of resistance with an increase of flow approach angle since the thickness reduces the free area of the screen as the approach angle increases (discussed in more detail in Chapter 6). It is therefore not accurate to assume an infinitely small thickness for porous baffles in most cases.

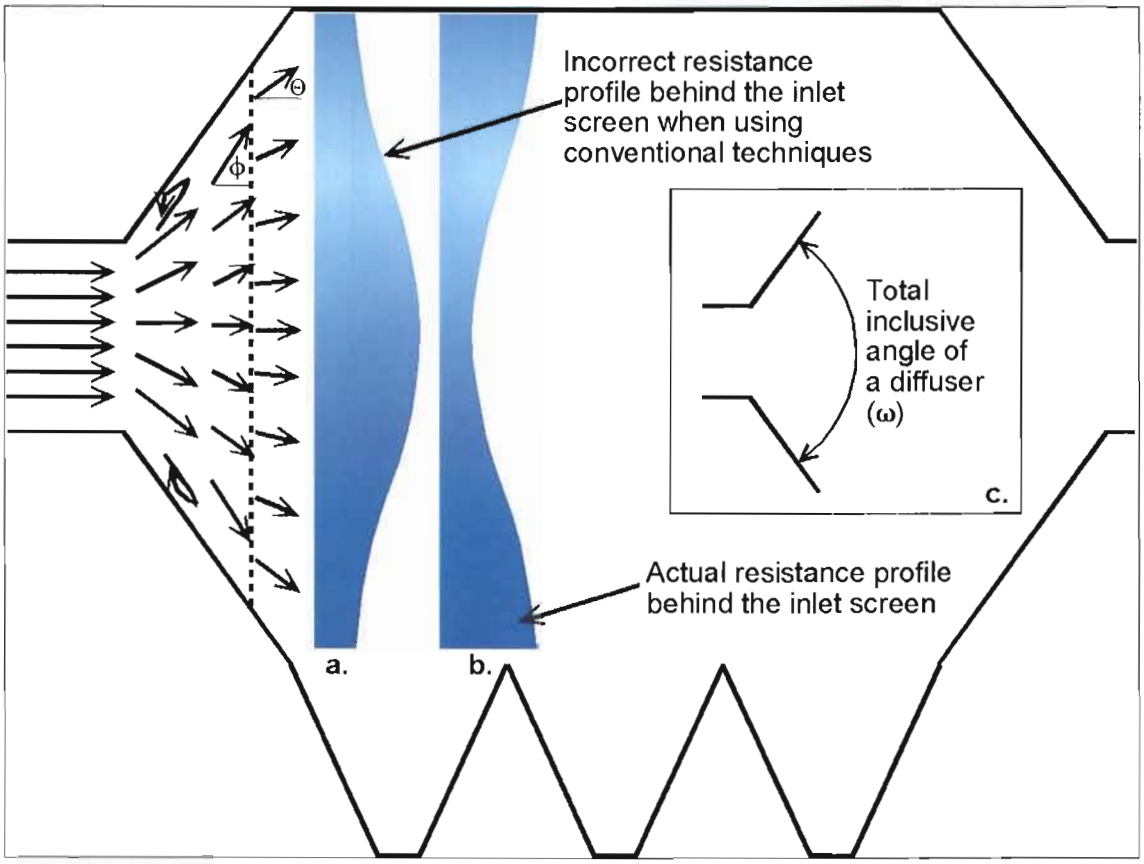

Figure 3: Pressure distribution behind a screen in a diffuser

Further research (Schubauer, Spangenberg and Klebanoff, 1950:5-6) has shown that a flow stream, which approaches a screen at some angle to the normal is deflected toward the normal when passing through the screen (as shown in Figure 3), i.e. if Φ is the angle of incidence, measured from the normal, and Θ is the corresponding exit angle from the screen, it is found that Θ is less than Φ. Since this deflecting phenomenon is recognised as an important characteristic of a screen, it becomes desirable to simulate the deflection of the flow when screens are used in diffusers. Due to the fact that a zero thickness is assumed, the influence on the change in flow

direction is underestimated. It can therefore be concluded that the assumptions that are made when using porous baffles in diffusers are not correct and may result in an inaccurate pressure and velocity distribution downstream of the screen.

The equation for calculating the perpendicular resistance of porous screens is the following (Koo & James, 1973:513):

$$K_p = \frac{2\Delta P}{\rho v^2} \tag{1.2}$$

Where: K_p = *Resistance coefficient for perpendicular approaching flow*
ΔP = *Pressure differential (Pa)*
ρ = *Density of the fluid (kg/m^3)*
v = *Perpendicular superficial approach velocity (m/s)*

When the flow approaches the screen surface at a non-perpendicular angle, this equation can be amended to the following (Livesey & Laws, 1978:249):

$$K_o = \frac{2\Delta P}{\rho v^2}\cos^2\phi \tag{1.3}$$

Where: K_o = *Resistance coefficient for oblique approaching flow*
ΔP = *Pressure differential (Pa)*
ρ = *Density of the fluid (kg/m^3)*
v = *Perpendicular superficial approach velocity (m/s)*
Φ = *Angle of incidence (°, refer to Figure 3)*

Equation (1.3) reduces to equation (1.2) in the case of an incidence angle of 0°. Although equation (1.3) represents the pressure loss coefficient at a flow approach angle other than perpendicular to the face of the screen, it only applies when the complete face of the screen is exposed to the approaching flow at a specific angle, e.g. when the screen covers the total flow area of the flow channel as shown in Figure 4. This equation cannot be used in diffusers as the flow approach angle continuously changes over the face of the screen (as was shown in Figure 3). Furthermore, this is a fixed coefficient and cannot be varied to allow for changes in the flow direction.

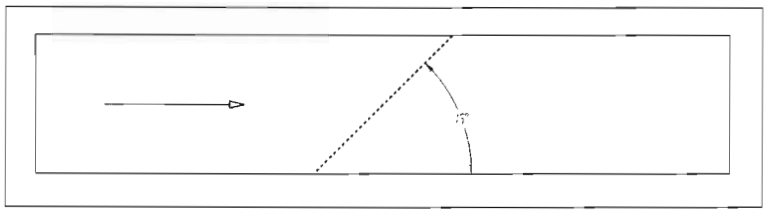

Figure 4: Oblique screen in flow stream

In a controlled environment, e.g. a laboratory based wind tunnel, it is possible to ensure that the approach velocity angle stays constant which will enable the accurate use of this equation. However, in industrial applications, it is almost impossible to maintain flow direction and therefore it is not accurate to use this equation for the calculation of angled pressure loss coefficients in uncontrolled environments. For this reason, it is necessary to either model the screen in detail, i.e. to model the exact amount of holes over the complete face of the screen to the exact scale, or to define a variable resistance coefficient, which would mathematically simulate the true pressure differential profile induced by the screen.

Due to the possible inaccuracies in the calculation of the pressure drop over a porous baffle in CFD modelling, the "filling effect" of screens and the change in the direction of the flow cannot be accurately simulated in a CFD model using conventional techniques. It is therefore necessary to develop a method to accurately predict flow through screens in a diffuser.

It can be concluded that the following factors have to be considered to accurately model the flow through screens in a diffuser:

- the change in the resistance as a function of the angle of incidence, the thickness and the Free Area Ratio (FAR) of the screen (the FAR is the ratio of flow area through the screen divided by the total flow area of the duct)
- the deflection of the flow stream as it passes through the screen

This study proposes to investigate advanced numerical methods for the simulation of porous screens in diffusers by integrating the variable resistance across a uniformly distributed porous screen into a commercial CFD code as a function of the angle of incidence and screen geometry. The theory is correlated with empirical data from a low speed (sub-sonic) wind tunnel, which is designed and constructed for this specific

purpose. User programming, which incorporates the newly developed equations, are then formulated to add these equations to current CFD programming codes for the purpose of interactively calculating the accurate effect of screens in diffusers.

Hypothetically, the CFD user would be able to enter the physical geometry of the screen into the developed user-defined functions with the CFD code calculating the variable resistance as a function of the angle of incidence and the deflection of the flow through the screen without the need for experimental work.

1.3 The importance of the study

The successful completion of this work would have the following advantages:

- A low speed wind tunnel is designed, constructed and commissioned for the testing of flow and pressure distributions. This facility is also calibrated for use in future studies.
- A methodology for testing screens in diffusers is developed.
- Empirical data is presented for specific screens that could be used as reference for future studies.
- From the experimental study, invaluable insight is gained into the behaviour of flow through large-angle diffusers.
- Improved modelling of velocity profiles.
- Improved modelling of the pressure distribution downstream of the screen.
- From the numerical study, invaluable insight is gained into the numerical methodology and practices.
- The investigation into the applicability of commercial turbulence models to wide-angle diffusers will aid future simulations of similar applications.

1.4 Problem statement

With the background and introduction given above, the problem statement can be defined as the following:

Current numerical methods do not sufficiently account for changes in the predicted pressure differential across porous screens in applications where the angle of incidence changes continuously across the face of the screen. No correlations could

be found to test newly developed methodologies. The purpose of this research is to investigate advanced numerical models using variable resistance factors for the accurate calculation of pressure differential and velocity profiles induced by a perforated screen in an aerodynamic diffuser with specific reference to the effect of angle of incidence and physical screen properties and to test these models empirically. Furthermore, these models will then be converted to user programming to be included in current CFD software which will enable the user to simply supply the physical screen properties and the CFD software will interactively and accurately calculate the pressure and velocity profiles behind the screen.

1.5 Delimitations

The following delimitations are applicable:

- This study included only square lattice screens. Currently, these screens are widely used in industry and therefore it was decided to focus only on this type of screen. Although other types (mainly round holed screens, but also round wire meshes and expanded metal screens) are sometimes used, it is not possible to include all of the different types in this study. It is recommended that the current research be expanded to other types of screens at a later stage.
- Screens tested covered the complete flow area, i.e. tests were not conducted on screens covering only part of the flow area.
- Only single screens were tested, i.e. screens can also be used in series (in line) to create additional resistance.
- All flows were assumed to be time independent (steady state) flows. This assumption is not always true in practise since power stations are forced to do load following. These load changes are however slow and far apart and other interference from control systems causes only small perturbations.
- Only incompressible flow was included.
- It was assumed that the process was adiabatic and isothermal, i.e. any heat transfer through the walls of the wind tunnel is not modelled and since changes to the temperature in the laboratory are very slow (no more than 15°C per day), it was assumed that the inlet and outlet temperatures remain equal and there were thus no density changes through the wind tunnel. For the CFD modelling, it was assumed that the air is an ideal gas with the density being a function of both

pressure and temperature. For this reason, the small variation in density through the screen as a function of the pressure drop was accounted for.

- This study did not include research into the laminar flow region due to the fact that the flow in actual ESP's are fully turbulent and therefore laminar flow behaviour was not considered. This refers only to the turbulence of the approaching flow. It should be noted that the flow may be laminar in some regions, especially downstream of the diffuser.

1.6 Outline of dissertation

Chapter 2 gives an in depth discussion into the literature survey conducted for this study. This discussion investigates the relevance of previous work, the applicability to this study and comments on the methods used and adopted approaches of relevant literature.

Chapter 3 investigates the feasibility of modelling screens in detail and the practical implications of detailed modelling. From this discussion, it will become clear why it is necessary to develop mathematical models to simulate screens in a diffuser rather than modelling screens in detail.

Chapter 4 discusses the design, construction and commissioning of a low speed wind tunnel. This discussion includes the test setup and test procedures, correlation of empirical data with literature and dynamic similarity of the wind tunnel.

Chapter 5 investigates the modelling of flow separation in wide-angle diffusers. The discussion commences with the detail of the CFD model used for this study and focuses on the modelling approach adopted, the sensitivity of the results to mesh refinement and the application of modelling assumptions. The remainder of this chapter focuses on the influence of numerical assumptions, i.e. turbulence models, numerical discretisation schemes and cell refinement, on the accurate prediction of the separation and re-attachment of the flow across a range of different diffuser angles.

Chapter 6 gives a detailed discussion of the mathematical and numerical approaches proposed. The discussion also includes a section on writing and compiling the user defined functions.

Chapter 7 presents the empirical and numerical results obtained and investigates the correlation between these results. This discussion also focuses on the applicability of the numerical model for general purposes.

Chapter 8 is the closing chapter and summarises the research and development that is presented by this study and also discusses the contribution made and practical applicability of the research performed. Recommendations are also made on possible future work and further research required.

1.7 Summary

This chapter gave an introduction to the problem and the relevant background pertaining to the physical area of application. The importance of this research was outlined and the delimitations applicable to this study were listed.

The next chapter gives an in depth discussion into the literature survey conducted for this study. This discussion investigates the general approaches used in previous studies, the applicability to this study and also comments on the methods reported by relevant literature.

CHAPTER 2: LITERATURE SURVEY

2.1 Introduction

This chapter gives an in depth discussion of the literature surveyed for this study. The discussion investigates the general trends used in previous studies, the applicability to this study and also comments on the methods used by relevant literature.

The influence of uniformly distributed resistances on flow has been a topic of research for quite some time with publications dating back to 1942 (Eckert and Pfluger). Researchers have focused on many different applications, screen configurations, flow-regimes and measuring techniques. This chapter investigates the applicability of these publications to the modelling of porous screens in aerodynamic diffusers using variable resistance factors.

The literature survey was divided into a number of specific topics that would later form the basis of this study. These topics include the following:

- Design, construction and commissioning of the wind tunnel
- Flow through porous screens in general
- Oblique flow through porous screens
- Experimental research on wide-angle diffuser and screen combinations
- CFD modelling of abrupt flow expansions and screen combinations
- Variable resistance factors

2.2 Design, construction and commissioning of the wind tunnel

Before commencing with the design of the low speed wind tunnel, a literature search was conducted to investigate the most commonly used methods and approaches and to determine the applicability of the information to this study.

Livesey and Laws (1972:186) as well as Schubauer, Spangenberg and Klebanoff (1950:23) used a closed loop approach. Due to financial constraints and space limitations, it was not possible to construct such a system and this approach was therefore discarded. Further research showed a general trend in the design of a low speed wind tunnel. Mc Carthy (1964:505), Pinker and Herbert (1967:15), Eckert and

Pfluger (1941:11), Plint and Böswirth (1978:26) and Taylor and Davies (1944:14) used a design that included the following basic setup:

1. A single in-line testing pipe or ducting. A single duct approach simplifies the design since it is not required to design turning vanes before the test section to ensure that the flow is well distributed as it enters the test section. This approach is also more economical since the amount of ducting and supports are reduced significantly. Frictional losses through the system are also minimised resulting in higher flow rates.
2. Some form of inlet bell mouth (also called an entrance nozzle in some references) to ensure a proper inlet flow distribution. The proper design of this inlet bell mouth is essential to ensure a uniform flow distribution at entry to the test section.
3. An inlet flow rate measurement to determine flow rate and to ensure stability of the flow.
4. The testing section. This test section would vary between studies depending on the specific aim and objective of the experimental work.
5. The flow generator. In most cases a fan is used, but other methods such as compressed air can also be used.

This basic setup was adopted for the design of the low speed wind tunnel that was used for this study. The design, construction and commissioning is discussed in more detail in CHAPTER 4.

2.3 Flow through porous screens in general

Eckert and Pfluger (1941), Livesey and Laws (1972, 1973, 1978), Elder (1959), Brundrett (1993) and Taylor and Davies (1944) conducted studies on the resistance coefficients of commercial round wire screens. The dynamics of flow passing through round wire screens are markedly different than with perforated plates and this study only includes the latter. This research is therefore not directly applicable. Livesey and Laws (1978:261) however did include an interesting discussion on the suppression and generation of turbulence by screens. A correlation is drawn between the Reynolds number of the wire and the resulting influence on the turbulence of the flow downstream of the gauze. *"Tests included parallel cylinder arrays and biplane orthogonal square grids, of either cylinders or square section bars, commercial woven*

mesh grids and punched plates." Results showed that at a sufficiently large distance downstream (40 mesh lengths), the turbulence is near to homogeneous and nearly isotropic [longitudinal to transverse velocity ratio (rms) 1.15]. The turbulent intensity is highest in close proximity to the grid and decays further downstream. The information supplied is however limited.

Taylor and Davies (1944:1, 5-8) also tested perforated metal sheets with circular holes in hexagonal and square arrays. A series of tests were conducted using wind tunnel and water tube experiments. Some tests showed good correlation between these two methods for the measured resistance coefficient (K), i.e. 1.6 percent. In other cases however the correlation was unsatisfactory where a difference of 22 percent was reported. Further research produced literature that reported better results and for this reason, it was decided to disregard these results. Furthermore, this study focuses on square holes in a square array and not circular holes.

Research conducted at a later stage included tests on non-uniform wire grids (Mc Carthy (1964:491), Livesey and Laws (1973) and Koo and James (1973:516)), which as mentioned in paragraph 1.5, is not applicable to this study. All screens included in this study are uniform across the total projection area of the flow.

Pinker and Herbert (1967) studied pressure losses associated with marginally compressible flow through square mesh wire gauzes, velocities range from 0.1 to 0.5 Mach. The emphasis of this study was on flows of much lower magnitude (0 to ±0.1 Mach) and not on wire gauzes. However, their findings on the contour of the pressure gradient line across the screen at low Mach numbers were found to compare very well with results from previous studies.

Budoff and Zorumski (1971) studied the flow resistance of perforated plates in tangential flow for flows up to a Mach number of 0.44. Porous screens were fitted at the connection between two pipes fitted in a "T" and the flow was moved tangentially across the face of the screen. Tests were conducted for both flow directions and results showed that flow resistances measured for normal flow into the tangential flow duct were higher than for the same normal flow out of the duct, indicating a discontinuity of flow resistance when normal flow was reversed. This increase in flow

resistance can be contributed to the fact that the flow entering the screen tangentially approaches the screen at an incidence angle of smaller than 90° thus reducing the free area ratio and increasing the resistance. If this flow is reversed, the angle of incidence is approximately 90° and therefore the FAR is a function of only the free area divided by the total area. The present study investigated the change of FAR as a function of angle of incidence and showed that the resistance increases as the angle of incidence is increased from the normal. Results from this study therefore concur with results presented by Budoff and Zorumski (1971) for the low Mach number cases. Further tests included an investigation of the influence of higher Mach numbers, but these results are not applicable to this study.

Turner (1969) was amongst the first researchers to attempt to define a computational method to define flow through non-uniform round wire gauzes in a two-dimensional approach. This research is however not applicable since the screens were round wire gauzes and were not uniformly distributed across the flow area.

In order to determine the accuracy of the experimental setup, it was required to test screens in a straight duct with perpendicular flow and results were compared to: The Handbook of Hydraulic Resistance (Idelchik 1986:389), Applied Fluid Dynamics Handbook (Blevins 1984:279) and Internal Flow Systems (Miller 1978:260). All these references include results from tests conducted on a large number of screens, which enabled the authors to produce graphical trends of resistance coefficients. This allows comparison of almost any available screen across a wide range of velocities. Furthermore, screens used in these literature sources covered the total projection area of the testing tunnel and flows were uniform.

2.4 Oblique flow through porous screens

Schubauer, Spangenberg and Klebanoff (1950) were amongst the first researchers to investigate the resistance of oblique flow through screens. The term "oblique" refers to flow that approaches the screen at an angle different to normal to the face of the screen as shown in Figure 5. With oblique flow however, the angle of incidence is always constant and therefore this research is only applicable where the flow approaching the screen is uniform and in line with the duct walls. In other words, the resistance is still constant across the screen although the absolute value of the resistance coefficient is increased at non-perpendicular angles. Flow is seldom

uniform and in line with the duct walls in industrial applications and therefore the use of this research is rather limited.

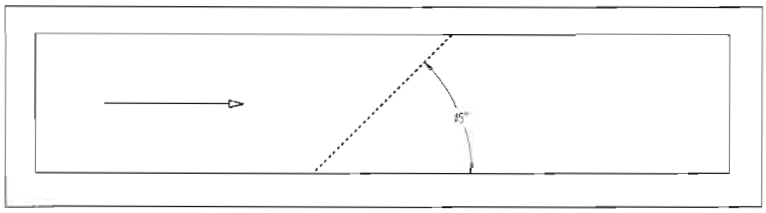

Figure 5: Oblique screen in flow stream

The research conducted by Schubauer, Spangenberg and Klebanoff (1950:18) focussed on oblique flow through round wire gauzes and are therefore not directly related to the present research. However, some of the general comments were found to be applicable and very interesting. It was concluded from the research that when a flow stream approaches a screen with a velocity U at the angle Φ and leaves at the angle Θ, the pressure drop is some function of U cos Φ. In other words, the pressure drop under these conditions is determined by the normal component of the approach velocity. It was also found that the eddies produced by a damping screen result in turbulence of small scale, which decays rapidly in the first few feet. However, the rate of decay becomes low at a turbulence level around 0.1 percent, and long distances are required if the screen itself is not to set a lower limit of the order of 0.1 percent. A screen should therefore be followed by a contraction of the stream to increase the mean speed and so decrease the percentage value of the turbulence. It was also found that a screen may produce abnormally high and slowly decaying longitudinal fluctuations, which were not completely understood. In general and based on the performance of damping screens throughout these experiments, it was found that screens of high K are less satisfactory as dampers than screens of low K. This applies both to turbulence and spatial variations. It appeared preferable to obtain a given reduction by using several screens of low K in series, rather than by using a single screen of high K.

Later research conducted by Hoffmann (2002) focused on oblique flow through expanded metal screens. This research was amongst the first to be conducted, which combined the resistance coefficients of oblique flow through screens with the introduction of mathematical modelling using CFD and by implementing the momentum

source term in the calculation of the Navier-Stokes transport equations using User Defined Functions (UDF's). This research was found to be most relevant to this study.

Screens were tested at a range of angles in a straight wind tunnel configuration (see Figure 5) and results from the individual tests were combined to allow for the calculation of the variable resistance coefficient. Due to specific requirements, this research focused on testing only expanded metal screens (as shown in Figure 6) and did not include square lattice and round holed flat porous screens. Furthermore, this approach does not compensate for the three dimensional diffusion of the flow in a diffuser. Also, the walls of the flow channel constrain the flow after the screen, i.e. the deflection of the flow is artificially "corrected" downstream from the screen. This is not the case in a wide-angle diffuser where the flow is allowed to expand into the total flow area.

However the calculation of the momentum source term was found to be most relevant to the approach employed by the present study and was used as the basis for further calculations. The mathematical approach is discussed in more detail in CHAPTER 6.

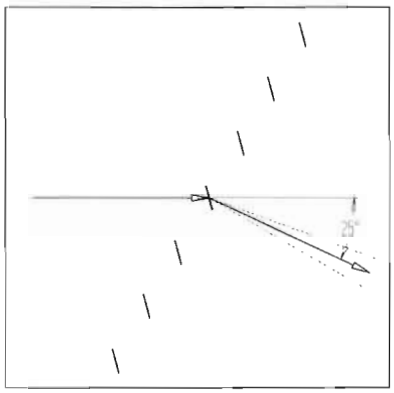

Figure 6: Oblique expanded metal screens in flow stream

2.5 Experimental research on wide-angle diffuser and screen combinations

The use of CFD for the modelling of screens is a recent development and subsequently information on this topic is limited. The literature survey was therefore aimed at finding experimental data that could be used as a reference for results from the CFD modelling. Although a large amount of experimental work has been done on screens in aerodynamic diffusers, many publications were related to the aeronautical industry and the use of porous screens or round wire meshes for the distribution of flow in

aeronautical applications. Unfortunately a substantial amount of this information was confidential and was therefore not available. A search on the NASA Technical Reports Database with the topic of "wide-angle diffusers" supplied only two articles dating back to 1948 (Schubauer and Spangenberg).

Schubauer and Spangenberg (1948) were amongst the first researchers to test screens in diffusers. The aim of the investigation was to clarify the "filling effect" commonly observed when a screen or similar resistance is placed at the mouth of a wide-angle subsonic diffuser. It was found that: When the pressure drop is many times the dynamic pressure, the flow through all pores of the screen is determined by the pressure drop and is nearly equal regardless of the condition of the approaching flow. The investigation was therefore restricted to fine screens of low solidity.

Different to the present study, diffusers were conical (circular cross section) and results could therefore not be compared directly. In the aeronautical industry conical diffusers are commonly used, but this is not the case in the power generation industry where ducting is normally rectangular especially in the region of the filtration system. Schubauer and Spangenberg (1948:8) adopted the following measurement technique: Systematic measurements were made with single screens at various positions in the diffuser. For each screen and each position, static- and dynamic pressure traverses were measured across two traverses 90° apart at several locations. Representative distributions across a section were obtained by averaging values of the two diameters. Most measurements were made at a single wind speed in the turbulent flow region. Furthermore, screens were tested in the centre of the diffuser and with different diffuser angles (Schubauer and Spangenberg 1948:29). These measuring techniques were adopted for the present study.

Unfortunately, diffusers were constructed with a transition radius and are not sharp edged as is the case in the power generation industry. The present study is aimed at the use of aerodynamic diffusers in the power generation industry and with sharp edged diffusers, flow separation occurs more frequently especially at increasing diffuser angles and higher Reynolds numbers. With rounded edges, flow separation may in some cases not occur and therefore the research by Schubauer and Spangenberg (1948) is not directly applicable. However, the discussion on the

mechanism of flow through a diffuser and screen combinations (Schubauer and Spangenberg 1948:11) were found to be of interest.

Moore and Kline (1958) conducted extensive research into the effect of vanes and of turbulence in two-dimensional wide-angle diffusers. Typical to diffusers in the aeronautical industry, the research was aimed at two-dimensional diffusers with an elliptical bell mouth type inlet. It was found that in the absence of vanes or other means of boundary layer control, all of the following parameters are important in determining the behaviour of the flow: divergence angle, ratio of throat width to wall length and free stream turbulence. It was found that the divergence angle alone is not the only determining factor. As mentioned previously, the aeronautical diffuser application is not directly applicable to the present study.

However, concurring with the research by Schubauer and Spangenberg (1948), Moore and Kline (1958) found that variations in Reynolds number and aspect ratio seem to have little effect on the flow regime for the range of aspect ratios normally encountered and for all Reynolds numbers in excess of a few thousand (i.e. in the transition region between fully laminar and turbulent flows). Based on these findings, experiments for the present study were conducted at only a single Reynolds number in the turbulent range.

Research conducted by Sahin and Ward-Smith (1991) focussed on multiple screens in wide-angle diffusers. This research was some of the first work conducted on the optimisation of the ESP inlet flow distribution using porous screens. Owing to factors arising during fabrication, the performance of even well designed perforated plate-diffuser combinations can be deficient in practice. Under such conditions, uniformity of the flow can be regained by applying local blanking of the perforated plate wherever high velocities are found. The work of Gibson and Schmitz (1999) was based on the approach suggested by Sahin and Ward-Smith (1991).

This is a purely practical approach focussing on multiple screens in a diffuser, which does not form part of the present study and therefore this research is not directly applicable. However, this research introduced a notion that any mathematical model is only as good as the manufacturing process and conformance to manufacturing

tolerances. This notion implies that although a mathematical model may work in a controlled environment, e.g. a laboratory based wind tunnel using ducts and screens manufactured to exact standards, this model may not work in all industrial applications due to manufacturing and installation errors. This notion instils a measure of uncertainty since the manufacturing of two ESP's from the same design drawings will differ, which may influence the practicality of any mathematical model. A requirement is therefore placed on the mathematical model to ensure that numerical errors are smaller than production errors. It is however very difficult to quantify the uncertainty of production errors.

2.6 CFD modelling of abrupt flow expansions and screen combinations

The development and application of mathematical turbulence models have been a topic of research for a considerable amount of time. Sir Horace Lamb stated in 1932 during an address to the British Association for the Advancement of Science (Adapco 2002):

"I am an old man now and when I die and go to heaven there are two matters on which I hope for enlightenment. One is quantum electrodynamics and the other is the turbulent motion of fluids. And about the former, I am rather optimistic."

Researchers have attempted for many years to understand and simplify turbulence mathematically, but still today it is a rather illusive subject although recent years have seen tremendous advancement in this field. This advancement in the mathematical simplification of turbulence has been driven by the CFD simulation codes to improve the code's ability to accurately predict the turbulent motion of fluids with simplified (averaged) mathematical models.

It should be noted that the standard momentum equations (Navier-Stokes equations) are capable of modelling turbulence accurately without the aid of simplified mathematical models. The problem comes in the number of cells that is required (due to the high levels of refinement) to model turbulence directly. This simulation technique is called Direct Numerical Simulation (DNS). Ferziger and Perić (2002:266-268) states the following solution methods for turbulence:

- Direct Numerical Simulation (DNS)
- Large Eddie Simulation (LES)

- Reynolds averaged Navier-Stokes (RANS) Equations
- Reynolds Stress models

Versteeg en Malalasekera (1995:49) state that a typical flow domain of 0.1m by 0.1m with a high Reynolds number turbulent flow might contain eddies down to 10 μm and up to 100 μm in size. Computing meshes of 10^9 up to 10^{12} points would therefore be required to be able to describe processes at all length scales. Therefore, at least one million cells (100*100*100) are required per cubic centimetre. The volume of the wind tunnel in the present study is approximately 1.2 m^3 or $1.2*10^6$ cm^3. Based on the above approximation, it can be seen that $1.2*10^{12}$ cells is required to model the wind tunnel with the DNS approach. These methods is discussed in more detail in CHAPTER 5, however it can be concluded that it is not practical to model high Reynolds number flows using DNS.

In the Reynolds-averaged approaches, all of the unsteadiness is averaged out, i.e. all unsteadiness is regarded as part of the turbulence. Furthermore, it is highly unlikely that a single RANS model will be able to represent all turbulent flows and therefore these models should be regarded as engineering approximations rather than scientific law (Ferziger and Perić 2002:292). It is in this area that the most development is taking place with the aim of developing a single RANS model that would be able to represent most flow applications.

Due to the highly competitive nature of the CFD industry, this research is confidential in most cases. Although it may be possible to find the mathematical formulation of these turbulence models, the integration of these models into the CFD codes is confidential. This part of the literature survey was aimed at finding information on the correct turbulence models to be used to predict the separation of turbulent flow in wide-angle diffusers. Direct requests to both the local agents of Star-CD and Fluent Inc. produced only a single paper on this matter, Vaivads *et al.* (1998). The survey was expanded to the validation cases (only the cases made available) of both codes and it was found that the traditional case: "Flow over a backward facing step" is used to validate turbulence models for diverging flow through abrupt expansions. Research has also been conducted on adapting the coefficients of current turbulence models (e.g. k-ε) in an effort to improve the accuracy of the predicted re-attachment of the flow across a

backward facing step (Craig *et al.* 1998). It is however not certain if the back step case is directly applicable to wide-angle diffusers. One of the aims of this study is therefore to investigate the applicability of commercial turbulence models to wide-angle diffusers.

The research conducted by Vaivads *et al.* (1998) focused on the optimisation of the RMC wind tunnel using the commercial CFD code Fluent Inc. Results presented were unfortunately rather limited, but did provide an excellent reference to better understand the flow through large angle diffusers and the techniques used for modelling these flows. All simulations were two-dimensional and the standard k-ε turbulence model was used. It is not certain if the simplification of using a two-dimensional model to represent a three dimensional diffuser does account for the three-dimensional diffusion effect of the flow as it passes through the diffuser and expands to fill the larger three-dimensional flow area. With experimental studies discussed earlier in this chapter, the static- and dynamic pressure profiles were measured and compared. Vaivads *et al.* (1998:3) compares the velocity magnitude and turbulence intensity.

Iaccarino (2000) conducted research into the prediction of turbulent flow in a diffuser with commercial CFD codes. The diffuser was modelled with an angle of only 10° and the standard k-ε turbulence model was compared to the v^2-f model. Results from this research showed that the standard k-ε model did not accurately predict the flow separation and re-attachment through the diffuser and results were also not reproducible between codes. The accuracy of the calculation when using the v^2-f model compared to experimental and LES data was found to be very good. It is not clear what the applicability of this research is to wide-angle diffusers. The aim of the present research is to supply a solution with the codes that are readily available and unfortunately, the v^2-f model is not included in any of the commercial CFD codes as a standard option. This model can be purchased additionally at considerable cost and is therefore not easily obtainable by the CFD Engineer for general industrial applications. For this reason, the present research did not include the v^2-f turbulence model.

Research conducted by Simonsen *et al.* (1998:703) was found to be very relevant to this thesis. The research focused on the numerical simulation of screens in ESP's by incorporating drag and lift forces into the Navier Stokes momentum equation by replacing the body forces. This approach allows for the change in flow direction

through the screens since these two forces work in tangential directions. The notion of using drag and lift coefficients are introduced by defining the following coefficients: C_D (non-dimensional drag), C_P (pressure coefficient) and C_L (lift coefficient). Similar to Vaivads *et al.* (1998), the standard k-ε turbulence model was used.

One of the possible restrictions of this work was the fact that tests were conducted on a single sided 45° diffuser (see Figure 7) with a single screen. As mentioned previously, it was thought that the single sided two-dimensional approach (assuming symmetry) does not account for the diffusion effect through an aerodynamic diffuser and results may therefore not be representative of three-dimensional diffusers. Furthermore, this approach does not account for the change in the angle of incidence of the approaching flow and the subsequent increase in the resistance factor. For this reason, the calculated resistance (pressure) coefficient is not variable, but fixed for a given screen free area ratio. The mathematical approach was however investigated further as discussed in Chapter 6.

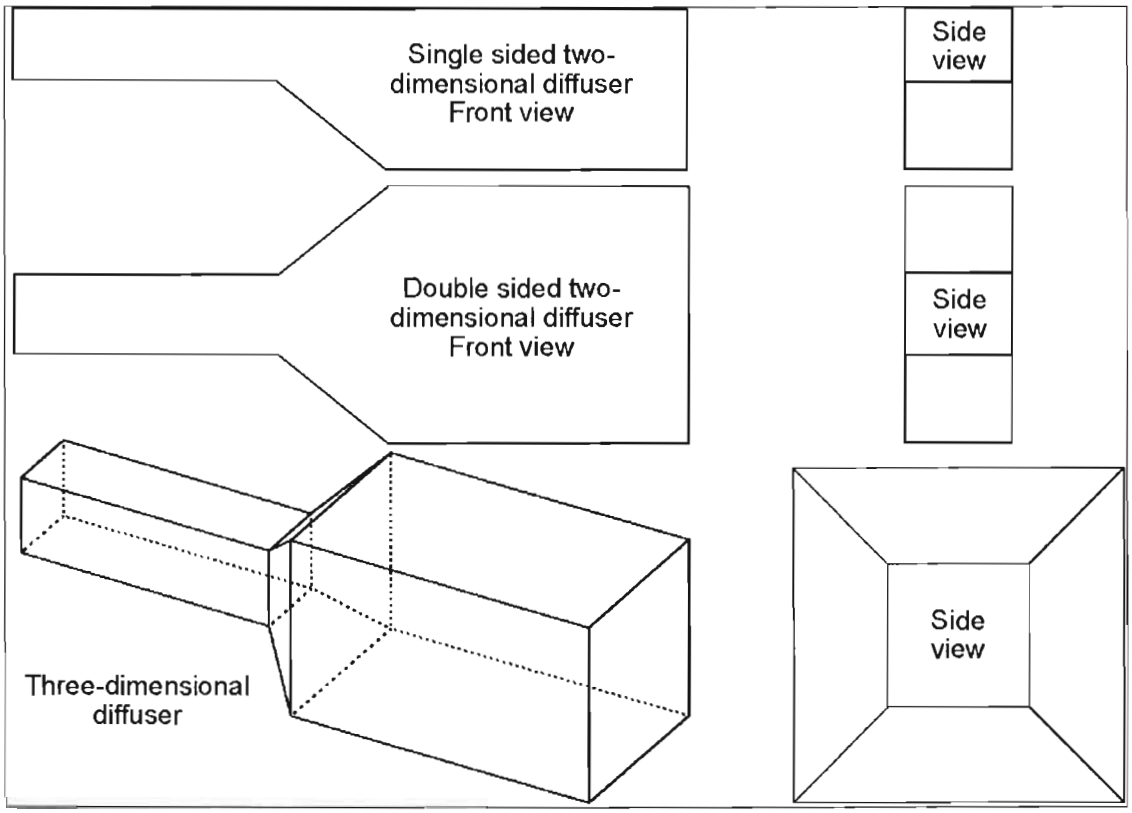

Figure 7: Diffuser types

Schmitz *et al.* (1998) compared three different approaches for modelling screens in diffusers:

- A detailed model of the screen in the diffuser with sufficient definition to incorporate a well-defined lattice screen into the model.
- Porous baffle approach. Due to the fact that the baffle cells have zero thickness, this approach is based on the mass transfer through the cell faces and is therefore an area-based method.
- Porous medium approach. Since the porous medium cells have a certain thickness, this approach is a volume-based method.

It was found that the detailed model compared well with the experimental velocity profile and the prediction of the pressure loss. However due to the high number of cells required, this approach is not practical when modelling large systems. With the porous baffle and porous media approach, the correlation was reasonable in some instances while poor in others. By introducing transverse resistance values to the porous media approach, a reasonable resistance value could be predicted. It can therefore be concluded that the porous media approach resulted in better correlation with empirical data than the porous baffle approach although it was stated that further development is required to correlate transverse resistance values.

Similar to research conducted by Simonsen *et al.* (1998) a one dimensional 45° diffuser was used. As mentioned previously, it was thought that this may be one of the possible restrictions of this work. Similar to previous studies, i.e. Simonsen *et al.* (1998) and Vaivads *et al.* (1998), the standard k-ε turbulence model was used. Furthermore, the user-defined resistance coefficients (α and β) were constant across the screen and did not allow for variations in the resistance due to changes in the angle of incidence.

2.7 Variable resistance factors

Apart from the research conducted by Hoffmann (2002), no information could be found on variable resistance factors for porous screens.

2.8 Summary

This chapter presented the literature survey that was conducted for this study. The survey was divided into a number of specific topics that would later form the basis of this study. These topics included the following:

- Design, construction and commissioning of the wind tunnel
- Flow through porous screens in general
- Oblique flow through porous screens
- Experimental research on wide-angle diffuser and screen combinations
- CFD modelling of abrupt flow expansions and screen combinations
- Variable resistance factors

A large number of literature sources were available on the design and construction of a wind tunnel, but it was found that many of these experimental sources included a basic setup, which was adopted for this study:

- A single in-line testing pipe or ducting.
- Some form of inlet bell mouth.
- An inlet flow rate measurement.
- The testing section.
- The flow generator.

Similarly, a large number of literature sources were available on flow through screens. It was found however that many of these focussed on round wire gauzes, non-uniform screens and transonic and supersonic flows. All of these factors fall outside the scope of this study and results from many of these sources could therefore not be used.

Oblique flow through screens was well represented in the literature although most studies also focused on round wire gauzes. Research conducted by Hoffmann (2002) supplied an excellent departure for this study and the mathematical approach was found to be most relevant although the screens tested were not included in this study.

The use of CFD for the modelling of screens is a recent development and subsequently information on this topic is rather limited. Although a large amount of experimental work has been done on screens in aerodynamic diffusers, many publications were related to the Aeronautical Industry and the use of porous screens or round wire

meshes for the distribution of flow in aeronautical applications. Unfortunately a substantial amount of this information was confidential and was therefore not available.

From the literature on the modelling of screens, it was found that the following were commonly applicable:

- A one-dimensional diffuser approach was adopted neglecting the three-dimensional diffusion of the flow through the diffuser.
- All studies used the standard k-ε turbulence model.
- Resistance coefficients were constant across the screen, neglecting the influence of increased resistance with a change in the angle of incidence due to the thickness of the screen.

Apart from the research conducted by Hoffmann (2002), no information could be found on variable resistance factors for porous screens or uniformly distributed resistances.

The following chapter investigates the feasibility of modelling screens in detail and questions the need for mathematical models.

CHAPTER 3: DETAILED MODELLING OF SCREENS

3.1 Introduction

This chapter focuses on the influence of the CFD model refinement on the pressure differential across a flat square lattice screen and investigates the feasibility of modelling screens in detail as opposed to developing mathematical models to simulate screens. To simplify this investigation, it was decided to use only a single screen in a straight duct with perpendicular flow approaching the screen. Figure 8 shows the square lattice screen used for this study. It can be seen that the screen consisted of a 10mm strip size and a 20 mm hole size, i.e. a Free Area Ratio (FAR) of 44.44 percent.

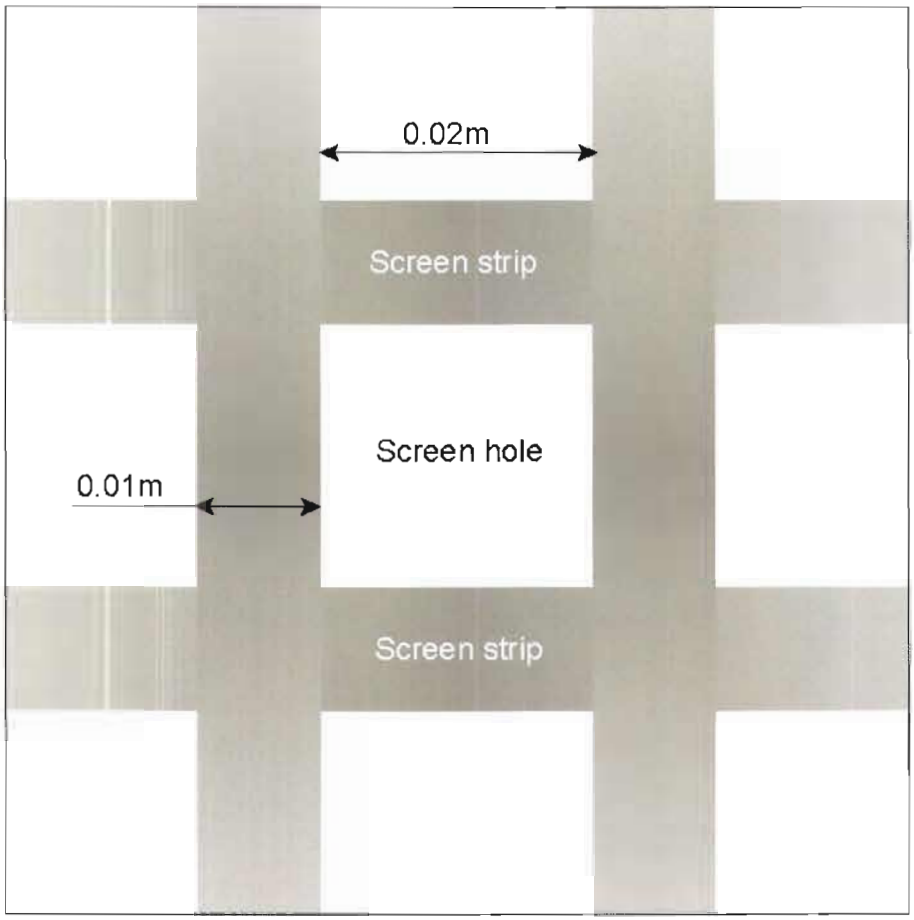

Figure 8: Detail of square lattice screen

The desired accuracy of the pressure differential calculated by the Computational Fluid Dynamics (CFD) software is dependent on the degree of refinement of the numerical mesh in close proximity to the screen. This is due to the fact that the degree of cell refinement applied to the model is proportional to the desired accuracy of the flow

simulation around and through the screen, producing better correlation to the actual flow conditions at the highest refinement levels. This will always be the case for laminar flow, but since mathematical models are used for turbulent flow, an optimum refinement level is reached beyond which the accuracy are not significantly improved. It is therefore necessary to determine the minimum degree of refinement required to achieve acceptable correlation between a turbulent numerical simulation and actual conditions. Furthermore, it is also required to determine the relationship between horizontal, vertical and axial refinement (see Figure 9). This chapter investigates these issues and reports on the findings.

3.2 CFD model

The mesh used for the CFD model consisted of a square duct, 0.75m in length (see Figure 9). The screen was positioned 0.15m from the inlet and a further 0.15m behind the screen was used as the testing region. The distance upstream and downstream from the screen was determined by calculating 15 times the lattice size. Idelchik (1986:392) states that flow requires 15 lattice sizes behind the screen to fully recover. This was confirmed by Janse van Rensburg (1997:23) and for this reason the testing section was positioned at a distance of 0.15m upstream and downstream of the screen. The remainder of the duct length was not refined and was used to ensure full recovery of the flow behind the screen. Symmetry boundaries were used on the sides of the model and the inlet velocity and temperature were set to 7.4 m/s and 20 °C respectively.

The commercial CFD code Star-CD was used with the following settings:

- the standard k-ε turbulence model
- the standard Upwind Differencing (UD) discretisation scheme
- default numerical relaxation
- the gas was assumed to be ideal

The above settings are generally accepted to be applicable to most industrial applications.

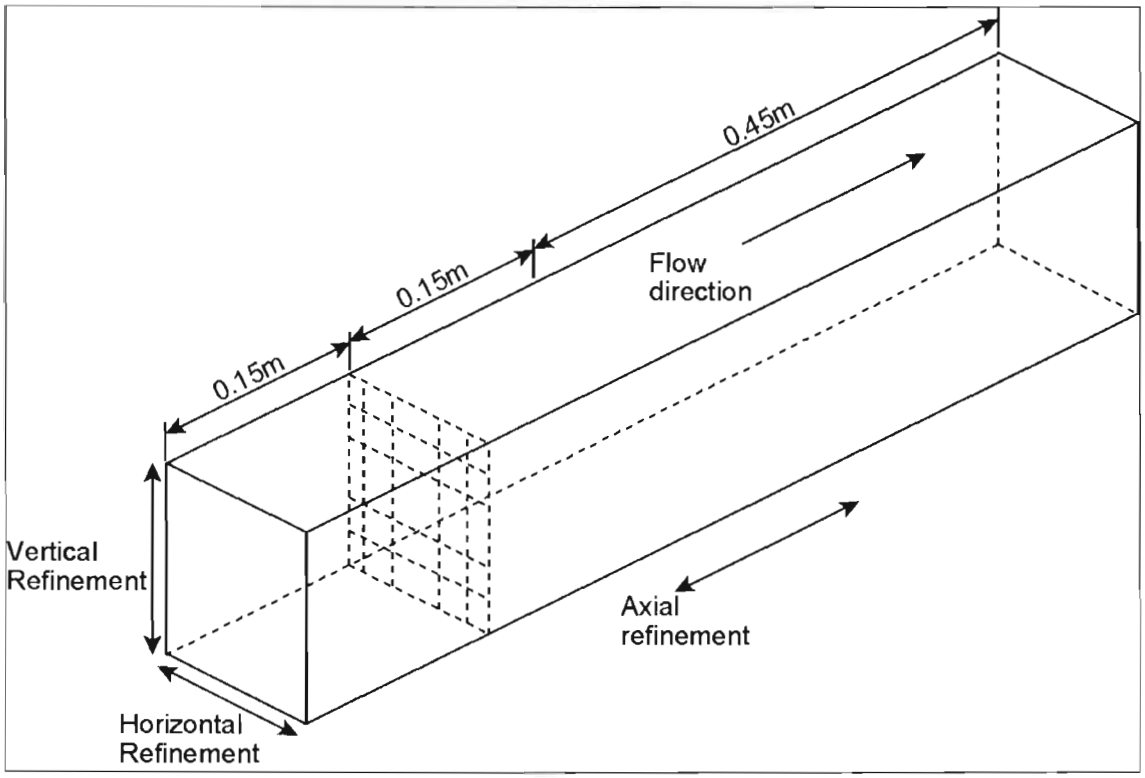

Figure 9: Model layout for the simulation of the square lattice screen

3.3 Results from literature

Three literature sources were consulted to find the correct pressure differential across the screen as shown in Table 1. The pressure differential at a given velocity can be calculated by manipulating equation (1.2):

$$\Delta P = \frac{1}{2} K \rho v^2 \qquad \textbf{(3.1)}$$

Table 1: Resistance factor values from literature

FAR	Miller[1]	Idelchik[2]	Blevins[3]	Average literature value
Resistance-factor (K)	6.1	6.12	5.94	6.05
ΔP (Pa)	166.83	167.48	162.55	165.62

1: Miller (1978:263)

2: Idelchik (1986:404)

3: Blevins (1984:314)

It can be seen that results from all literature sources compare well and it can therefore be stated that the true pressure differential across the screen should be in the range of 162.55 Pa to 167.475 Pa at a velocity of 7.4 m/s and a density of 1 kg/m^3.

3.4 Discussion of results

For the purpose of this study, the vertical and horizontal refinement was always kept similar and was therefore equally refined for each of the different test series. For the remainder of this chapter the horizontal and vertical refinement is referred to as the perpendicular refinement (see Figure 10). Five series of tests were conducted where the perpendicular refinement was constant for each series of tests while the axial refinement was increased for each simulation. Table 2 shows a summary of test conditions for each series of tests. Incremental refinement where the cell size was increased incrementally away from the screen was not included in this study.

Table 2: Description of test cases included

Test series	Perpendicular refinement	
	Number of cells used for the screen hole	Number of cells used for the screen lattice
Series 0	1	1
Series 1	2	1
Series 2	4	2
Series 3	6	3
Series 4	8	4

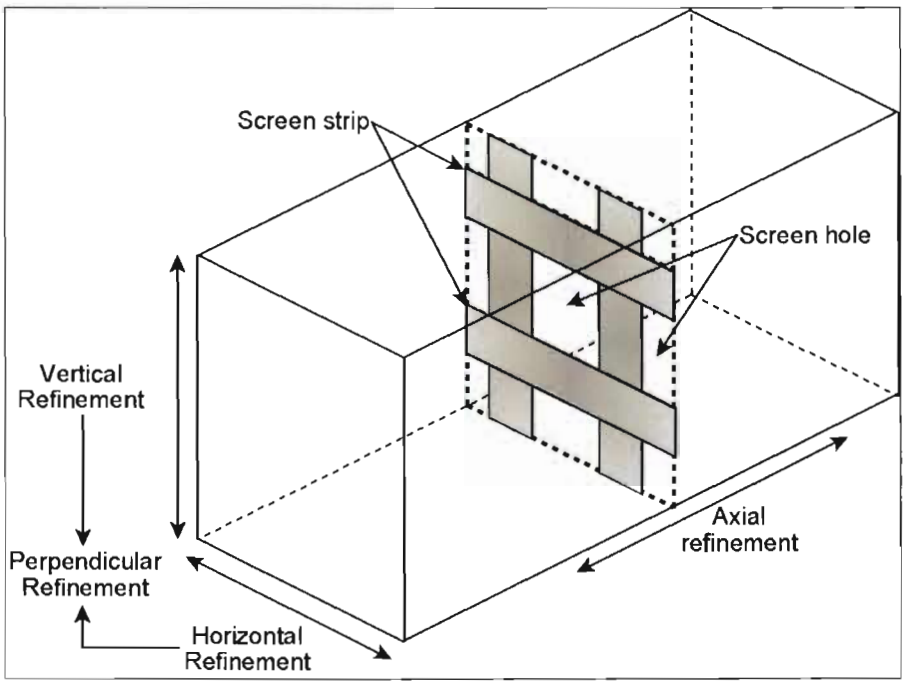

Figure 10: Explanation of numerical cell refinement

Table 3 shows results from all tests conducted. It can be seen that the pressure loss values predicted for tests number 1 and 2 for series 1,2 and 3 are abnormally high. This can be contributed to the fact that the aspect ratio of the cells for these tests is unacceptable producing inaccurate results. This is further confirmed by the fact that the values of tests 1 and 2 increase from series 1 to 3. For this reason, series 4 only consisted of 18 tests.

Table 3: Predicted pressure drop (Pa)

Test number	Axial Refinement	Series 0 (1 cell in hole)	Series 1 (2*2 cells in hole)	Series 2 (4*4 cells)	Series 3 (6*6 cells)	Series 4 (8*8 cells)
1	2	148.98	209.49	573.57	757.51	-
2	4	104.76	120.32	178.75	387.83	-
3	6	99.86	109.56	145.36	185.98	245.70
4	8	101.91	109.77	130.69	152.20	176.36
5	10	105.71	113.02	125.74	140.29	154.91
6	12	109.81	117.05	124.55	135.15	145.41
7	14	113.82	121.20	125.29	133.06	140.67
8	16	117.58	125.26	126.87	132.79	138.38
9	18	120.99	128.97	128.79	133.46	137.73
10	20	124.09	132.44	130.81	134.64	138.33
11	22	126.95	135.65	132.85	136.09	139.40
12	24	129.59	138.64	134.89	137.63	140.72
13	28	134.45	144.29	138.65	140.87	143.79
14	32	139.02	149.63	142.24	144.28	146.95
15	36	143.62	154.87	145.57	147.62	149.90
16	40	148.32	160.14	148.61	150.62	152.61
17	44	153.11	165.40	151.36	153.31	155.07
18	48	158.03	170.70	153.88	155.76	157.32
19	56	168.17	181.39	158.30	160.09	161.34
20	64	178.72	192.01	162.24	163.86	165.06

Note: To simplify the interpretation of these results, predicted pressure drops are formatted according to the following criteria:

- Values exceeding a margin of 10 percent above the correct range of pressure drops are marked in .

- Values within ±10 percent of the correct range of pressure drops are not marked.
- Values lower than a margin of 10 percent below the correct range of pressure drops are marked in [ ].

If these results are compared to results from the literature, it can be seen that values recover to the range of true pressure drop (162.6 Pa to 167.5 Pa). Although some CFD results at lower refinement levels do predict the pressure drop within an acceptable range (i.e. ±10 percent), it can be seen that the prediction is only consistent at the axial refinement value of approximately 40 and higher. Although all curves tend to the true range, the degree of axial refinement required to achieve this correlation is extremely high.

The curve of pressure differential against axial refinement value for each test series is presented in Figure 11. It can be seen that all curves follow the same trend. The pressure differential decreases with an increase in axial refinement of up to 15 times. This trend is then reversed as the axial refinement is further increased. It was expected that the lines would remain horizontal and that the gradient would tend to 0, however, the pressure differential continues to increase with an increase in axial refinement.

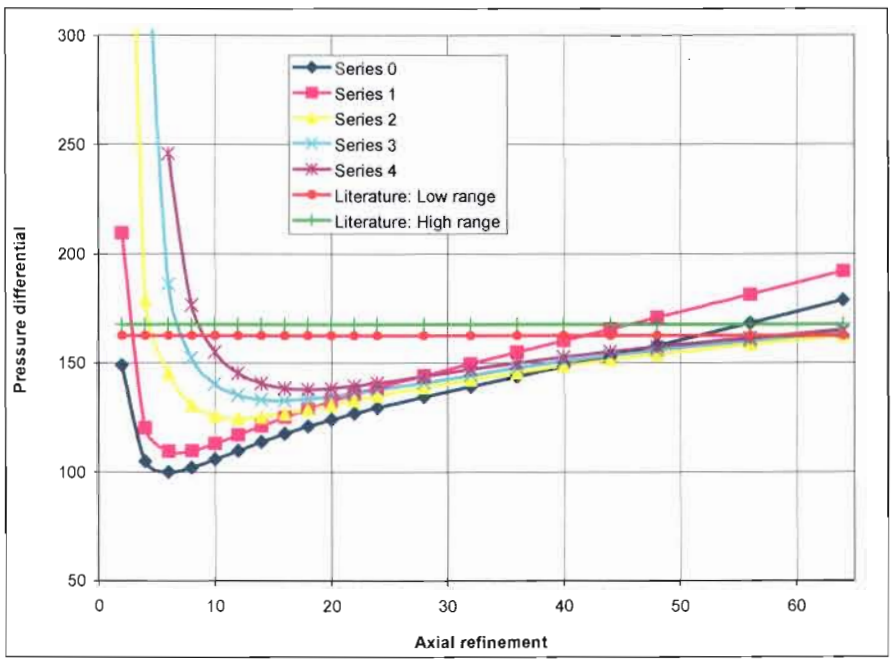

Figure 11: Results from screen refinement tests

It can be concluded that the cell refinement in close proximity to the screen has a major influence on the calculation of the pressure differential across the screen. However, results for series 2, 3 and 4 (i.e. perpendicular refinement ranging from 4 to 8) are reasonably similar from an axial refinement value of 32 onwards. Furthermore, the degree of axial refinement required to achieve good correlation to actual flow conditions are extremely high while Figure 11 shows that an increase in perpendicular refinement does not significantly improve the accuracy of the solution. Therefore, although a more accurate simulation is achieved with a perpendicular refinement of 8, the improvement, when compared to results for a perpendicular refinement of 4, is not significant.

3.5 Practical implications of the findings

Considering the fact that a typical precipitator screen is in the region of 22 m by 22 m square, the screen used for this study would require approximately 730 repetitions in the width and depth respectively resulting in 532900 holes in the screen. Considering that the best result was achieved with 64 cells per hole (perpendicular refinement of 8 by 8), the amount of cells required to model only the single layer of cells representing the screen would be 31.4 million cells. Furthermore, considering that an axial refinement of 64 was required to get an acceptable pressure differential across the screen, $2.2*10^9$ cells would be required to model only a single screen.

Even with only 16 cells in the hole (4 by 4 refinement), 546 million cells would be required to model a single screen. Considering the fact that screens are often used in sets of two or three, $1.638*10^9$ cells would be required to model three screens. Considering the fact that the transition from the highly refined screen section to the remainder of the ESP geometry should be implemented gradually, it can be conceivable that the remainder of the geometry can easily account for an additional 10 million cells. The total number of cells for such a simulation can therefore amount to $1.65*10^9$ cells.

To put this number into perspective, current models of ESP's do not often exceed 2 million cells. These models require between 1GB to 2GB of memory to solve only the momentum equations and would require approximately 48 to 96 hours to reach convergence on a single processor Pentium 4 system depending on the complexity of the model. By applying this information to the detailed modelling of the screens, it can

be concluded that the detailed modelling of the inlet screens would require approximately 825 times more resources. Therefore, if the simulation was split onto a computer cluster of 256 processors, each containing between 1GB and 2GB of memory, the simulation would still take 3.2 times longer to solve assuming that no solution time is lost for the administration and transfer of the data between the different processes. If a data administration loss of only 50 percent is assumed across 256 processors, the solution would still take 6.4 times longer than current simulation techniques.

Even if it were economically possible to purchase a large computer system, the long solution times would be unacceptable since it is often required to complete a large number of simulations during the optimisation of an ESP, which would render this approach costly and impractical.

3.6 Summary

This chapter focused on the influence of numerical mesh refinement on the predicted pressure differential across a flat square lattice screen to investigate the feasibility of modelling screens in detail as opposed to developing mathematical models to simulate screens.

It was found that the accuracy of the pressure differential calculated by the CFD software is highly dependent on the degree of refinement of the numerical mesh in close proximity to the screen. It was shown that a perpendicular refinement ranging between 4 and 8 supplied similar results beyond an axial refinement of 32. As could be expected, the most accurate results were obtained with the highest level of refinement. Considering the vast computing resources required at tremendous cost, it can be concluded that it is not viable to model screens in detail even in a simple and controlled application as discussed here. For this reason, it is required to derive mathematical models that would accurately simulate the influence of the screen on the flow that passes through the screen. The development of such models is the focus of this study.

The following chapter discusses the experimental setup used to obtain empirical data that serves as validation for the mathematical models and postulations.

CHAPTER 4: EXPERIMENTAL SETUP

4.1 Introduction

In order to validate mathematical theory, assumptions or postulations, it is required that results from such calculations are compared to experimental data. Since empirical data on this specific subject is very limited, it was required to include the design and construction of a low speed wind tunnel in this study. This chapter discusses the design, construction and commissioning of the experimental setup.

Figure 12 shows a schematic layout of the experimental facility. The low speed wind tunnel was designed to represent a wide-angle diffuser typically used in ESP's.

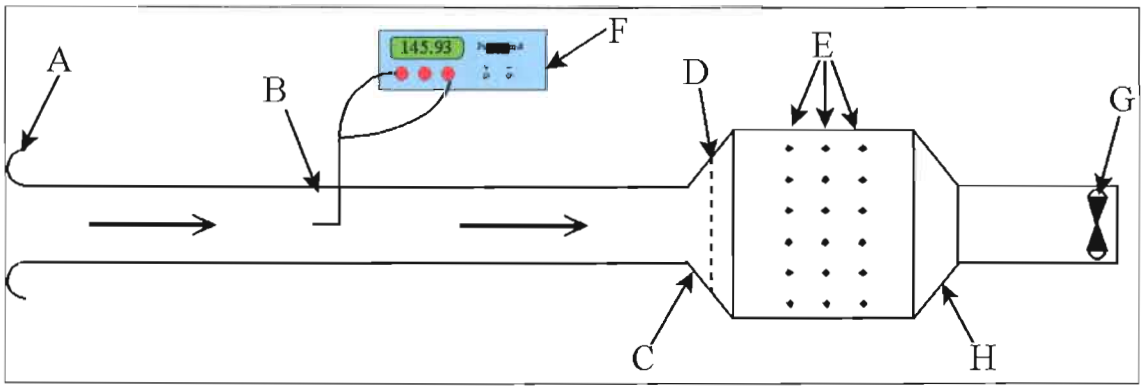

Figure 12: Schematic layout of experimental facility

Where:

A → Inlet bell mouth
B → Pitot static tube measuring the average inlet velocity
C → Diverging diffuser
D → Distribution (perforated) screen
E → Measurement points for downstream pressure distribution
F → Digital pressure anemometer
G → Fan
H → Reducer

4.2 CAD design

Figure 13 shows a three dimensional view of the CAD design. Due to budget constraints, the cost of this facility was kept to a minimum. The approach was to

design a modular structure using simple but effective flange type connections with modules that could be replaced as required. Each module was mounted on an individual movable trolley to facilitate ease of use. An adjustment was designed between the trolley and the wind tunnel conduit to allow for easy alignment of the different modules (see Figure 14).

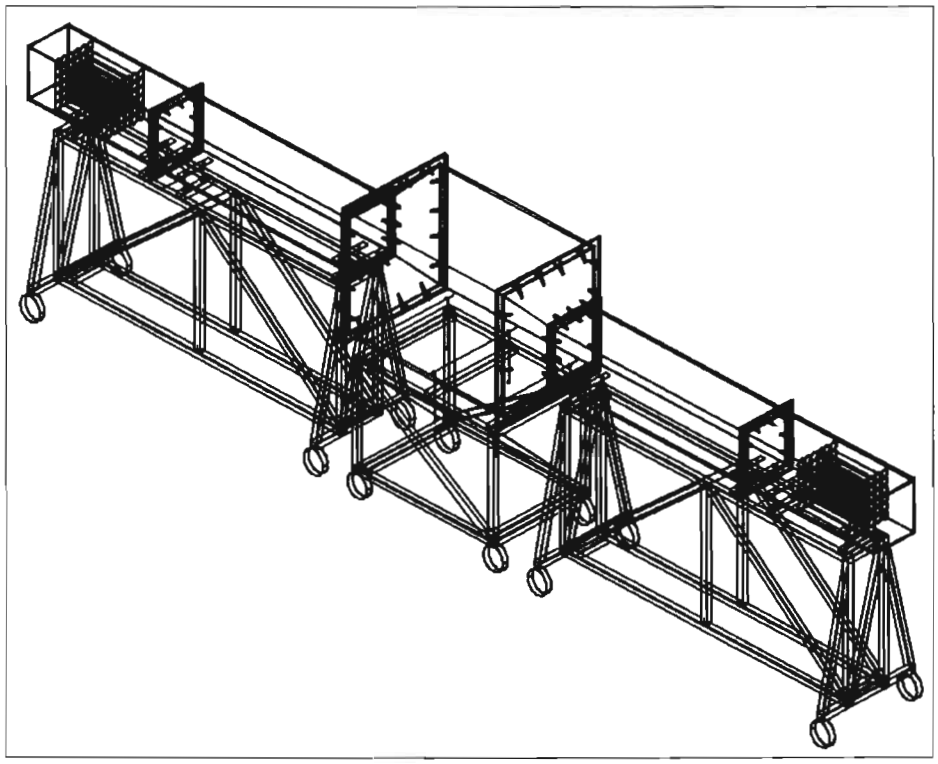

Figure 13: Three-dimensional view of the CAD design

Figure 14: Adjustable alignment supports on the trolley's

Figure 15 and Figure 16 shows the side and plan elevation of the CAD design respectively. The initial design did not include an inlet bell mouth. It was decided to first measure the flow distribution to determine the necessity of such a diffuser. The inlet flow distribution is discussed in paragraph 4.5.

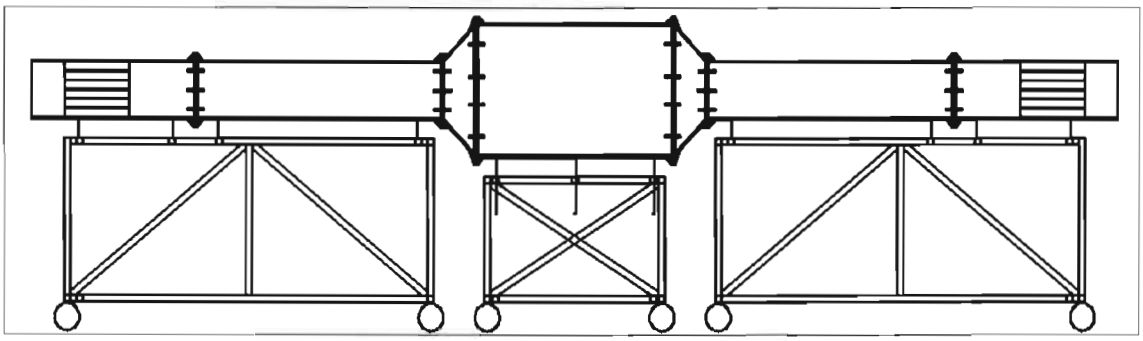

Figure 15: Side elevation

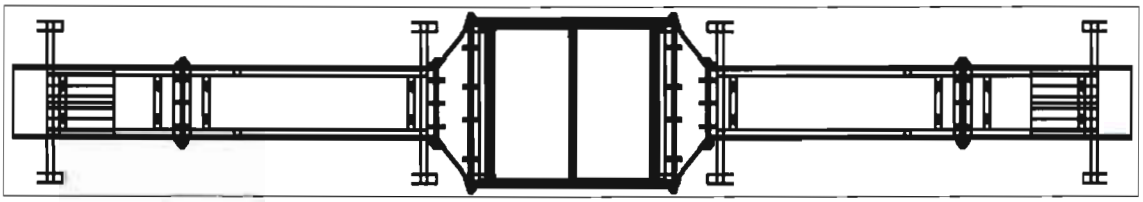

Figure 16: Plan elevation

4.3 Manufacturing

The material selection for the manufacturing of the wind tunnel is shown in Table 4. Figure 17 shows photographs of the assembled wind tunnel.

Table 4: Material and component selection

	Component	Material
1.	Trolleys	Standard SA508 steel
2.	Wind tunnel: top, bottom and rear walls	Polyethylene
3.	Module flanges	Polyethylene
4.	Front walls	Clear transparent acrylic
5.	Inlet flow diffuser	160mm standard PVC piping
6.	Trolley wheels	Heavy duty rubber castors
7.	Fan support structure	Standard SA508 steel
8.	Fan inlet section	Laminated wood/steel sheeting

Thanks to a donation from Eskom TSI, the fan and the inlet section to the fan was not manufactured and due to the modular design philosophy, these sections could merely be added to the wind tunnel.

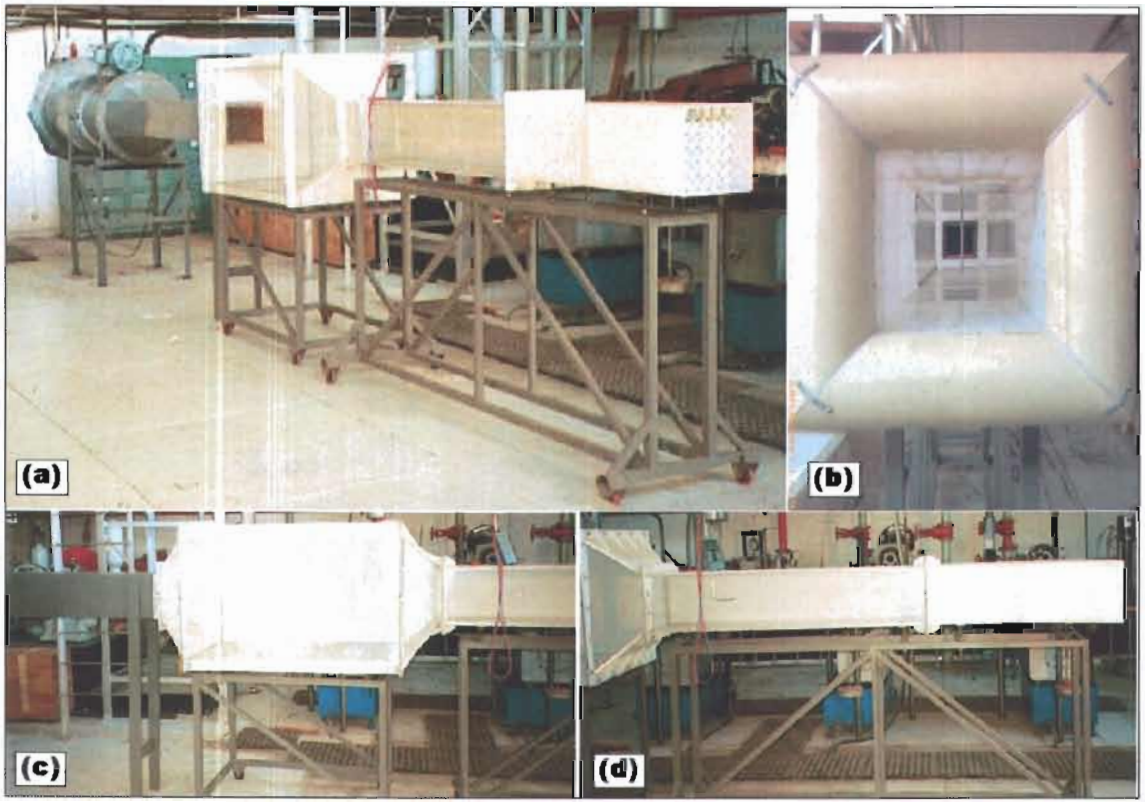

Figure 17: Wind-tunnel after manufacturing

Figure 17a shows the assembled unit before the design and installation of the inlet bell mouth (Figure 17b). Figure 17c and d show the different test sections to be used for perpendicular- and variable impingement flow angles. It can be seen that the front walls of the wind tunnel is transparent to enable flow visualisation.

4.4 Instrumentation

Due to the high cost of test equipment and budget constraints, the choice of measuring equipment was rather limited. Although it was required to keep the cost down, it was also imperative to ensure that the equipment would supply accurate results. For this reason, it was decided to use Pitot static tubes combined with hand held Airflow micro manometers (Model PVM100) to measure velocities and static, dynamic and total pressure distributions. The calibration certificates for all instruments are presented in ANNEXURE B. A highly sensitive MEDM500 Airflow manometer was used to confirm calibration tests for the smaller hand held units.

Dry bulb and wet bulb temperatures were measured using a calibrated Hygrometer (Serial number XM784) and the specific volume was read from the CSIR Psychrometric chart (see ANNEXURE C) for the altitude of 1400m above sea level or 85.6kPa atmospheric pressure. The atmospheric pressure was measured using a standard mercury barometer. Figure 18 shows the wind tunnel during testing.

Figure 18: Test setup

4.5 Inlet flow profile

Initially, the wind tunnel was not designed with an inlet bell mouth, but included only a series of small pipes that would act as a flow-straightening device (see Figure 17a). Tests however revealed a poor inlet flow distribution as shown in Figure 19. Screens were positioned in the inlet in an attempt to improve the flow distribution, but it can be seen that the screens only reversed the poor flow distribution. Based on these results, it was decided to remove the pipes and design an inlet bell mouth.

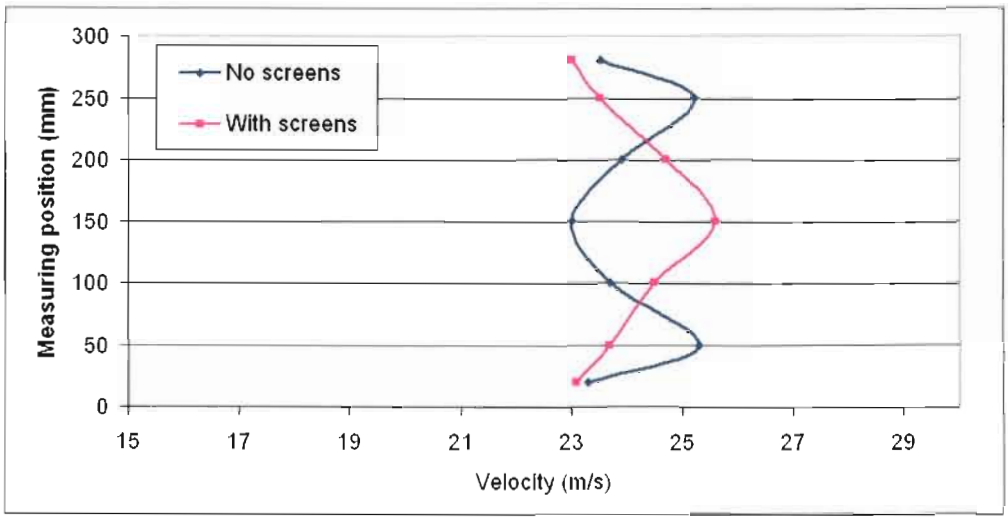

Figure 19: Initial inlet flow distribution

A literature survey was conducted to determine the optimal shape of the inlet bell mouth. This research showed that inlet bell mouth design can be rather complicated and can include round and elliptical designs. Fried and Idelchik (1989:43) state that: *"When the flow enters a straight tube or conduit, it separates by inertia from the inner surface close behind the entrance if the inlet orifice edge is insufficiently rounded. When the inlet wall is thickened, bevelled or rounded or when the edge of the inlet tube or conduit is adjacent to the wall into which the tube is mounted, the flow passes the inlet edge more smoothly and the separation zone becomes shorter, thus decreasing the inlet resistance."*

For this application, it can therefore be concluded that the radius of the inlet bell mouth should be sufficiently large enough for separation of the flow *not* to occur and thus result in a uniform flow distribution directly downstream of the inlet bell mouth. Japikse and Baines (1998) focuses on the turbo machinery diffuser application, which is not applicable to this study. Plint and Böswirth (1978:26, 161, 166) suggest a complex elliptical inlet bell mouth. This type of design would however require expensive and precise bending or moulding equipment that was not available. Budget constraints dictated the need for a simple yet effective design. For this reason, it was decided to opt for a simple design and to test the efficiency of this simple approach using CFD before investigating more expensive and complex layouts. Figure 20 shows a schematic presentation of the intended design.

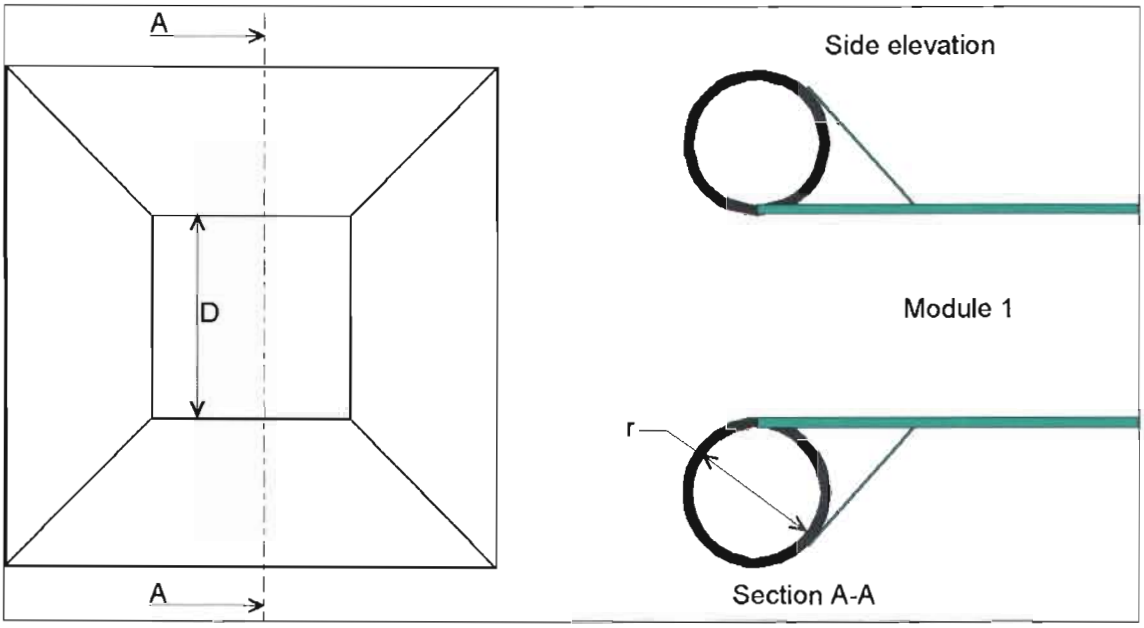

Figure 20: Design of the inlet bell mouth

The ratio of inlet bell mouth radius to pipe dimension r/D (see Figure 20) determines the efficiency of the bell mouth, i.e. a larger bell mouth radius will result in a lower probability for the separation of flow and thus create a more uniform flow distribution in the duct. Idelchik (1996:164) states that the resistance of the inlet bell mouth does not increase above a ratio of 0.2 suggesting that the radius of the bell mouth should be larger than 20 percent of the pipe dimension. To keep to the design philosophy of a simple and cost effective design, it was required to investigate the availability of off-the-shelf components. It was found that a standard plumbing PVC pipe had a diameter of 160mm and could be obtained at low cost. This would result in an inlet bell mouth ratio of 0.53, which is well above the ratio of 0.2 suggested by Idelchik (1996:64). The next step in the design process was to test the efficiency of this diffuser using CFD.

The first CFD model included only a two-dimensional section of the wind-tunnel, but results obtained appeared to be incorrect as shown in Figure 21. It was not expected that the inlet profile would extend as far upstream (into the atmosphere around the inlet) as was predicted by the two-dimensional model.

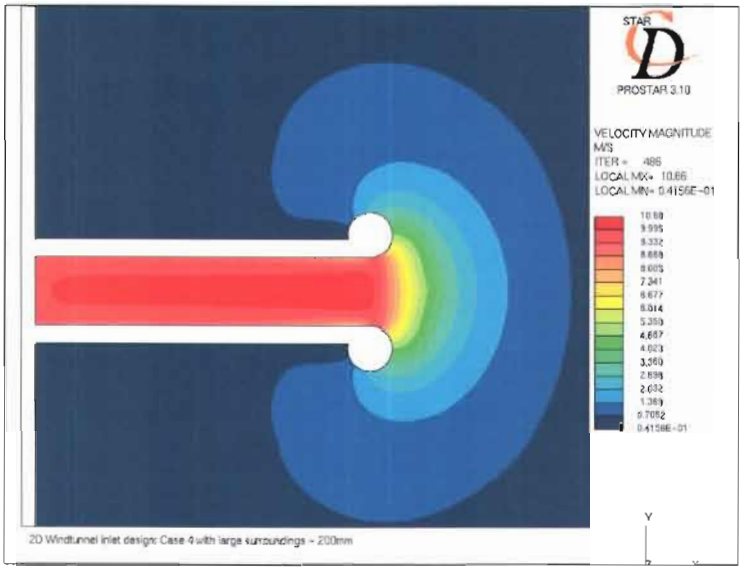

Figure 21: Unphysical results with two dimensional CFD model

To ensure accurate modelling of the inlet bell mouth, it was decided to create a 180° three-dimensional model of the inlet section and thus eliminate the assumption of two-dimensional symmetry. Figure 22 shows the numerical mesh used for this analysis.

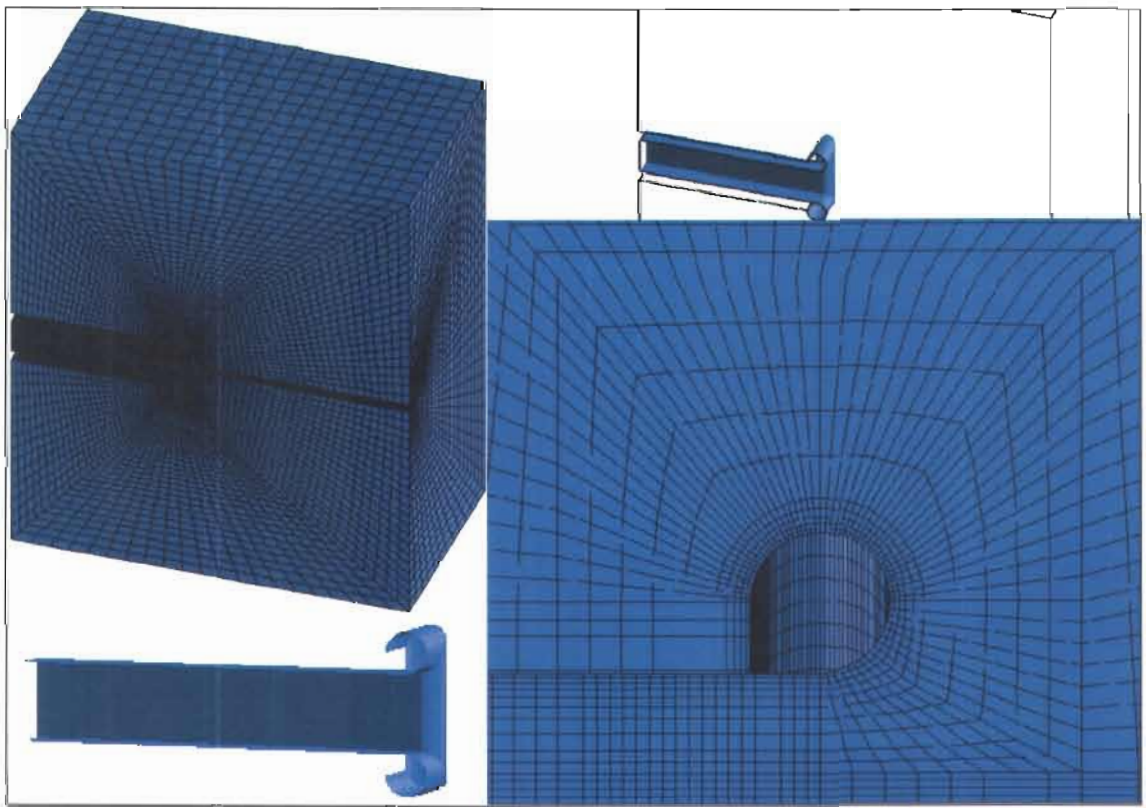

Figure 22: CFD mesh used for the design of the inlet bell mouth

It can be seen that the mesh was refined in the boundary layer region to accurately model wall functions. Wall functions are discussed in more detail in CHAPTER 5. An atmospheric pressure boundary was used for the inlet and flow was induced through the wind tunnel with a suction boundary to ensure accurate development of the flow profile in the inlet bell mouth.

Figure 23 shows results from the CFD model. It can be seen that an inlet bell mouth with a diameter of 160mm and a square duct size of 300 mm by 300 mm is creating a well-developed turbulent flow distribution. The Reynolds number determines whether the flow is laminar or turbulent and is discussed in the following paragraph.

The difference between the results predicted by the two-dimensional and three-dimensional models can mainly be contributed to the fact that the three dimensional effect of the inlet bell mouth was not taken into account. By assuming symmetry boundaries on the sides of the model, the solution was forced to assume an infinite width for the wind tunnel basically simulating flow between two flat plates of infinite width.

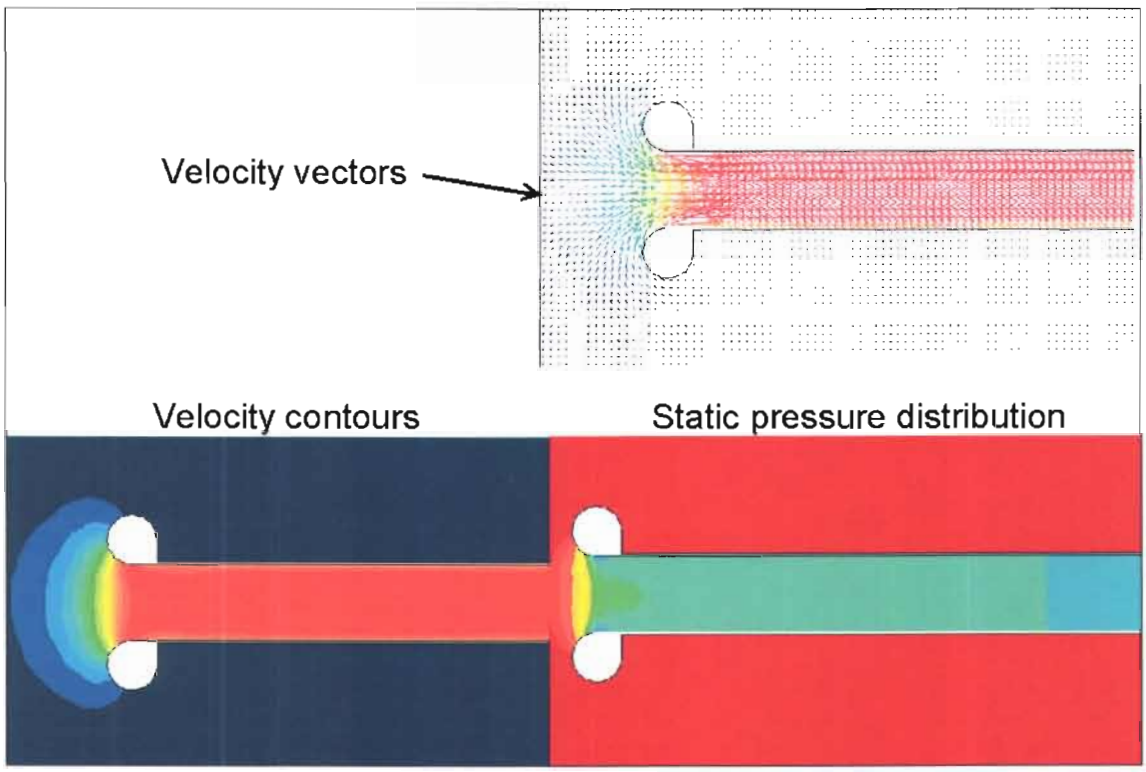

Figure 23: Results from the inlet bell mouth CFD model

After constructing the inlet bell mouth, flow distribution measurements (traverses) were taken at three different velocities over the total velocity range of the fan, i.e. 3.7 m/s, 8.9 m/s and 22.6 m/s, with no screens in the flow stream. It should be noted that the range of velocities was reduced with the inclusion of screens in the flow stream due to the added resistance and therefore the higher value of 22.6 m/s could not be achieved ith screens in the flow stream. The exact positions of the traverse measuring points was calculated according to the ratios outlined in the Airflow Pitot Static Tube Leaflet for square duct traverses using 36 measuring points (Airflow Developments Ltd. Leaflet AI 133/984).

Figure 24 shows the average of the normalised flow distributions through the wind tunnel for the range of velocities. The three dimensional plots are shown in Figure 99 to Figure 104 (ANNEXURE A). It can be seen that the flow distribution measured in the wind tunnel is well developed. Furthermore, the empirical data showed a better-developed flow profile than the CFD results, i.e. a lower correction factor. CFD modelling techniques are discussed in more detail in Chapter 5. Furthermore, it can be seen that the distribution improves with higher velocities. This can however also be due to the fact that the error in measurement of the instruments is more pronounced for the lower velocities since the percentage uncertainty is increased with lower absolute readings (see paragraph 4.8).

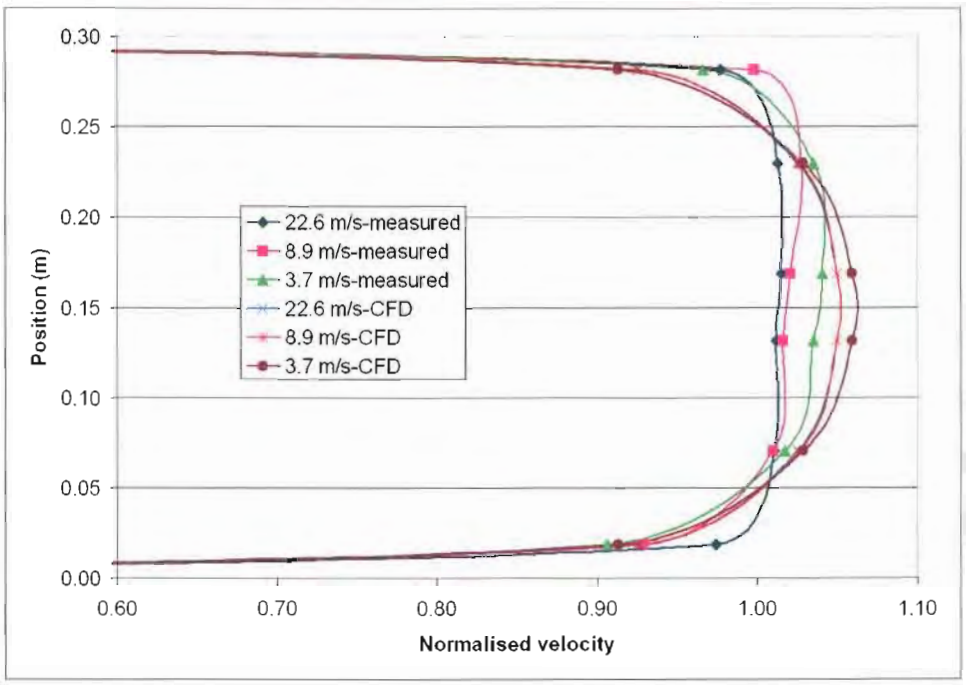

Figure 24: Average of normalised velocities through the wind tunnel

Velocity was calculated as a function of the square root of the dynamic pressure head with corrections for temperature, atmospheric pressure and relative duct static pressure (Airflow Pitot Static Tube Leaflet AI 133/984):

$$v = 1.291\sqrt{\frac{1000}{B} * \frac{T}{289} * \frac{100000}{100000 + P_s} * P_v} \quad \textbf{(4.1)}$$

Where:
- v = *Velocity (m/s)*
- B = *Barometric pressure (mbar)*
- T = *Dry ball air stream temperature (K)*
- P_s = *Relative duct static pressure (Pa)*
- P_v = *Dynamic pressure (Pa)*

Based on the above flow distributions, a correction factor was calculated that would enable the measurement of only the central position. This value could then be corrected to supply the average approach velocity. According to the Airflow Pitot Static Tube Leaflet (AI 133/984) the average of the calculated velocities can be used as the average duct velocity as long as the majority of the readings do not vary by more than approximately 25 percent from the mean value. The largest deviation from the average was measured for the low velocity case where only two values deviated from the average by approximately 20 percent. Table 5 and Figure 25 show the correction across the range of velocities. It can be seen that the correction factor reduces with an increase in average velocity, which is consistent with the distributions shown above. It can also be seen that the trend is nearly linear and that the correction factor ranges between 3.7 and 5.3 percent.

Table 5: Velocity correction factor

Velocity	Correction	Linear curve fit	Deviation	Percent error
3.670	1.053	1.053	-2.429E-04	-0.02 percent
8.859	1.048	1.048	8.890E-04	0.08 percent
22.565	1.037	1.037	-2.657E-04	-0.03 percent

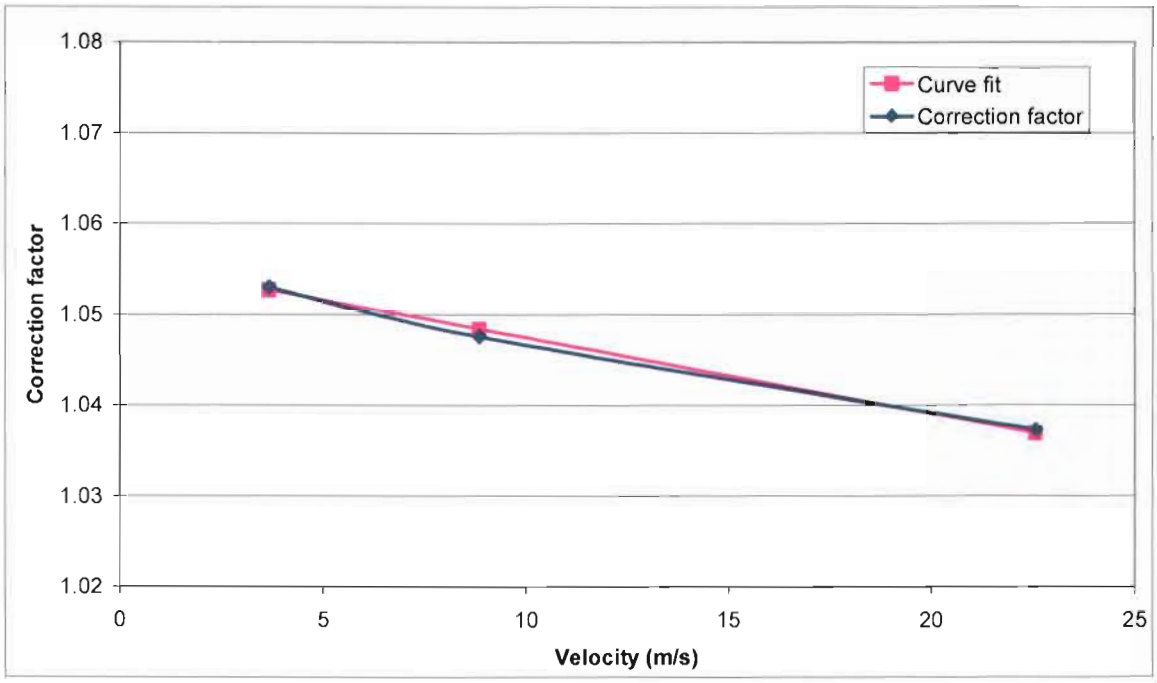

Figure 25: Velocity correction factor

It can therefore be concluded that the inlet bell mouth creates a well-developed flow distribution across the whole range of velocities and that a single measurement in the centre of the duct with a correction factor not exceeding 6 percent can be used to calculate the average duct velocity. Even at a very low velocity of 1 m/s, the Reynolds number is approximately 1.6e4 and therefore the flow is turbulent. This well developed inlet flow distribution forms a solid basis for any further tests.

In order to ensure the accurate development of the boundary layer profile near the wall, it is essential that the wall functions are calculated accurately in the CFD code. The wall functions are dependent on the cell size and Reynolds numbers (being a function of the velocity) near the wall and are expressed by the y+ value. Adapco (2002) states that the y+ value should be higher than 30 and lower than 300 for pipe flow. Figure 26 shows the y+ value near the walls of the inlet pipe for the range of inlet velocities. It can be seen that the y+ value for the 3 m/s case is lower than the prescribed value of 30 near the wall, but are well within the prescribed limit for both the 10m/s and 20 m/s cases. The low y+ value for the low velocity case may account for the change in the flow profile at lower Reynolds numbers. The influence of wall functions and the y+ value is discussed in more detail in Chapter 5.

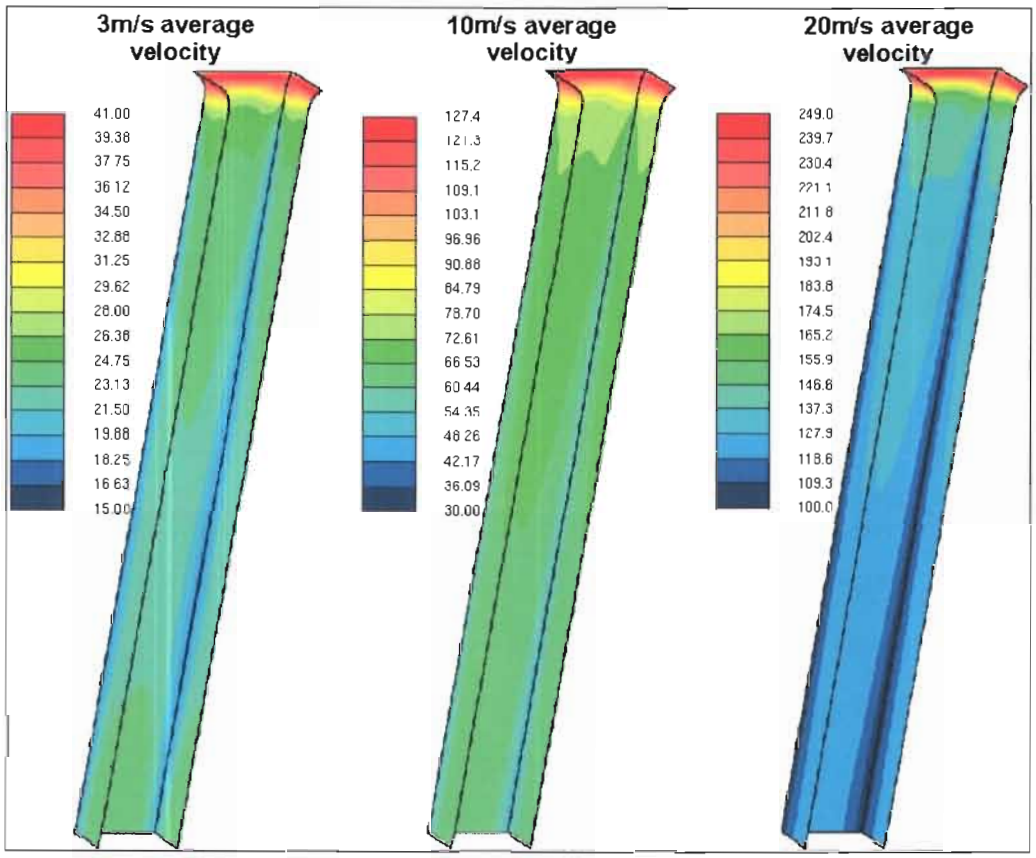

Figure 26: y+ values in the inlet pipe

4.6 Similarity

To ensure applicability of the results to actual conditions, it was necessary to investigate the dynamic similarity of the flow through the wind tunnel with typical actual flow conditions.

4.6.1 Applicability of dimensionless groups

Since the experiments were conducted without any heat transfer it is assumed that the process is adiabatic and isothermal. For this reason, it is not required to consider the Prandtl number (which is important for heat convection), Eckert number (heat dissipation) or Grashof number (natural convection). Furthermore, the flow through the wind tunnel is assumed to be steady state flow and therefore the Strouhal number (Oscillating flow), does not apply. Since only single phase flow is modelled, the Froude number and Weber number, which are both applicable to free surface modelling, does not apply (White 1988:265).

4.6.2 Mach number

The speed of sound is defined by (White 1988:517):

$$C = \sqrt{\gamma RT} \tag{4.2}$$

Where: C = *Speed of sound (m/s)*

γ = *Specific heat ratio*

R = *Gas constant (kJ/kg.K)*

T = *Gas temperature (K)*

The Mach number is calculated by (White 1988:265):

$$Ma = \frac{v}{C} \tag{4.3}$$

Where: Ma = *Mach number*

v = *Velocity of flow (m/s)*

C = *Speed of sound (m/s)*

At approximately 85.5kPa and 20°C (293K), γ=1.4 and R=287 kJ/kgK, the speed of sound is 343.1m/s. With no screen in position, the maximum approach (free stream) velocity was measured to be 22.7 m/s. However with a screen FAR of 30 percent, it was found that the additional resistance reduced the approach velocity to no more than 15 m/s. Based on these values, the peak velocity through the screen is calculated to be approximately 50 m/s through the screen holes. Figure 27 shows the flow as it contracts through the screen. It can be seen that the ratio between the peak velocity (v_{peak}) and the free stream velocity (v_f) is:

$$v_{peak} = \frac{v_f}{FAR} \tag{4.4}$$

As the screen thickness increases, a re-circulation zone is created that results in a further contraction of the flow area through the screen and thus an increase in the peak velocity. In cases where the venturi effect is pronounced, some correction factor has to be applied to equation (4.4). Fried and Idelchik (1989:262) show that the venturi effect becomes significant if the ratio between the thickness of the screen and the hydraulic diameter is equal to 0.2 and higher. The influence of the recirculation zone becomes more significant if the angle of incidence is not perpendicular and may have a

significant influence on the results predicted by numerical models. With the screens tested, the highest value of this ratio was only 0.033. For this reason, the venturi effect was considered negligible and equation (4.4) therefore applies. Considering the maximum superficial velocity, the Mach number in the wind tunnel did not exceed 0.15.

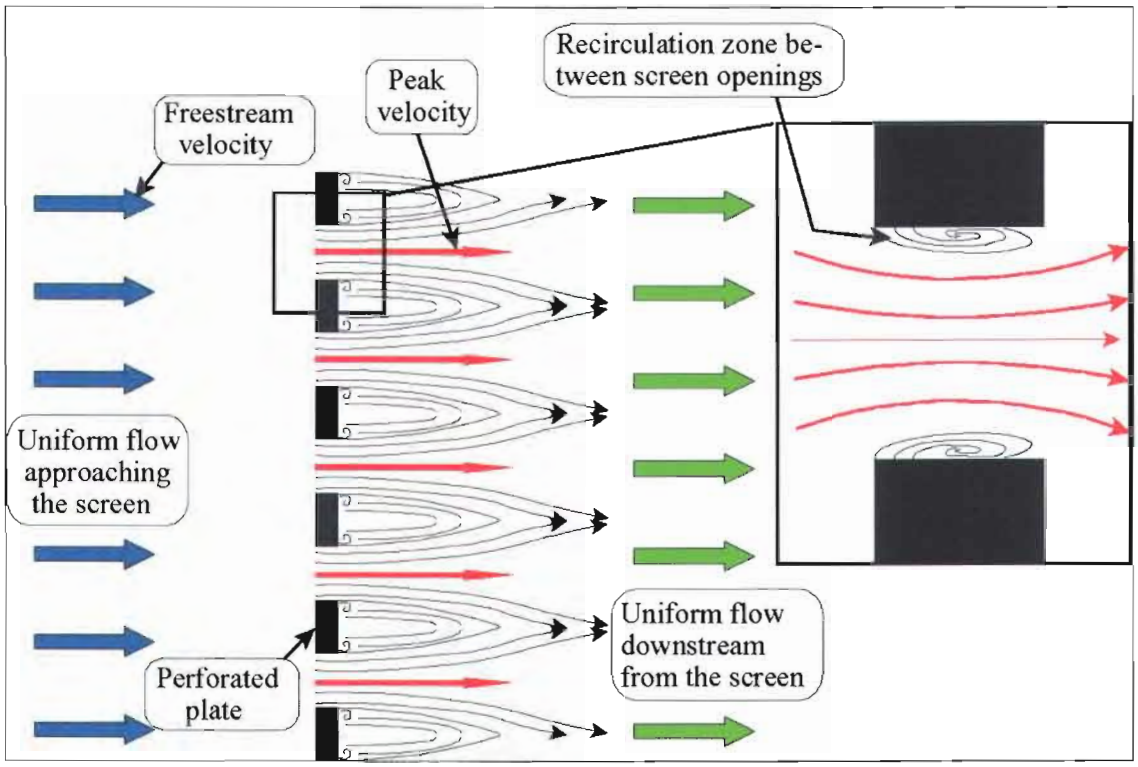

Figure 27: Venturi effect through screens

According to White (1988:512) flow is divided into the following classifications:

- Flow is completely incompressible up to a Mach number of 0.3 where density effects are negligible.
- Between a Mach number of 0.3 and 0.8, flow is subsonic where density effects are important, but no shock waves appear.
- Between a Mach number of 0.8 and 1.2, flow is transonic where shock waves first appear, dividing subsonic and supersonic regions of the flow.
- Between a Mach number of 1.2 and 3.0, flow is supersonic where shock waves are present, but there are no subsonic regions.
- With a Mach number larger than 3.0, flow is hypersonic where shock waves and other flow changes are especially strong.

For actual conditions, a typical case is considered using Arnot Power Station Unit 1 as an example. Bosch (1993:Table 2) states that the gas temperature was measured to

be 140°C. Based on an inlet duct size of 1.62m by 5.18m and a volume flow rate of 625 m^3/s, split equally into two casings, the gas velocity is 37.3 m/s. At this temperature, the speed of sound is 407.4 m/s and the Mach number is 0.091. It can therefore be concluded that, in both cases, the flow is fully incompressible and therefore the Mach number is not applicable. Due to the fact that the modelling includes flow in ducts and separation in wide-angle diffusers, it is important to consider the Reynolds number and the Euler number. According to White (1988:265) the Reynolds number should always be included in any dynamic similarity flow calculation and the Euler number where the ratio between pressure and inertia influences results.

4.6.3 Reynolds number

The Reynolds number is calculated by the following equation (White 1988:261):

$$Re = \frac{\rho v D_H}{\mu} \tag{4.5}$$

Where:

Re = *Reynolds number*

ρ = *Density of the fluid* (kg/m^3)

D_H = *Hydraulic diameter or a comparative length depending on the application (m)*

v = *Perpendicular superficial approach velocity (m/s)*

μ = *Viscosity (kg/m.s)*

The hydraulic diameter is defined as (White 1988:322):

$$D_H = \frac{4 * Area}{Wetted \quad perimeter} \tag{4.6}$$

The range of velocities in the wind tunnel varies from 3 m/s to 22.5 m/s. With a hydraulic diameter of 0.3 m, a viscosity of $1.8*10^{-5}$ and a density of approximately 1 kg/m^3 (at the ambient pressure of 85.5 kPa and ambient temperature of 20°C) the Reynolds number ranges between $5*10^4$ and $3.8*10^5$. Again, the example of Arnot Power Station Unit 1 is used to calculate the actual Reynolds number (Bosch 1993:Table 2). With a duct size of 1.62 m by 5.175 m, the hydraulic diameter is 2.468 m. The velocity is 37.3 m/s as calculated above. At a duct pressure of 82.4 kPa and duct temperature of 413.2 K, the gas density is 0.703 kg/m^3. Using this input data, the actual Reynolds number is calculated as $1.4*10^6$. Compared to the maximum

Reynolds number in the wind tunnel of $4*10^5$, it can be seen that the wind tunnel cannot match the exact Reynolds number. In order to achieve the actual Reynolds number, it would be required to have an inlet velocity of approximately 80 m/s, which would require a very powerful fan. Table 6 shows the Reynolds number comparison through the wind tunnel and a typical case: Arnot Power Station.

Table 6: Comparison of Reynolds numbers

		Velocity (m/s)	Reynolds number
1	Wind tunnel low velocity	1.0	$1.7*10^4$
2	Wind tunnel medium velocity	12.0	$2.0*10^5$
3	Wind tunnel high velocity	22.5	$3.8*10^5$
4	Actual case (Arnot Power Station)	37.3	$1.4*10^6$

It can be seen that although the Reynolds number in the wind tunnel is lower than that of the actual conditions, the flow is still turbulent even at the very low velocity of 1 m/s. Furthermore, it was shown in CHAPTER 2 that most of the experimental studies conducted in literature was at only a single turbulent Reynolds number.

For this reason, it can be concluded that results from the wind tunnel are applicable for the turbulent Reynolds number range from 10^4 to 10^6 and higher for smooth walled ducts.

4.6.4 Euler number

According to White (1988:261, 265), the Euler number is the ratio between the pressure and the inertia (dynamic pressure component). The Euler number is often written in terms of pressure differences:

$$Eu = \frac{\Delta P}{\rho v^2} \tag{4.7}$$

Where: Eu = *Euler number*

ΔP = *pressure differential (Pa)*

ρ = *Density of the fluid (kg/m^3)*

v = *Flow velocity (m/s)*

Comparing the Euler number, equation (4.7), with the resistance coefficient, equation (1.2), it can be seen that the only difference is a factor of 2. It can therefore be concluded that if the resistance coefficient correlates with literature, the Euler number also correlates. This correlation is discussed in paragraph 4.9.

4.7 Measuring techniques and the influence on the accuracy of results

This discussion focuses on the measuring technique and not on the uncertainty of the measurements, which is discussed in paragraph 4.8. A number of factors, which might influence the accuracy of measurements, were taken into consideration:

- In order to ensure well-averaged static pressure measurements, it was necessary to locate a number of tapping points around the circumference of the wind tunnel. All these points were joined in order to measure the average static pressure at a certain position along the length of the duct. It was decided to make use of four positions (in the centre of each of the walls) around the tunnel in order to minimise the possibility of errors.

- The tapping points upstream of the testing section were positioned away from the screen by a distance equal to at least 15 times the lattice size. This is required to ensure that any upstream influences due to the resistance caused by the screen do not influence the measurement.

- The pressure tapping points downstream of the test section must be a certain distance from the face of the screen. According to The handbook of Hydraulic Resistance (Idelchik 1986:392) this distance must be at least 15 times the lattice size. The lattice size of a screen refers to the width of the screen strip facing the approaching flow. It was shown by Janse van Rensburg (1997:22, 23) that approximately 10 to 15 times the lattice size is required for the flow to re-attach and recover to a turbulent flow distribution. Earlier studies correspond with this finding (Pinker and Herbert, 1967:15) and describe it as: *"A large and abrupt fall approximately in the plane of the gauze (screen) followed by a fairly sharp rise immediately behind the gauze."* Schubauer, Spangenberg and Klebanoff (1950:29) also confirm this pressure profile behind the screen.
  Figure 27 showed that the air passes through the screen as a number of high velocity jets and the flow only recovers a certain distance behind the screen. These

jets have a significant influence on the profile of the pressure across the screen and can be directly related to the profile shown by line DG in Figure 28. The Hydraulic Gradient Line (HGL) for the system is represented by line AC in Figure 28 with ΔP1 being the pressure differential across the screen. Line DE shows the gradual pressure loss due to friction against the tunnel surface. As the flow accelerates through the free screen area, a very large sudden pressure drop is encountered with a sudden recovery to F. If the pressure drop is measured within this region (ΔP2), the value would be much greater than the true pressure drop over the screen. The true value would be the difference between the parallel lines DE and FG (ΔP3). For this reason, it is necessary to locate the static pressure tapping far enough downstream of the testing position in order to measure the true pressure drop (ΔP3) for all different screens to be tested.

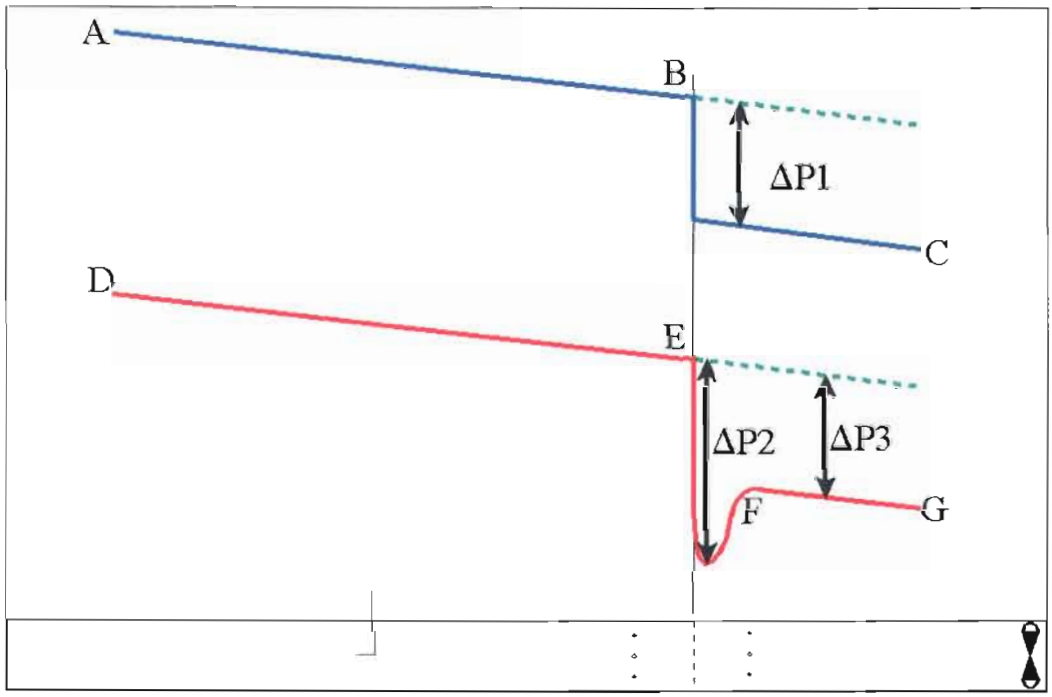

Figure 28: Schematic representation of the Hydraulic Gradient Line

- All instruments were calibrated before being used in order to determine the percentage error that should be accounted for. After calibration, a calibration certificate is issued for each instrument. The calibration certificate for the electronic pressure manometers used presented an inaccuracy of ±20.1 Pa (see ANNEXURE B). Furthermore, the calibration laboratory can only provide a 95 percent confidence level, which can result in substantial inaccuracies especially in the low

velocity regions where measurements fall within the range of uncertainty. Measurement uncertainty is discussed in paragraph 4.8.

- The stability of the fan can have a significant influence on the accuracy of measurements. Instability of a fan is called electrical surging and occurs when a certain device runs at alternating speeds with high and low peaks. If the speed of the fan varies, the volumetric flow rate also varies resulting in a change in the velocity of the flow. Due to the fact that measurements are taken manually, it may take some time to record all the readings used for one measurement. If the flow is surging within the time required to take one set of full measurements, it is possible that one reading can be taken at a high peak and the next at a low peak, which would produce an incorrect measurement. To ensure the stability of the fan, an additional pitot static tube and manometer was used to monitor the average velocity through the wind tunnel.

- All readings were taken manually and therefore a factor of human error must also be considered. Although readings were taken with great care, the possibility exist that some degree of error was present. It must also be noted that most of the values from the literature were read from graphs and are therefore subject to a reading error.

All these factors emphasise the necessity of validating results against other literature sources.

4.8 Experimental uncertainty analysis

4.8.1 Introduction

Holman (1978:38) distinguishes between the following two data sampling methods:

- Single-sample data, which refers to data for which some uncertainties may not be discovered by repetition.
- Multi-sample data obtained in those instances where enough experiments are performed so that the reliability of results can be assured by statistics.

Frequently, cost prohibits the collection of multi-sample data, and the experimenter must be content with single-sample data and be prepared to extract as much

information as possible from such experiments. This approach also applies to this study.

The real errors in experimental data are those factors that are always vague to some extent and carry some amount of uncertainty. The intent of this paragraph is to determine just how uncertain a particular observation may be and to devise a consistent way of specifying the uncertainty in analytical form. It is better to speak of experimental uncertainty instead of experimental error because the magnitude of an error is always uncertain.

"It is equally as unfortunate to overestimate uncertainty as to underestimate it. An underestimate gives false security, while an overestimate may make one discard important results, miss a real effect, or buy much too expensive equipment" Holman (1978:43).

4.8.2 Types of errors

Holman (1978:39) lists the following types of errors that may cause uncertainty in an experimental measurement:

- First, there can always be those gross blunders in apparatus or instrument construction, which may invalidate the data. The careful experimenter should be able to eliminate most of these errors.
- Second, there may be certain fixed errors, which cause repeated readings to be in error by roughly the same amount, but for some unknown reason. These fixed errors are sometimes called systematic errors.
- Third, there are the random errors, which may be caused by personal fluctuations, random electronic fluctuations in the apparatus or instruments, various influences of friction, etc. These random errors usually follow a certain statistical distribution, *but not always*.

Holman (1978:41-81) and Niemand (2003) suggest a number of different methods for analysing the uncertainty of experimental and simulation data. Only two of the approaches are discussed:

- Error analysis on a common sense basis
- Uncertainty analysis based on the uncertainty of the primary variables

4.8.3 Error analysis on a common sense basis

The term "common sense" has many connotations and means different things to different people. The common sense analysis can take many forms:

- The common sense analysis of the experimental data based on sound engineering judgement of the experimenter to recognise unphysical results and to repeat such tests. An example of this approach is when a volume of water is heated by an element, but the instrument shows a decline in fluid temperature. Engineering judgement suggests that the fluid temperature can only increase and that an error is therefore measured.
- Another rule of thumb that could be used is that the error in the result is equal to the maximum error in any parameter.
- A final common sense analysis would combine all the errors in the most detrimental way in order to determine the maximum error in the final result. It is however highly unlikely that all the errors would combine in this manner and therefore this approach may often lead to an overestimation of the experimental error and should therefore be avoided.

4.8.4 Uncertainty of the primary variables (theory)

With this approach, the uncertainty in the calculated result is based on the uncertainty of the primary measurements. The result J is a given function of the independent variables x_1, x_2, x_3, ...,x_n such that (Holman 1978:41):

$$J = J(x_1, x_2, x_3, ...x_n) \tag{4.8}$$

Let Q_R be the uncertainty in the result and Q_1, Q_2, Q_3, ...,Q_n be the uncertainties in the independent variables. If the uncertainties in the independent variables are all given with the same odds, then the uncertainty in the result having these odds is given as:

$$Q_R = \left[\left(\frac{\partial J}{\partial x_1} Q_1 \right)^2 + \left(\frac{\partial J}{\partial x_2} Q_2 \right)^2 + ... + \left(\frac{\partial J}{\partial x_n} Q_n \right)^2 \right]^{1/2} \tag{4.9}$$

Where: Q_R *is the uncertainty of the result*

$Q_{1...n}$ *is the uncertainty of the independent variables* ($x_{1...n}$) *of the function J.*

The uncertainty propagation in the result Q_R predicted by equation (4.9) is a function of the squares of the uncertainties in the independent variables. This means that if the

uncertainty in one variable is significantly larger than the uncertainties in the other variables, then it is the largest uncertainty that predominates and the others may probably be neglected, which is one of the common sense approaches discussed in the previous paragraph.

The applicability to this analysis is in the calculation of the velocity:

$$v = 1.291\sqrt{\frac{1000}{B} * \frac{T}{289} * \frac{100000}{100000 + P_s} * P_v} \qquad \textbf{(4.10)}$$

Where:

B = *Barometric pressure (mbar) with an uncertainty of ±5 percent.*

T = *Gas temperature (°C) with an uncertainty of ±1 °C and with a confidence level of 95 percent, see Figure 106 ANNEXURE B.*

P_s = *Duct static pressure (Pa) with an uncertainty not exceeding ±(0.028 percent of reading + 0.04 Pa + Instrument resolution) with a confidence level of no less than 95 percent, see Figure 105 ANNEXURE B.*

P_v = *Dynamic pressure (Pa) with an uncertainty not exceeding ±(0.028 percent of reading + 0.04 Pa + Instrument resolution) with a confidence level of no less than 95 percent, see Figure 105 ANNEXURE B.*

In order to calculate equation (4.9), it is required to determine the partial differential equations for all the variables of equation (4.10). The chain rule as discussed in Gieck (1990:H4) is used for this purpose:

If:

$$y = f\left[u(x)\right] \qquad \textbf{(4.11)}$$

then

$$y' = f'(u) * u'(x) \qquad \textbf{(4.12)}$$

or

$$\frac{dy}{dx} = \frac{dy}{du} * \frac{du}{dx} \qquad \textbf{(4.13)}$$

The chain rule is now applied to the following simplified version of equation (4.10):

$$y = 1.291\left[u(x)\right]^{\frac{1}{2}} \tag{4.14}$$

thus

$$\frac{\partial y}{\partial x} = \frac{1}{2} * 1.291\left[u(x)\right]^{-\frac{1}{2}} * \frac{\partial u}{\partial x} \tag{4.15}$$

From this equation, it is now possible to write the partial differential equations for all the variables of equation (4.10):

$$\frac{\partial v}{\partial B} = \frac{1}{2} * 1.291\left[\frac{1000}{B} * \frac{T}{289} * \frac{100000}{100000 + P_s} * P_v\right]^{-\frac{1}{2}} * \left[\frac{-1000}{B^2} * \frac{T}{289} * \frac{100000}{100000 + P_s} * P_v\right]$$

(4.1)

$$\frac{\partial v}{\partial T} = \frac{1}{2} * 1.291\left[\frac{1000}{B} * \frac{T}{289} * \frac{100000}{100000 + P_s} * P_v\right]^{-\frac{1}{2}} * \left[\frac{1000}{B} * \frac{1}{289} * \frac{100000}{100000 + P_s} * P_v\right]$$

(4.2)

$$\frac{\partial v}{\partial P_v} = \frac{1}{2} * 1.291\left[\frac{1000}{B} * \frac{T}{289} * \frac{100000}{100000 + P_s} * P_v\right]^{-\frac{1}{2}} * \left[\frac{1000}{B} * \frac{T}{289} * \frac{100000}{100000 + P_s} * 1\right]$$

(4.3)

For the variable P_s, it is required to use the chain rule again:

$$\frac{\partial v}{\partial P_s} = \frac{1}{2} * 1.291\left[\frac{1000}{B} * \frac{T}{289} * \frac{100000}{100000 + P_s} * P_v\right]^{-\frac{1}{2}} * \left[\frac{1000}{B} * \frac{T}{289} * \frac{-100000}{(100000 + P_s)^2} * P_v\right]$$

(4.4)

The detailed uncertainty calculation for each velocity is shown in ANNEXURE D.

4.8.5 Summary of uncertainty calculation

Table 7 shows a summary of the results and Figure 29 shows the trend line of the uncertainty at increasing velocities and Figure 30 shows the band of uncertainty. It can be seen that measurements at low velocities have an uncertainty value of

approximately 9 percent, but the value then decreases significantly and the trend tends toward a constant value of approximately 2.5 percent above a velocity of 10 m/s (Reynolds numbers of approximately $1*10^5$).

Table 7: Summary of calculated uncertainty values (percentage)

Velocity (m/s)	Reynolds number	Dynamic pressure (Pa)	Value of uncertainty
22.37	$3.7*10^5$	250.0	2.52 percent
9.232	$1.5*10^5$	42.7	2.79 percent
3.540	$5.4*10^4$	6.3	8.64 percent

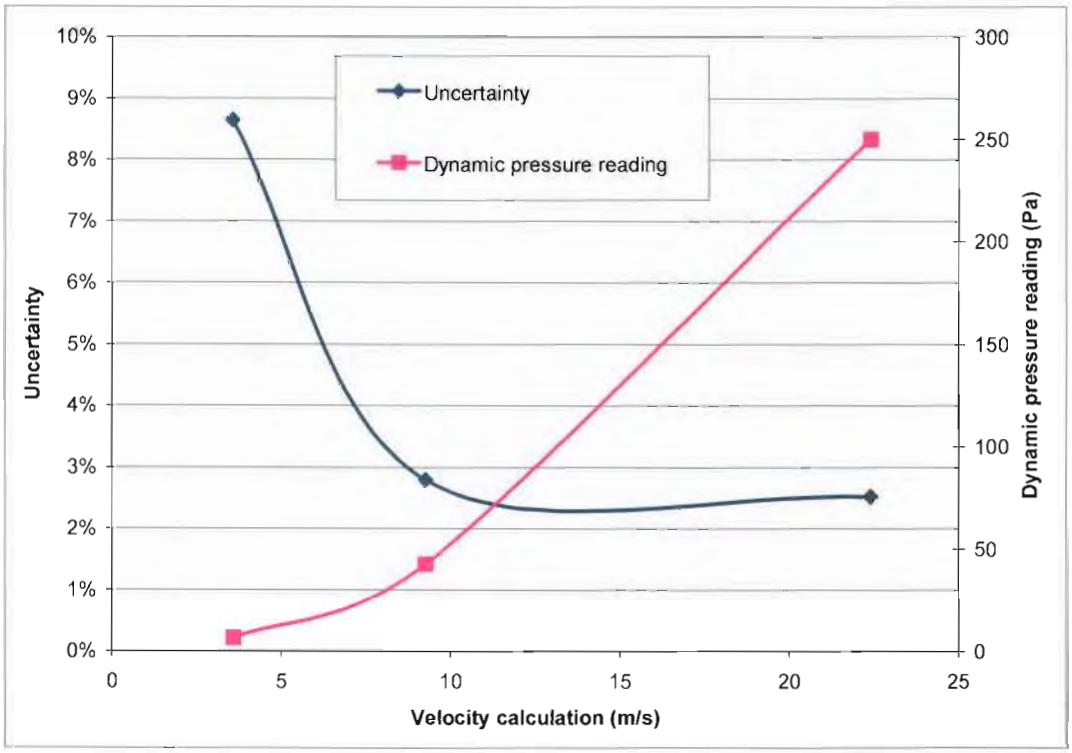

Figure 29: Trend of uncertainty

The main reason for the high uncertainty value at low velocities is the fact that the instrument uncertainty is defined as ±(0.028 percent of reading + 0.04 Pa + Instrument resolution). The instrument resolution is 1 Pa and with the dynamic pressure reading ranging between 6 Pa and 250 Pa, it can be seen that the influence of this uncertainty is pronounced at lower dynamic pressure values. To improve the uncertainty at low velocities, it was required to compare results to literature in order to investigate the

accuracy of the measurements at low velocities. This comparison is discussed in the following paragraph.

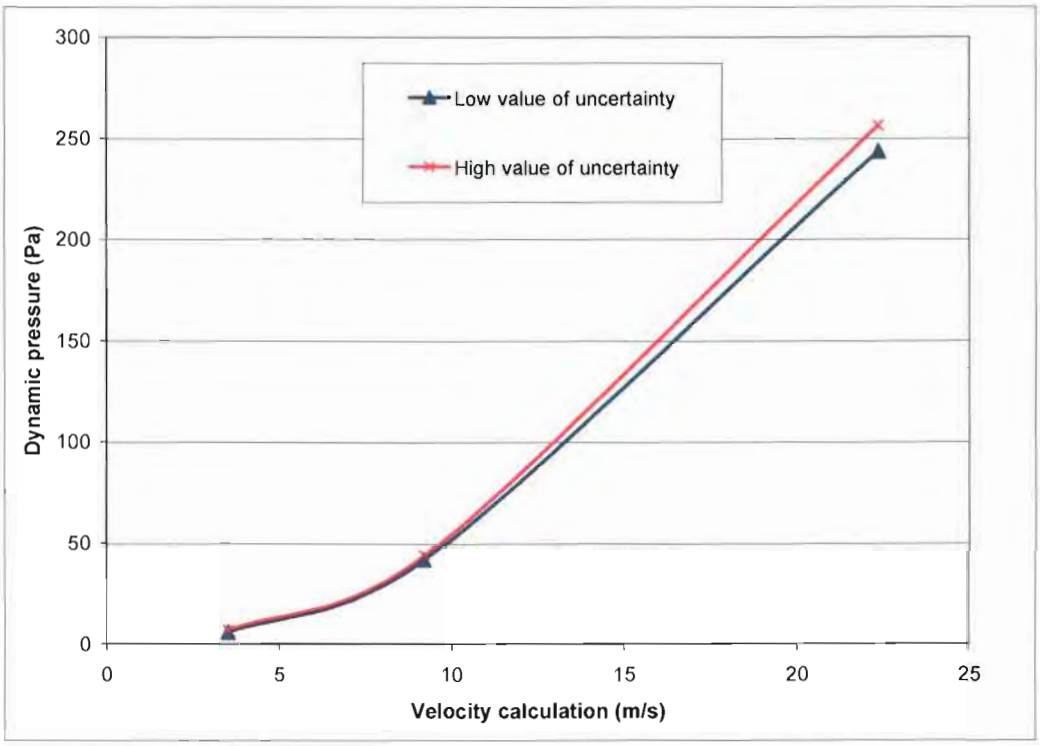

Figure 30: Band of uncertainty for the dynamic pressure measurement

It can therefore be concluded that the uncertainty of measurements is below 3 percent for Reynolds numbers exceeding $1*10^5$ and increases to approximately 9 percent for Reynolds numbers in the region of $5*10^4$.

4.9 Resistance coefficient comparison (K)

In order to ensure the accuracy of measuring techniques and to improve the uncertainty of measurements especially in the low velocity region, it is required to test screens for which empirical data is available in literature and to compare experimental data to literature. Three screens, across a wide range of FAR's, were selected for this purpose: 30 percent, 50 percent and 70 percent FAR square lattice screens. The test screen was secured in the straight section of the wind tunnel and the resistance coefficient (see equation (1.2)) calculated across the full range of velocities. Figure 110 to Figure 112 in Appendix D show results from this correlation and Table 8 shows a summary of the results. It can be seen that the percentage error does not exceed 3 percent, which is regarded as acceptable considering the uncertainty of the equipment

and flow tests in general. The value of 3 percent compares well with the uncertainty value calculated in paragraph 4.8. Brundrett (1993:241) quotes standard deviation (percentage error) for different studies ranging from ±2.5 percent to ±20 percent.

Table 8: Resistance coefficient comparison (K)

FAR (percent)	Miller[1]	Idelchik[2]	Blevins[3]	Average literature value	Average measured value	Percentage error
30	19.000	18.200	17.000	18.067	17.56	2.87 percent
50	4.000	4.000	3.800	3.933	3.90	0.83 percent
70	0.910	0.970	1.100	0.993	0.971	2.2 percent

1: Miller (1978:263)

2: Idelchik (1986:404)

3: Blevins (1984:314)

4.10 Repeatability tests

In order to ensure repeatability of the measurements, the above-mentioned accuracy tests were repeated for two screens on three different days and at different ambient conditions. Figure 113 and Figure 114 in Appendix D show examples of typical repeatability results and Table 9 shows a summary of the results. It can be seen that the largest deviation from average was calculated to be 1.1 percent resulting in a repeatability of 98.9 percent.

Table 9: Repeatability of results (percentage)

	Test information	Average K-Factor
1	30 percent FAR screen: Test 1	17.54
2	30 percent FAR screen: Test 2	17.44
3	30 percent FAR screen: Test 3	17.71
Overall Average		**17.56**
Largest deviation from average		**0.9 percent**
4	50 percent FAR screen: Test 1	3.89
5	50 percent FAR screen: Test 2	3.94
6	50 percent FAR screen: Test 3	3.87
Overall Average		**3.90**
Largest deviation from average		**1.1 percent**

4.11 Summary

This chapter discussed the design, construction and commissioning of the experimental setup. The design philosophy was defined and the completed wind tunnel was shown after construction. The selection of materials and measuring devices was also discussed. In order to ensure applicability of the results, dynamic similarity was investigated and compared to an actual case.

During the commissioning phase of the wind tunnel, several tests were conducted to ensure the accuracy and repeatability of results. The first phase of commissioning focused on generating a well-developed turbulent inlet flow profile. It was shown that, after some development work, the inlet flow profile resembled a well-developed turbulent flow profile. It was concluded that the inlet bell mouth creates a well-developed flow distribution across the whole range of velocities and that a single measurement in the centre of the duct with a correction factor not exceeding 6 percent can be used to calculate the average duct velocity.

The measuring techniques and the factors influencing the accuracy of experimental data were discussed. A detailed uncertainty analysis was also conducted to determine the uncertainty of the measurements. It was concluded that the uncertainty of measurements is below 3 percent for Reynolds numbers exceeding $1*10^5$ and increases to approximately 9 percent for Reynolds numbers in the region of $5*10^4$. To reduce the uncertainty at low velocities, results were compared to literature and it was found that results compare very well even at low velocities.

Finally, the accuracy of the wind tunnel was investigated and empirical data was compared to different literature sources. It was shown that the accuracy of empirical data is within 3 percent, which is deemed acceptable considering values stated in literature sources. The repeatability of experimental data was also investigated and a repeatability of 98.9 percent was achieved.

It can be concluded that the experimental setup has been verified and that all further empirical data obtained from this facility is deemed accurate within 3 percent, with an uncertainty not exceeding 3 percent (at high Reynolds numbers) and is 98.9 percent repeatable.

The following chapter presents a discussion on the separation of flow in wide-angle diffusers in order to determine the degree of accuracy to which the turbulence models in commercial CFD codes can predict separation and re-attachment of the flow. The CFD modelling approach, assumptions and simplifications are discussed in detail.

CHAPTER 5: SEPARATION OF FLOW IN WIDE-ANGLE DIFFUSERS

5.1 Introduction

This chapter investigates the separation of flow in wide-angle diffusers in order to determine the degree of accuracy to which the turbulence models in a commercial CFD code can predict separation and re-attachment of the flow. The CFD modelling approach, assumptions and simplifications are also discussed in detail.

The essence of this chapter is the accurate modelling of the separation of the flow as it enters into the diffuser section. In order to ensure accurate modelling, it is required to gain a better understanding of the expected flow patterns through diffusers. Literature was consulted and Idelchik (1996:19, 240) predicted highly unstable flow patterns that require a significant length downstream from the diffuser for the flow to recover as shown in Figure 31(a).

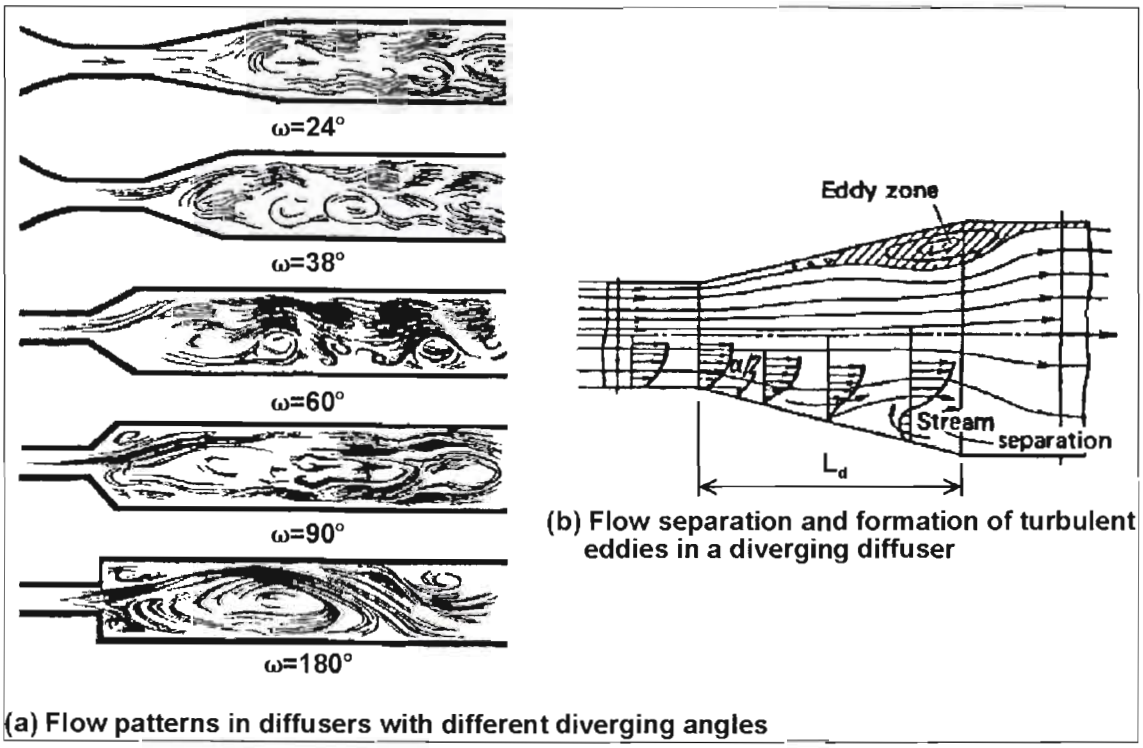

(a) Flow patterns in diffusers with different diverging angles

(b) Flow separation and formation of turbulent eddies in a diverging diffuser

Figure 31: Flow through diffusers with different diverging angles (adapted from Idelchik, 1996)

Idelchik (1996:239) states that: "*The increase in the resistance coefficient of a diffuser (of a given length) with further increases in the divergence angle is caused by enhanced turbulence of the flow, separation of the boundary layer from the diffuser wall and resultant violent vortex formation.*" When flow enters a diffuser, flow separation occurs when the walls of the diffuser are diverging with a total inclusive angle greater than approximately 16° (Schubauer & Spangenberg, 1948:1-4). Figure 31(b) shows how localised eddy zones are generated as a result of the separation of the boundary layer. These eddy zones increase in size and instability with an increase in the diffuser angle. For this application, where the inclusive angle ranges between 60° and 120°, it was expected that the flow would separate in all of the cases and it could therefore be assumed that the large diffuser angle would result in increased instability of the flow, which will complicate measurements in large angle diffusers. From this instability, it was concluded that any measurements would require averaging over a period of time to show trends rather than to measure exact flow profiles.

Idelchik (1996:239) furthermore states that the main characteristics of diffusers with straight walls are the divergence angle ω (see Figure 31), the area ratio $FAR=A_F/A_T$, the speed of sound C and the relative length L_d. These quantities are connected by the following relationship for square type plane diffusers (not applicable to conical diffusers):

$$\frac{L_d}{C} = \frac{FAR - 1}{2\tan\frac{\omega}{2}} \qquad \textbf{(5.1)}$$

Given that the flow conditions at the entrance remain unchanged and that either the relative length L_d (see Figure 31) or the area ratio remains constant, an increase in the divergence angle ω (starting from ω = 0°) will result in the successive achievement of the four main flow regimes:

- Stable regime, non-separating flow *("separation-free" diffusers).*
- Regime with a large non-developed flow separation, where the size and intensity of the separation change with time *(regime of strongly oscillating flows, diffusers with local flow separation).*

- Regime of fully developed flow separation, where the major portion of the diffuser is occupied by an extensive zone of reverse *circulation (diffusers with substantial flow separation).*
- Regime of jet flow, where the main flow is separated from the diffuser walls over the whole perimeter *(diffusers with complete flow separation).*

Given the geometrical layout of the wind tunnel, it was expected that the flow would fall into one of the latter three regimes depending on the diffuser angle. To confirm the flow distribution through the diffuser section, it was required to either visualise the flow passing through the wind tunnel or to measure the flow distribution in the diffuser section. These experiments are discussed in Section 5.2.

Idelchik (1996:240) also states that the inception of flow separation in a diffuser is a function of both its geometric parameters and the flow regime at its inlet (Reynolds number $Re=\rho v D_H/\mu$ and Mach numbers $Ma=v/C$, see paragraph 4.6), as well as of the condition of the flow at the inlet (the displacement thickness of the boundary layer or the "momentum loss" thickness and the level of turbulence). In the previous chapter, it was established that the flow is incompressible and turbulent. For this reason, it would be of great importance to ensure the accurate modelling of turbulence and of the boundary layer in the CFD model. The CFD model is discussed further in Section 5.5.

It can be seen that the flow patterns through large angle diffusers are highly unstable and complex and that the modelling of the flow has a rather high level of uncertainty. The ultimate aim of this project is to accurately model the flow through screens in a diffuser, but before this goal could be reached, it was required to first gain a better understanding of the flow through the diffuser without screens in position. This Chapter focuses on the topic of flow through wide-angle diffusers and investigates these flow patterns both experimentally and numerically.

5.2 Experimental testing of flow through wide angle diffusers

5.2.1 Introduction

The previous Chapter included a detailed discussion into the testing methods and procedures generally applicable. In this section, the discussion focuses only on the

experimental work conducted to investigate flow patterns through wide-angle diffusers. In order to gain a better understanding of the flow separation (if any) and the general flow patterns through wide-angle diffusers, it was decided to adopt two different approaches:

- Flow visualisation
- Measurement of the flow distribution

These tests were repeated for two different diffuser angles, i.e. 60° and 120° inclusive angle, regarded to be the enveloping cases for diffuser angles generally used in ESP's.

5.2.2 Flow visualisation

At the start of this experimental work, it was not certain if the flow could be successfully visualised and if any trends could be observed from this exercise. For this reason, it was decided to adopt two different methods for the visualisation of the flow:

- Using light-weight strings or tufts to visualise the direction and movement of the flow.
- Smoke injected into the flow stream

5.2.2.1 Strings or tufts

Before any visualisation could be done, it was required to find an appropriate background that would be conducive to human visualisation and photography. At first, matt black thin cardboard sheets were fixed to the rear walls and floor of the wind tunnel. It was found however that these sheets showed a grey tint on the photographs as shown in Figure 32. These sheets were then removed and the walls, roof and floor were painted with matt black "chalk board" paint. This proved to be a better background although the grey tint was still evident.

Figure 32 shows that the tufts were fixed to the floor of the diffuser in a straight line in an attempt to find the re-attachment point of the flow. At this stage, it was not clear whether the flow re-attaches in the relatively short distance between the inlet and outlet diffuser. It was found that this method supplied very limited results and that it does not give the researcher a better understanding of the flow distribution through the diffuser section.

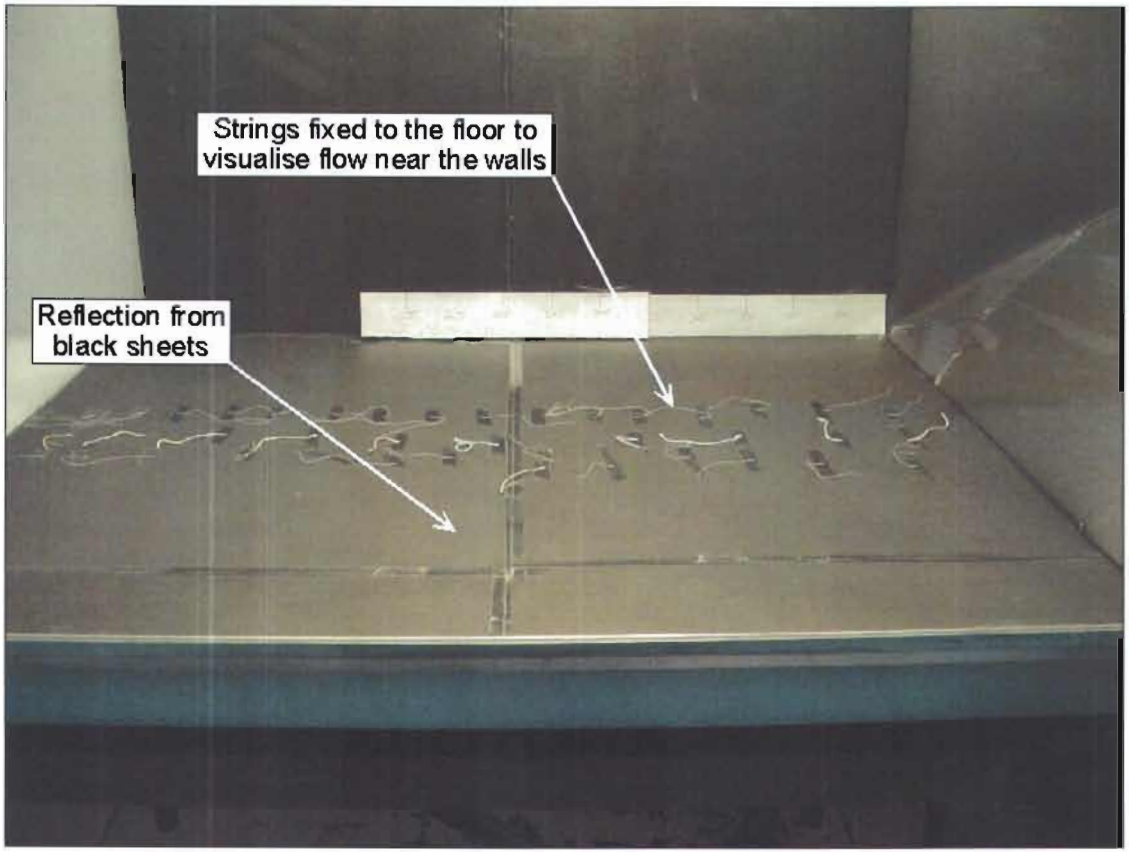

Figure 32: Strings used to visualise flow near the walls

5.2.2.2 Smoke injected into the flow stream

Since the re-attachment of the flow (or lack thereof) could not be shown using the tufts, it was decided to construct a probe that would inject smoke into the wind tunnel in a similar fashion as the previous approach with the strings. This probe is shown in Figure 33. It can be seen that the probe worked well to inject the smoke rather evenly into the wind tunnel, but this approach did also not supply an answer to the issue of flow re-attachment. No conclusive deductions could be made from these results.

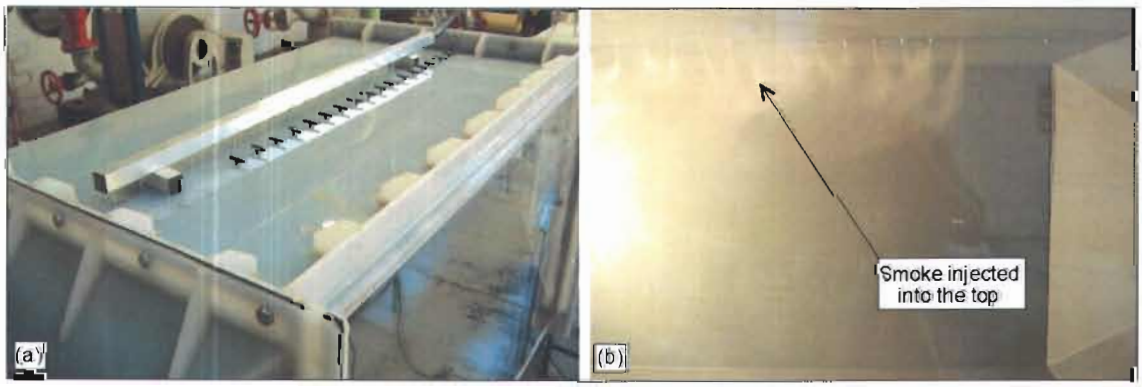

Figure 33: Flow visualisation using smoke

In order to gain a better understanding of the flow through the diffuser section, different smoke streams were injected just before entry into the diffuser section, see Figure 34. From these tests, it could be seen that the flow does not re-attach in the relatively short distance between the inlet and outlet diffusers. The wind tunnel geometry was based on a typical ESP geometry with a relatively short distance between the inlet and outlet diffusers. For this reason, it was not possible to increase the length between the inlet and outlet diffusers in order to enforce re-attachment. Such a configuration would not be applicable. It should also be noted that an ESP has several banks of collection plates between the diffusers that are not included in this study. The focus of this study is on the inlet diffuser and the flow distribution before entry into the collection plates.

To confirm these findings, the literature survey was expanded and it was found that these trends compare well with results presented by Vaivads (1998) as discussed in paragraph 2.6. Although the visualisation of the flow using smoke did not supply quantitative results regarding the flow profile through the diffuser section, it did provide an excellent method to better understand the general flow profiles and behaviour. The improved understanding of the behaviour of the flow served as a good preparation for the measurement of the flow distribution.

5.2.2.3 Lighting and photography

A 500W flood-light was used to supply the lighting for the photography. The light was tested at several different positions and it was found that the best results were achieved with the light positioned in such a way that the light beams can be reflected from the smoke streams. Positioning of the light was difficult due to the reflection from the transparent acrylic front walls. It was also found that the camera's flash could not be used, as shown in Figure 34. However, it was observed that the flash showed excellent definition of the smoke trails. It is therefore expected that a camera with a remote flash would supply best results if the flash could be positioned in such a way that it does not reflect from the front walls, but reflects from the smoke trails. It is suggested that this system is used in conjunction with a powerful light. It may also be possible to achieve better results with Stroboscope photography (also known as Spark photography), where the flow is "frozen" momentarily by using a stroboscope light resulting in better photography. Such equipment is however expensive and due to the rather limited information available from the visualisation of the flow, it was decided not to pursue this any further.

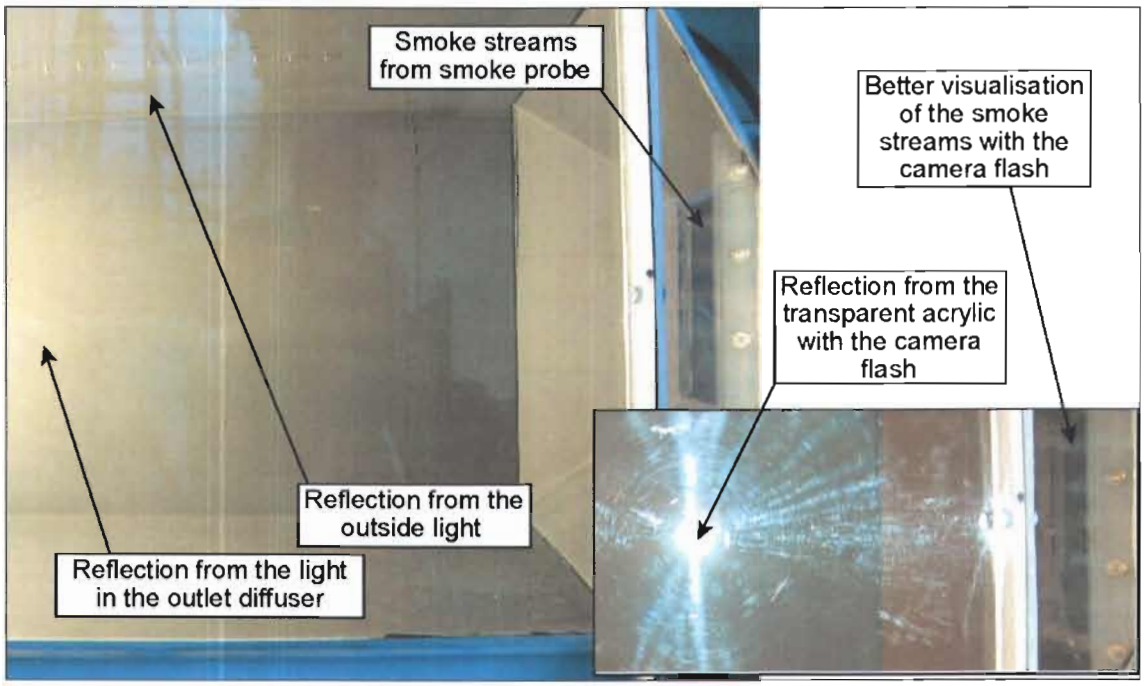

Figure 34: Smoke injection in the inlet diffuser with the light in the outlet diffuser

It was also found that, during the daytime, the background of the laboratory was reflected from the transparent acrylic (see Figure 34). Since it was not possible to restrict the light from entering the laboratory, it was decided to create a simple dark room environment by hanging black sheets from the roof and thus restrict the reflection of the light from the transparent acrylic. This method proved quite efficient and eliminated all external reflections as shown in Figure 35.

It was decided to use a digital camera since digital photography made it possible to take unlimited photographs at no extra cost (development of photographs) and thus experiment with lighting, focus and photo angles. The digital approach saved time since photographs could immediately be downloaded onto a laptop computer and the test could then be repeated immediately if the desired result was not achieved.

It can be concluded that the visualisation of the flow using smoke serves as an excellent tool to gain a better understanding of the general flow patterns, but it does not supply any quantitative results. In order to determine the flow profile more definitive, it was required to include flow measurements as well.

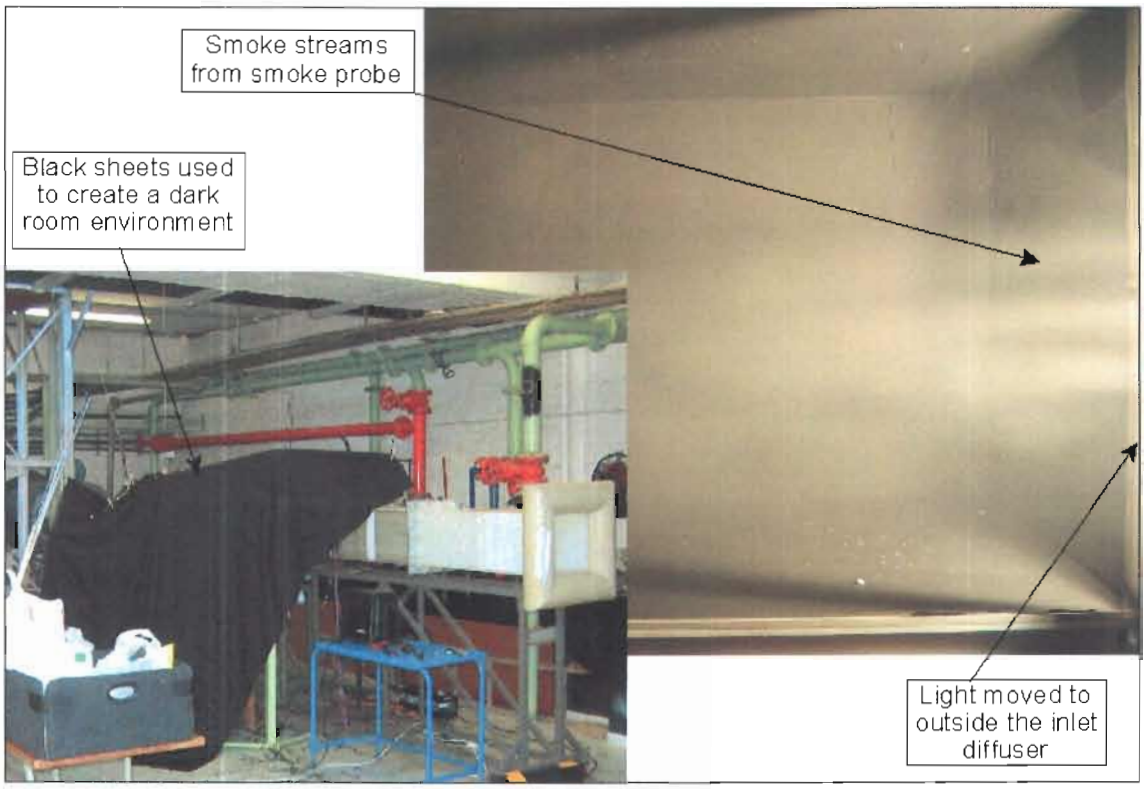

Figure 35: Dark room environment and results

5.2.3 Flow distribution measurements

The test methods discussed in Chapter 4 were adopted to test the flow profile through the diffuser section. Based on the flow visualisation conducted with the smoke trails, the traverse of measurement points was refined to a distance of 50mm between consecutive points. One of the trends highlighted in the literature survey (see paragraph 2.5) was to test a vertical and horizontal traverse only and not to complete a full traverse (grid or matrix of measurement points) for each test, as shown in Figure 36. This assumption was necessary since 13 points (every 50mm) were measured vertically and horizontally for each test resulting in 26 measurements. If a full traverse of points were tested, the required number of measurements would be 169 (13*13), which calculates to 6.5 times more measuring points. With each test being repeated at least three times to determine the spread of the data, the tests would take 19.5 times longer. It has been proven to great length in literature (see paragraph 2.5) that a vertical and horizontal traverse of the data is sufficiently representative of the flow field and for this reason it was decided to measure only vertical and horizontal traverses.

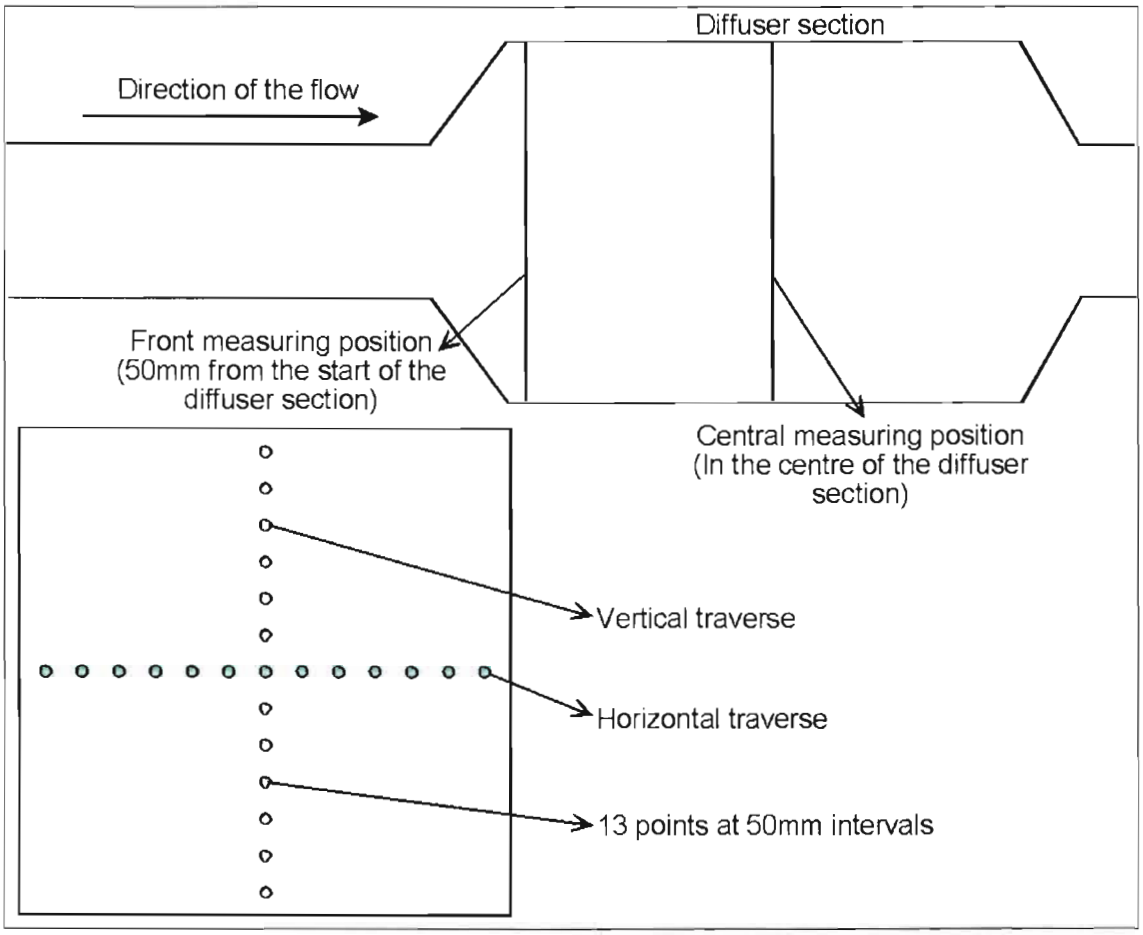

Figure 36: Explanation of measuring traverses

Tests were conducted using a pitot static tube connected to a digital manometer to measure static and dynamic pressure. From these measurements, the velocity was calculated as discussed in Chapter 4. With a pitot static tube, it is imperative to ensure that the pitot tube is always exactly in line with the flow, both horizontally and vertically in order to accurately measure the horizontal velocity component. To achieve this, a drill stand was modified so that the pitot tube could slide up and down while still remaining vertical as shown in Figure 37. A guide was also fitted to the front of the stand to ensure that the pitot tube remained in line horizontally as well.

It was concluded in paragraph 2.5 that variations in Reynolds number have little effect on the flow regime for the range of aspect ratios normally encountered and for all Reynolds numbers in excess of a few thousand (i.e. in the transition region between fully laminar and turbulent flows). Based on this conclusion, it was decided that all tests were to be conducted at a single Reynolds number in the region of $2.5*10^5$.

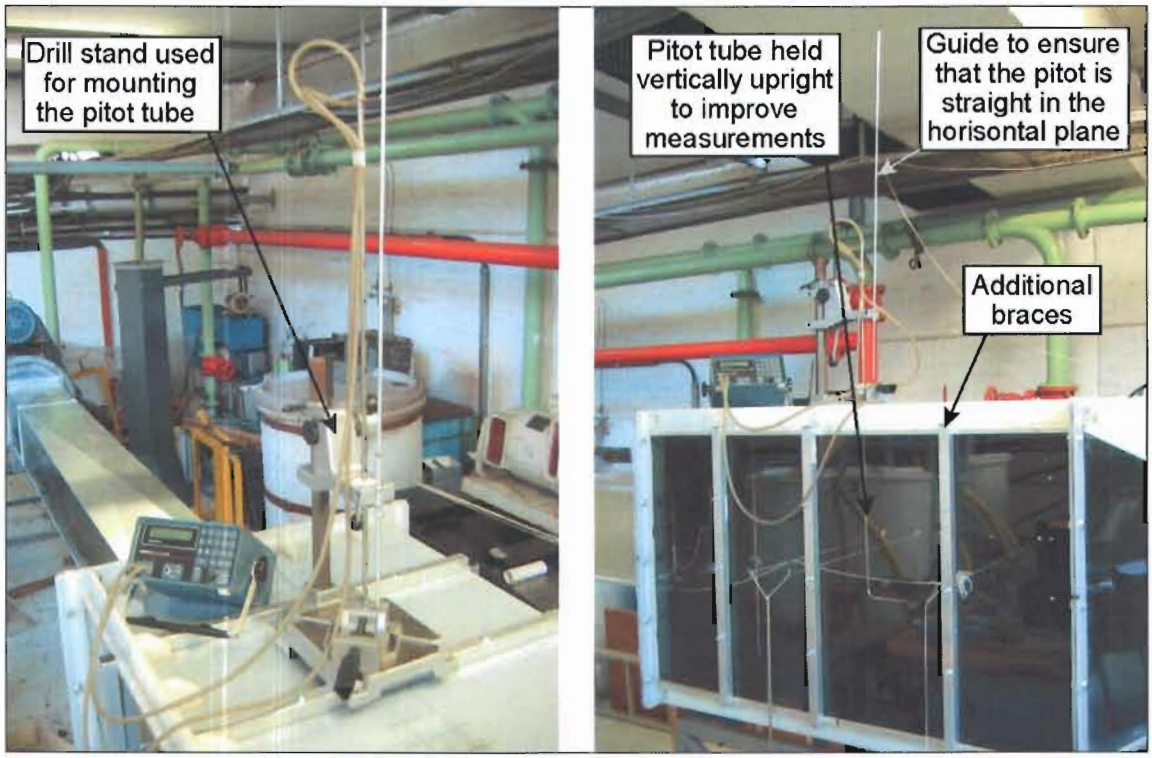

Figure 37: Drill stand used for mounting the pitot static tube

5.2.4 Oblique flow profile through the diffuser section

Initial tests revealed an oblique flow profile through the diffuser section as shown in Figure 38. Since the experimental setup was expected to be symmetrical, the "common sense" approach would suggest that this oblique flow was not physical. It was expected that the flow profile would be symmetrical from top to bottom and from front to rear. This oblique flow profile was not predicted by the CFD model since it is created using an exact geometry. It was therefore required to investigate the cause of this profile.

After consultation with different people, the following possible causes for this flow profile was considered:

- Poor construction of the diffusers.
- Error in the measurements or techniques.
- Drifting of the instruments.
- A change in the inlet flow profile.
- "Roping" of the flow through the wind tunnel due to the axial fan arrangement.
- Separation of the flow entering the fan due to a poorly designed inlet diffuser into the fan.

- The Coanda effect.
- Misalignment of the separate components of the wind tunnel assembly.

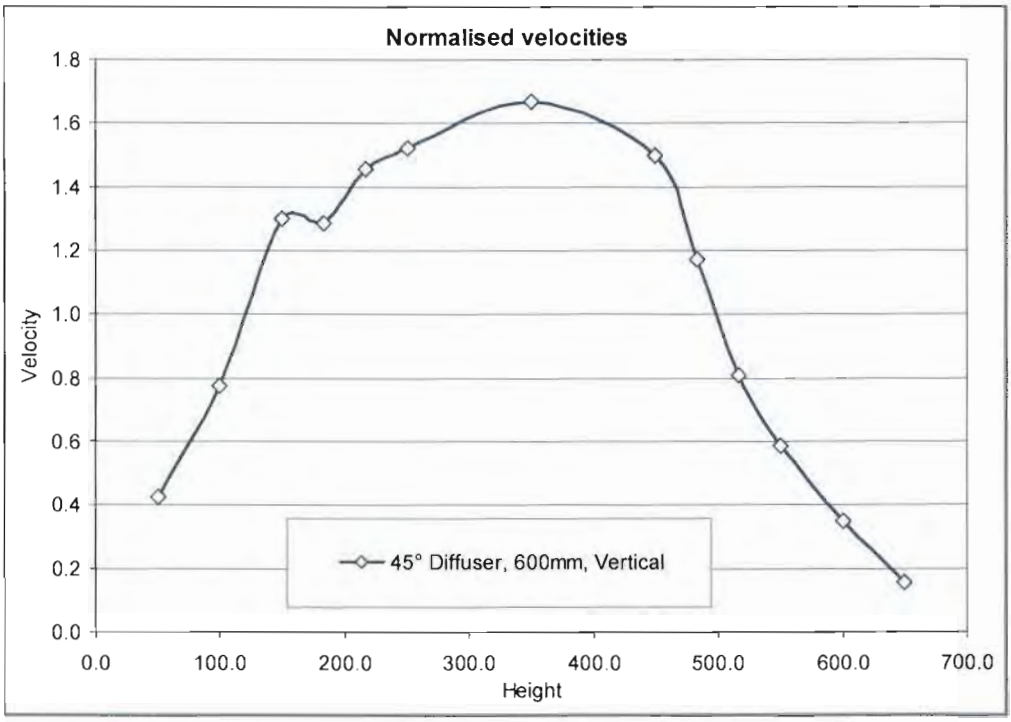

Figure 38: Oblique flow profile initially measured

5.2.4.1 Poor construction of the diffusers

It was thought that the material used to construct the diffuser sections, i.e. polypropalene and wood, was bending under the forces that acted upon it resulting in unsymmetrical geometry at the entry into the diffuser section. To test this, the diffuser was rotated by 180° and the test was repeated. It was however found that results from the second test compared very well with results from the initial test and that the diffuser geometry was therefore not the reason for the oblique flow pattern.

It was however observed that the geometry of the diffuser bending or connection point was not consistent for all four sides of the diffuser. For this reason, it was decided to fit thin cardboard sheets bent to the exact angle in the diffuser in order to ensure symmetrical separation of the flow as it enters the diffuser. This modification is shown in Figure 39. It was found however that these modifications did not solve the problem.

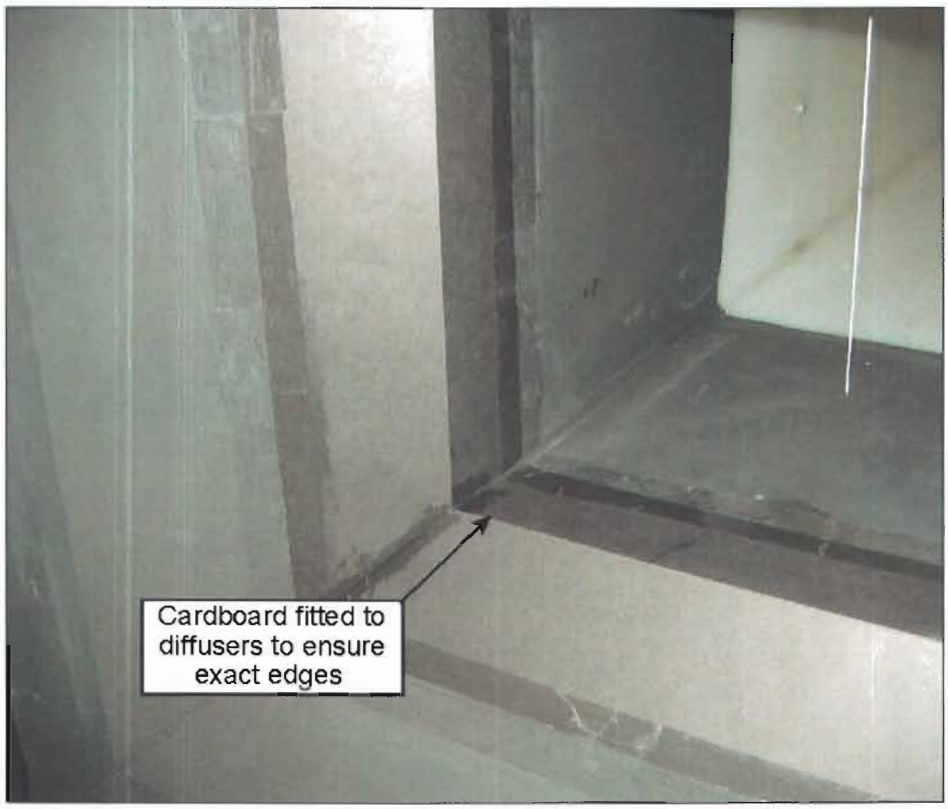

Figure 39: Cardboard fitted to ensure exact edges

5.2.4.2 Error in the measurements or techniques

Another possible cause could be an error in the measurement points or techniques and for this reason a thorough investigation was done into the techniques used. The first test was to repeat measurements with a different pitot static tube and manometer. It was found that results compared rather well.

The points on the pitot tube were marked to the exact size of the diffuser section, i.e. 700mm, but it was found that the negative pressure inside the wind tunnel was bending the large front, rear and top sheets of the diffuser section. Measurements showed that the width of the diffuser section was reduced by 40mm in the centre and since the front wall was used as the reference point, an error was made in the measuring points. This error resulted in a non-symmetrical traverse being measured across the centre of the diffuser section suggesting an unsymmetrical flow pattern. Additional braces were fitted to keep the large sheets from bending inward as shown in Figure 37.

5.2.4.3 Drifting of the instruments

It was found that the instruments were prone to drift away from the zero value to which it was set before the test commenced when the batteries start running down. Unfortunately, these instruments could not be used with a power supply, which would have solved the problem. For this reason, the instrument reading was checked after each test at the zero condition to ensure that the instrument reading did not drift away from the zero value during testing.

5.2.4.4 A change in the inlet flow profile

A non-symmetrical inlet flow profile could be the cause of the oblique flow profile in the diffuser section. Tests conducted in the inlet section during Chapter 4 were repeated to ensure that the technique and setup did not change. These tests would also show if the inlet profile was no longer symmetrical. It was found however that results compared very well with results obtained previously and therefore a poor inlet flow profile was ruled out as the cause.

5.2.4.5 "Roping" of the flow through the wind tunnel due to the axial fan arrangement

It was then considered (although highly unlikely) that the fan was creating an upstream effect causing a rope type flow pattern through the diffuser section thus accounting for the non-symmetrical flow pattern. To ensure that no roping occurred, flow straighteners (i.e. a bank of straight pipes packed into the wind tunnel) were positioned just before the fan to ensure that the flow entering the fan is parallel to the walls of the wind tunnel thus reducing the possibility of upstream flow effects created by the fan. It was found however that this modification did not solve the problem either.

5.2.4.6 Separation of the flow entering the fan due to a poorly designed fan inlet diffuser

As mentioned in Chapter 4, the wind tunnel was constructed using sections of previous experimental facilities to reduce costs. The diffuser into the fan was such a component. The previous application of this diffuser was in a closed loop wind tunnel where the testing section was far removed from the fan and it's diffusers. With the in-line approach adopted for this setup, the efficiency (or lack thereof) of such key components could play a significant role in the distribution of the flow. It was found that the diffuser was expanding the flow from a 250mm square duct to a 700mm diameter flange at an angle of approximately 25° while the fan inlet diffuser is only 350mm. As

discussed previously, it is known that this arrangement would definitely result in the separation of the flow. For this reason, it was decided to replace this diffuser. Due to the 350mm inlet diffuser of the fan, it was found that the diffuser could be much smaller expanding the flow from a 300mm square duct to a 350mm diameter fan inlet. The improved design is shown in Figure 40. It was found that although this modification did improve the flow profile, the problem was not completely resolved.

Figure 40: New connection duct between diffuser and fan inlet

5.2.4.7 The Coanda effect

In some discussions, it was considered that the unsymmetrical flow pattern could be attributed to the Coanda effect. The Coanda effect was discovered by a Romanian Aerodynamicist, Henri Coanda, in 1930. He observed that a stream of air (or other fluid) emerging from a nozzle tends to follow a nearby curved surface, if the curvature of the surface or angle the surface makes to the stream is not too sharp (Naudin 1999:1).

Another example is when a stream of water is flowing along a solid surface, which is curved slightly away from the stream, the water will tend to follow the surface. This is easily demonstrated by holding the back of a spoon vertically under a thin stream of water from a faucet (Raskin 1994:11). If you hold the spoon so that it can swing, you will feel it being pulled toward the stream of water as shown in Figure 41. The effect

has limits: If you use a sphere instead of a spoon, you will find that the water will only follow a part of the way around. If the surface is too sharply curved, the water will not follow, but will just bend a bit and break away from the surface.

Due to the definitive angle of the diffuser, it was thought that the surface is too sharp to establish the Coanda effect in this application. Although it is possible that the Coanda effect may result in some "bending" of the flow, it was thought that the poor flow distribution in the diffuser section could not be attributed to the Coanda effect.

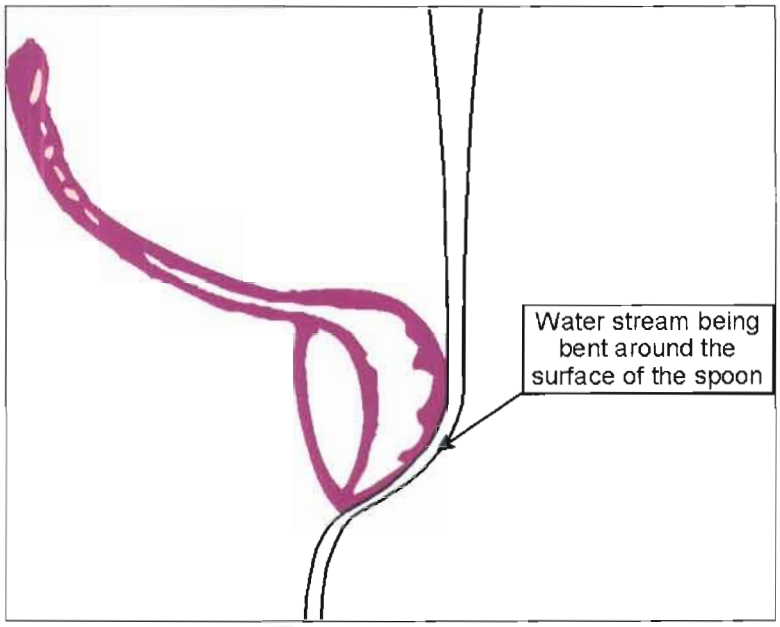

Figure 41: Explaining the Coanda effect

5.2.4.8 Misalignment of the separate components of the wind tunnel assembly

After much deliberation and investigation, it was found that the main cause of the unsymmetrical flow pattern was due to the misalignment of the separate components of the wind tunnel. This was discovered by aligning a string from the front of the wind tunnel to the back and viewing the complete experimental setup from a vantage point high up. It became clear immediately that the front of the wind tunnel was badly misaligned in the horizontal plane. This test was repeated and it was found that the same applied for the vertical plane. This misalignment is not clear to the naked eye since the complete wind tunnel is over 9 meters long and with the diffuser test section in the middle, a line-of-sight is not visible thus resulting in poor alignment occurring rather easily.

To solve this problem, it was decided to fit a rather primitive alignment system by attaching a string to the centre point of the fan and stretching it to the centre point of the inlet through the middle of the wind tunnel. Guide strings were then fitted to all the different sections allowing for the alignment of each individual section. This simple alignment system is shown in Figure 42. Much more expensive alignment systems are available, but due to a limited budget, these systems could not be tested or used.

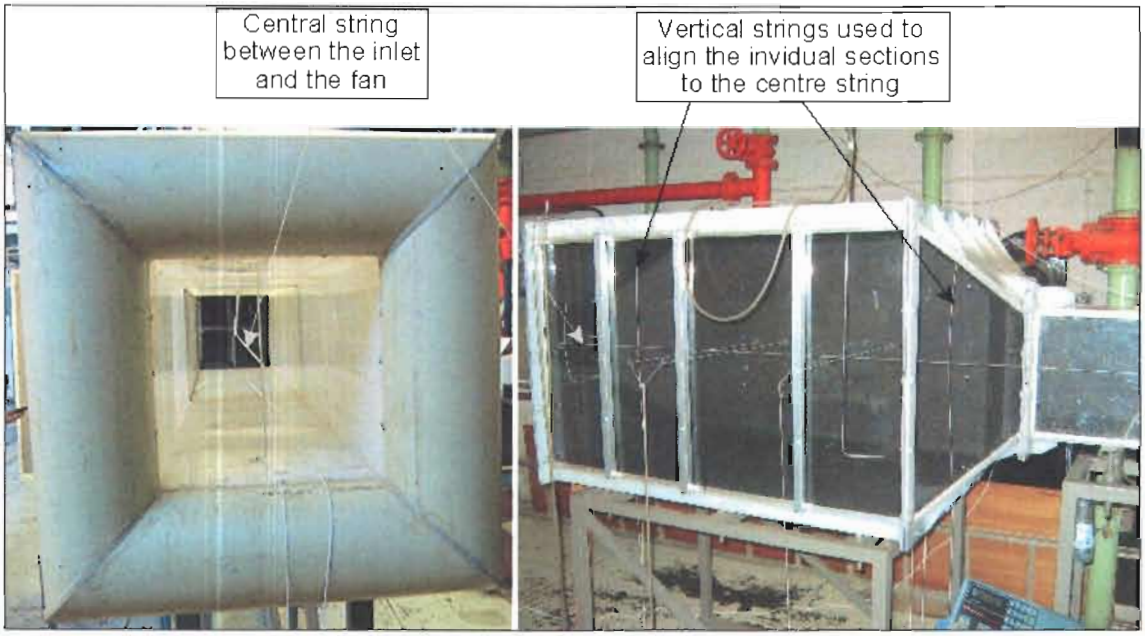

Figure 42: Simple alignment system

To better understand the sensitivity of the system to misalignment, the inlet duct of the CFD model was rotated by only 1° to simulate a misalignment of the inlet section with the diffuser section. Results are shown in Figure 43. It can be seen that with a misalignment of only 1°, the flow distribution is rather severely affected resulting in a non-symmetrical flow distribution. It can also be seen that some negative flows are predicted near the walls of the diffuser section. These negative flows were also observed in the visualisation of the flow patterns using smoke trails through the wind tunnel.

This test therefore proves that the cause of the non-symmetrical flow pattern inside the diffuser is the misalignment of the individual components of the wind tunnel. It was difficult to align the sections within a tolerance of 1° with the alignment system used here. More expensive systems may result in better alignment, but as mentioned previously these systems could not be tested. Based on this finding, it is concluded

that asymmetrical flow distribution measurements is due mainly to the misalignment of the wind tunnel components, given that all other geometries and inlet flow profiles are symmetrical. This would also explain why the inlet flow distribution was still symmetrical and why the rotation of the diffuser section did not result in any major changes to the un-symmetry of the flow distribution.

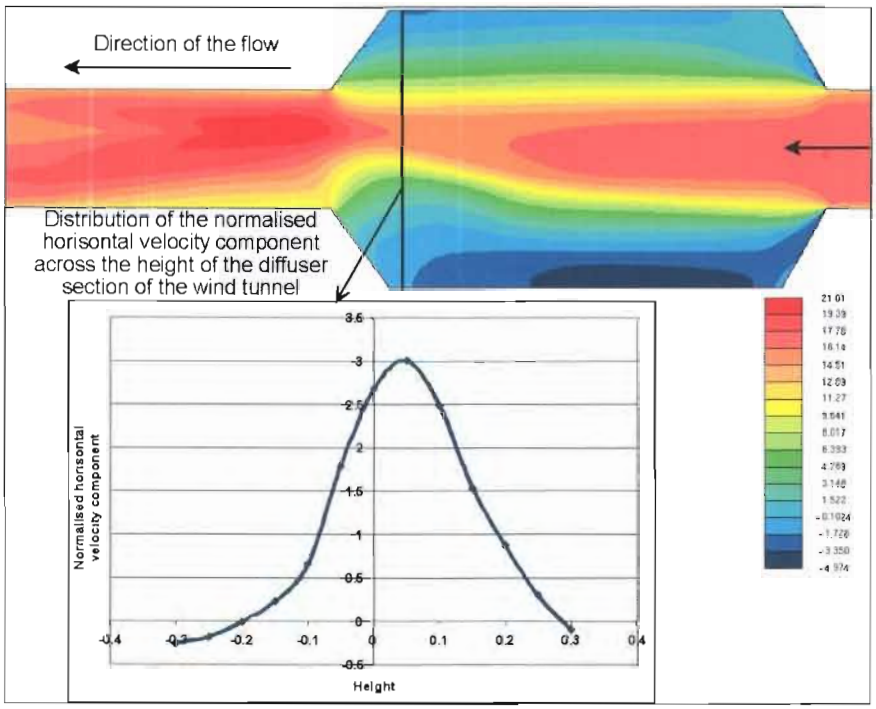

Figure 43: Oblique flow profile with the inlet section rotated through 1°

5.3 Experimental results

5.3.1 Introduction

Since the diffusers used in practice range between 60° (inclusive angle) and 120°, it was decided to test the flow patterns through these diffuser angles thought to be the enveloping cases for this specific application.

To accurately predict the flow distribution through the diffuser section, it was decided to measure both in the inlet and in the centre of the diffuser (see Figure 36). A traverse of 13 points (every 50mm) was measured at these two positions to show the distribution of the flow at each point. As stated in 2.5, several literature sources showed that a vertical and horizontal traverse is sufficiently representative of the flow distribution through the diffuser section. For this reason, all traverses were measured both

vertically and horizontally. Furthermore, all tests were repeated at least three times to show a statistical range of data and to minimise the probability of measuring error.

5.3.2 120° Diffuser

From Figure 44, it can be seen that the distribution in the front of the diffuser section is significantly higher in the centre part of the graph, which is consistent with the flow profiles observed during the visualisation of the flow. All flow measurement values were normalised to the average velocity, i.e. v/v_{mean}. The vertical and horizontal distributions compare relatively well and results show good repeatability between different tests. The effects of misalignment are less pronounced in the front of the diffuser and therefore both profiles are quite symmetrical.

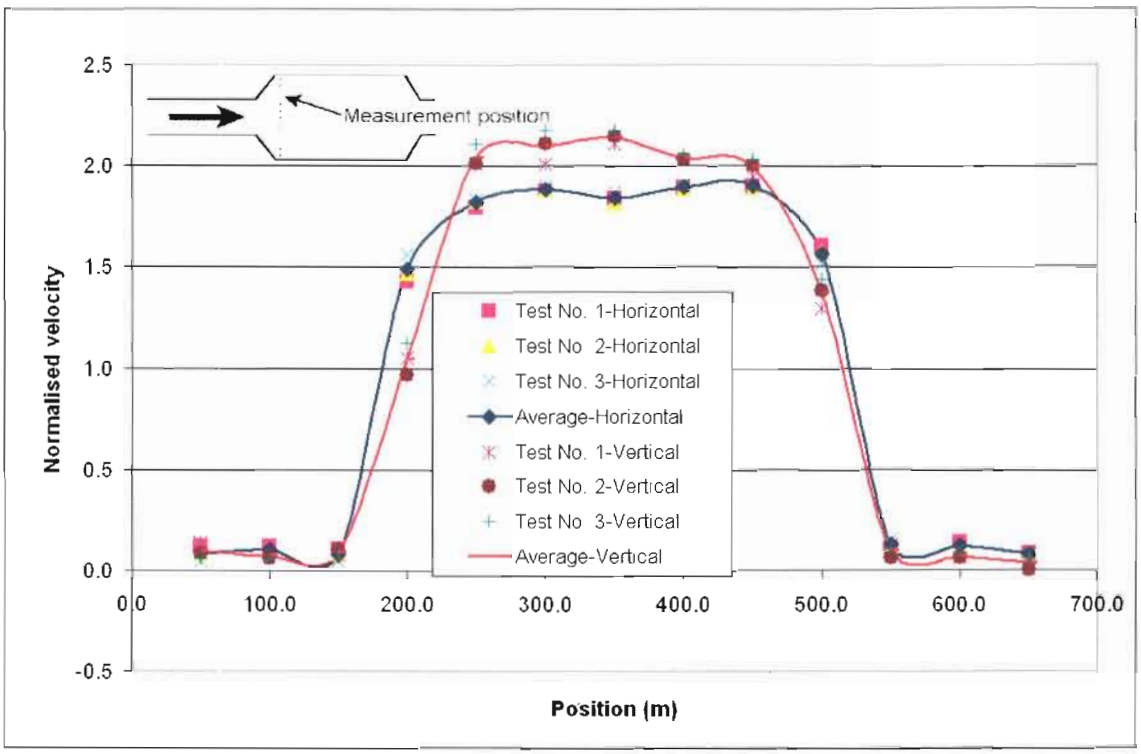

Figure 44: Normalised flow distribution in the front of the 120° diffuser

The flow distributions measured in the centre of the diffuser section are shown in Figure 115. It can be seen that the horizontal distribution is quite symmetrical and that results show good repeatability. These results were achieved with the best possible alignment of the different sections of the wind tunnel and the improvement can be seen when compared to Figure 38. The vertical distribution is marginally unsymmetrical. It was thought that this is due to a slight misalignment as was discussed in paragraph 5.2.4.8.

5.3.3 60° Diffuser

Figure 45 and Figure 116 (Annexure F) show the normalised flow distributions (v/v_{mean}) through the 60° diffuser at the front and the centre respectively. It can be seen that the repeatability of these tests is not as good as for the 120° diffuser. Flow visualisations showed that the flow is highly unstable, which complicated measurements. It can also be seen that the measured distributions are not symmetrical. This asymmetrical flow pattern can possibly be attributed to the misalignment of the wind tunnel.

Due to the large angle of the 120° diffuser, it is very similar to a backward step configuration resulting in a definite separation of the flow. It is therefore expected that the flow can be categorised to fall within a specific regime (as discussed in paragraph 5.1). With the 60° diffuser, it is however possible that the flow alternates between different flow regimes resulting in unstable and unsymmetrical flow patterns. Any minor unsymmetrical influence, e.g. geometry of the diffuser, may cause the flow to become unsymmetrical resulting in the flow patterns presented below.

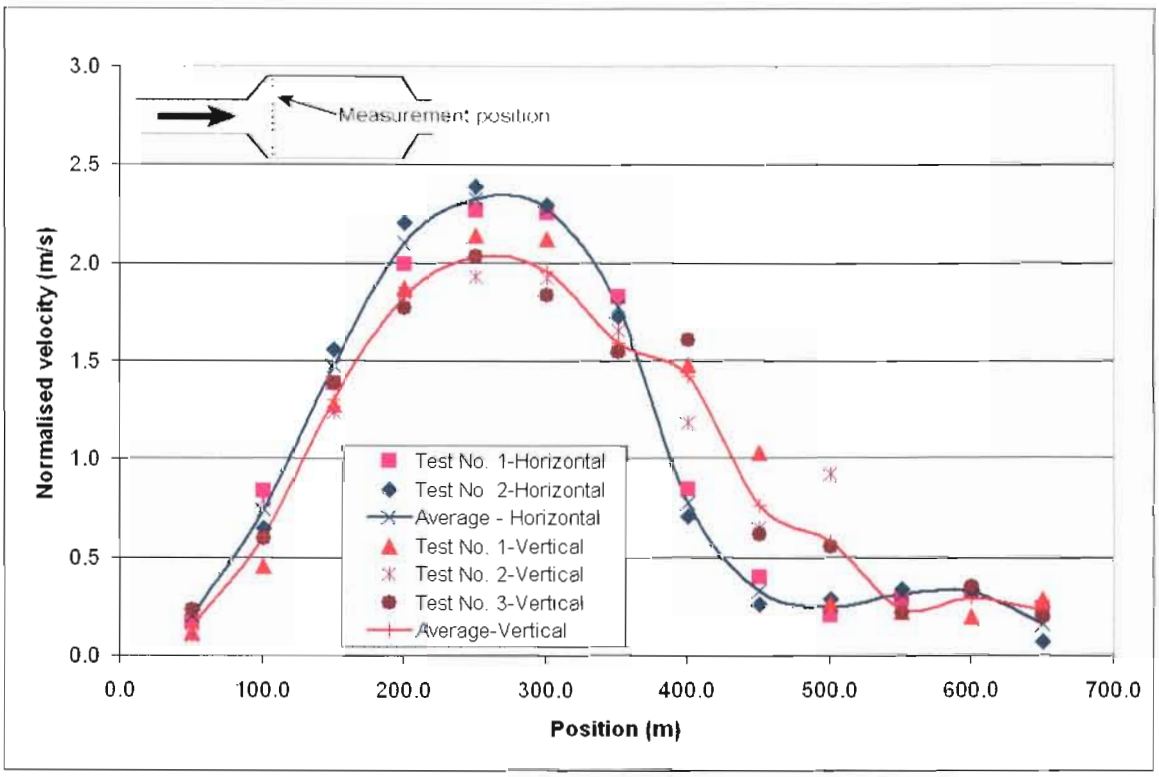

Figure 45: Normalised flow distribution in the front of the 60° diffuser

5.4 The modelling of turbulent flow

5.4.1 Introduction

The essence of this chapter is the accurate modelling of the separation of the flow as it enters into the diffuser section. An essential part of this is the use of a turbulence model that would best simulate the turbulent behaviour of the flow as it expands into the larger diffuser section. To better understand the modelling of turbulence, it was essential to investigate the different models available and their applications. This section focuses on the topic of turbulence modelling.

This study does not propose the development or optimisation of a turbulence model for the accurate prediction of flow through a wide-angle diffuser. However, since the standard k-ε turbulence model failed to accurately predict the re-attachment point in the study conducted by Iaccarino (2000), which included a diffuser of considerably smaller angle, the initial aim of this research is to investigate the prediction of the flow through the diffuser for this specific application. Before continuing with the modelling of turbulence, it is essential to first understand the nature of turbulent flow.

5.4.2 Properties of turbulent flow

Continuing the discussion in section 2.6, turbulent flows are characterised by the following properties (Ferziger and Perić 2002:265):

- Turbulent flows are highly unsteady.
- They are three-dimensional.
- They contain a great deal of vorticity. Vortex stretching is one of the principal mechanisms by which the intensity of turbulence is increased.
- Turbulence increases the rate at which conserved quantities are stirred. Stirring is a process in which parcels of fluid with differing concentrations of at least one of the conserved properties are brought into contact. The actual mixing is accomplished by diffusion. Nonetheless, this process is often called turbulent diffusion.
- By means of the processes just mentioned, turbulence brings fluids of differing momentum content into contact. The reduction of the velocity gradients due to the action of viscosity reduces the kinetic energy of the flow; in other words, mixing is a dissipative process. The lost energy is irreversibly converted into internal energy of the fluid.

- It has been shown in recent years that turbulent flows contain inherent structures, i.e. repeatable and essentially deterministic events that are responsible for a large part of the mixing. However, the random (chaos) component of turbulent flows causes these events to differ from each other in size, strength and time interval between occurrences, making study of them very difficult.
- Turbulent flows fluctuate on a broad range of length and time scales. This property makes direct numerical simulation of turbulent flows very difficult.

In short it can be stated that: Turbulent flow is a highly unsteady flow condition, the flow variables show a coincidental variation over time and spatial coordinates such that statistical averages can be observed. From these properties, it can be seen that the modelling of turbulence is a subject of extreme complexity.

5.4.3 Turbulence models and their uses

There are six basic numerical methods (classification schemes) for the solution of turbulence (Ferziger and Perić 2002:266):

- Direct numerical simulations (DNS)
- Large Eddy simulations (LES)
- Two point closure
- One point closure: Reynolds Averaged Navier Stokes Equations (RANS)
- Integral equations
- Correlations

Some specific models and their uses are discussed in the following paragraphs, but for more detail on these methods and their respective uses refer to Ferziger and Perić 2002, Chapter 9.

5.4.3.1 Direct Numerical Simulation (DNS)

As mentioned previously: The standard momentum equations (Navier-Stokes equations) are capable of modelling turbulence accurately without the aid of simplified mathematical models. However, the number of cells required to model turbulence directly poses a problem since this requires very powerful computing resources. This simulation technique is called DNS. Ferziger and Perić (2002:267-268) states: *"In order to assure that all the significant structures of the turbulence have been captured,*

the domain on which the computation is performed, must be at least as large as the physical domain to be considered or the largest turbulent eddy. A useful measure of the latter scale is the integral scale (L) of the turbulence, which is essentially the distance over which the fluctuating component of the velocity remains correlated. Thus, each linear dimension of the domain must be at least a few times the integral scale. A valid simulation must also capture all of the kinetic energy dissipation. This occurs on the smallest scales, the ones on which viscosity is active, so the size of the grid must be no larger than a viscously determined scale, called the Kolmogoroff scale, η. For homogeneous isotropic turbulence, the simplest type of turbulence, there is no reason to use anything other than a uniform grid. In this case, the argument just given shows that the number of grid points in each direction must be at least L/η; it can be shown that this ratio is directly proportional to $Re_L^{3/4}$. *Here* Re_L *is a Reynolds number based on the magnitude of the velocity fluctuations and the integral scale; this parameter is typically about 0.01 times the macroscopic Reynolds number engineers use to describe a flow. Since this number of points must be employed in the three coordinate directions, and the time step is related to the grid size, the cost of a simulation scales as* Re_L^3."

To put this into perspective: If $Re_L=(0.01)*Re$ and $Re\approx5*10^5$ (applicable to the wind tunnel) the number of grid points in each direction would scale to approximately $(0.01*5*10^5)^3$, $125*10^9$ cells for the large scale (as large as the physical domain to be simulated). This is a rather vague approximation. Using the approximation suggested by Versteeg and Malalasekera (1995:49) it was found that approximately $1.2*10^{12}$ cells are required to model the wind tunnel (see paragraph 2.6). Both approximations show that this approach can only be used for very low Reynolds number flows and even then, the simulation cost is extremely high.

Advantages

- This is the most exact method of modelling turbulence.

Disadvantages

- The control volumes (numerical cells) must be smaller than the smallest turbulent eddy.

- This method is very expensive regarding time and computer resources required.
- DNS solutions are inherently transient.

5.4.3.2 Large Eddie Simulation (LES)

With this approach, the governing equations are filtered to distinguish between the large- and small scale turbulent eddies. Larger eddies are solved more exact than the smaller eddies where turbulence models are used. In the context of LES, the Sub Grid Scale (SGS) Reynolds stresses are required and the models that describe these stresses are called the SGS turbulence models.

Advantages

- Most suited to the simulation of mixing flow.
- Less expensive regarding time and computer resources required than DNS.

Disadvantages

- The control volumes (numerical cells) must be smaller than the largest turbulent eddy, which is dependent on the flow domain.
- This method is still very expensive regarding time and computer resources required.
- LES solutions are inherently transient and three-dimensional.

5.4.3.3 Reynolds Averaged Navier Stokes (RANS) models

Only the k-ε models are included in this discussion. These models work on the principal that an analogy exists between the viscous stresses and the Reynolds stresses and therefore a turbulent viscosity is introduced. These models are also known as the eddy viscosity models. The turbulent viscosity is assumed to be isotropic, i.e. the relationship between the Reynolds stresses and the average rate of deformation is the same in all directions resulting in a scalar rather than a vector approach. This approximation introduced by the k- ε models is called the Boussinesq approximation and makes provision for the transport of turbulence through the average flow velocity and diffusion. This approach also makes provision for the creation and depletion of turbulence. To achieve this, two partial differential equations are solved: (a) turbulent kinetic energy k and (b) the rate of dissipation of the turbulent kinetic energy ε.

Advantages:

- Suitable for a wide range of industrial applications.
- This model is well established.
- Simple start (initial) and boundary conditions.

Disadvantages:

- Cannot solve flow with large stresses very accurately, e.g. bent curves, mixing- or rotational flow.
- Is dependent on the quality of the mesh.
- The inherent weakness of all these models is that they assume isotropic turbulence.

Star-CD Version 3.15 includes some variations on the k-ε model for high Reynolds numbers (Star-CD v3.15 Methodology manual 2001:2-1):

- The standard k-ε model in which the high (turbulent) Reynolds number forms of the k and ε equations are used in conjunction with algebraic 'law of the wall' representations of flow, heat and mass transfer for the near wall region.
- The Renormalisation Group (RNG) version of the k-ε model. This is employed in high Reynolds number form in conjunction with the 'law of the wall' functions.
- A modified version of the k-ε model, called the Chen k-ε model, which employs both the production and dissipation time scales in closing the dissipation equations. This model is also utilised in high Reynolds number form in conjunction with the 'law of the wall' functions.
- The high Reynolds number quadratic k-ε model in conjunction with the 'law of the wall' representations of flow, heat and mass transfer for the near wall region.
- The high Reynolds number cubic k-ε model in conjunction with the 'law of the wall' representations of flow, heat and mass transfer for the near wall region.

All of these models are compared to test the prediction of the flow separation through wide-angle diffusers (see paragraph 5.6).

5.4.3.4 The v2f model

Since the research into this field is ongoing, better turbulence models are being developed continuously. One such model is the v^2-f model and it can be described as (Laurence, Uribe, Utyuzhnikov 2003:2): a turbulence model where the wall normal component, v^2, and its source term f, are retained as variables in addition to the traditional k and ε (energy dissipation) parameters of the k-ε eddy viscosity models. This model was developed by Durbin (Ferziger and Perić, 2002:301) who suggested that the problem is not that the Reynolds number is low near the wall (although viscous effects are certainly important), but that the impermeability condition (zero normal velocity) is far more important. This suggests that instead of trying to find low Reynolds number models, one should work with a quantity that becomes very small near the wall due to the impermeability condition. Such a quantity is the normal velocity (usually called v by engineers) and its fluctuations (v'^2) and so Durbin introduced an equation for this quantity. It was found that the model also required a damping function f, hence the name v'^2–f (reduced to v2f). This model appears to give better results at essentially the same cost as the k-ε model, but is most applicable to low Reynolds number flows. The v2f model does however require a fine (two-layer) mesh near the wall to accurately model wall effects, which increases the number of cells.

This model is however supplied as an add-on to the commercial CFD codes and can be purchased at additional cost. The intention with this study is to use the standard features that are supplied with the CFD codes to enable the end user to also benefit from this research without the need for additional software. For this reason, this model was not included in this study.

From the above discussion, it can be concluded that the k-ε model is best suited for use in this study for the following reasons:

- it does not require excessive time and computing resources
- it is suitable for a wide range of industrial applications
- it is well established
- it requires simple start- and boundary conditions
- it does not require a transient solution
- it is supplied with all the major commercial CFD codes at no extra cost
- it was used in many of the related research projects (see paragraph 2.8.)

It was shown in paragraph 2.6 that the k-ε model does not accurately predict the exact re-attachment point of separation flows on the microscopic level. With large angle diffusers, it is expected that the flow will separate and re-attach at some point and that this re-attachment may not be accurately predicted by the k-ε model. The visualisation of the flow has shown that it does not re-attach in the relatively short diffuser section used in this study. For this reason, it is essential to test the applicability of the k-ε model to this specific application. Other turbulence models supplied with Star-CD Version 3.15 were also tested.

5.4.4 The importance of y+ values

Since the separation of the flow in the diffuser is a function of the flow regime at its inlet, it is important to understand the turbulent boundary layer. Anderson, Tannehill and Pletcher (1984:224) reports the following zones in the turbulent boundary layer for a typical incompressible flow over a smooth flat plate (see Figure 46):

- The linear viscous sub-layer where viscous stresses dominate the flow adjacent to the surface.
- The buffer zone where viscous and turbulent stresses are of similar magnitude
- Fully turbulent log-law zone where turbulent (Reynolds) stresses dominate. The above three regions form the inner region collectively called the "Law of the wall" zone.
- Outer region or "Law of the wake" zone.

Although this is applicable to a flat plate, it is expected that the walls forming the square geometry of the wind tunnel inlet would result in a similar boundary layer although the thickness of the boundary layer would be limited. The inner region occupies 10 to 20 percent of the total thickness of the wall layer (Versteeg and Malalasekera 1995:60). In this region, the shear stress is (almost) constant and equal to the wall shear stress. For further detail on this topic, the reader is referred to Versteeg and Malalasekera (1995:60-62). For the purpose of this discussion, it is important to note that the y+ values should fall within a certain range to accurately model the boundary layer effects. In Section 4.5, it was stated that the y+ value should be higher than 30 and lower than 300 for pipe flow (Adapco 2002) and that the y+ value is a function of the cell size near the wall and of the flow velocity. Figure 47

shows the y+ values in the CFD model and it can be seen that the values in the pipe section range between 110 and 130. In the diffuser section, the values are reduced to just above 30. It can therefore be concluded that the y+ values fall well within the prescribed limit for typical velocities that are included in this study.

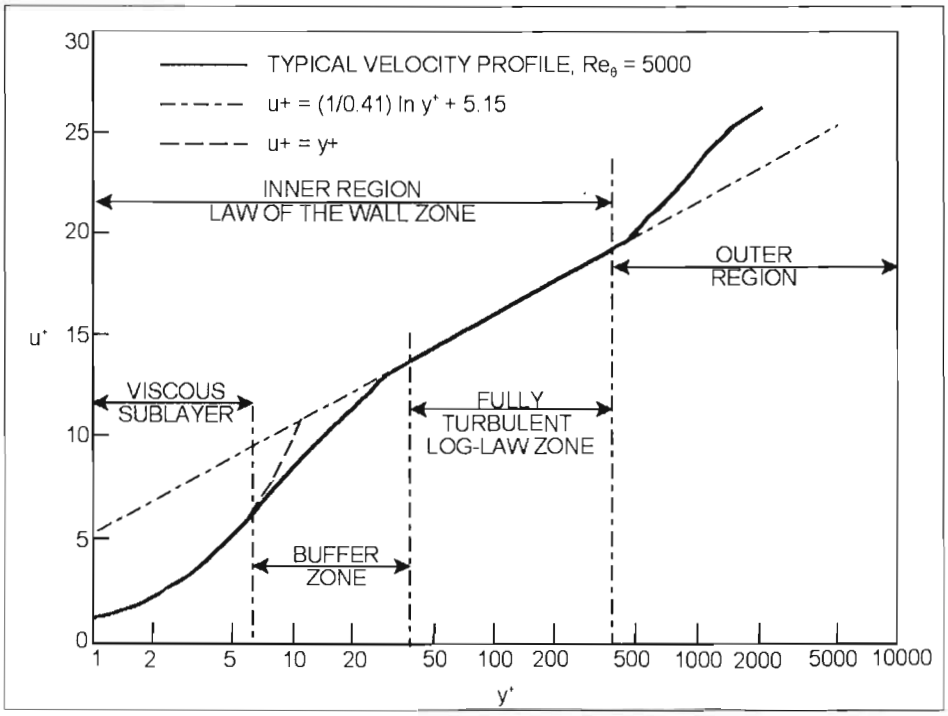

Figure 46: Zones in the turbulent boundary layer for flow over a smooth flat plate (adapted from White, 1991)

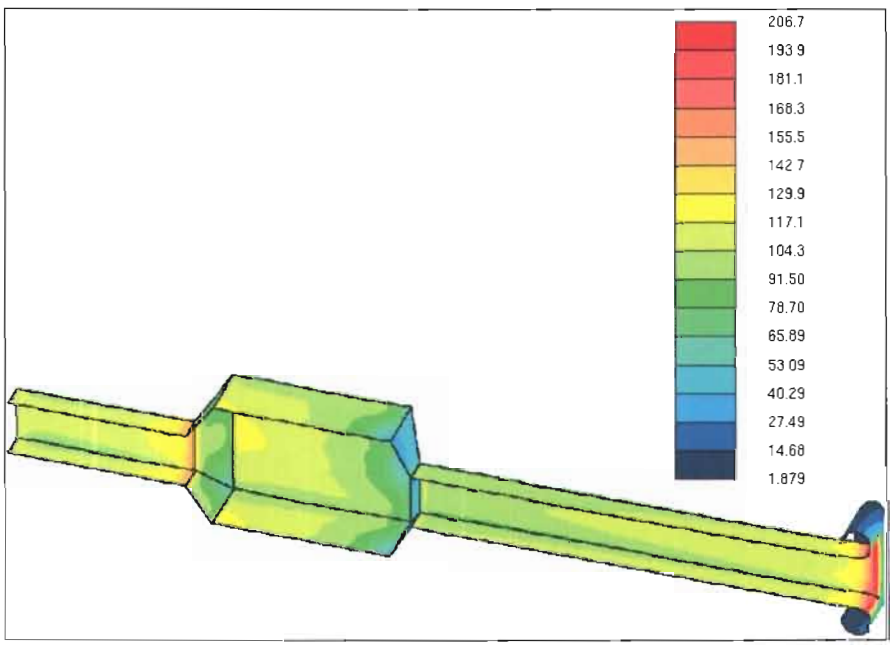

Figure 47: y+ values in the CFD model

White (1991:413) shows that the separating flow profile is significantly different than the flat plate values, as shown in Figure 48, because the velocity approaches zero resulting in very small y+ values. Results from the CFD simulations showed similar y+ behaviour in the diffuser section with separating flow as shown in Figure 47.

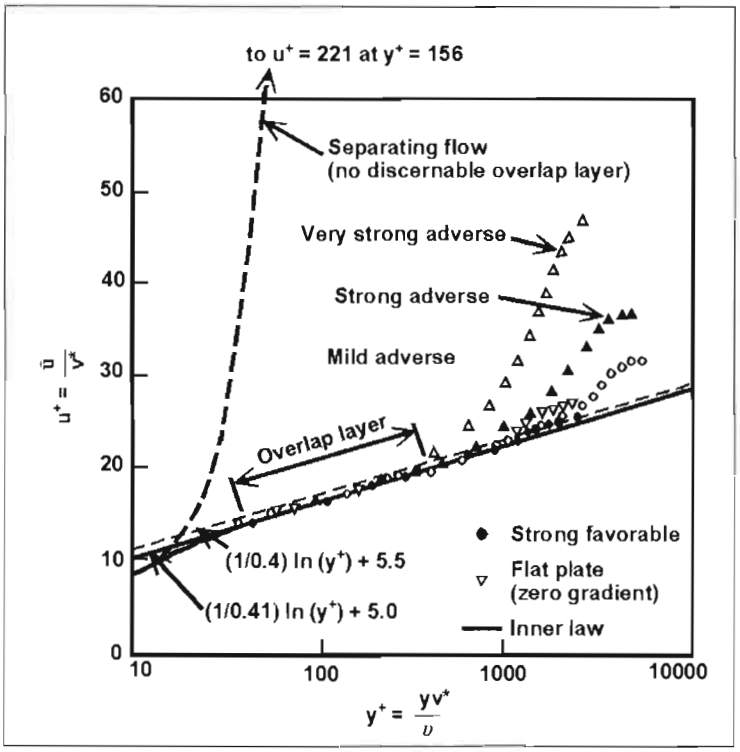

Figure 48: Zones in the turbulent boundary layer with separating flows

(adapted from White, 1991)

5.5 The CFD model

5.5.1 Introduction

This thesis does not include a detailed discussion into the methods and theory of Computational Fluid Dynamics (CFD). Some detail is included in the discussion as is required to better explain a certain notion or concept, but for further information the reader is referred to Ferziger and Perić (2002), Versteeg and Malalasekera (1995) and Patankar (1980). The commercial CFD code Star-CD Version 3.15 for Windows was used for this study (Star–CD User- and Methodology Manuals 2001).

The finite volume mesh is shown in Figure 49. It can be seen that the inlet was modelled as a large cavity before entry into the wind tunnel. The model included a detailed inlet bell mouth to produce a well-developed flow distribution into the wind

tunnel, as discussed in paragraph 4.5. It can be seen that cells near the walls have been refined to better simulate wall effects. The 60° diffuser is shown here although a similar model was constructed for the 120° diffuser. This model consisted of 208192 cells in total requiring approximately 190MB of system memory to solve using double precision.

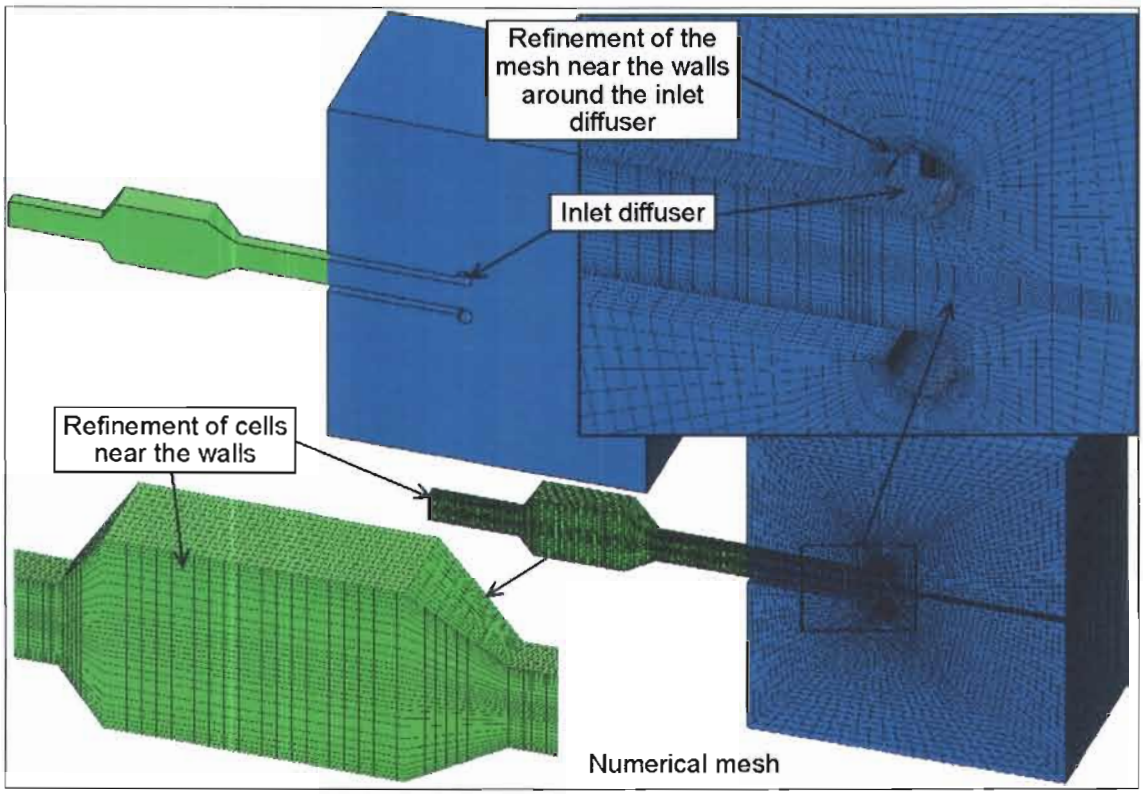

Figure 49: Finite volume mesh used for this study

5.5.2 Assumptions and simplifications

5.5.2.1 Symmetry

A 180° model of the wind tunnel was created assuming symmetry across a vertical plane in the centre of the wind tunnel as shown in Figure 50. Due to hardware limitations, it was not possible to include a full three-dimensional model of the wind tunnel. Theoretically, it would have been possible to include only a 90° section applying symmetry boundaries to both the vertical and horizontal planes. It was however decided to include as much detail, as was allowed by the hardware limitations, to enable the modelling of non-symmetrical effects at least in one direction.

5.5.2.2 Inlet and outlet boundaries

An inlet type boundary in the outward direction (see Figure 50) was used to induce the flow through the wind tunnel. For this boundary, the mass flow was fixed (rather than the velocity magnitude) to allow for the correct development of the approaching flow profile. The flow entered the control domain through an atmospheric pressure boundary, which also allowed for the development of the flow distribution into the wind tunnel.

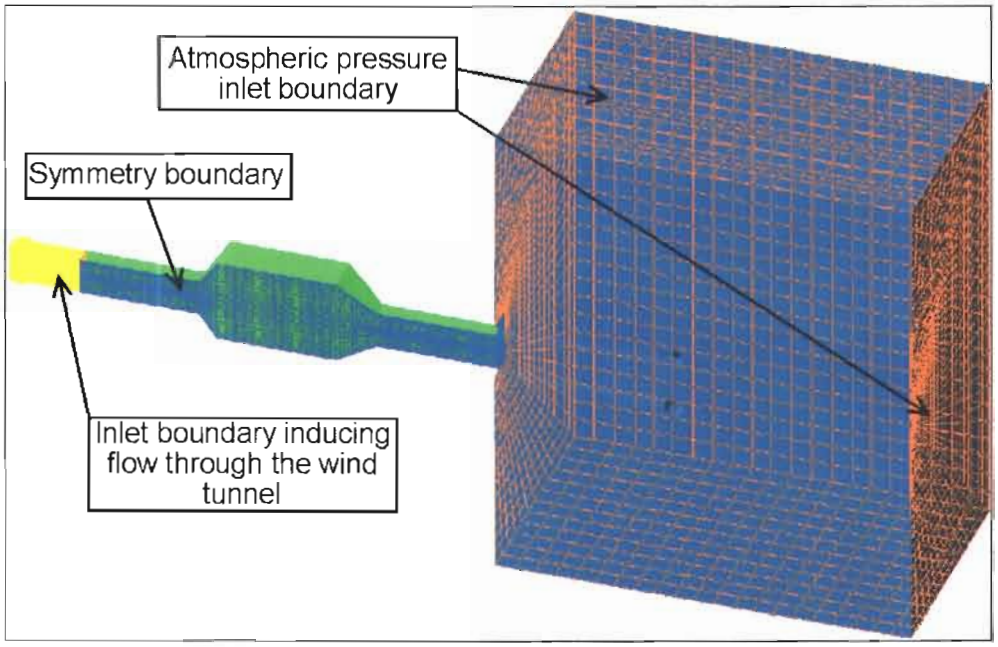

Figure 50: Boundaries used to define the control volume

5.5.2.3 Thermo-physical properties

The energy equation was not solved for: Since no heat, other than friction, was added or extracted from the flow, it was decided not to include the energy equation in the calculation of the momentum flow field. This would only result in extended solution times and it was thought that it would not add any value to the solution.

The effect of buoyancy was switched off due to the small change in temperature through the wind tunnel. Since the maximum change in temperature through a single day is approximately 15°C, the instantaneous change in the temperature of a gas stream passing through the wind tunnel is negligible. For this reason, the change in density was neglected and it was assumed that the density remains constant for each individual test. It should however be noted that the laboratory tests were repeated

exactly and that the density (as a function of the temperature) was changed for each simulation although these values remained constant for this specific simulation.

All turbulence models and discretisation schemes were used as prescribed by the CFD code and no coefficients were changed. The altering of these coefficients does not fall within the scope of this study.

5.5.3 Convergence of solution algorithm residuals

The maximum residual tolerance was kept at 0.001, which is the standard setting for the Star-CD code. The convergence of important field variables such as u, v and w velocities, turbulent energy and energy dissipation was also monitored. It was found that only the mass flow rate would not converge fully as shown in Figure 51. It was thought that this is due to the inherent instability of the separating flow through the diffuser section. Mass flow rate can only be solved in Star-CD using the CD- and MARS discretisation schemes, which is unbounded and is resulting in an inherent instability due to the transient nature of the separating flows. For this reason, none of the simulations reached convergence and were stopped manually at 2000 iterations. The atmospheric pressure inlet boundary and the size of this boundary may have had an influence on the convergence of mass flow.

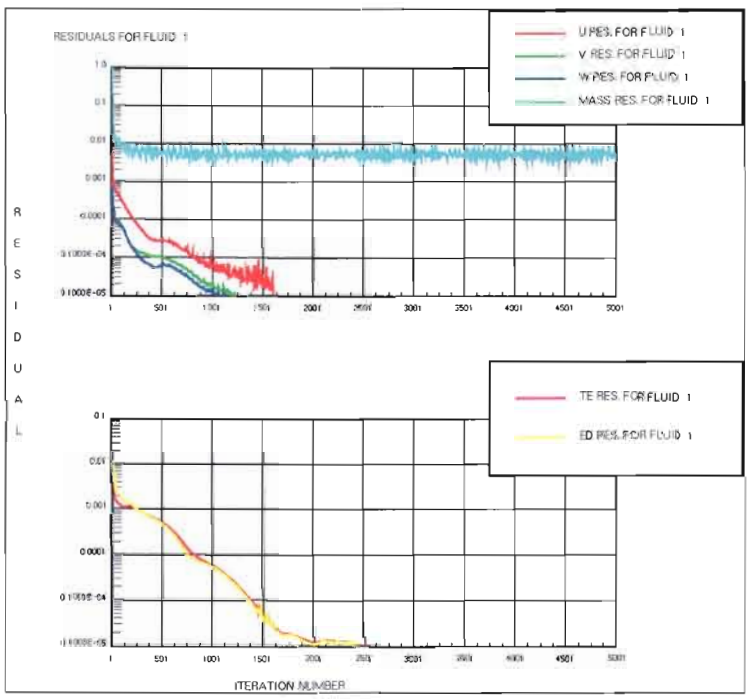

Figure 51: Graphs of solution algorithm residuals

5.5.3.1 Solution parameters

With density constant, it was found that default relaxation of the solution algorithm residuals could be used. The sensitivity of the relaxation factor was tested and it was found that the solution algorithm was quite sensitive to the description of density. If the ideal gas law was applied for the calculation of density, it was found that the solution algorithm would diverge rather easily requiring under-relaxation of the numerical solution algorithm. This can be attributed to the atmospheric pressure boundary used at the inlet.

For all simulations, the Algebraic Multigrid Solver (AMG) was used and not the Conjugate Gradient Solver (CG). All simulations were conducted in double precision and executables were compiled locally for each simulation, i.e. the pre-complied solver was never used. Only the SIMPLE algorithm was included in the simulations. Testing of the other two solution algorithms, i.e. SMPISO and PISO, does not form part of the scope of this study.

5.5.4 Discretisation schemes

The following schemes offered by Star-CD was included:

- The default Upwind Differencing (UD) discretisation scheme
- The Central Differencing (CD) discretisation scheme
- MARS: Monotone Advection and Reconstruction Scheme. The MARS scheme operates in two steps: Reconstruction and Advection. For further detail, refer to the Star-CD v3.15 Methodology manual (2001:4-7). Further information could not be found on this scheme due to the confidentiality of the information.
- QUICK: Quadratic Upwind Interpolation for Convective Kinematics.

The two main approaches are the UD and CD schemes and the others are mainly combinations or derivatives of these schemes. Table 10 and Figure 52 show some detail of discretisation schemes and its implementation. For further information on discretisation practices used in Star-CD, refer to the Star-CD v3.15 Methodology manual (2001:4-1 to 4-10). It is important to note that Star-CD does not use the UD discretisation scheme for mass flow. The user can only choose between CD and MARS for mass flow. For this reason, some schemes (e.g. QUICK) were tested with both CD and MARS.

Table 10: Properties of discretisation schemes

	Conservativeness	Boundedness	Transportiveness	Order
UD	Yes	Yes	Yes	First
CD	Yes	No	No	Second
MARS	NA	NA	NA	Second
QUICK	Yes	Yes	Yes	Third

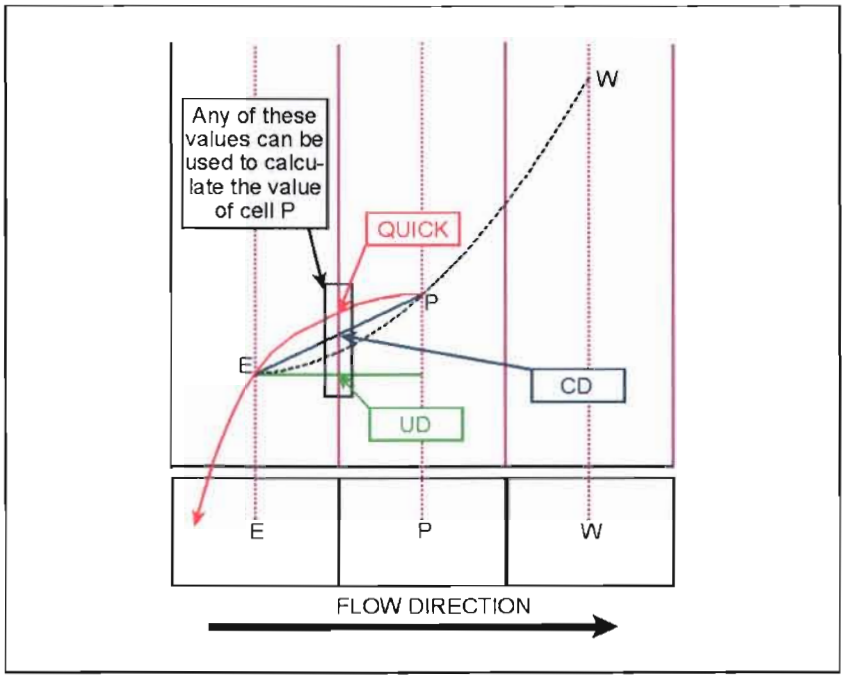

Figure 52: Explanation of discretisation schemes

5.6 Results from the CFD model

5.6.1 120° Diffuser

5.6.1.1 The influence of different turbulence models

The following turbulence models that are supplied as part of the Star-CD CFD code, were tested:

- High Reynolds number k-ε
- Chen
- High Reynolds number Cubic
- High Reynolds number Quadratic
- RNG

Comparative results are shown in Figure 53 and Figure 117 for the front and central positions respectively. It can be seen that the difference between the turbulence models is not significant. It was expected that the different turbulence models would predict vastly different flow distributions. These similar trends may be due to the fact that all the turbulence models supplied with Star-CD Version 3.15 are basically derivatives of the default k-ε model.

It can also be seen that only the k-ε model predicts symmetrical flow patterns while the other models show asymmetrical behaviour. As discussed in paragraph 5.1, flow through wide-angle diffusers are highly unstable and complex and it would appear that the other models are more sensitive to this instability. The k-ε model seems to average the unstable flow better thus simplifying the comparison between experimental and numerical data. The unsymmetrical behaviour of some schemes may also be attributed to the fact that the solution algorithm was not fully converged.

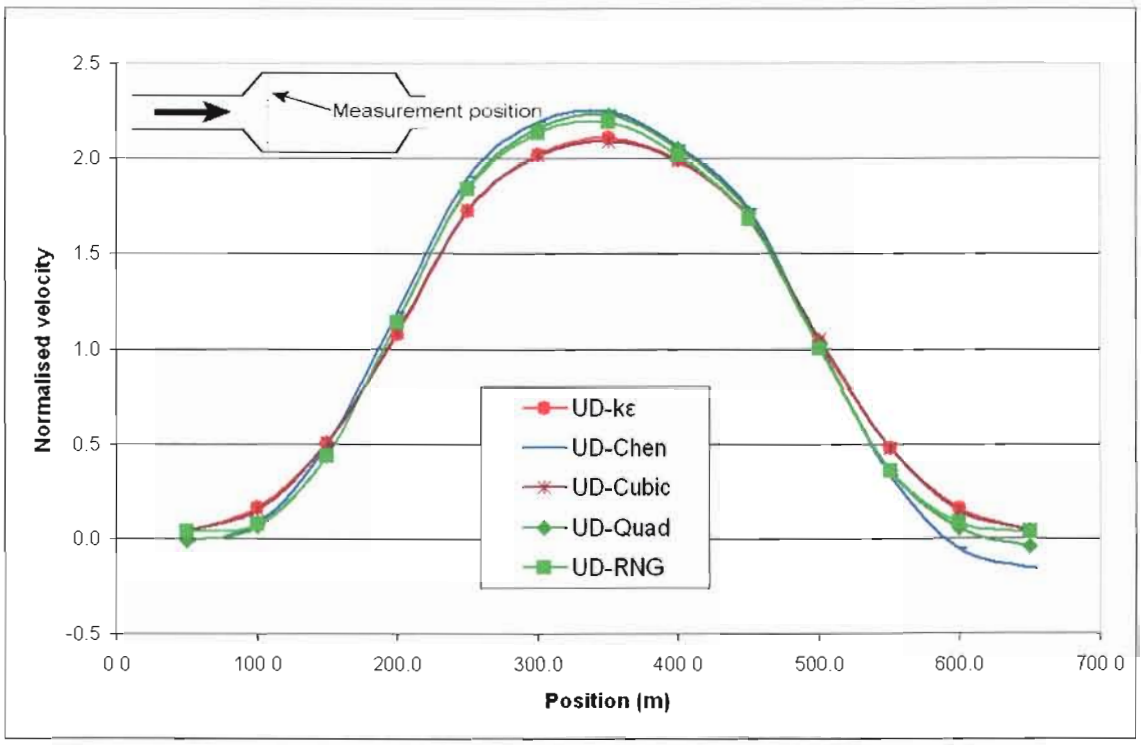

Figure 53: Testing different turbulence models on the 120° diffuser front position

5.6.1.2 The influence of discretisation schemes

Figure 54 and Figure 118 show the predicted flow profiles with different discretisation schemes. It can be seen that the compressive first order UD scheme shows a different profile than the higher order schemes. The term "compressive" refers to the fact that

the UD scheme uses the value upstream as the cell value for each iteration (see Figure 52). This results in a compressed flow field rather than an expanded flow field.

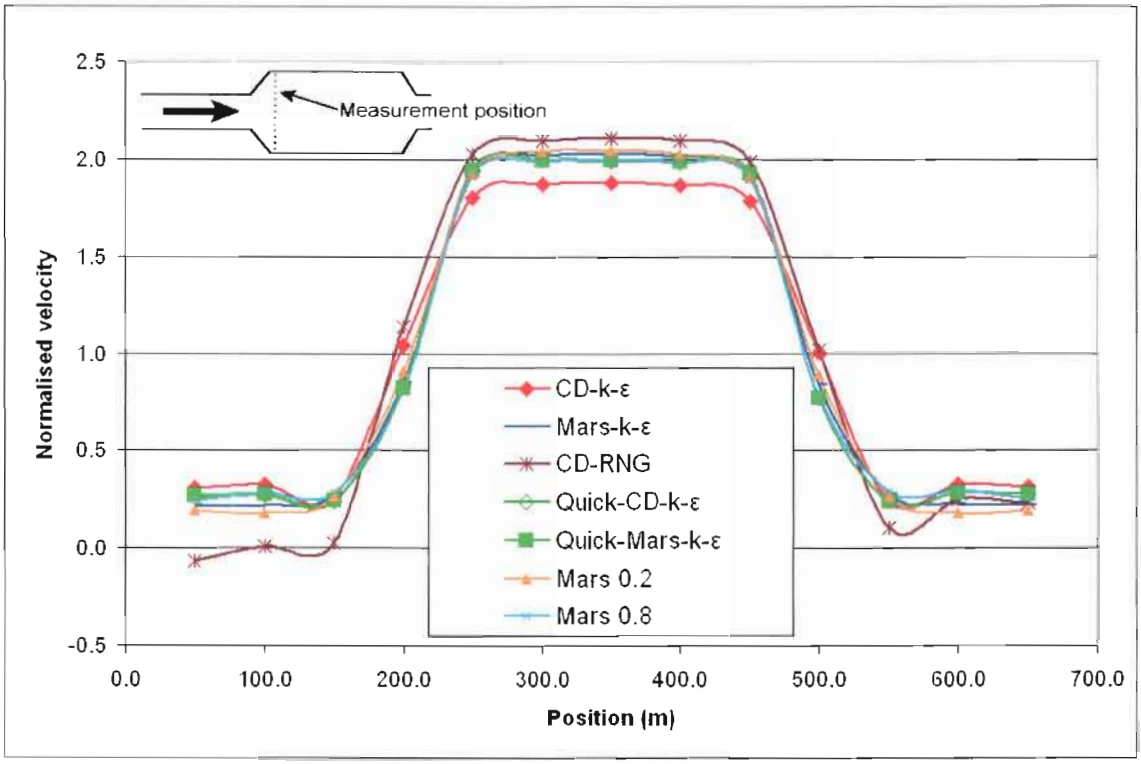

Figure 54: Testing discretisation schemes on the 120° diffuser front position

In the case of CD and MARS, the value of the cell downstream is included in the calculation of the cell value thus resulting in an expansion of the flow field and also a significant difference in the prediction of the flow distribution. QUICK, being a third order scheme, uses the value of two cells upstream and one cell downstream to fit a quadratic relationship through these values in order to predict the value of the cell being solved. Since this is not a simple linear upwind approximation, it can be seen that the predicted flow distribution compares well with other discretisation schemes.

The compressibility of some schemes can be adjusted by changing the blending factor between the UD and CD approaches. The MARS scheme was tested where the default blending factor of 0.5 was changed to 0.2 and 0.8 to test the sensitivity of this setting. It can be seen that the effect is negligible for the 120° diffuser.

5.6.2 60° Diffuser

5.6.2.1 The influence of different turbulence models

Figure 55 and Figure 119 show the predicted flow distributions through the 60° diffuser with different turbulence models. It can be seen that, in this instance, the difference is more significant than with the 60° diffuser. In paragraph 5.7, these results are compared with the experimental data to investigate which model best predicts the actual flow profile.

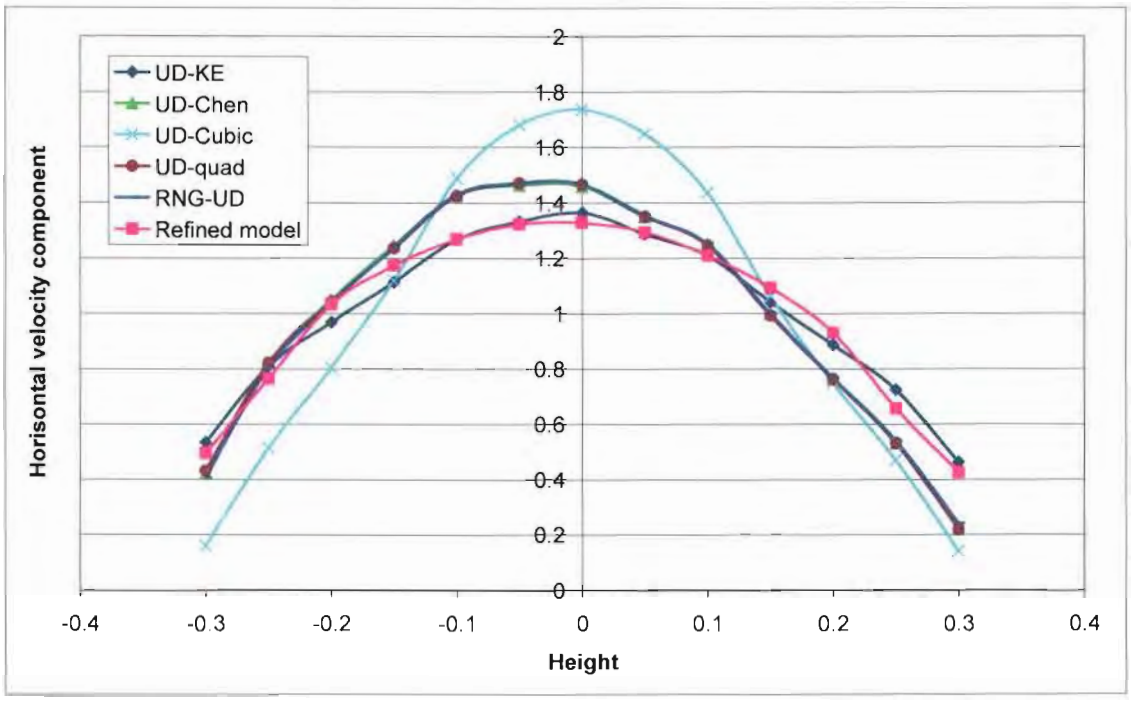

Figure 55: Testing different turbulence models on the 60° diffuser front position

5.6.2.2 The influence of discretisation schemes

Similar to the 60° diffuser, the influence of discretisation schemes on the flow distribution is quite significant as shown in Figure 56 and Figure 120.

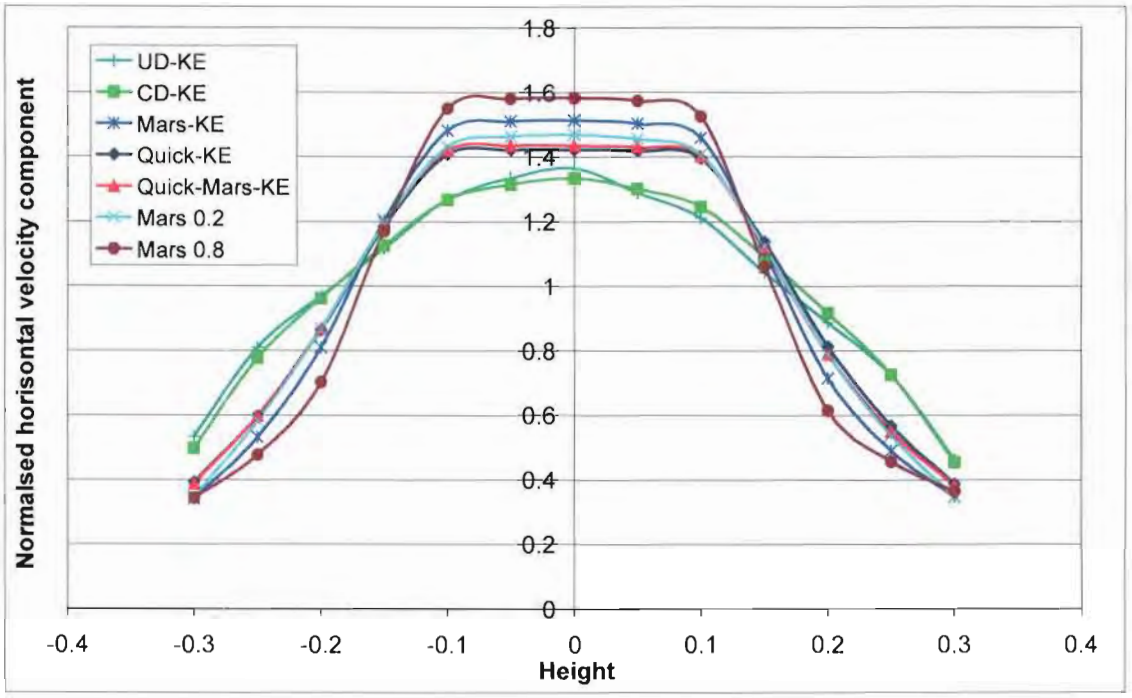

Figure 56: Testing discretisation schemes on the 60° diffuser front position

5.6.2.3 The influence of numerical mesh refinement

With a cell count of 208000 cells, the discretisation of the flow domain is already considered to be relatively fine. To further ensure grid independence, the diffuser section and one meter upstream and downstream was refined twice in all three directions, i.e. 8 times the number of cells. This refinement resulted in a cell count exceeding 627000 for the 60° diffuser. It should be noted that these simulations were conducted with the standard UD discretisation scheme and k-ε turbulence model.

The comparison between the predicted flow distributions for low and high cell refinement is shown in Figure 57 and Figure 121 at the front and centre of the diffuser section respectively. It can be seen that the refinement of the diffuser section had no significant influence on the predicted flow profile. Hardware limitations did not allow for further refinement of the model, although it was thought that no significant changes in the flow profiles would be predicted with an even finer model. Due to its less diffusive nature, second order discretisation schemes should reach mesh independence even faster than 1st order schemes.

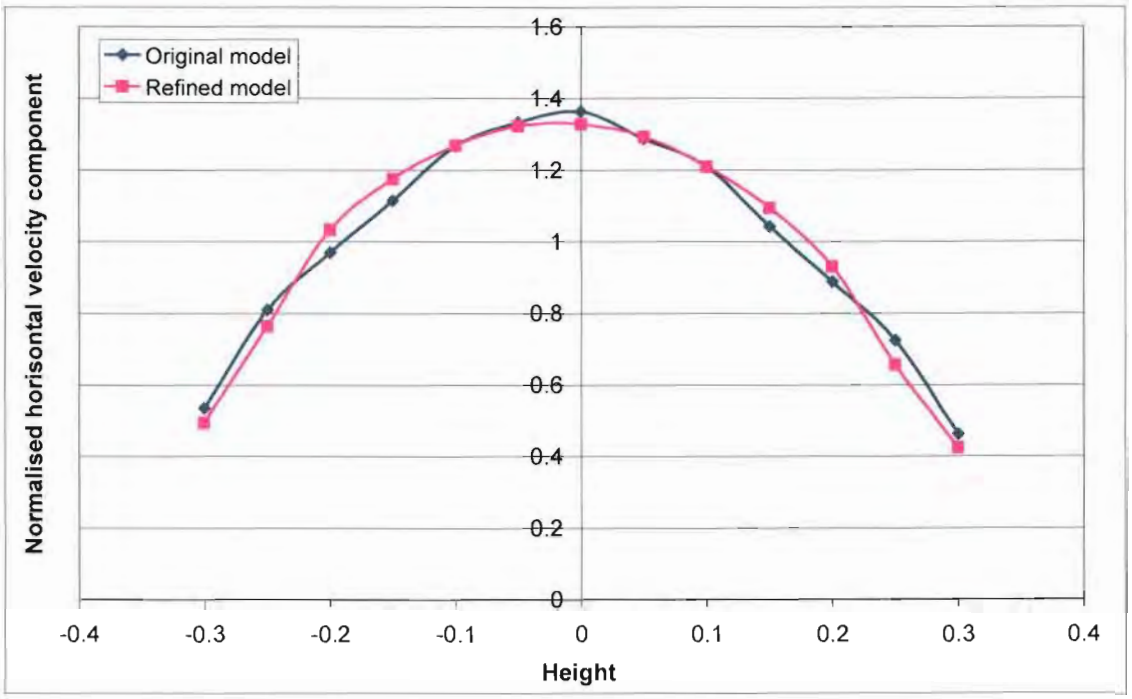

Figure 57: The influence of cell refinement on the flow distribution through the 60° diffuser

5.7 Comparison of results

5.7.1 120° diffuser front position

Figure 58 and Figure 59 show the comparison between the experimental data and the CFD results for the 120° diffuser in the front position. It can be seen that the UD discretisation scheme (Figure 58) does not compare very well with the experimental data while the higher order schemes (Figure 59) used with the standard high Reynolds number k-ε turbulence model show a better correlation.

In general, Star-CD suggests the use of the MARS scheme and the k-ε turbulence model for most flow applications. The difference between the different higher order schemes is not significant and it can be concluded that the best results were achieved with the MARS discretisation scheme together with the standard k-ε turbulence model as suggested by Star-CD.

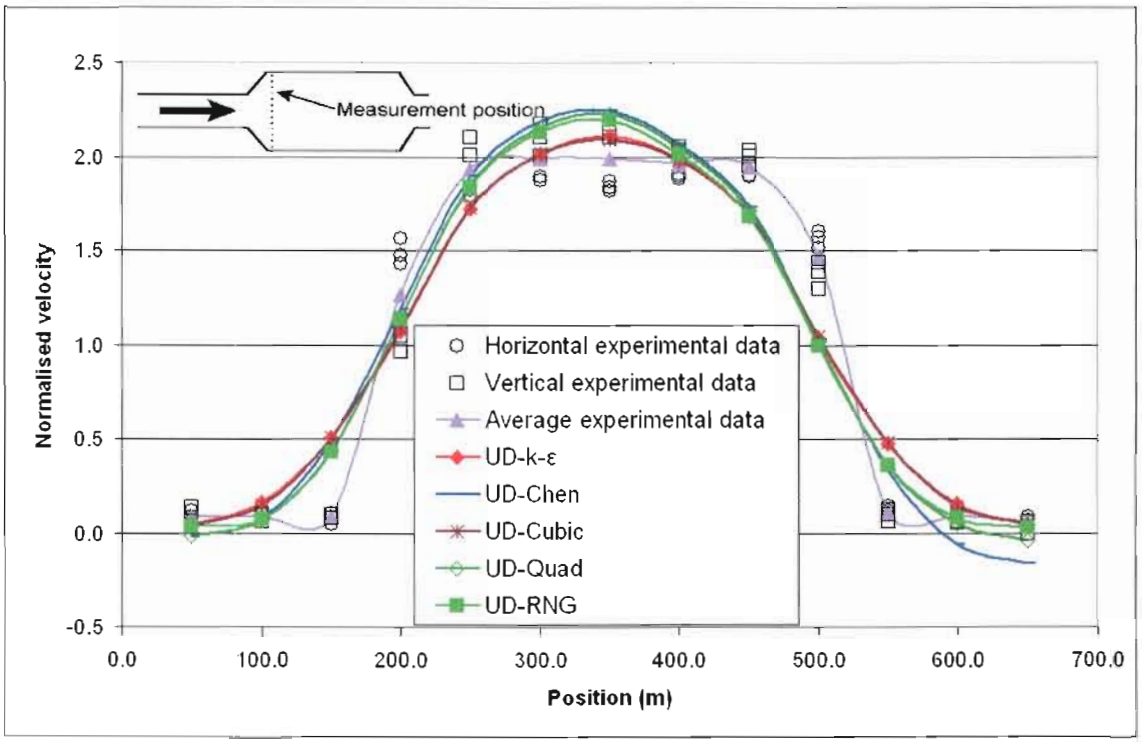

Figure 58: Comparing different turbulence models with test data, 120° diffuser front

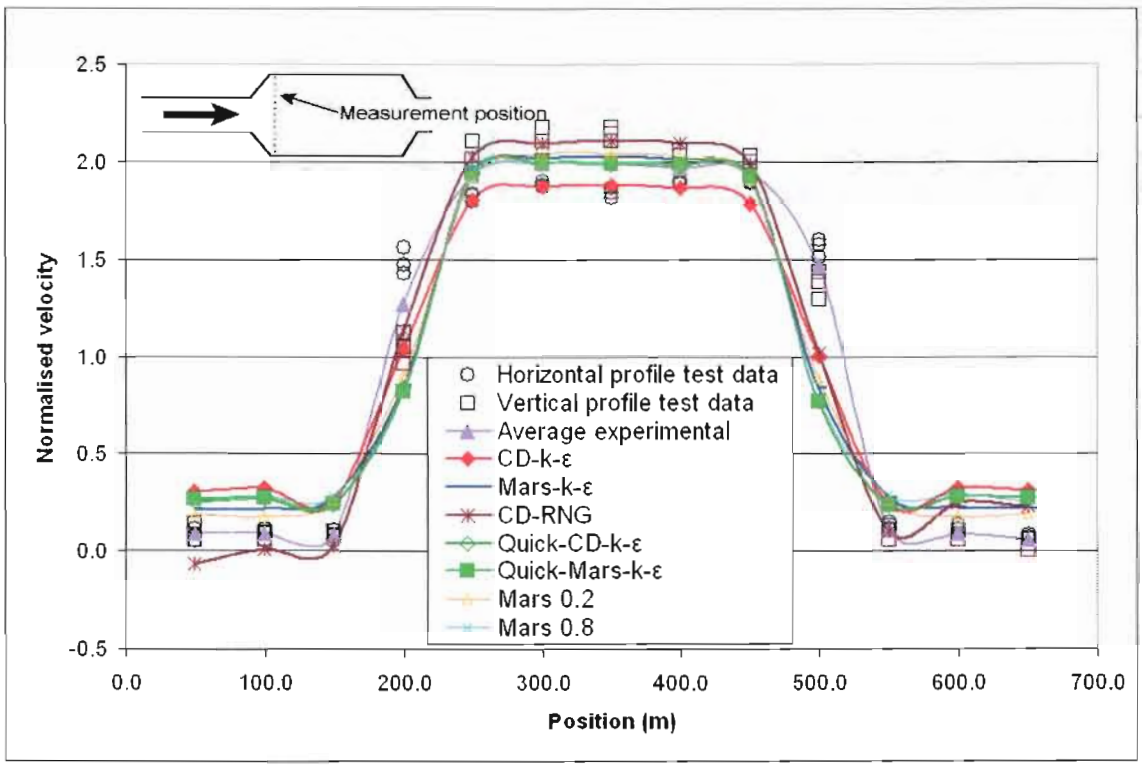

Figure 59: Different discretisation schemes with test data, 120° diffuser front

5.7.2 120° diffuser central position

Figure 60 and Figure 61 show the comparison between the experimental data and the CFD results for the 120° diffuser in the central position. Again, the higher order schemes used with the standard high Reynolds number k-ε turbulence model show a good correlation.

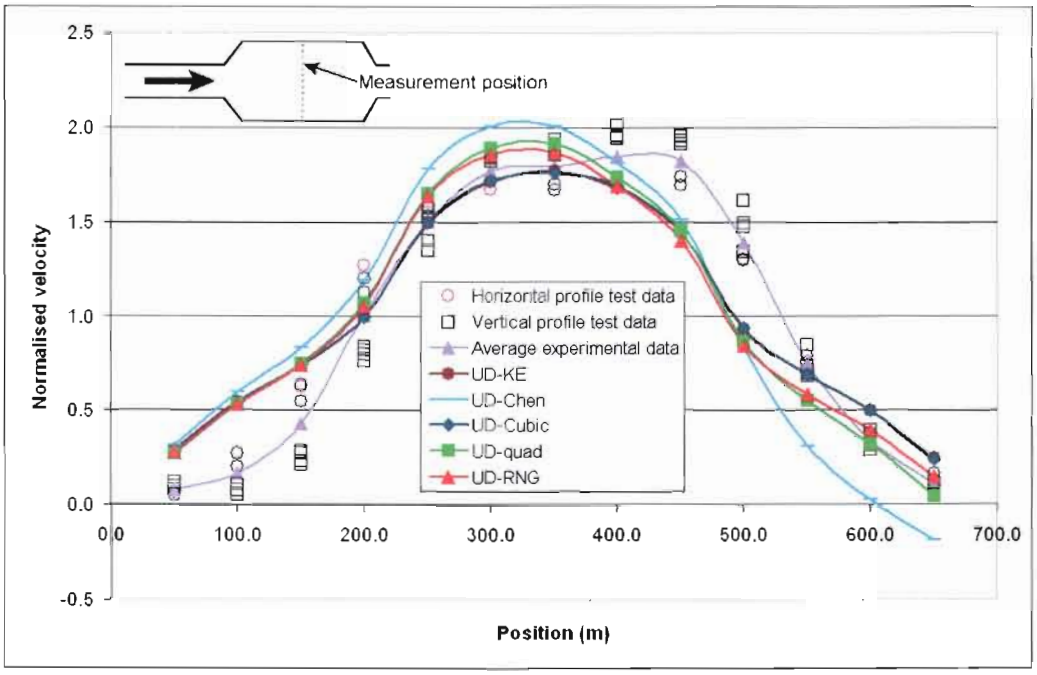

Figure 60: Different turbulence models with test data, 120° diffuser centre

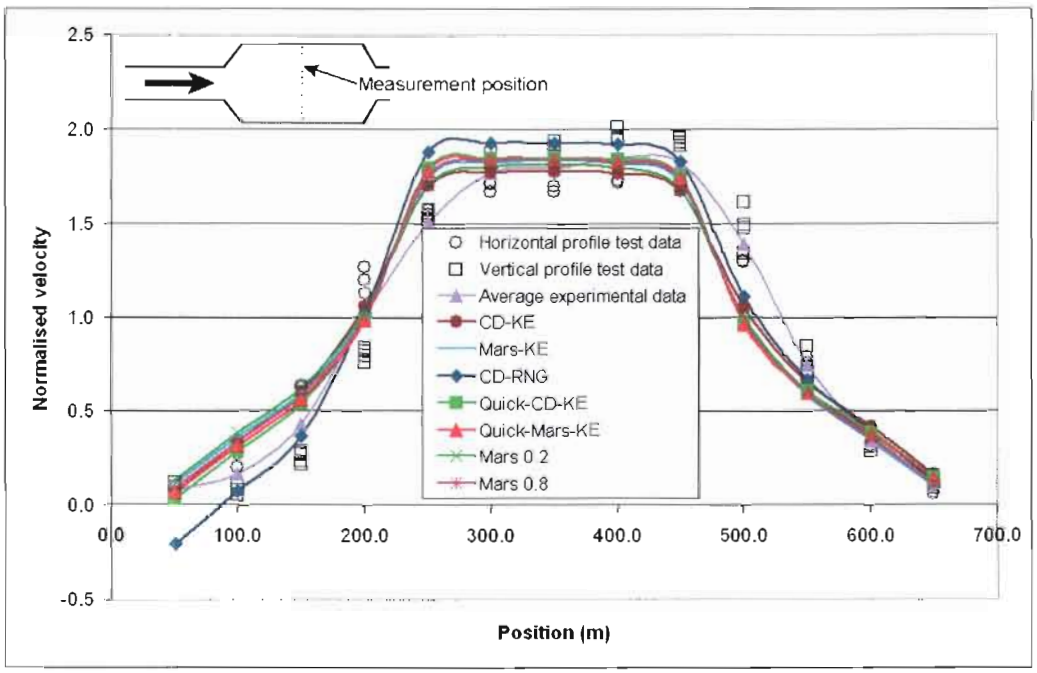

Figure 61: Different discretisation schemes with test data, 120° diffuser centre

5.7.3 60° diffuser front position

Figure 62 and Figure 63 show the comparison between the experimental data and the CFD results for the 60° diffuser in the front position. It should be noted that the un-symmetry of the experimental data was corrected by moving the profile to the centre of the wind tunnel. This adaptation of the results enabled the comparison to the CFD results.

As discussed in paragraph 5.3.3, the experimental results from the front of the 60° diffuser show a localised peak in the centre of the diffuser section. This peak can possibly be contributed to the fact that the flow does not separate immediately from the diffuser side-walls, as is the case in the 120° diffuser. This flow pattern was not predicted very well by any of the CFD results. The UD scheme together with the k-ε turbulence model shows the best prediction of these results. The MARS scheme with the k-ε turbulence model under predicted the high peak in the centre of the wind tunnel.

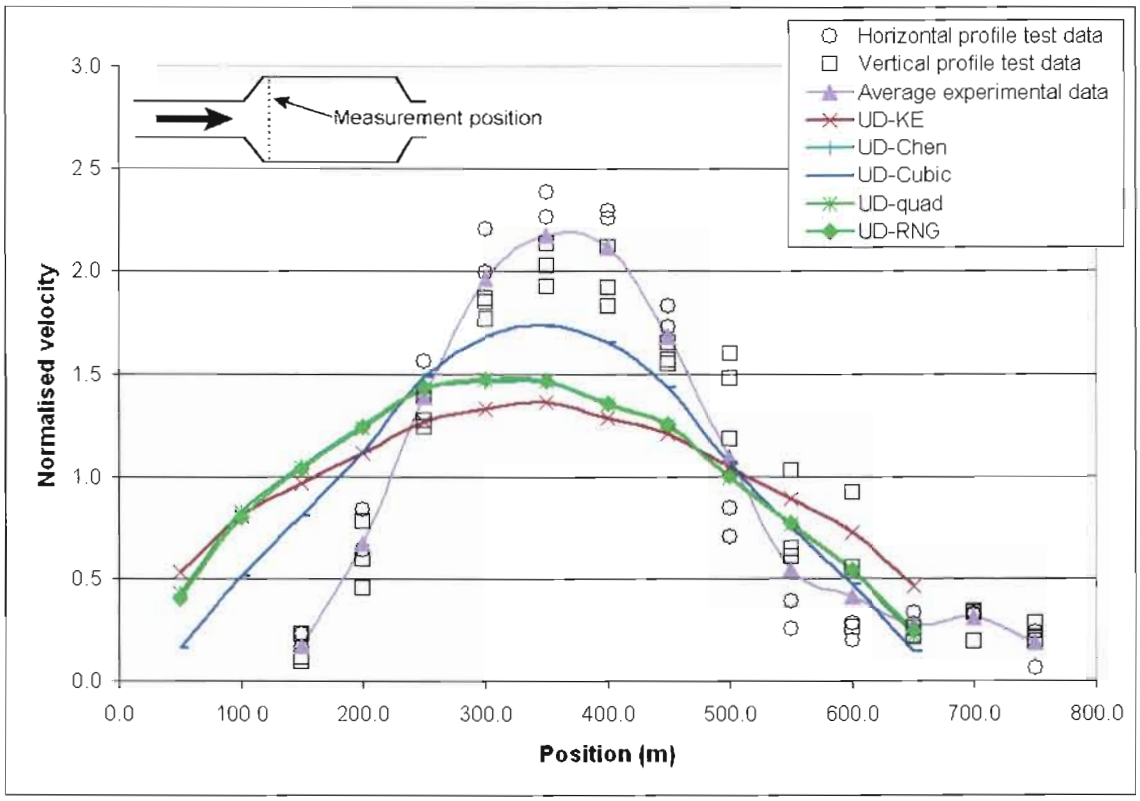

Figure 62: Different turbulence models with test data, 30° diffuser front

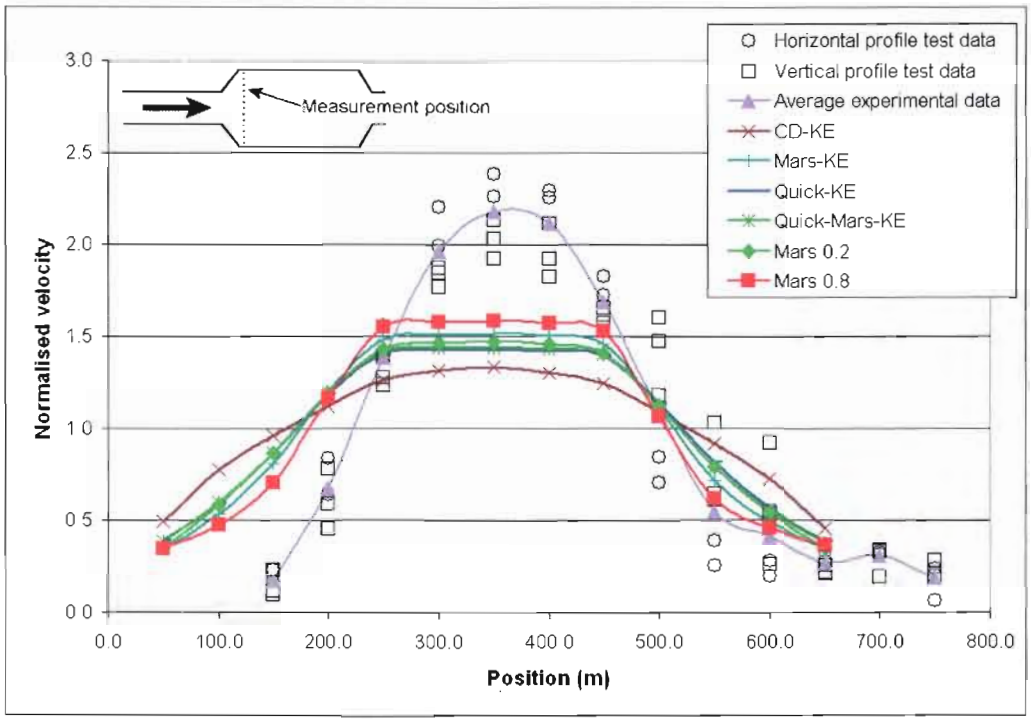

Figure 63: Different discretisation schemes with test data, 60° diffuser front

5.7.4 60° diffuser centre position

Figure 64 and Figure 65 show the comparison between the experimental data and the CFD results for the 60° diffuser in the central position.

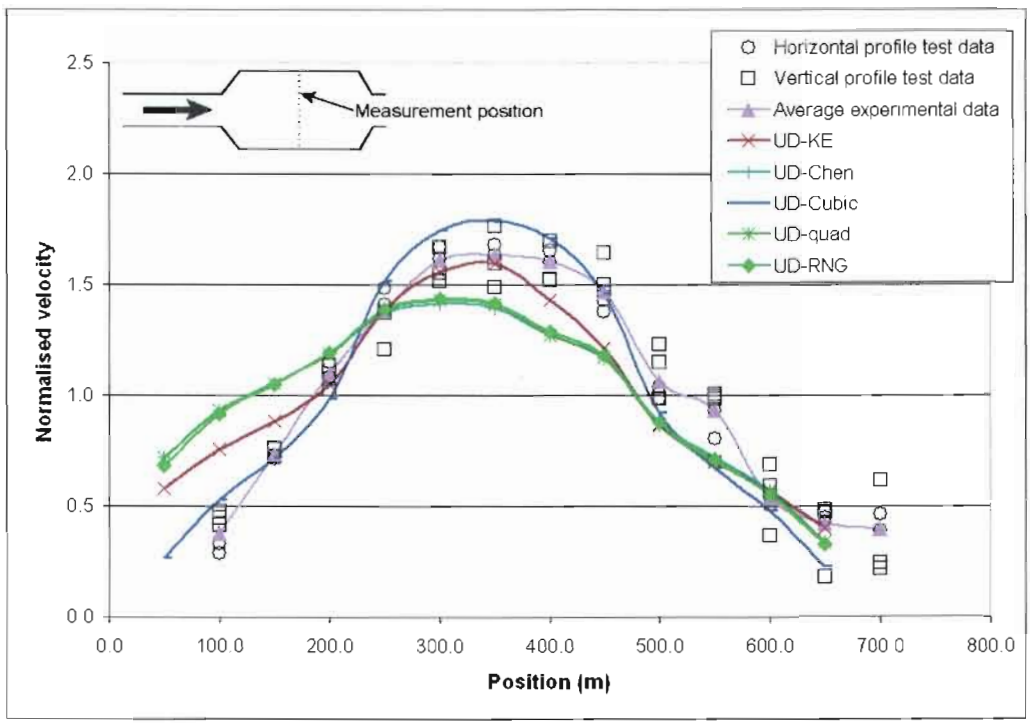

Figure 64: Different turbulence models with test data, 60° diffuser centre

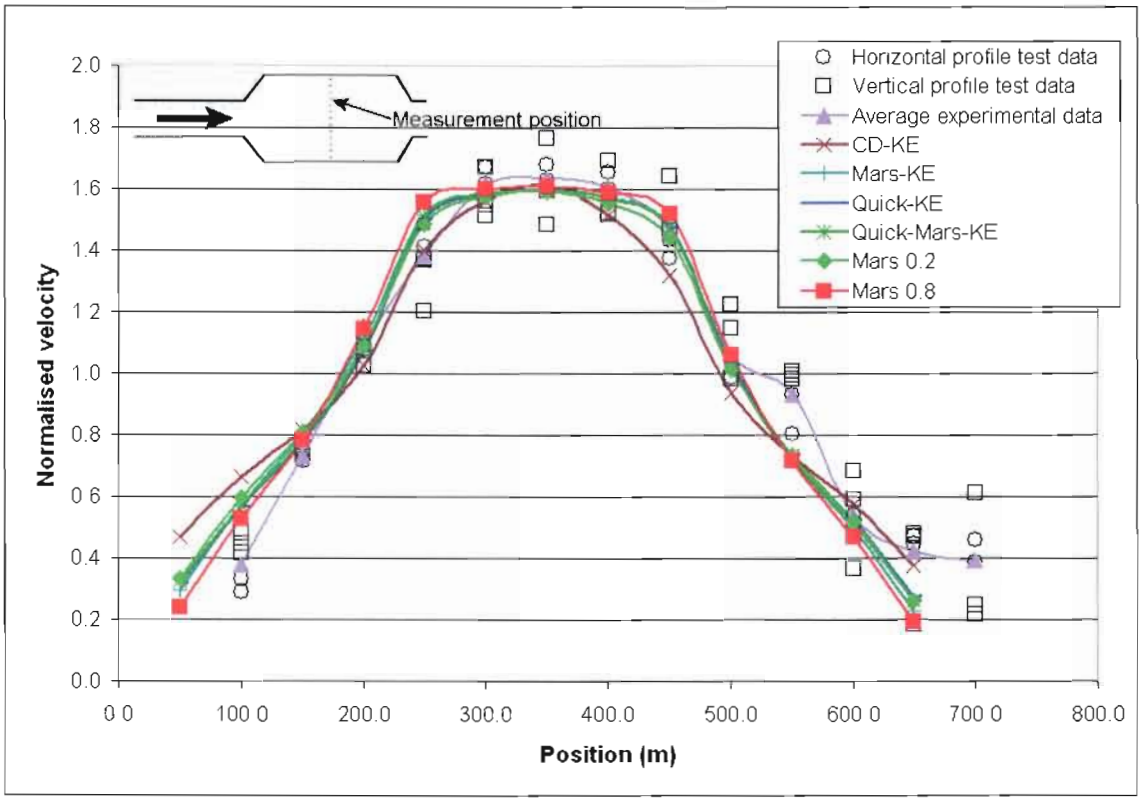

Figure 65: Different discretisation schemes with test data, 60° diffuser centre

The experimental data was also adapted to correct the un-symmetry of the results and enable comparison to the CFD results. It can be seen that the localised peak in the centre of the diffuser has been reduced significantly and that the combination of the MARS scheme and k-ε turbulence model shows a good correlation to the experimental data.

5.8 The influence of discretisation schemes on the inlet flow profile

In paragraph 4.5, it was shown that the CFD model did not predict the inlet flow profile accurately and that results did not compare very well with the experimental data. This CFD simulation was conducted with the UD scheme and since the higher order schemes showed a rather significant difference in the prediction of the flow distribution in the diffuser, it was decided to test the effect on the inlet flow profile as well.

Figure 66 shows results with the MARS and CD schemes. It can be seen that these schemes show a marginally better correlation, but that the predicted flow distribution still shows a high peak in the centre, which is not similar to the experimental data.

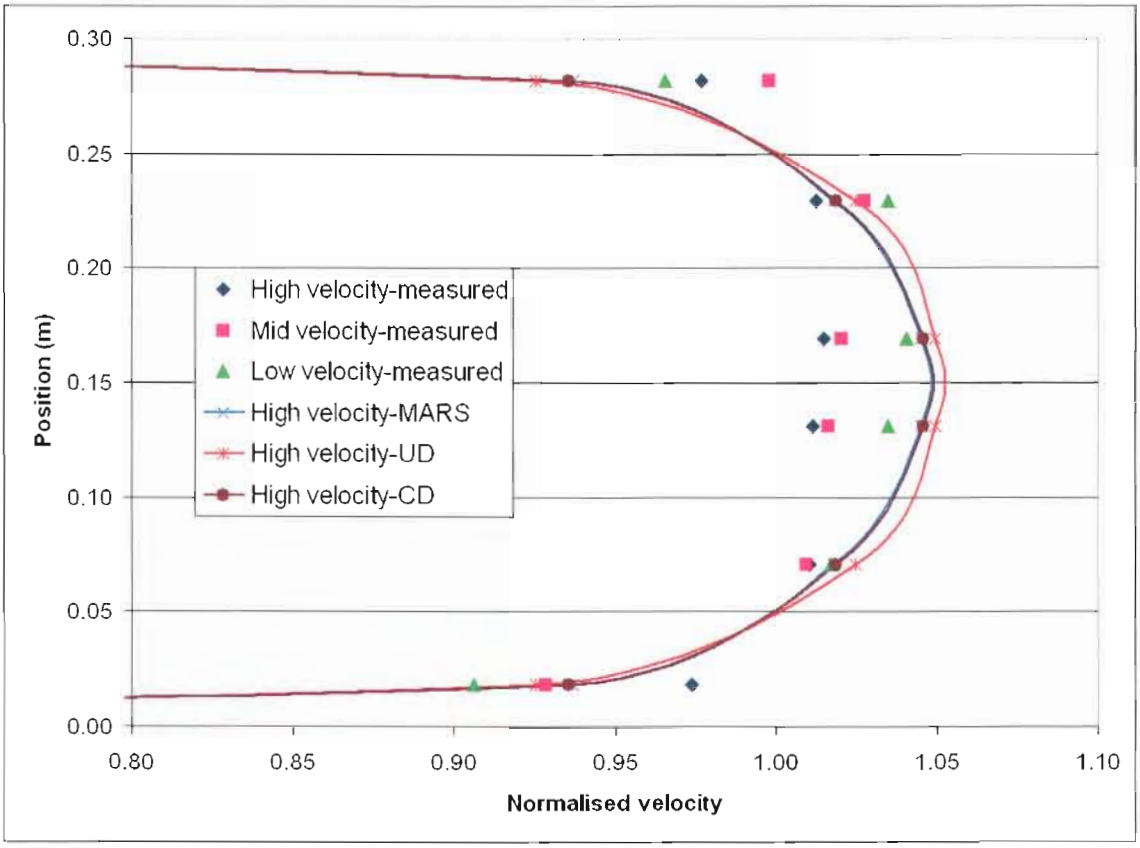

Figure 66: The influence of discretisation schemes on the inlet flow profile

5.9 Summary

The ultimate aim of this project is to accurately model the flow through screens in a diffuser, but before this goal could be achieved, it was required to first gain a better understanding of the flow through the diffuser without screens. This Chapter focused on the topic of flow through wide-angle diffusers and investigated these flow patterns both experimentally and numerically.

The emphasis was on the separation of flow in wide-angle diffusers in order to determine the degree of accuracy to which the turbulence models in a commercial CFD code can predict separation and re-attachment of the flow. The nature and behaviour of flow through wide-angle diffusers was also discussed and it was found that the flow patterns through large angle diffusers are highly unstable and complex and that the modelling of the flow has a rather high level of uncertainty.

The experimental investigation was discussed in detail and it was found that the visualisation of the flow using tufts or smoke did not supply quantitative results regarding the flow profile through the diffuser section, it did provide an excellent method to better understand the general flow profiles and behaviour. The improved understanding of the behaviour of the flow served as good preparation for the measurement of the flow distribution.

Initial results showed an oblique flow profile in the diffuser section and after extensive investigation, it was concluded that this unsymmetrical flow distribution was mainly due to the misalignment of the wind tunnel components, given that all other geometries and inlet flow profiles are symmetrical. Results from the experimental study were also presented.

To gain a better understanding of the modelling of turbulence, it was required to investigate the behaviour and properties of turbulent flow by reviewing related literature. It was concluded that turbulent flow is a highly unstable flow condition. The flow variables show a coincidental variation over time and spatial coordinates such that statistical averages can be observed. From these properties, it was concluded that the modelling of turbulence is a subject of extreme complexity and that it may have a significant influence on the predicted results.

Since the separation of the flow in the diffuser is a function of the flow regime at the inlet, it is important to understand the turbulent boundary layer and to ensure that the y+ values are within the prescribed limits. It was concluded that the y+ values across the range of velocities that are included in this study fall well within the prescribed limit.

Results from the CFD model showed that only the k-ε model predicted symmetrical flow patterns. The behaviour of flow through wide-angle diffusers is highly unstable and complex and it would appear that the other models are more sensitive to this instability. The k-ε model seems to average the unstable flow better thus simplifying the comparison between experimental and numerical data.

The CFD model was generated with a high level of refinement resulting in a good representation of the flow field. It was however required to investigate grid independence. Results showed that additional refinement of the model did not have a significant influence on the predicted flow profiles due to the already fine mesh used for the analyses.

Results from the CFD model with different discretisation schemes and turbulence models were compared to the experimental data. It was found that the flow pattern in the front of the 60° diffuser was not predicted very well by any of the CFD results. The MARS scheme with the k-ε turbulence model under predicted the high peak in the centre of the wind tunnel. For all the other flow distributions, it was found that the best results were achieved using the MARS discretisation scheme together with the standard k-ε turbulence model as suggested by Star-CD. Furthermore, it was found that the difference between the different higher order schemes or the different turbulence models was not significant.

The following chapter discusses the proposed theoretical approach adopted for the simulation of the variable resistance across the screens in the CFD model.

CHAPTER 6: PROPOSED THEORETICAL APPROACH

6.1 Introduction

This chapter discusses the proposed theoretical approach adopted for the simulation of the variable resistance across a porous screen in the CFD model. The first section is dedicated to the formulation of the variable resistance across a typical screen defining the mathematical theory to include parameters such as flow impact angle and the screen geometry. The second part of this chapter discusses the methodology used to implement the calculated variable resistance across a screen in the CFD code. This section gives a brief introduction to the CFD theory and also discusses the implementation of User Defined Functions (UDF's).

6.2 Mathematical approach to calculate a variable resistance across a screen

The resistance of a screen is mainly determined by the ratio between the restricted flow area (free area) to the total flow area of the flow channel. This relation is called the Free Area Ratio (FAR) and is calculated by the following equation for perpendicular flow:

$$FAR = \frac{Free\ \ Area}{Total\ \ Area} \tag{6.1}$$

In the case of a square lattice screen this translates to (see Figure 67):

$$FAR = \frac{a * b}{(a + w)(b + v)} \tag{6.2}$$

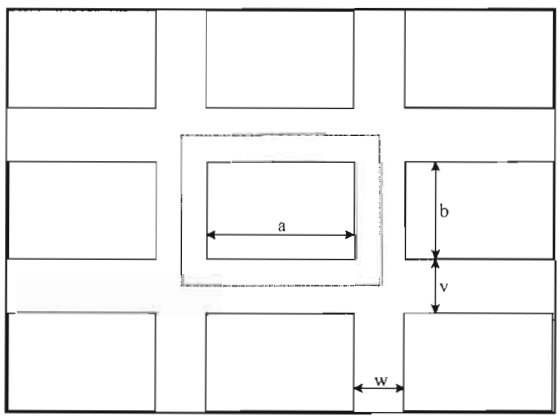

Figure 67: Perpendicular FAR calculation

However, when the angle of incidence of the approaching flow changes from perpendicular to the face of the screen, the thickness of the screen reduces the free flowing area thus increasing the resistance. This increase is directly proportional to the increase in the impact angle. For this reason, it is required to define the FAR as a function of the flow impact angle. The two-dimensional FAR can be described by the following equation (see Figure 68):

$$FAR = \frac{\{(a\cos\theta) - (t\sin\theta)\} * b}{\{(a\cos\theta) + (w\cos\theta)\} * \{b + v\}} \quad \textbf{(6.3)}$$

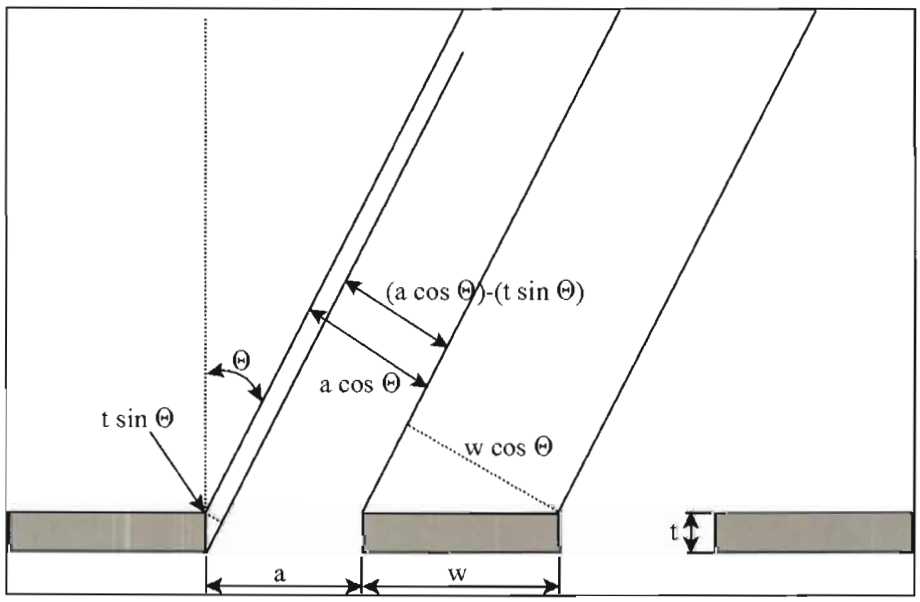

Figure 68: Two-dimensional effect of flow inlet angle

Based on this approach, the three-dimensional FAR is defined by the following equation (see Figure 69):

$$FAR = \frac{\{(a\cos\theta) - (t\sin\theta)\} * \{(b\cos\Phi) - (t\sin\Phi)\}}{\{(a\cos\theta) + (w\cos\theta)\} * \{(b\cos\Phi) + (v\cos\Phi)\}} \quad \textbf{(6.4)}$$

Where: a = Hole size (m)

θ = Angle of incidence in the horizontal plane (°)

Φ = Angle of incidence in the vertical plane (°)

w = Hole pitch height (m)

v = Hole pitch width (m), see Figure 69.

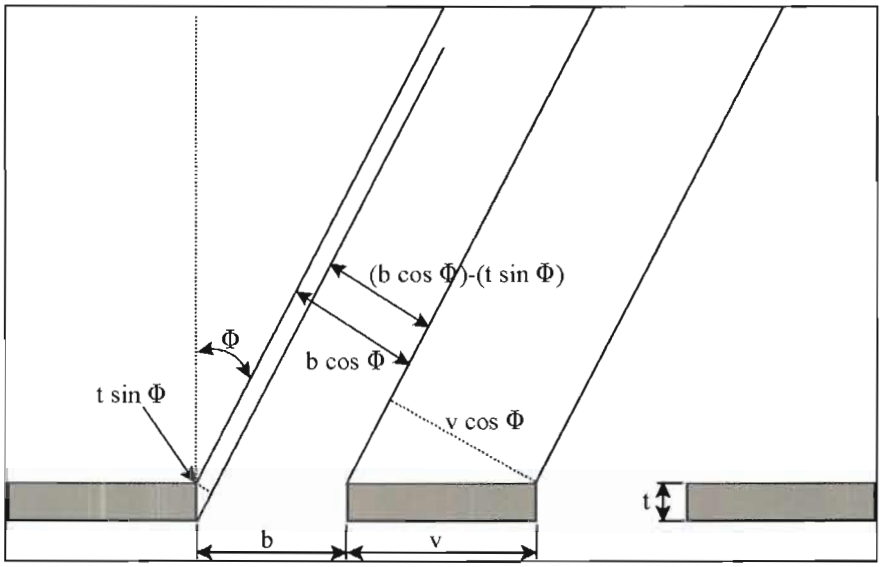

Figure 69: Three-dimensional effect of flow inlet angle

Using a similar method, the effect of the flow incidence angle on the FAR of a screen with circular perforation can be defined by the following:

$$FAR = \frac{\pi D * (D\cos\theta - t\sin\theta)}{4w\cos\theta * v} \quad \textbf{(6.5)}$$

Where:D = Hole diameter (m)

θ = Angle of incidence (°)

w = Hole pitch height (m)

v = Hole pitch width (m), see Figure 69.

Note: For screens with equally spaced holes in the horizontal and vertical direction, the values of v and w would be equal. This study only included such screens.

From the above, it can be seen that the calculated change in FAR is based on the free area of the screen viewed at a non-perpendicular angle and the assumption that the flow only passes through the free area. Due to the deflection of the flow, this assumption may not be correct and therefore requires verification. It can therefore be concluded that the above equations calculate the change in flow area as a function of:

- flow incidence angle
- screen thickness
- lattice size and
- hole size

The change in FAR can now be related to the change in resistance across the screen resulting in a variable resistance applied in the CFD model.

6.3 The relation between the FAR and the resistance coefficient

Since the FAR cannot be used to calculate the resistance across a certain screen directly, it is required to find a relation between the FAR of the screen and the resistance coefficient (K). The latter is defined by the following equation (as discussed in paragraph 1.2):

$$K = \frac{2\Delta P}{\rho v^2} \tag{6.6}$$

Fortunately, a vast amount of research has been done on the relation between the resistance coefficient and the FAR for a great number of screens including the ones used in this study. This relation for porous screens is shown in Figure 70 and Table 11. Since the relation was determined empirically, it was required to fit a curve to the empirical data. This curve fit was in the form of a fifth order polynomial:

$$K = a(FAR)^5 + b(FAR)^4 + c(FAR)^3 + d(FAR)^2 + e(FAR) + f \tag{6.7}$$

Where: a = -4444.8297
b = 13200.9818
c = -15548.5414
d = 9129.9442
e = -2705.0564
f = 331.5113

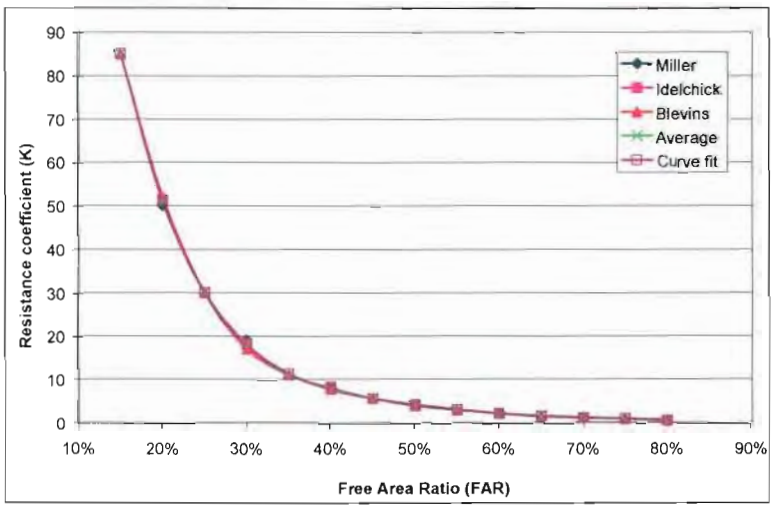

Figure 70: The relation between the FAR and the resistance coefficient

Table 11: The relation between the FAR and the resistance coefficient

	FAR	Miller[1]	Idelchik[2]	Blevins[3]	Average	Curve fit
	(%)					
1	15%			85.0	85.000	85.046
2	20%	50.0	51.5	52.0	51.167	51.009
3	25%			30.0	30.000	30.148
4	30%	19.0	18.2	17.0	18.067	18.006
5	35%			11.0	11.000	11.268
6	40%	8.0	8.3	7.7	7.983	7.603
7	45%			5.5	5.500	5.492
8	50%	4.0	4.0	3.8	3.933	4.062
9	55%			2.8	2.800	2.921
10	60%	2.0	2.0	2.0	2.000	1.990
11	65%			1.5	1.500	1.336
12	70%	0.9	1.0	1.1	0.993	1.008
13	75%			0.8	0.780	0.866
14	80%	0.4	0.4	0.5	0.450	0.418

Table references:

1: Miller (1978:263)

2: Idelchik (1986:404)

3: Blevins (1984:314)

It can be seen that the curve fit error becomes quite significant at very high FAR's (low resistances), which is consistent with the uncertainty of the measuring equipment at very low pressure drop measurements (as was shown in paragraph 4.8). These values fall outside the scope of this study and therefore have no any impact on the results.

Idelchik (1986:404) and Blevins (1984:314) show that the relation presented in Figure 70 is true for both square and round holed perforated (porous) screens. The relation is only dependent on the FAR regardless of the hole geometry. It should also be noted that this relation is only applicable for relatively thin screens, i.e. with a screen width to hole size ratio of less than 0.2. If this ratio increases, the relation between K and FAR should be adapted to the relations for screens with a higher thickness, as shown in Idelchik (1986:404).

ρ = *Density of the fluid (kg/m^3)*

C_1 = *User defined variable*

C_2 = *User defined variable*

Star-CD's approach is the following: Ignoring convective acceleration and diffusion, the porous medium model reduces to Darcy's law:

$$-K_i u_i = \frac{\partial P}{\partial \xi_i} \tag{6.10}$$

Where: ∂P *is the pressure drop (Pa)*

$\xi(i=1, 2, 3)$ *represents the mutually orthogonal orthotropic directions*

K_i *is the permeability*

u_i *is the superficial velocity in direction* ξ *(m/s)*

The permeability K_i is assumed to be a quasi linear function of the superficial velocity magnitude |u| of the form:

$$K_i = \alpha_i |u| + \beta_i \tag{6.11}$$

Where α and β are user defined coefficients, which may either be uniform or spatially varying. This spatial variance ability of the equation can therefore be used to implement the variable resistance across the screen (calculated in paragraph 6.2) with the deflection of the flow passing through the screen.

It should be noted that the simplified momentum equation (6.10) is valid provided that (Star-CD v3.15 Methodology manual, 2001:8-2):

$$\frac{(\alpha U + \beta)L}{\rho U} >> 1 \tag{6.12}$$

Where L and U are a characteristic overall dimension of the distributed medium and a characteristic velocity through it respectively.

Combining equations (6.10) and (6.11), the pressure gradient that is calculated in the momentum equation by Star-CD across a porous medium is represented by:

$$\frac{\partial P}{\partial \xi_i} = \alpha_i |u| u_i + \beta_i u_i \tag{6.13}$$

It can be seen that equation (6.13) is similar to equation (6.9) except that Star-CD regards viscosity and density as part of the user defined variables while the Fluent variables do not include viscosity and density. Fluent implements this as a momentum sink in the full Navier-Stokes equations. Comparing the permeability coefficients defined in Star-CD with the definition of the Fluent source term, the comparison between the Star-CD and Fluent variables is defined by:

$$\alpha = \frac{C_2 \rho}{2} \tag{6.14}$$

and

$$\beta = \frac{\mu}{C_1} \tag{6.15}$$

In laminar flows through porous media, the pressure drop is typically proportional to the velocity and the constant C_2 in the source term can be considered to be zero. For the current study, the flow is turbulent and therefore the term C_2 cannot be ignored.

6.5 Implementing the variable resistance into the CFD code

The first step was to calculate the variable FAR as a function of the impact angle and the geometry of the screen using equation (6.4). The resistance coefficient was then calculated from the relation given by equation (6.7). By making the pressure drop the subject of equation (6.6) the relation between the pressure drop and resistance coefficient is given by:

$$\Delta P = \frac{K \rho v^2}{2} \tag{6.16}$$

Assuming that the velocity is always positive, that $\partial\xi$ is some length dL and that $\beta \rightarrow 0$, equation (6.13) can be written as:

$$\frac{\Delta P}{\Delta L} = -\alpha u^2 \tag{6.17}$$

For unit length, the equation for pressure drop becomes:

$$\Delta P = \alpha u^2 \tag{6.18}$$

Combining equations (6.18) and (6.6), the value of α is now directly related to the variable resistance coefficient (K_v):

$$\alpha = \frac{K_v \rho}{2} \tag{6.19}$$

The value of α, now being a function of the flow incidence angle and screen geometry, is used in the standard calculation of the pressure drop across the screen in the direction of the flow, i.e. equation (6.13). It was expected that the increased resistance (with an increase in the angle of incidence) would result in a natural tendency for the flow to change direction in the CFD model similar to the actual conditions. Research conducted by Schmitz et. al. (1998) showed that the porous medium tends to redirect the flow passing across the porous medium. If it is found that this natural "bending" of the flow does not result in an accurate prediction of the exit angle, it would be required to apply transverse resistance coefficients to ensure the correct change in the flow direction behind the screen. Results are discussed in the following chapter.

6.6 User defined functions (UDF)

The UDF used in Star-CD to define the porosity of a porous medium is called poros1.f. The properties of the flow field directly upstream of the porous medium are passed on to the UDF. These properties include (amongst others):

- The number of the cell type that was used to define the screen in the CFD model. A certain porosity identity number is assigned to a cell type. The CFD code is informed that the resistance factors for this porosity number is not constant, but is calculated by a UDF. The CFD code then activates the UDF and it is compiled with the solution executable to be included in the numerical solution.
- Three dimensional velocity components in cartesian coordinates. These components were used to calculate the magnitude of the flow velocity and the angle of incidence.
- Density of the flow.
- Three dimensional velocity components in the local coordinate system of the porous medium.

The UDF then calculates the values of α and β (β≈0) in the I, J and K directions, i.e. ALI, ALJ, ALK, BTI, BTJ, BTK, and these values are passed back to the CFD code to implement resistance factors in the three directions. The I, J and K directions refer to three directions of the local cell orientation. For the purpose of this study, these values remained in the same orthogonal orientation than the global coordinate system.

This UDF was also used to define the geometrical specification of the screen. A user input section was defined at the top of the UDF (see ANNEXURE E) where the user has to include the physical properties of the screen. These properties include the thickness of the screen, hole size and hole pitch. All UDF's developed for this study is shown in ANNEXURE E.

6.7 Summary

This chapter discussed the theoretical approach adopted for the simulation of the variable resistance across a porous screen in the CFD model. The first section was dedicated to the formulation of the variable resistance across a typical screen defining the mathematical theory to include parameters such as flow impact angle and the screen geometry.

The second part of this chapter discussed the proposed methodology to include the calculated variable resistance across a screen into the CFD code. This section also gave a brief introduction to the CFD theory on porous media and the implementation of User Defined Functions (UDF's).

The following chapter presents the empirical and numerical results obtained and also investigates the correlation between these results. The discussion also focuses on the applicability of the numerical model for general purposes and investigates the need for correction of the proposed theoretical approach discussed in this chapter.

CHAPTER 7: DISCUSSION OF RESULTS

7.1 Introduction

This chapter presents the empirical and numerical results obtained with screens positioned in the diffusers and also investigates the correlation between the results. The discussion also focuses on the applicability of the numerical model for general purposes and investigates the need for correction of the proposed mathematical approach or hypothesis discussed in the previous chapter.

This discussion is subdivided into two main sections:

- Preparation and development of required user coding and input data
- Discussion of results

The first section focuses on the preparation and development work that was required before starting with the simulations. This section includes a brief discussion on some of the related theory, but all the information could not be included. The reader is referred to the Star-CD v3.15 Methodology manual (Version 3.15 2001:Chapter 8) for further information.

The second section of this Chapter focuses on the results that were obtained and comments on the correlation between results from the different modelling approaches with the empirical data.

7.2 Preparation and development of required user coding and input data

7.2.1 User defined functions

User defined functions (UDF's) were discussed briefly in the previous chapter with the focus mainly on the UDF used to define the resistance of a porous medium, i.e. poros1.f. This discussion elaborates on the other coding required as input into the main UDF's. All the user coding that was used or developed during this study is presented in ANNEXURE E and is also provided in digital format on a CD that accompanies this thesis.

7.2.1.1 User input file

Currently, Star-CD v3.15 for Windows uses Fortran coding that is compiled by using the standard Absoft v8.0 compiler for Windows. The main UDF's are compiled with a "*.f" extension and other miscellaneous input files with a "*.inp" extension. The latter were used to define the screen properties using a file called "inpdata.inc". This file feeds all the screen information into the main UDF's. The advantage of this approach is that the user does not need to access the main coding thus reducing the possibility of accidentally changing the coding. This file is shown in ANNEXURE E.1 and it can be seen that all the required inputs are introduced through this file.

Section one of this file is self-explanatory and the variables defined in section two can be explained as:

SP = Porous medium thickness. This is the thickness of the porous medium in the direction of the approaching flow (perpendicular to the face of the screen).

BA = Ratio between alpha and beta. The focus is on defining the variable value of alpha, but beta cannot be zero. The user can define the ratio between alpha and beta to be as low as the simulation would allow before becoming unstable.

RELAO = Velocity relaxation factor after the velocity was initialised. The code is further under relaxed as this number is increased, i.e. this ratio indicates the weight of the velocity value calculated in the previous iteration.

IOFF = Offset between rows of cells used for the definition of the cell neighbour lists.

ICTY = Number of the first cell type defining the porous medium. It is required that each row of cells in the porous medium should have a separate cell type.

MONC = Monitor cell that is printed with the solution results.

MON2 = Second monitor cell that is printed with the solution results.

MON3 = Third monitor cell that is printed with the solution results. The user can choose any cell numbers that he wishes to monitor during the course of the solution.

IPID = ID number of the porosity definition for the porous medium. Only one porosity ID should be assigned to the porous medium.

AINI = This variable defines the initialisation velocity and is used in conjunction with the RELAO variable to ensure a more stable start to the solution.

ITWR = The user may choose an iteration number to write the calculated porosities and other results. This is an additional monitoring function for the user.

CORF = A correction factor was programmed into the code if the need should arise to implement a semi-empirical correction factor. This correction factor was set to a value of 1, which essentially disables this function.

DLL = Lower limit of FAR value. For this research, the lower limit of the FAR was set to 0.05 (5 percent). The validity of this value is discussed in paragraph 7.4.

DUL = Upper limit of FAR value. For this research, the upper limit of the FAR was set to 0.95 (95 percent). Keep in mind that the FAR value of the screens tested varied between 30 and 70 percent.

RIJ = Ratio between the perpendicular and transverse resistance coefficients.

7.2.1.2 Additional common block definition

In Fortran, variables can be assigned as local or global variables. To define global variables, it is required to write a variable into a common block (vector). A number of common blocks were required for this set of user coding and for this reason it was decided to use an additional common block file (cblocks.inc) that is called at the beginning of each UDF. Using this approach ensures consistency since it is not required to update each UDF if a change is made to the common block definition. The common block definition file is shown in ANNEXURE E.2.

7.2.1.3 Neighbour cell list definition

Since the velocity value of the cells upstream of the screen is used in the calculation of the resistance coefficient, it was required to define a neighbour cell list. A simple approach to define the neighbour lists was adopted using cell number offsets. This is not the best approach since this method imposes the limitation that the mesh must be structured. However, the emphasis of this study is not on the programming structure of Star-CD and for this reason, this simple approach is sufficient to investigate the hypothesis. It was therefore decided not to spend additional time on the former

approach. The definition of the cell neighbour lists is done through the posdat.f file and is shown in ANNEXURE E.3.

7.2.1.4 Scalar definition

In order to view the calculated FAR's and resistances, these values were stored in scalar variables defined through common blocks that could be retrieved in Prostar and displayed as additional scalar values. This capability helped with the debugging of the user coding. The user can now view all the calculated scalars across the area of the screen and it helps to better understand the behaviour of the flow. The file used for this is called scalfn.f and is shown in ANNEXURE E.5.

7.2.2 Investigating convergence behaviour

A study was conducted into the convergence behaviour of the diffuser model generated in Star-CD using the porous medium approach. The emphasis was on the following:

- The influence of the solution algorithm under-relaxation.
- The influence of the inlet and outlet boundary definition on the convergence of the solution algorithm.
- The influence of mesh refinement in the region of the diffuser and screen.
- The influence of the ratio between the perpendicular and transverse resistance factors.
- The thickness of the porous medium in the perpendicular direction.

7.2.2.1 The influence of under-relaxation

It was found that the inclusion of a diffuser resulted in an instability of the solution algorithm that required under-relaxation. The initial under-relaxation was set only marginally lower than the default values, i.e. 0.6, 0.25 and 0.6 (with the default being 0.7, 0.3, 0.7). It was found that this under-relaxation was not sufficient and the values were further reduced to 0.5, 0.2 and 0.5. This level of under-relaxation resulted in a very stable solution algorithm yielding the lowest residual values. It was also found that the solution algorithm would not converge fully if the diffuser was included irrespective of the relaxation. It was thought that this can be contributed to the unsteady flow through the diffuser and the instability that this introduces into the solution.

7.2.2.2 The influence of the inlet and outlet boundary definition on the convergence of the solution algorithm

It was mentioned in previous chapters that the model was constructed with an atmospheric pressure inlet boundary. It was found that this type of inlet boundary introduces a large amount of instability into the solution algorithm. The boundary was firstly reduced in size in an attempt to also reduce the instability. Although this reduction in size did result in a more stable solution algorithm, it was still not satisfactory requiring low under-relaxation in order to reach a solution. Even with the solution algorithm under relaxed, it was found that the solution algorithm convergence remained at an unacceptable level (i.e. 1e-2 with 1e-3 the default value).

Based on these results, the inlet bell mouth and atmosphere was removed with the inlet boundary (suction end upstream of the diffuser) defined in the straight duct section. It was found that the solution algorithm was rather unstable with a suction inlet boundary regardless if the flow entered the domain through a pressure- or outlet boundary. When using a normal inlet boundary combined with an outlet boundary downstream from the diffuser section, it was found that the outlet boundary had to be moved quite far away from the diffuser section not to get reverse flow into the outlet boundary. This combination was found to be most stable although the solution algorithm still did not converge to the default level of 1e-3. Based on these results, it was decided to use a user defined inlet profile (representing the flow profile measured in the wind tunnel) coupled to a standard outlet boundary. This approach resulted in significantly improved results as discussed in paragraph 7.2.3.

7.2.2.3 The influence of mesh refinement in the region of the diffuser and screen

It was found that mesh refinement of approximately four rows of cells upstream and downstream from the screen resulted in a more stable solution algorithm. Furthermore, cell refinement in the region of the diffuser also resulted in a more stable prediction of the recirculation zone thus yielding a more stable solution algorithm. It is however important to still ensure that the y+ values are correct and not too low, which is the case if the cells in the near wall boundary layer are too fine.

7.2.2.4 The influence of the ratio between the perpendicular and transverse resistance factors

The user defined resistance coefficients are multiplied by the length of the porous medium in order to calculate the correct pressure drop (see equation (6.17)). With the perpendicular coefficient, this length is merely the thickness of the porous medium and is therefore easily calculated. However, when the transversal coefficients are calculated if the flow is not perpendicular to the face of the screen, then the distance that the flow passes through the porous medium increases significantly until this length is equal to the total width of the screen (at a 90° incidence angle). In this instance, the pressure drop and the resulting change in the direction of the flow is overestimated. For this reason, it is required to define the transversal coefficients as low as possible.

Initially, this ratio was set to 0.0001 and results were found to be unphysical with the solution algorithm eventually diverging. The cells around the perimeter showed velocity vectors impinging into the walls. The cells around the perimeter were then refined, but the solution algorithm still diverged. Two rows of perimeter cells were then defined as a separate porous medium and the transverse resistance set to 0.1 times the perpendicular resistance in an attempt to direct the flow away from the walls. This approach resulted in a very stable solution algorithm while also allowing the definition of low transverse resistance values for the remainder of the porous medium cells. The advantage therefore is that the transverse resistances do not influence the results by forcing the flow perpendicular through the screen. It was also found that the refinement of the cells upstream and downstream from the screen was essential in the stability of the solution algorithm.

7.2.2.5 The thickness of the porous medium perpendicular to the flow

In order to simulate a baffle using a porous medium, it was assumed that the porous medium should be as thin as possible to minimise any unphysical influence that the porous medium may have on the flow through the screen. It was however found that a very thin porous medium definition resulted in an unstable solution algorithm. This is due to the very high value of the resistance coefficient that is required to introduce the pressure drop across this very small dL value (see equation (6.17)). Conversely, it was found that a porous medium definition of large thickness may influence the direction of the flow as it exits the screen. While the porous baffle approach generally underestimate the change in direction through the screen, excessive thickness of the

porous medium may result in an overestimation. For the purpose of this study, the porous medium was 0.5mm thick (t) with the diffuser size at the screen position being 500mm (D). The t/D ratio was thus 0.001.

Results from the study into the convergence behaviour was implemented for the remainder of the simulations and it was found that the solution algorithm convergence was significantly improved when compared to the previous sections of this research as shown in Figure 71. For most simulations the solution algorithm reached convergence where previously very few simulations would converge further than 0.01.

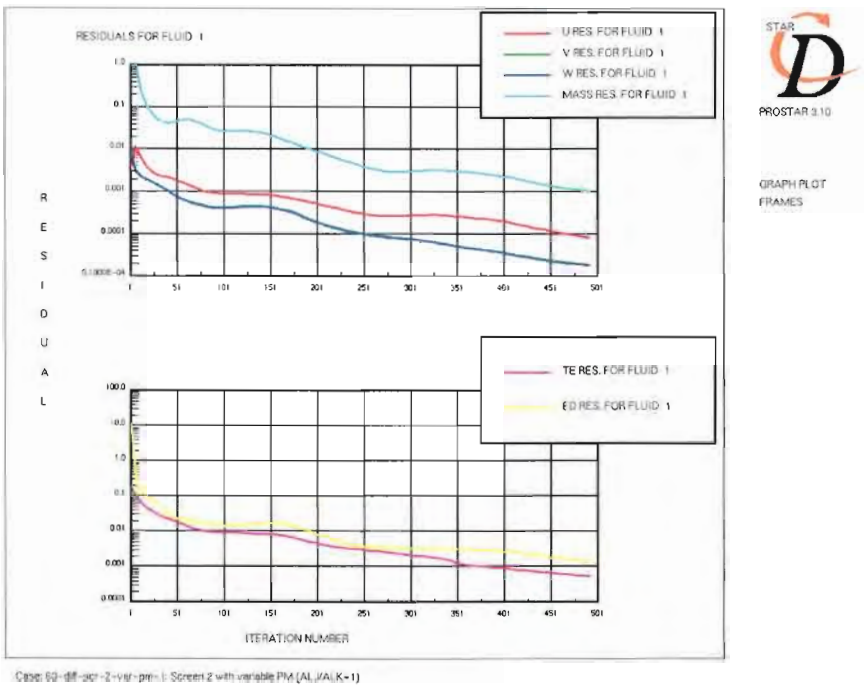

Figure 71: Improved solution algorithm convergence

7.2.3 User defined inlet boundary

Based on results from the investigation into the convergence behaviour (see section 7.2.2), it was decided to define the inlet boundary as a fixed mass flow inlet type boundary rather than using the atmospheric pressure inlet boundary. This would however require that the inlet profile (as measured in the wind tunnel) be implemented through user coding. The UDF that defines inlet boundaries is called bcdefi.f and is shown in ANNEXURE E.4 and this UDF defines the correct profile in both the

horizontal and vertical planes. Figure 72 shows the resulting inlet boundary velocity profile.

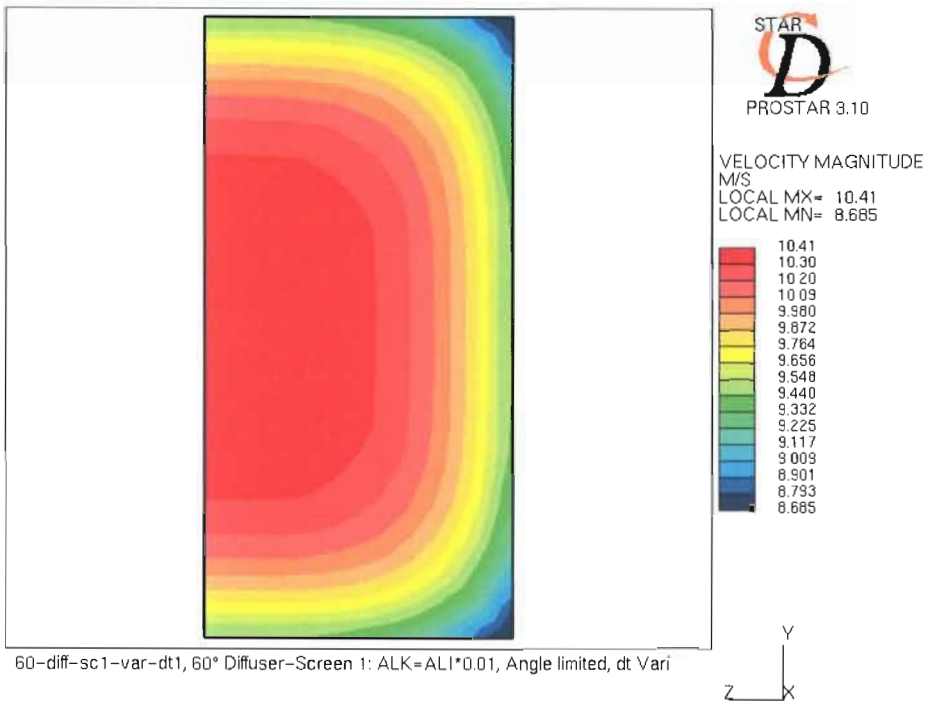

Figure 72: User defined inlet velocity profile

7.2.4 The porous medium approach

The theory behind the porous medium approach was discussed extensively in previous chapters and therefore this discussion does not include any further theoretical background. In order to test the equations, a spreadsheet was generated where the angle of incidence is defined manually in both the xz and xy planes. With this method, it was possible to test the equations before starting with the user coding and to investigate the limits that may have to be implemented. An example of such a spreadsheet is shown in ANNEXURE G.

The variable resistance was calculated using the poros1.f file shown in ANNEXURE E.6. It can be seen that the input files inpdata.inc and cblocks.inc are read in at the start together with the standard inputs and common blocks of Star-CD. The velocities defined for the first iteration were initialised to improve the stability of the code. These velocities were then under-relaxed for the following iterations using the previously initialised velocity and the neighbour velocity. In order to access the previously calculated velocity, it was required to store these values in additional common blocks

(vectors). The under-relaxation is controlled by the user with the "RELAO" variable that is defined in the input file. Under-relaxation allows the user to control the ratio of the value calculated during the previous iteration and the one calculated during the current iteration in the result for a given variable. For this study, the calculation is further under relaxed as this relaxation factor approaches 1. In steady state applications, this should not have any bearing on the results although the solution algorithm may require more iterations to converge.

The neighbour cell velocities that were defined in posdat.f are then retrieved for use in the calculation of the variable porosity. The next step is to calculate the angle of incidence based on both the vertical and horizontal velocity components. It was found to be crucial that limits are defined for all the calculated variables. Figure 73 shows a schematic of the imposed limit on the angle of incidence. The limiting angle is calculated by the ARCTAN of the ratio between the hole size and the screen thickness.

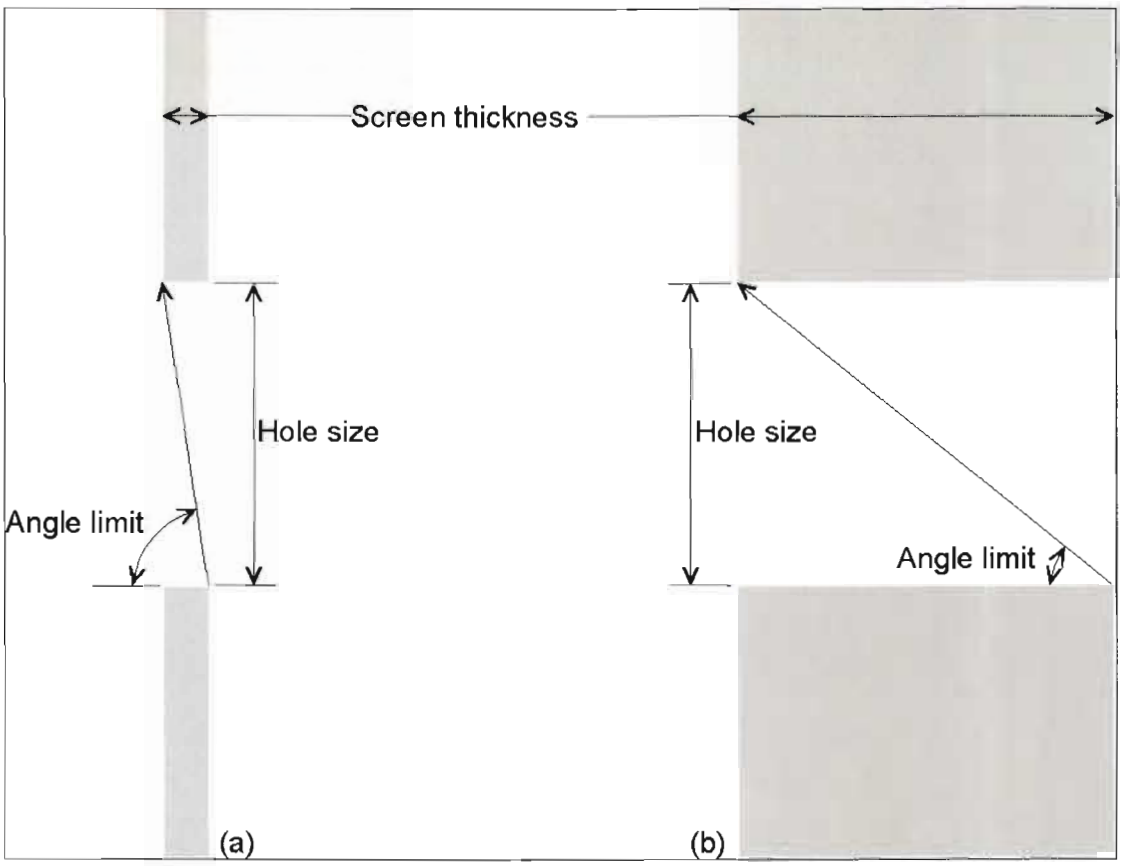

Figure 73: Implementation of the angle of incidence limit imposed

If the approach angle is larger than or equal to the limit angle, then the angle used in the calculation of the resistance value is set to 95 percent of the limit angle. This number was chosen to ensure that the FAR is calculated to a value closely resembling the true value. If the angle of incidence equals the limit angle, then the FAR becomes zero resulting in an infinitely large resistance value, which subsequently causes the solution algorithm to become unstable. It can be seen that this limit is imposed more frequently with screens of larger thickness. The influence that this limit had on the results is discussed in paragraph 7.4.

A print statement was included to notify the user of any limit that has been reached. In most instances, it was found that the limits were only reached in the first iterations and were then applied only in extreme cases as the solution algorithm reaches convergence. Applying limits to the values allowed the solution algorithm to overcome initial instabilities and advance to such a level that it becomes more stable thus not requiring the limitations any longer. With diffusers being modelled where the recirculation zones are distinctly unstable, the implementation of certain solution algorithm limits was found to be unavoidable.

Since the calculated resistance value is multiplied by the length (dL) of the porous medium (see equation (6.17)), it was required to define the resistance per unit length thus dividing by the thickness of the porous medium for Star-CD to accurately calculate the resistance value. It should however be noted that the resistance could not merely be divided by the perpendicular thickness of the porous medium, since the distance that the flow passes through the porous medium is a function of the angle of incidence (see Figure 74). If the flow passes through the porous medium at an angle other than perpendicular, then the solver multiplies the resistance with the full distance that the flow travels through the porous medium resulting in increasingly larger resistance factors as the angle increases from 0° (perpendicular to the face of the screen). The code then overestimates the resistance values near the walls of the diffuser. For this reason the true thickness was calculated by using the angle of incidence and dividing the calculated resistance by the total distance that the flow passes through the porous medium. This adaptation of the length was required due to the assumption that the transversal resistance coefficients (α_y and α_z) are small (as discussed in paragraph 7.2.2.4).

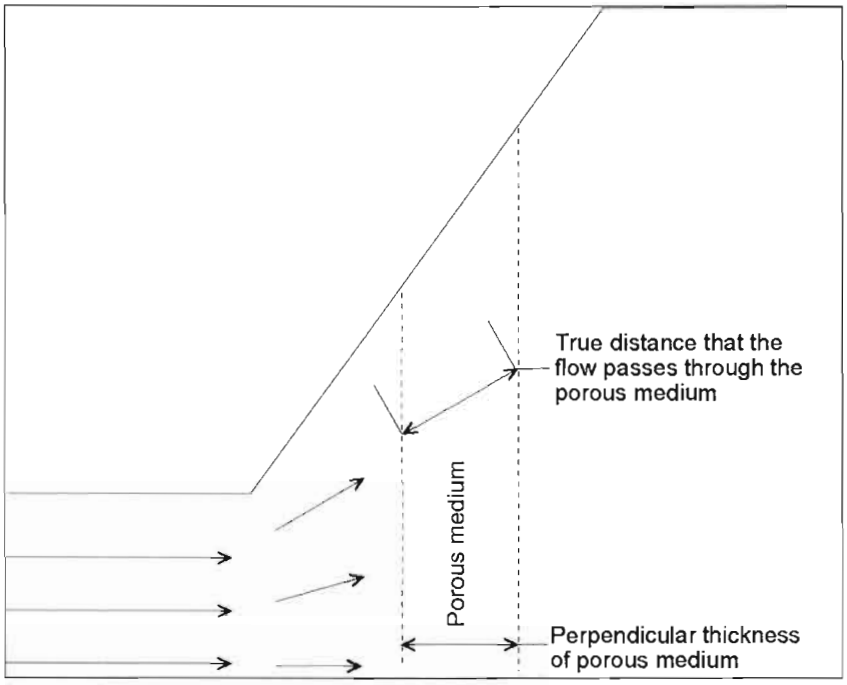

Figure 74: True length of porous medium

7.2.5 The momentum source approach

It was found that the physical parameters of some screens did not conform to the limitations set by Star-CD (see Star-CD v3.15 Methodology manual 2001:8-2 and equation (6.12)). For this reason the resistance values were implemented by using a negative momentum source (momentum sink). This source is introduced through the use of a UDF called sormom.f after switching on the momentum source function in Star-CD. *Although this approach was not included in the original scope of this project, it was decided to investigate this option and include the results in the study.*

After reviewing the literature and examples (Star-CD v3.15 Methodology manual 2001:8-2 to 8-8) it was found that there are two ways of implementing the momentum sink:

- Explicitly as a source that is introduced on the right hand side of the Navier Stokes equation (see equation (6.8)).
- Implicitly where the source is calculated and again multiplied by the solver with the velocity of the cell. This source is thus implicitly coupled to the convection term in the Navier Stokes equation (see equation (6.8)).

It is recommended that the solution of the momentum equations should be under-relaxed (~0.2) if the explicit method is used suggesting that the explicit approach is more prone to instability than the implicit approach (see Star-CD v3.15 Methodology manual 2001:8-8). It would therefore be beneficial to use the implicit- rather than the explicit approach.

A very simple test case was constructed (see Figure 75) to test the implementation of the calculated resistance coefficients as momentum sink terms compared to the porous medium approach. The theoretical pressure drop is calculated using the simplified porous medium equations:

$$dP = \alpha * u^2 \tag{7.1}$$

and

$$dP = \beta * u \tag{7.2}$$

Using a porous medium with an average approach velocity of 5m/s, the following results were obtained: With α equal to 10 and β equal to zero the theoretical pressure drop is 250 Pa, the pressure drop calculated by Star-CD was 245 Pa. With α equal to zero and β equal to 10 (the theoretical pressure drop thus being 50Pa), the total pressure drop calculated by Star-CD was 49.4 Pa. It can therefore be seen that the porous medium approach shows relatively good correlation with the theoretical pressure drops. The small differences are due to the fact that the values were not extrapolated to the faces of the porous medium to give exact values.

If the resistance is implemented through a negative momentum source term (momentum sink), there are a number of different options: The momentum sink can be implemented through α or β either implicitly or explicitly. Since the variable value of α is defined for the porous medium approach, the focus was on implementing the momentum sink implicitly using the same variable α.

If the momentum sink is implemented using the implicit approach (see ANNEXURE E.7), it was found that the pressure drop is 233.9Pa where the theoretical value should be 250Pa (an under-prediction of 6.4%). The velocity in the momentum sink region ranges between 4.4 and 4.9 with the average approach velocity being 5m/s (see Figure 75), which explains the under-prediction of the pressure drop when using this

approach. The solution algorithm reached the standard convergence (i.e. 1E-3) in 31 iterations.

The momentum source is implemented by the following equation:

$$S = S1 - S2(U) \quad \textbf{(7.3)}$$

Where: S2 represents the implicit source
S1 represents the explicit source

The user has no control over the value of U since it is calculated by the solver. With the explicit approach, the neighbour cell velocity can be used and then the explicit approach is not influenced by the reduction of velocity in the momentum sink region. However, since the U value of the code forms an inherent part of the implicit approach, the extraction of momentum from the flow domain is under predicted resulting in a lower pressure drop across the momentum sink region.

The lower value of the velocity through the momentum sink region is due to the extraction of momentum from the flow domain. This reduction in velocity seems unphysical and the question that immediately arises is: How does the code maintain the conservation of mass? The density, flow area and mass flow remains constant while the velocity is reduced. In response to this question, CD-adapco explained that: *"This issue is similar to the checkerboard effect, even in that case the solver thinks that the field is converged and mass is conserved but the solution is clearly unphysical. Here something similar happens. Star-CD does not use staggered grids but collocated grids, and the pressure-velocity coupling algorithm is Rhye-Chow, so the details of these approaches are different."* (see Ferziger and Perić 2002 for more information on these topics). This does however not solve the under-prediction of the pressure drop.

The implementation of negative momentum source terms was simulated in Fluent and it was found that the velocity is not reduced as it is in Star-CD and the pressure drop is calculated accurately. Since Star-CD was used for all the preceding work, it was not advisable to change to a different code at this stage of the study. For this reason, it was required to investigate workaround solutions to this problem.

The first option was to define the source term explicitly (see ANNEXURE E.8) using the S1 term in the momentum sink definition. The advantage of using the explicit approach

is that the user can define the value of the source term and it is not a function of the velocity calculated in the solver. The disadvantage is that the code supposedly becomes less stable with the explicit approach. However, it was found that the solution algorithm converged in only 13 iterations compared to 31 iterations for the implicit approach. This is not surprising, since a constant value for the source term was used. The proper explicit implementation would still require the upstream neighbour velocity, which may influence the convergence of the explicit approach. Since the approach velocity was known, it was hard-coded as if using the approach velocity (neighbouring cell before the momentum sink) and not the local cell velocity. The pressure drop was then calculated to be 250.8Pa. Although this approach yielded the correct pressure drop, the question of numerical stability was raised. Results are shown in Figure 75. This approach was tested in the diffuser model, but it was found to be very unstable as discussed in paragraph 7.3.

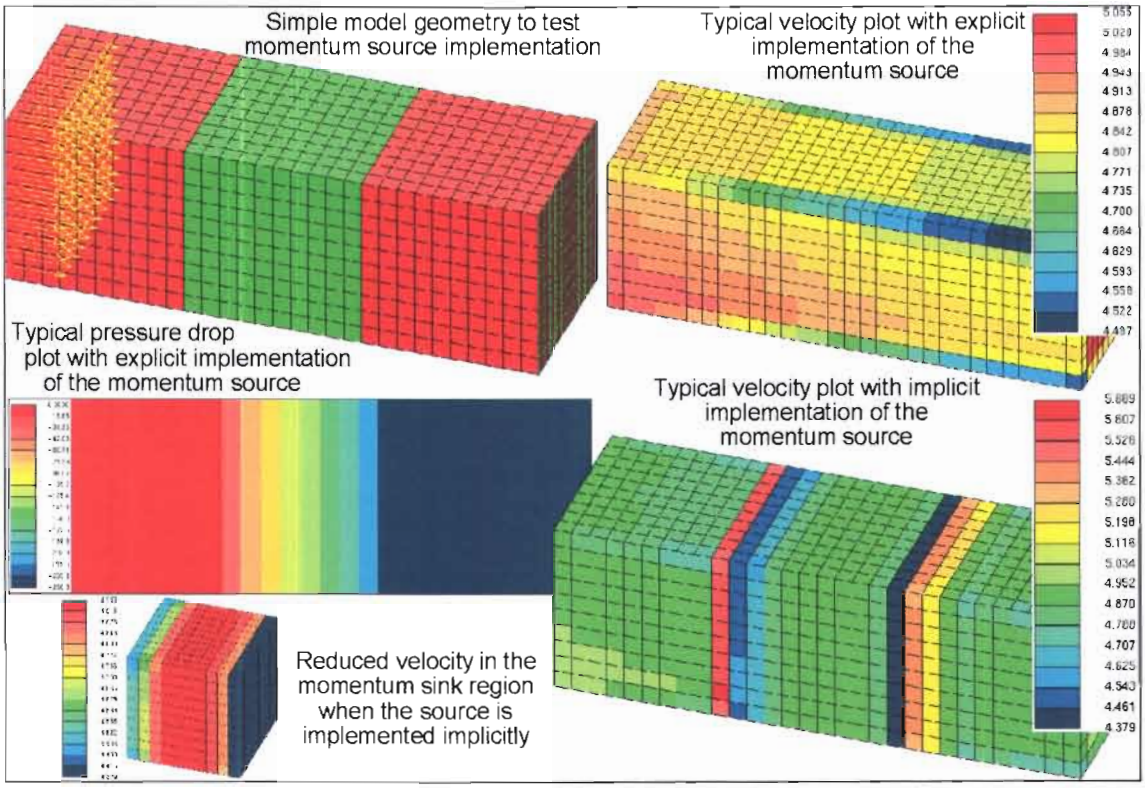

Figure 75: Implementation of momentum sources

The second workaround option was to define the source term implicitly, but to apply a linear correction factor to the calculated pressure drop (see ANNEXURE E.9). This correction factor was defined as the ratio between the approach (neighbour) cell velocity divided by the calculated local cell velocity. This correction factor was then

multiplied with the calculated momentum sink in order to correct the under prediction of the implicit momentum source. It is also required to use the neighbour cell velocity in the definition of the implicit source term S2. This approach yielded a pressure drop of 254Pa, which is an over-prediction of only 1.6 percent. Although this is not a purely mathematical solution to the under prediction of the pressure drop, it is the only available solution since the user does not have any further access to the solver other than through UDF's. Based on this information, it was decided to implement the variable resistance using a momentum sink with the corrected implicit approach. It should be noted that the velocities through the momentum sink region were still reduced and that it was only the pressure drop that was corrected for.

7.2.6 The simple porous baffle approach

A conventional method of modelling screens in a diffuser is by using a simple baffle (local planar resistance) to represent the screen. The pressure drop implemented in the solution algorithm is calculated by (Star-CD v3.15 Methodology manual 2001:8-3):

$$dP = -\rho v_a(\alpha \mid v_a \mid +\beta) \tag{7.4}$$

Where:

- dP = *Pressure differential across the porous baffle (Pa)*
- ρ = *Density of the fluid (kg/m^3)*
- α = *User defined variable (kg/m^4)*
- β = *User defined variable (kg/m^3.s)*
- v_a = *Perpendicular approach velocity (m/s)*

Assuming that the velocity is always positive, that $\beta \rightarrow 0$ and combining equation (7.4) with (6.6), it can be shown that:

$$\alpha = \frac{K}{2} \tag{7.5}$$

A variation of this approach where the value of α is again divided by 2 was first suggested by Schmitz et. al. (1998):

$$\alpha = \frac{K}{4} \tag{7.6}$$

Although there is no mathematical reasoning behind this approach, it was found that it did show a rather good correlation with empirical data for 50 percent FAR screens. For

this reason it was decided to also include it in this study. Results are discussed in paragraph 7.4.

7.2.7 The variable porous baffle approach

It was decided to also investigate the possibility of using a porous baffle where the resistance coefficient is defined as a variable resistance through user coding. It was found however that a baffle boundary could not be defined in Star-CD through user coding. The α and β values can only be defined as constant values. Since this is not a standard function, variable baffle resistance values could not be included in this study. It is recommended that this option should be further investigated with later versions of Star-CD.

7.2.8 Limitations to this coding

The following limitations are applicable:

- Due to the implementation of the neighbour list assignment using a cell number offset, this research can only be used in structured meshes.
- A maximum number of three cells is allowed through the thickness of the porous media or momentum sink regions. Due to the simulated thickness of the porous medium (0.5mm), the aspect ratio of the cells become undesirable with more cells through the thickness. For this reason, the code was developed for only three cells, but it can be expanded in order to allow the user to simulate more than three cells through the thickness of the porous medium.
- The porous medium should always be on the Y-Z or X-Y planes of the standard orthogonal coordinate system. The current version of the coding cannot calculate the angle of incidence for porous media that are not on these planes.

7.3 Solution algorithm

Based on the discussion in the previous paragraph, a solution algorithm can be constructed. Figure 76 shows the simplified solution algorithm for the calculation of variable resistances using both the porous medium and momentum sink approaches.

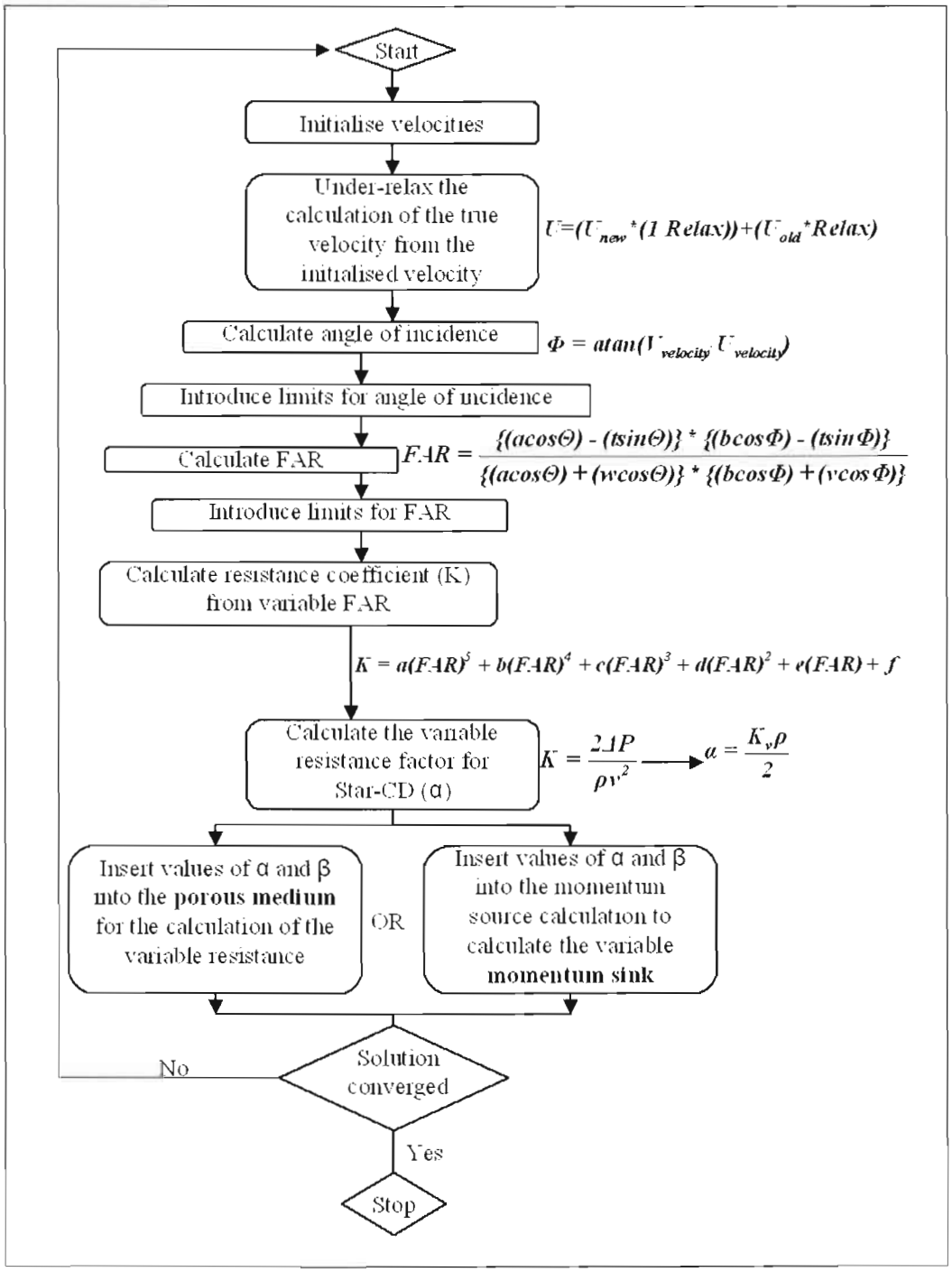

Figure 76: Solution algorithm

7.4 Discussion of results

7.4.1 Screens included in this study

Five different screens were tested in both the 30° and 60° diffusers. As mentioned previously, it was decided to include only square lattice screens since the behaviour of

round holed screens is expected to be similar. These screens were chosen to test specific topics:

- The influence of the thickness of the screen.
- The influence of the screen FAR.
- The influence of the ratio between the lattice width of the screen holes to the size of the flow area (w/D_H).

Table 12: Screens included in this study

Screen number	FAR (Percentage)	Thickness (mm)	Hole size (mm)	Pitch (mm)	Lattice size (mm)
1	50	0.5	15.4	21.7	6.3
2	50	6.0	15.4	21.7	6.3
3	50	0.5	50.5	71.4	20.9
4	30	0.5	15.2	27.8	12.6
5	70	0.5	15.5	18.5	3.0

Where:
- FAR refers to the ratio between the free area divided by the total flow area.
- Hole size refers to the size of the hole in both vertical and horizontal directions.
- Pitch refers to the length between successive lattices.
- Lattice size refers to the size of the solid parts of the screen (lattices).

7.4.2 General trends observed from the experimental data

In order to show general trends from the experimental data, the traverses measured for both the vertical and horizontal flow profiles were averaged and were compared to results for the other screens. Figure 77 and Figure 78 show these comparisons for the 60° and 120° diffusers respectively in the central diffuser position. Comparisons in the front of the diffuser are shown in ANNEXURE F, Figure 122 for the 60° diffuser and Figure 128 for the 120° diffuser.

With the smaller diffusion angle of the 60° diffuser, it can be seen that the flow profiles are more uniform in general. With the 120° diffuser, it can be seen that the separation of the flow is more pronounced resulting in higher flows in the middle part of the duct.

The influence of the screen thickness can be clearly seen when comparing the 0.5mm screen with the 6mm 50 percent FAR screen. It can be seen that the screen thickness acts as a flow-straightening device that redirects the flow towards the centreline of the duct.

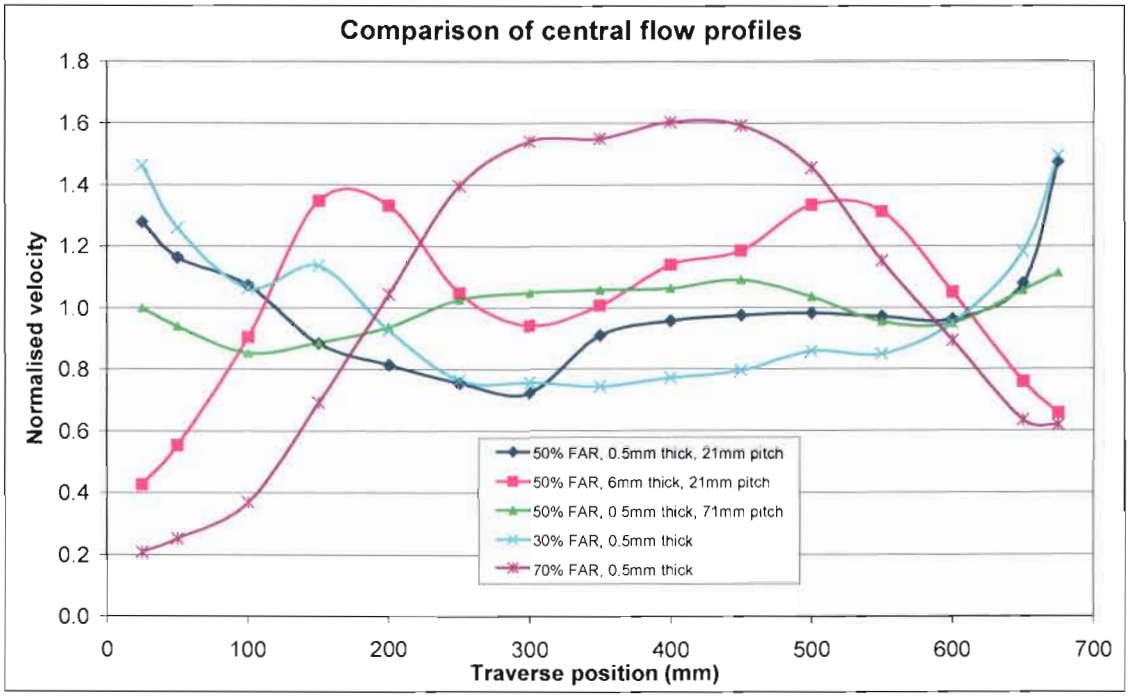

Figure 77: Averaged profiles in the central diffuser position 60° diffuser

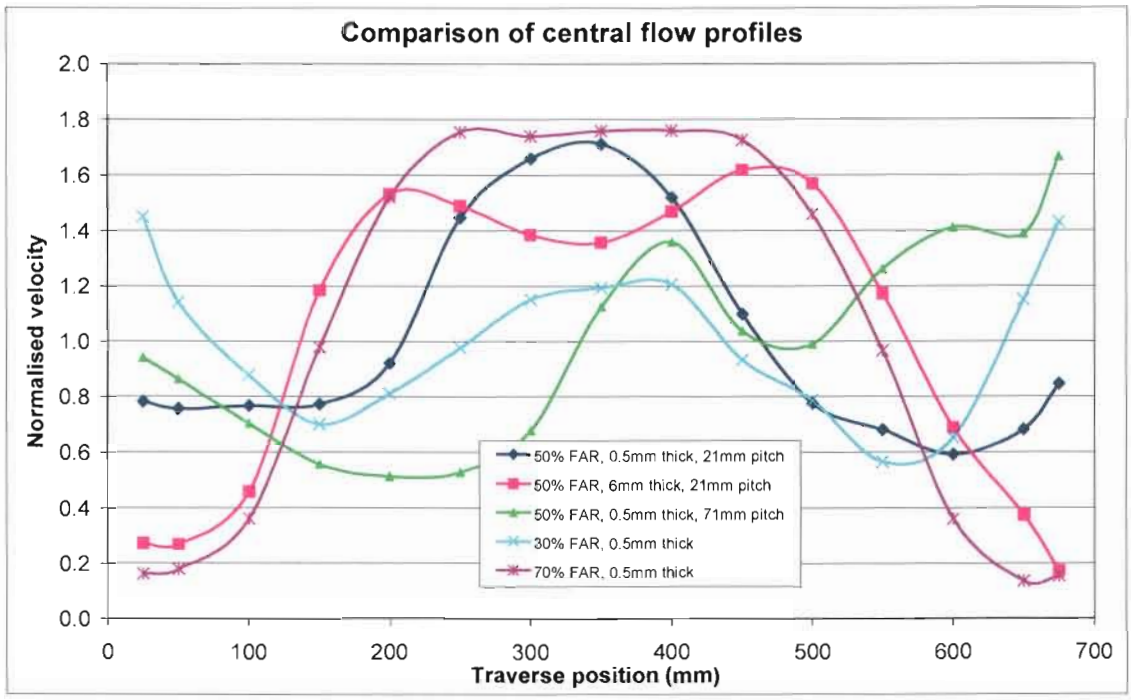

Figure 78: Averaged profiles in the central diffuser position 120° diffuser

From the 60° diffuser results, it can be seen that the 30 percent FAR screen reverses the inlet flow profile with high flow near the walls of the diffuser. This reversal of the flow pattern is not as prominent with the thin 50 percent FAR screen. When the number of flow paths is then reduced, it can be seen that the 50 percent FAR screen with large pitch shows a near uniform flow profile. Both the thick 50 percent FAR screen and the 70 percent FAR screens show a pronounced central flow profile.

Table 13 shows the measured pressure drop for the screens tested in both diffusers. It can be seen that the pressure drop did not increase significantly with an increase in screen thickness. A change in the pitch did however result in a marginal increase in resistance. As could be expected, a change in FAR has a major influence on the pressure drop across the screens.

Table 13: Measured pressure drop (Pa)

	60° diffuser	**120° diffuser**
50 percent FAR, 0.5mm thickness, 21mm pitch	192.3	232.5
50 percent FAR, 6mm thickness, 21mm pitch	194.1	245.3
50 percent FAR, 0.5mm thickness, 71mm pitch	200.2	284.0
30 percent FAR, 0.5mm thickness	340.1	390.7
70 percent FAR, 0.5mm thickness	164.0	217.2

7.4.3 Numerical model geometry

Based on the study conducted into the convergence behaviour (paragraph 7.2.2), a new numerical model was generated to ensure the best possible results from this study. The updated model is shown in Figure 79. The following improvements were made to the previous model:

- The boundary layer of the inlet pipe was refined in order to ensure accurate calculation of Y+ values.
- Three cells were used in the porous medium region. Two cells would have been sufficient for the porous medium approach, but three cells were advised for the momentum sink approach. Due to the discontinuity in pressure gradient at the porous/fluid interface, all gradients in cells adjacent to the interface of a porous medium are based on linear extrapolation of pressure. Hence a

minimum of two cell layers is necessary within the porous region (see Star-CD v3.15 Methodology manual 2001:8-4). No clear guideline could be found for the number of cells required for the momentum sink region, but the advice from Star-CD was to use as many cells as possible.

- The cells before and after the screen were refined significantly, i.e. at least four cells upstream and downstream from the screen with the same thickness of the porous medium cells.
- Cells in the transition between the inlet duct and the diffuser were refined to ensure better simulation of the flow separation.

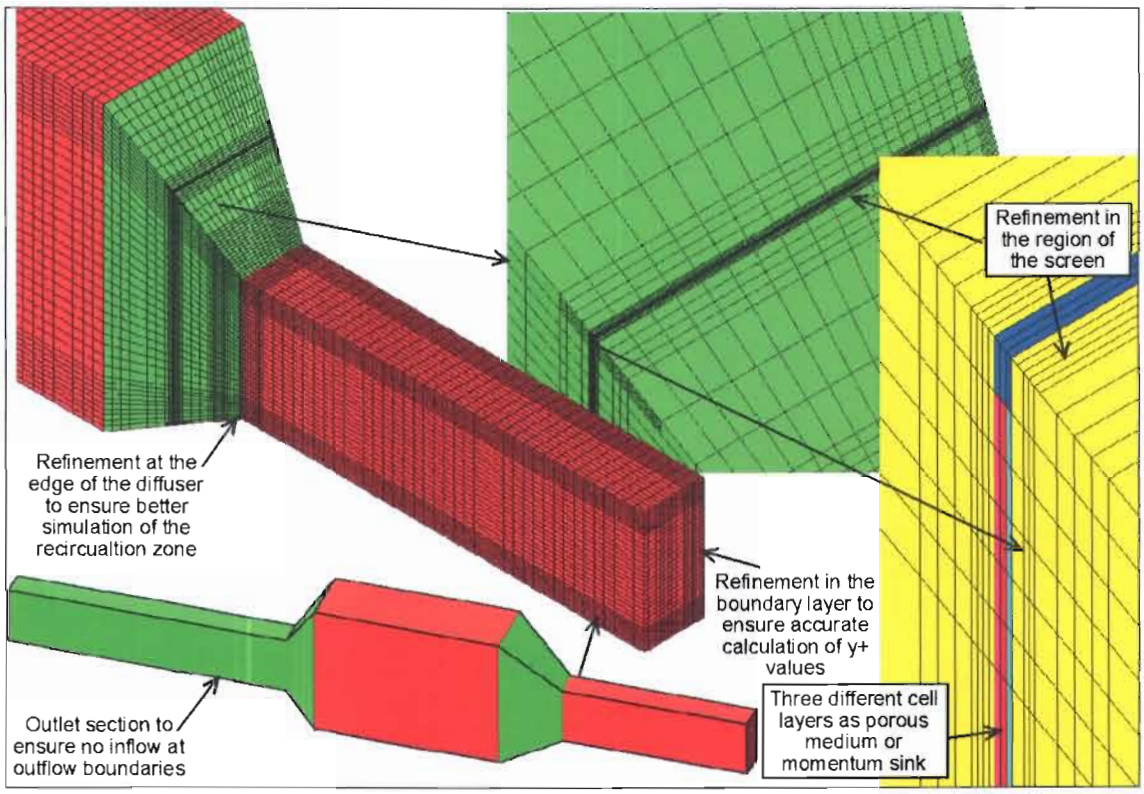

Figure 79: Numerical model geometry

7.4.4 General notes on CFD simulations

- All simulations in this chapter were conducted with the k-ε high Reynolds number turbulence model unless otherwise stipulated.
- The MARS discretisation scheme was used.
- The Algebraic Multi Grid (AMG) solver was used.
- Double precision was used for all runs.
- Density was assumed to be constant.

- All simulations were under-relaxed as discussed in paragraph 7.2.2.
- No simulations were restarted from previous results.
- After the study into the convergence behaviour, it was found that the convergence levels achieved was improved when compared to previous sections of this study. All of the simulations for the 60° diffuser converged while the highest residual found with the 120° diffuser did not exceed 3e-3.

7.4.5 60° Diffuser: Screen One (50 percent FAR, 0.5mm thickness)

A number of simulations were conducted with this first screen to test the influence of several different parameters in order to determine the simulations required for the remainder of the screens. A similar methodology was adopted as for previous experimental work as shown in Figure 80.

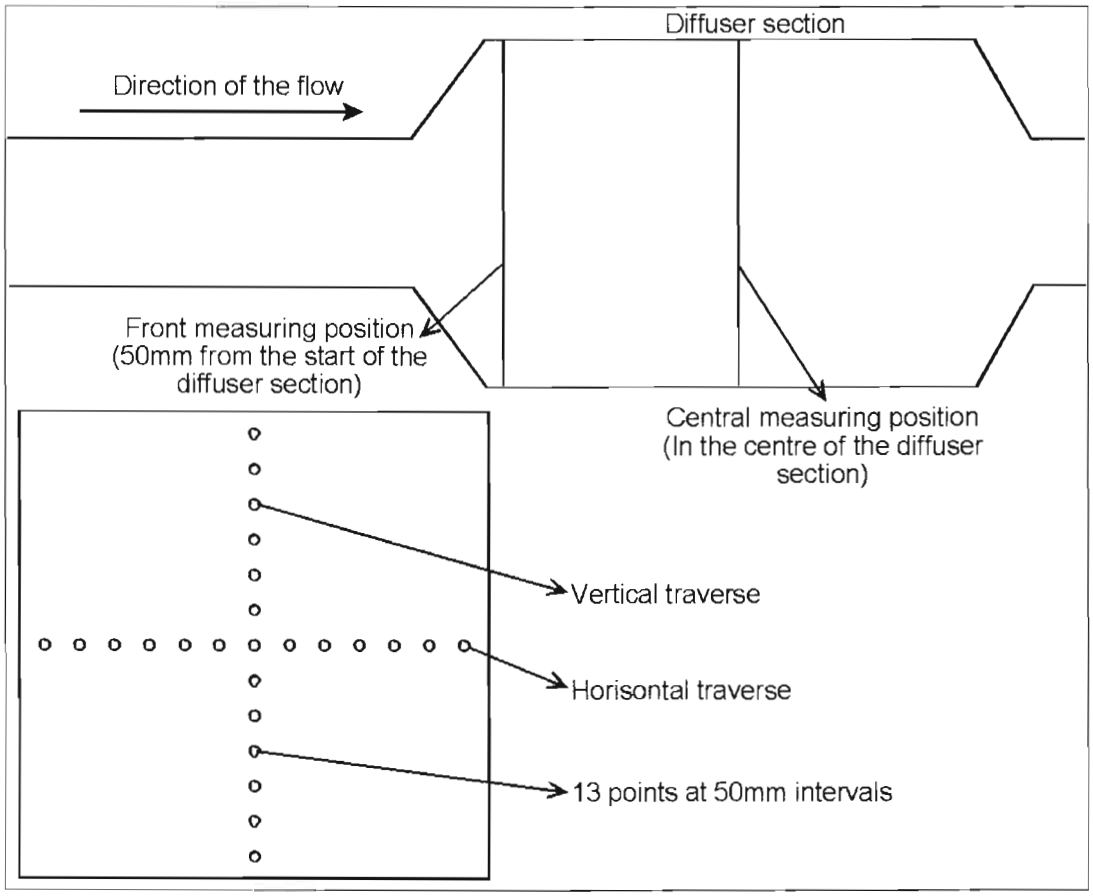

Figure 80: Explanation of measuring traverses used for screens

It should however be noted that the frontal measuring position was moved to 200mm into the diffuser for the 120° diffuser. Due to the large angle of this diffuser, the 50mm position was found to be in the recovery region of the flow for some screens. The jetting through the screen could be observed in the measurements.

7.4.5.1 The influence of the turbulence model

In paragraph 5.6 the influence of the turbulence model was investigated with the open diffusers and it was found that the turbulence model did not have a significant influence on the results. It should however be noted that the models tested were all derivatives of the k-ε model and this statement need to be proven with more advanced turbulence models such as v2f. It was decided to test this influence again with the screens in place in order to make sure that the influence is still negligible.

Three different comparisons are shown in Figure 81 and it can be seen that the difference between the k-ε and RNG turbulence models is minimal. It was only with the variable porous media approach that a subtle difference could be observed. The RNG turbulence model still did not show a better correlation with the experimental data. For this reason, it was decided to conduct all further simulations with the k-ε turbulence model.

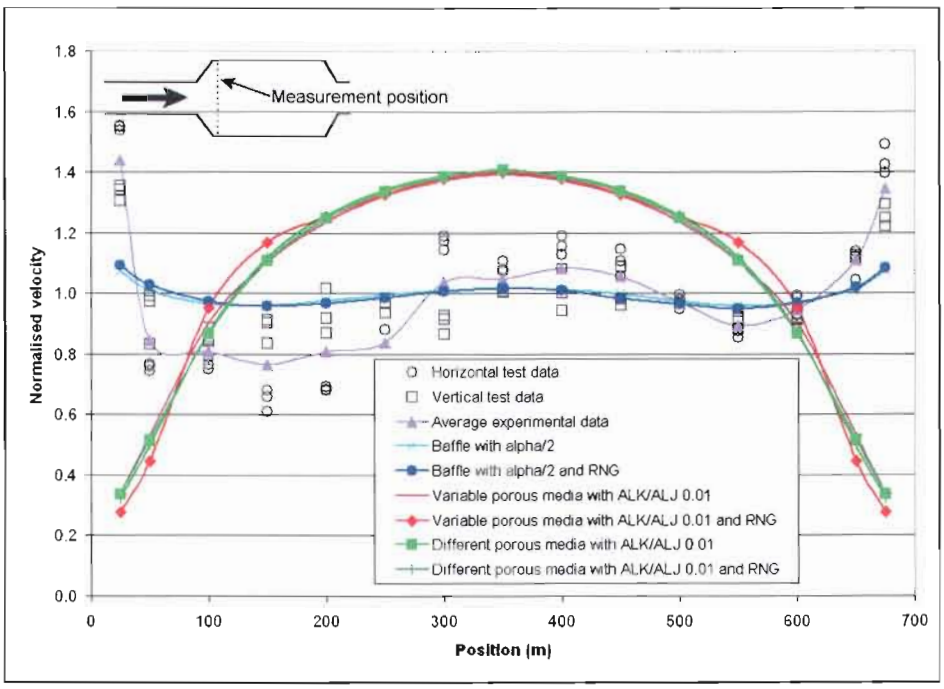

Figure 81: Testing the influence of different turbulence models

7.4.5.2 The influence of turbulent intensity

The influence of the turbulent intensity in the porous medium was investigated by increasing the value from the default 0.1 to 0.5. This test was also conducted with the user defined inlet velocity profile. Comparative results are shown in Figure 82 and it can be seen that the increased turbulent intensity did result in a change in the predicted flow profile although the change is not significant and the results did not show an improved comparison with the experimental data.

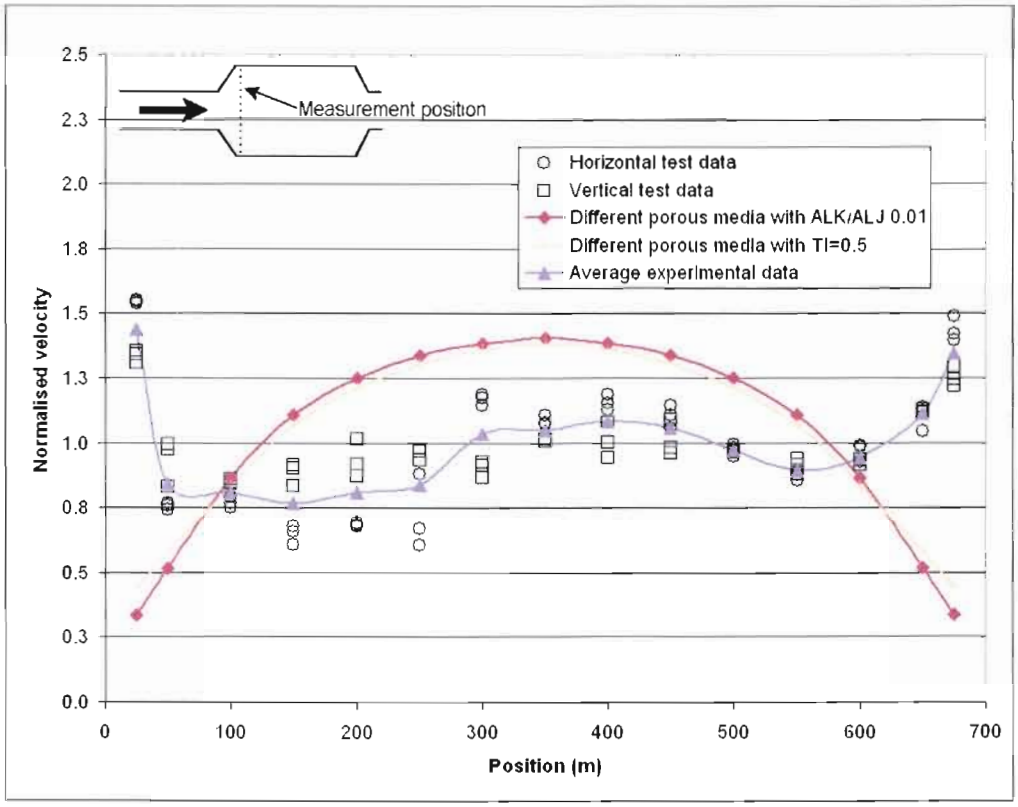

Figure 82: Testing the influence of the turbulent intensity

7.4.5.3 The ratio between the perpendicular- and transverse resistance coefficients.

As mentioned previously, the transverse resistance coefficients (ALJ and ALK) should be set to a value as close to zero as possible. This is required so that the porous medium does not overestimate the change in flow direction as the flow passes through the screen. These values were defined as a ratio of the perpendicular coefficient (ALI). It was found that this ratio could not be set lower than 0.01. Any value smaller than this resulted in a very unstable solution algorithm that did not converge further than 2e-2, which is not a satisfactory convergence level. All further simulations were therefore conducted with this ratio set to 0.01.

7.4.5.4 Comparing the conventional porous medium approach with using different porous media

With the conventional porous medium approach, the transverse resistance coefficients (ALJ and ALK) were set to the same value as the perpendicular coefficient, i.e. the resistance is homogenous or isotropical. This approach was adapted by defining two separate porous media in the centre and around the perimeter of the screen. ALJ and ALK were set to a ratio of 0.01 of ALI for the central region and 0.5 of ALI for the perimeter region thus resulting in an an-isotropical or non-homogenous resistance. This change resulted in a rather significant difference in the predicted flow profile that showed a better correlation with the experimental data as shown in Figure 83. It can however be seen that this approach still does not predict the flow profile very accurately.

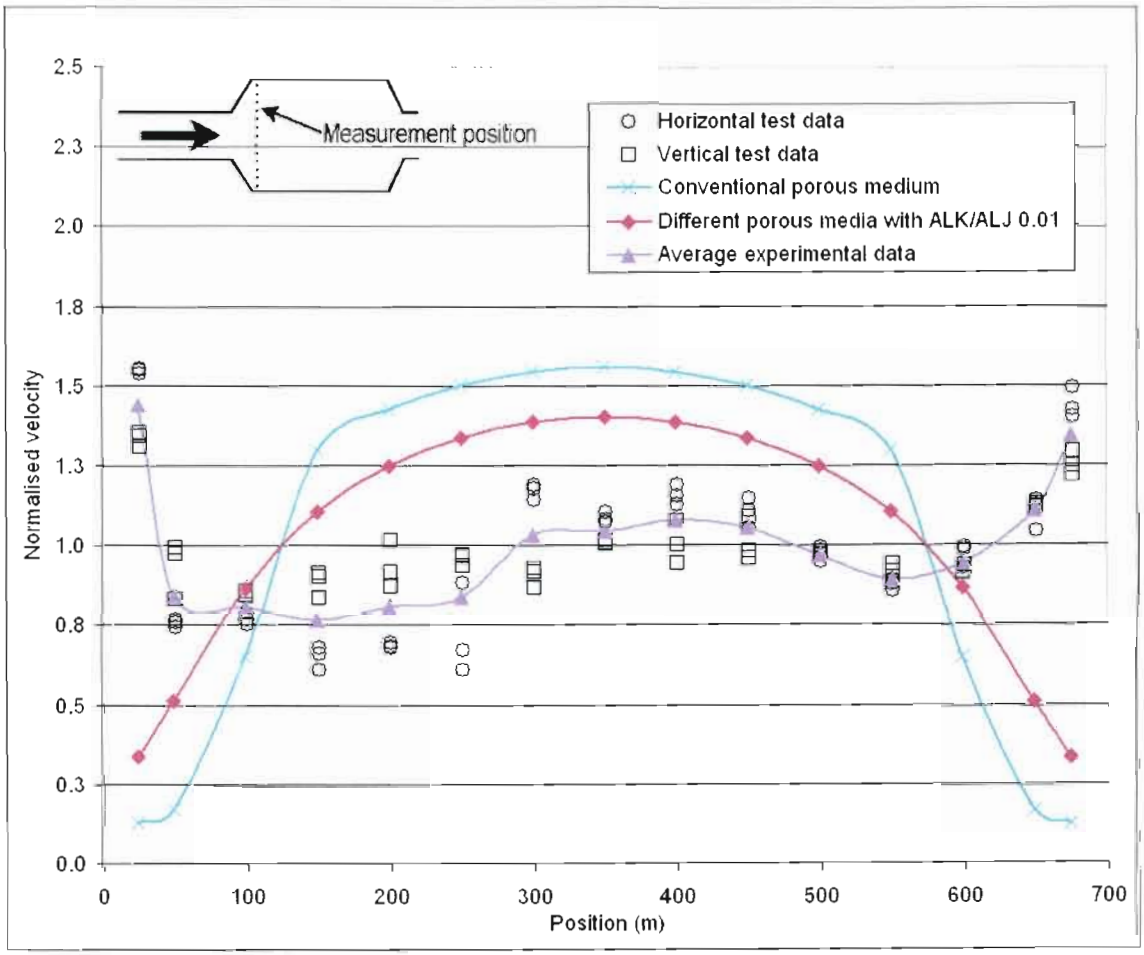

Figure 83: Comparing different porous medium approaches

incidence were reported for a large number of cells during the simulation while the implicit approach did not report any limits being reached. Similar to the test case discussed in paragraph 7.2.5, it was also found that the flow field and predicted pressure drop was unphysical. The explicit approach diverged after 2330 iterations.

With the implicit approach, the solution algorithm converged after 1007 iterations even with the very low relaxation values. Results from this approach for the frontal position is shown in Figure 85 and it can be seen that these results compare very well with the experimental data. It can be concluded that this is the only approach that accurately predicts the higher flow near the walls of the diffuser. Only limited results are shown here while the remainder is shown in ANNEXURE F.

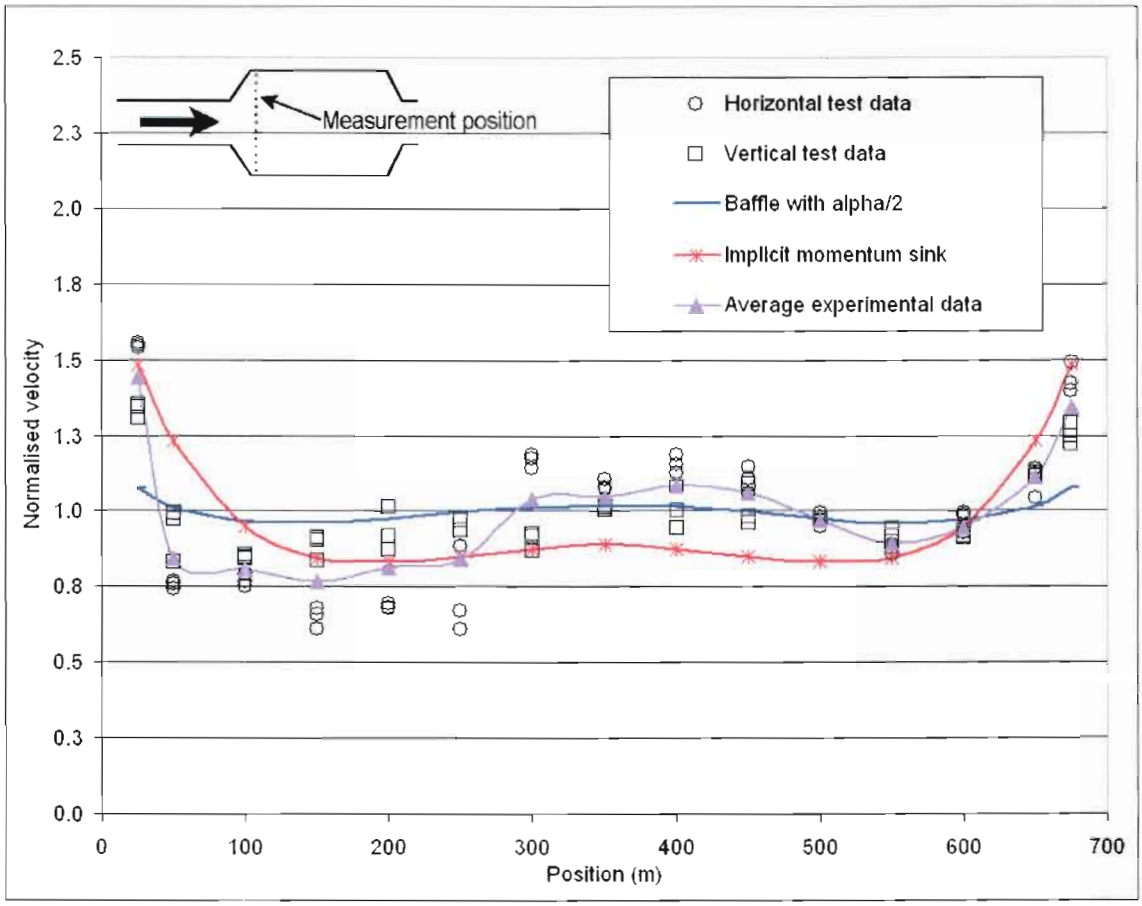

Figure 85: Implicit momentum sink results (frontal duct position)

7.4.5.7 Pressure drop prediction

The total pressure drop predicted by the CFD model for each of the different cases is compared to the measured values in Table 14. It can be seen that the porous medium approach in general shows a reasonably good correlation to the measured pressure

drop with an under prediction ranging between 10 and 20 percent. It was found that the solution algorithm diverged for both cases where the ratio between the transverse and perpendicular resistance values was set to 0.001.

The conventional baffle approach showed a similar result while the baffle with the reduced resistance value under-predicted the pressure drop by approximately 24 percent with both the k-ε and RNG turbulence models. With the implicit momentum sink approach, the pressure drop was under predicted by only 11.3 percent.

Table 14: Pressure drop comparison with the 60° diffuser screen 1 (Pa)

		CFD pressure drop (Pa)	Pressure drop comparison	Measured Total Pressure Drop
1	Conventional porous medium	171.01	-11.08%	192.31
2	Different porous media with ALJ/ALK 0.001	Diverged	Diverged	
3	Different porous media with ALJ/ALK 0.01	170.95	-11.11%	
4	Different porous media with RNG	172.73	-10.18%	
5	Variable porous media with ALJ/ALK 0.001	Diverged	Diverged	
6	Variable porous media with ALJ/ALK 0.01	166.05	-13.65%	
7	Variable porous media with ALJ/ALK 0.01 using RNG	163.81	-14.82%	
8	Different porous media with ALJ/ALK 0.01 with Turbulent Intensity 0.5	170.97	-11.10%	
9	Conventional baffle	168.37	-12.45%	
10	Baffle with alpha divided by 2	145.43	-24.38%	
11	Baffle with alpha divided by 2 and RNG turbulence model	145.36	-24.42%	
12	Implicit momentum sink	170.64	-11.27%	

7.4.5.8 Colour contour plots of the calculated resistance values

Figure 86 shows the scalars that were defined in order to plot the calculated values during post processing of results. The cells plotted represent the screen in the diffuser. A total of six scalars were defined, which includes the calculated variable FAR, resistance coefficient, α value in the perpendicular direction, α value in the transverse

directions and the adjusted porous medium length. It can be seen that the FAR is calculated to be 50.3 percent in the centre where the angle of incidence is perpendicular. This corresponds to the theoretical FAR value calculated with the spreadsheet shown in ANNEXURE G. The FAR is then reduced as the angle of incidence increases away from perpendicular resulting in an increase in the resistance coefficient. The perpendicular resistance value of a 50.3 percent FAR screen is 3.98 as shown in the centre part where the flow is mostly perpendicular. Interesting to note is the recovery of the angle of incidence to perpendicular in the corners of the screen as the flow is forced through the screen in these regions. Flow profiles could not be measured directly in front of the screen and it is recommended that a study be conducted to investigate the flow profiles between the inlet to the diffuser and the screen. It should however be noted that it could potentially prove problematic to measure this flow profile due to the uncertainty of the flow angle. A different approach to a pitot static tube would therefore be required.

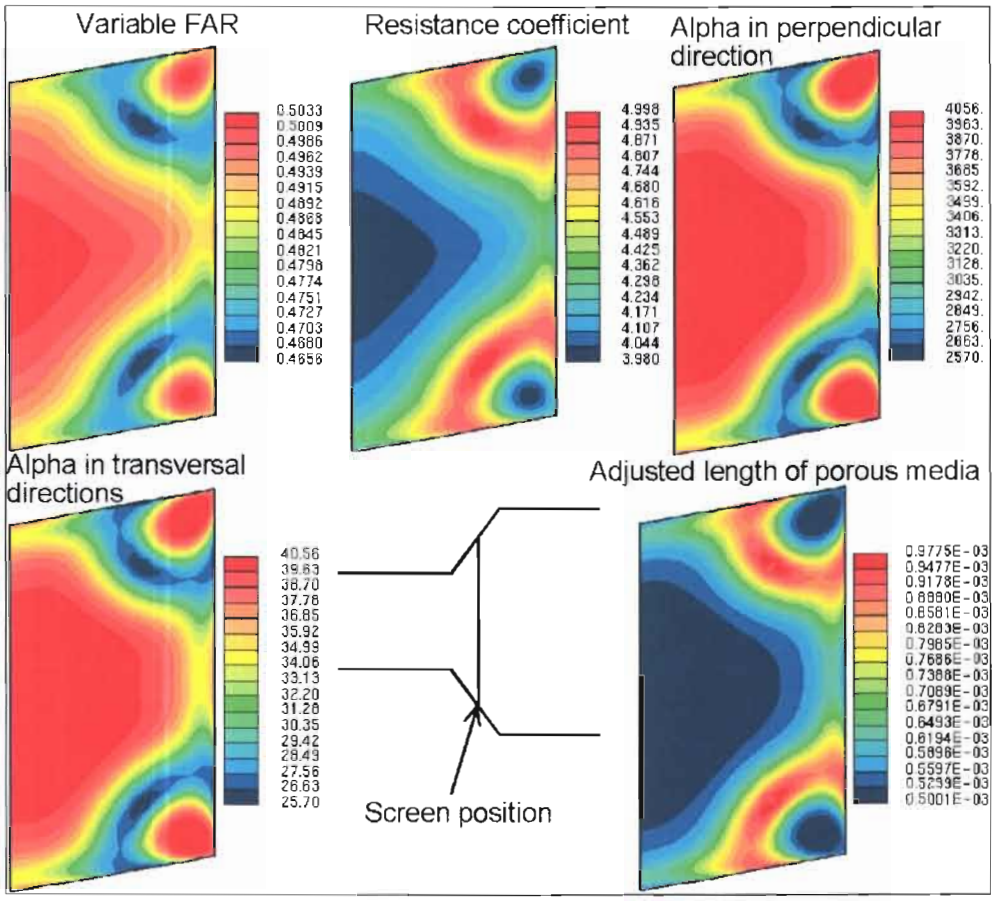

Figure 86: Scalars representing the calculated values of the screen

7.4.5.9 Conclusions and recommendations

It can be concluded that the porous baffle approach with $\alpha=k/4$ shows a reasonably good correlation with empirical results while the best correlation was predicted with the momentum sink approach for the thin 50 percent FAR screen in the 60° diffuser. Furthermore, the total pressure drop is under predicted by a margin ranging between 10 and 25 percent with the cases that reached convergence. Diverged simulation results are not taken into consideration.

From the results presented and discussed in the previous paragraph, the following recommendations are made for the remainder of the CFD simulations:

- The standard k-ε high Reynolds number turbulence model should be used for all further simulations.
- All simulations should be conducted with the ratio between the perpendicular (ALI) and transverse resistance coefficients (ALK/ALJ) set to 0.01.
- Since the turbulent intensity value did not have a significant influence on the results, it is recommended that all further simulations be conducted with the default value of 0.1 for the porous media approach.

Based on the above discussion, it was decided to choose a solution method that showed the best results from each of the three approaches, i.e. porous baffles, porous media and momentum sinks. The following simulations were therefore included for the remainder of the screens:

- Porous baffle with $\alpha=k/4$.
- Variable resistance porous media with ALJ and ALK set to 0.01 of ALI. The transverse resistance values for the porous medium around the peripheral were set to 0.5 of ALI.
- Implicit momentum sink approach with the correction factor to compensate for the under-prediction of the momentum sink term due to the reduced velocity in the momentum sink region.

7.4.6 60° Diffuser: Screen Two (50 percent FAR, 6mm thickness)

7.4.6.1 Comparison of flow profiles

Figure 87 shows the comparative flow profiles in the central diffuser position and it can be seen that the baffle approach does not show a good comparison. This is due to the fact that this approach does not incorporate the influence of the screen thickness. With this screen being 6mm thick (compared to the 0.5mm thickness of screen 1), the flow is forced perpendicular by the longer flow path through the screen (compare empirical results from Figure 87 with Figure 123). This phenomenon is not captured by the baffle approach where the resistance value is applied constant across the total area of the screen. It may be possible to simulate the influence of the screen thickness if the variable resistance approach with porous baffles were available in Star-CD Version 3.15. It is recommended that this approach should be further investigated with later versions of Star-CD.

It can be seen that the variable resistance porous media approach does capture the influence of the thicker screen with a good correlation near the walls. This approach does however not accurately predict the lower flow profile in the centre of the duct. The momentum sink approach predicts a high flow in the centre of the diffuser contrary to the lower flow measured in this region. Due to the thickness of this screen, the flow would be channelled as it passes through the screen and therefore the assumption that the ratio between ALI and ALJ/ALK is 0.01 may influence the results negatively. For this reason it was decided to include a simulation where this ratio is set to 1 (conventional approach). It can be seen that the difference in the centre of the diffuser section is minimal. Figure 124 shows that the higher flow in the middle part of the flow profile in the front of the diffuser is more pronounced. This could be expected due to the fact that the flow is channelled towards the perpendicular direction through the porous media when this ratio equals 1. This approach still did not result in a good prediction of the flow field.

It can be concluded that none of the approaches predicted the flow profile accurately with the variable porous media approach showing the best results for the 50 percent FAR screen with large thickness in the 60° diffuser.

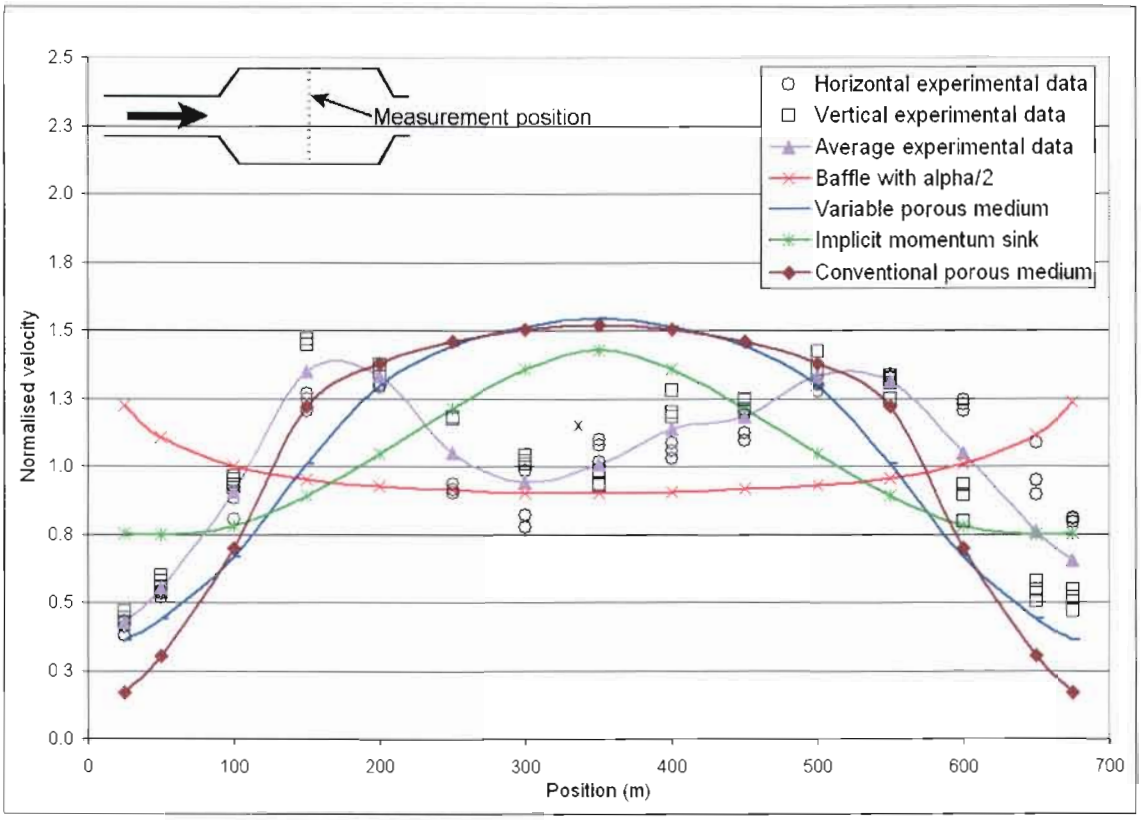

Figure 87: 60° diffuser central position with screen 2

7.4.6.2 Pressure drop prediction

Table 15 shows the predicted pressure drop. It can be seen that the variable porous media approach over predicted the total pressure drop by 35 percent and the momentum sink approach by 80 percent. The porous baffle approach under-predicted the total pressure drop by 25 percent.

Table 15: Pressure drop comparison with the 60° diffuser screen 2 (Pa)

		CFD pressure drop (Pa)	Pressure drop comparison	Measured Total Pressure Drop
1	Variable porous media with ALJ/ALK 0.01	261.35	34.63%	194.12
2	Variable porous media with ALJ/ALK 1	258.83	33.34%	
3	Baffle with alpha divided by 2	146.11	-24.73%	
4	Implicit momentum sink	349.63	80.11%	

It is possible that the over prediction of the pressure drop may be due to an incorrect representation of the flow through the screen. The variable resistance is limited by the

ratio of the screen thickness over the hole size as was shown in Figure 73. With thin screens, this ratio is very small and the resultant FAR limit that is imposed does not have a large influence on the screen resistance profile. With thicker screens however, this ratio becomes large with the FAR being limited to 0.05 over a rather large section of the screen as shown in Figure 88. Results are shown for the variable porous media approach where the ratio between ALI and ALJ/ALK was 0.01.

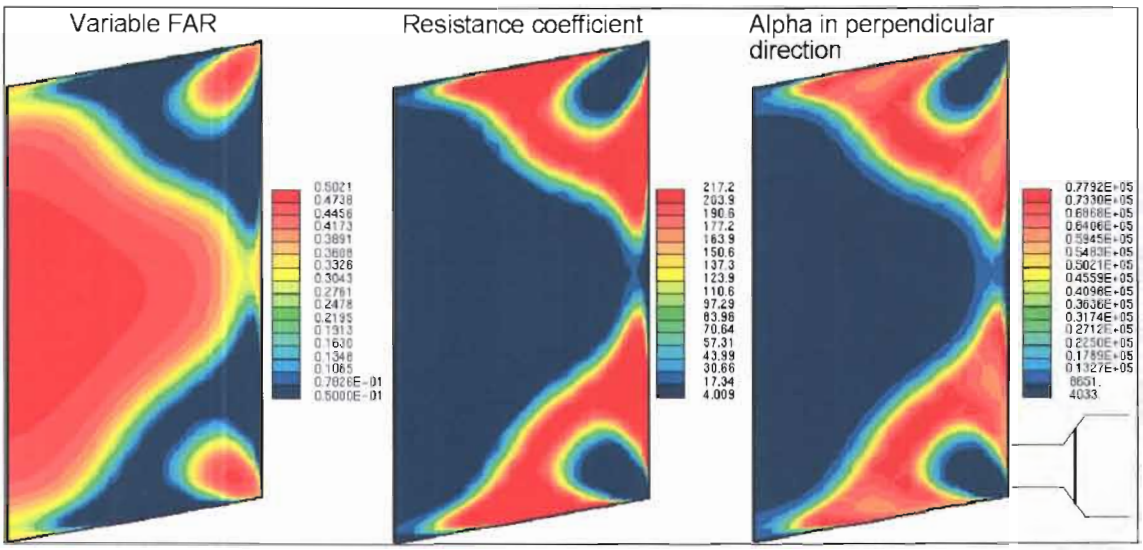

Figure 88: Scalars showing the calculated FAR and resistance factors of the screen

It can be seen that the FAR ranges between 5 and 50 percent (50 percent being the value for perpendicular flow). Compared to the thin screen discussed in the previous paragraph where the FAR ranged between 46 and 50 percent, it can be seen that the screen thickness has a major influence on the variable FAR. The variable resistance factor is increased from the perpendicular value of 3.98 to 217.2 where the maximum resistance calculated for the thin screen was only 5 (see Figure 86).

Figure 89(a) shows how flow with a large angle of incidence is allowed to pass through a thin screen with very little redirection of the flow. If flow at a similar angle of incidence passes through a thicker screen (b), then the flow is redirected with the exit angle significantly smaller than the angle of incidence. The change in effective flow area is the root cause for the higher pressure loss, which in turn forces the flow to straighten through the screen. It was believed that the definition of the variable resistance factor would accurately capture this phenomenon. However, the

requirement to impose limits on these resistance factors resulted in a limited application of this approach. The assumption made regarding the transversal resistance factors (see paragraph 7.2.4) may also have an influence on these results. Further research would be required to optimise the implementation of limits to ensure the accurate solution of the flow through screens with larger thickness.

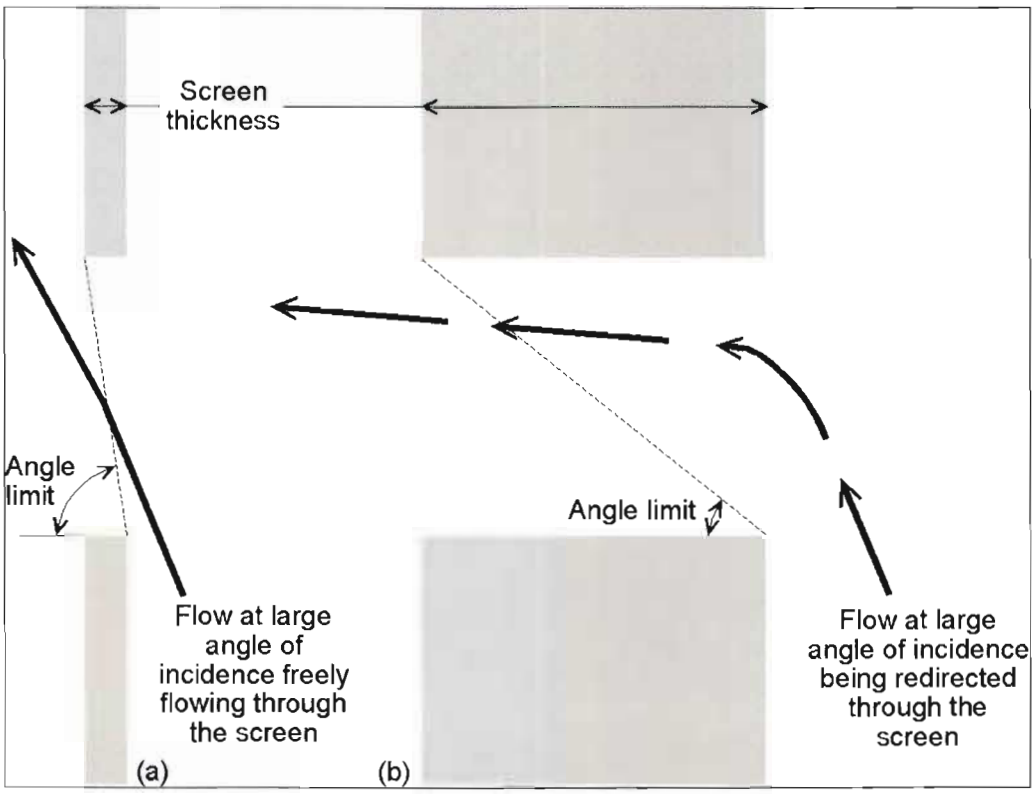

Figure 89: Flow passing through screens with different thicknesses

It can therefore be concluded that although the variable resistance approach does compensate for a change in screen thickness, it still does not accurately predict the pressure drop or flow profile across a thicker screen. It did however show an improvement from the conventional porous medium and porous baffle approaches (see Figure 87). Further research would however be required to improve on this approach especially for screens with larger thickness.

7.4.7 60° Diffuser: Screen Three (50 percent FAR, 0.5mm, 71mm pitch)

7.4.7.1 Comparison of flow profiles

From Figure 90 it can be seen that the flow profile is best predicted by the porous baffle approach. The momentum sink over predicts the higher flow near the walls while the porous medium does not predict an increase in the flow near the walls. The conventional porous medium approach shows the worst prediction of the flow profile. Based on these results, it can be concluded that the porous baffle approach shows the best prediction for a screen with 50% FAR given that the screen is very thin, i.e. the ratio between screen thickness and lattice size is smaller than 0.1.

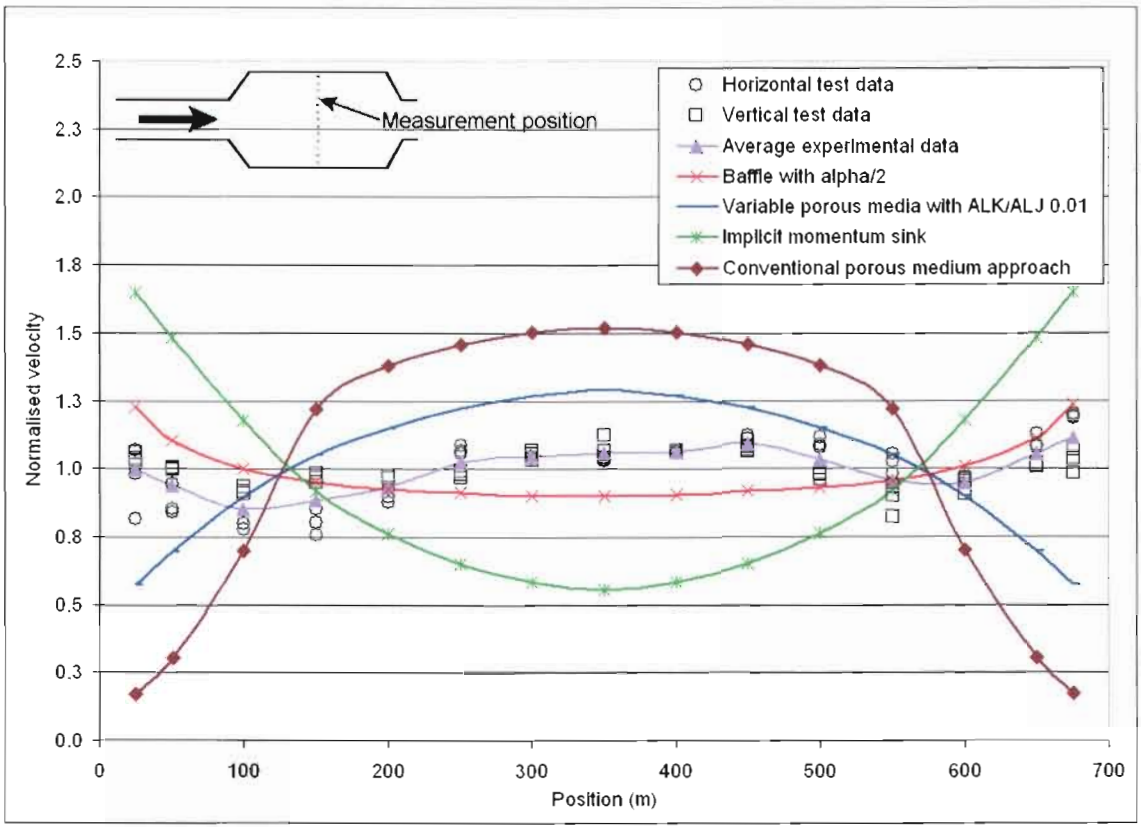

Figure 90: 60° diffuser central position with screen 3

7.4.7.2 Pressure drop prediction

In this instance, it was found that the porous baffle approach under-predicted the pressure drop by 27.3 percent, while the pressure drop is under-predicted by 16.7 percent and 17.9 percent for the other approaches respectively.

Table 16: Pressure drop comparison with the 60° diffuser screen 3 (Pa)

		CFD pressure drop (Pa)	Pressure drop comparison	Measured Total Pressure Drop
1	Variable porous media with ALJ/ALK 0.01	164.35	-17.91%	200.21
2	Baffle with alpha divided by 2	145.57	-27.29%	
3	Implicit momentum sink	166.84	-16.67%	

7.4.8 60° Diffuser: Screen Four (30 percent FAR, high resistance screen)

7.4.8.1 Comparison of flow profiles

Figure 91 shows that the CFD results did not predict the flow profile very well with the very high resistance screen. The momentum sink approach shows the best prediction, although the higher flow near the walls are over-estimated. Further research would be required to improve on the predicted CFD results.

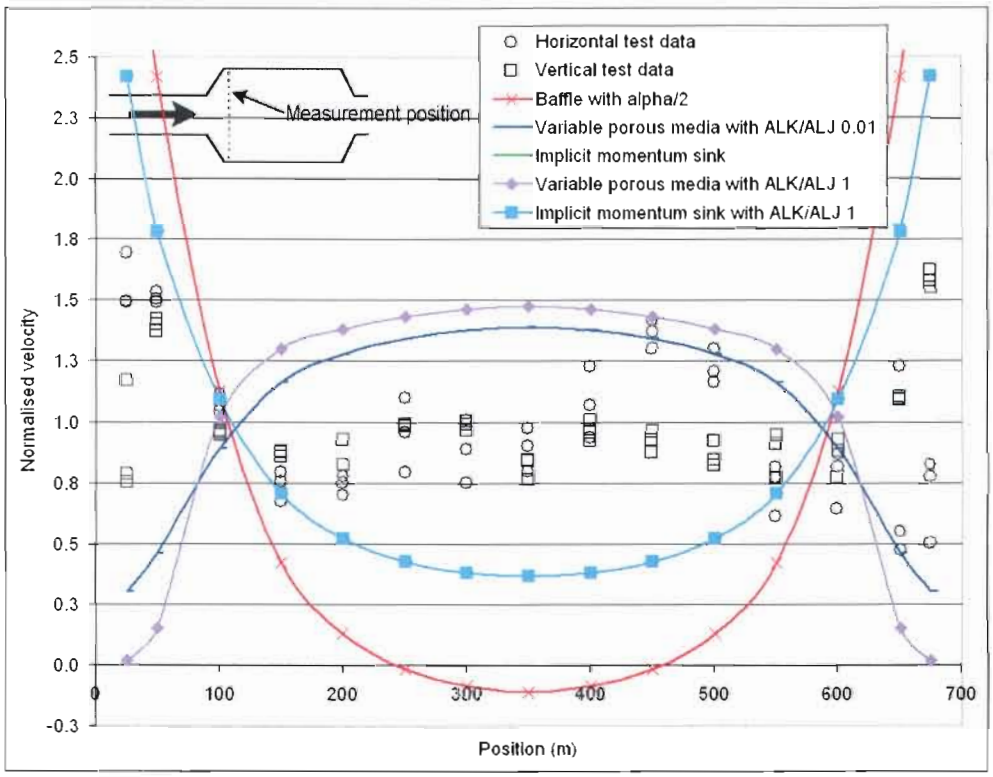

Figure 91: 60° diffuser frontal position with screen 4

7.4.8.2 Pressure drop prediction

Although the flow profile was not predicted very well, it can be seen that the pressure drop prediction was reasonably good with both the porous medium and momentum

sink approaches. The porous baffle approach showed an under prediction of 38.6 percent.

Table 17: Pressure drop comparison with the 60° diffuser screen 4 (Pa)

		CFD pressure drop (Pa)	Pressure drop comparison	Measured Total Pressure Drop
1	Variable porous media with ALJ/ALK 0.01	309.73	-8.94%	340.14
2	Variable porous media with ALJ/ALK 1	310.28	-8.78%	
3	Baffle with alpha divided by 2	208.81	-38.61%	
4	Implicit momentum sink	352.92	3.76%	
5	Implicit momentum sink with ALJ/ALK 1	352.97	3.77%	

7.4.9 60° Diffuser: Screen Five (70 percent FAR, low resistance screen)

7.4.9.1 Comparison of flow profiles

With the low resistance screen, the variable porous medium approach shows a very good prediction of the flow profile as shown in Figure 92. The porous baffle also shows a reasonably good correlation with the empirical data, but the momentum sink approach shows an under-prediction of the peak flow regions.

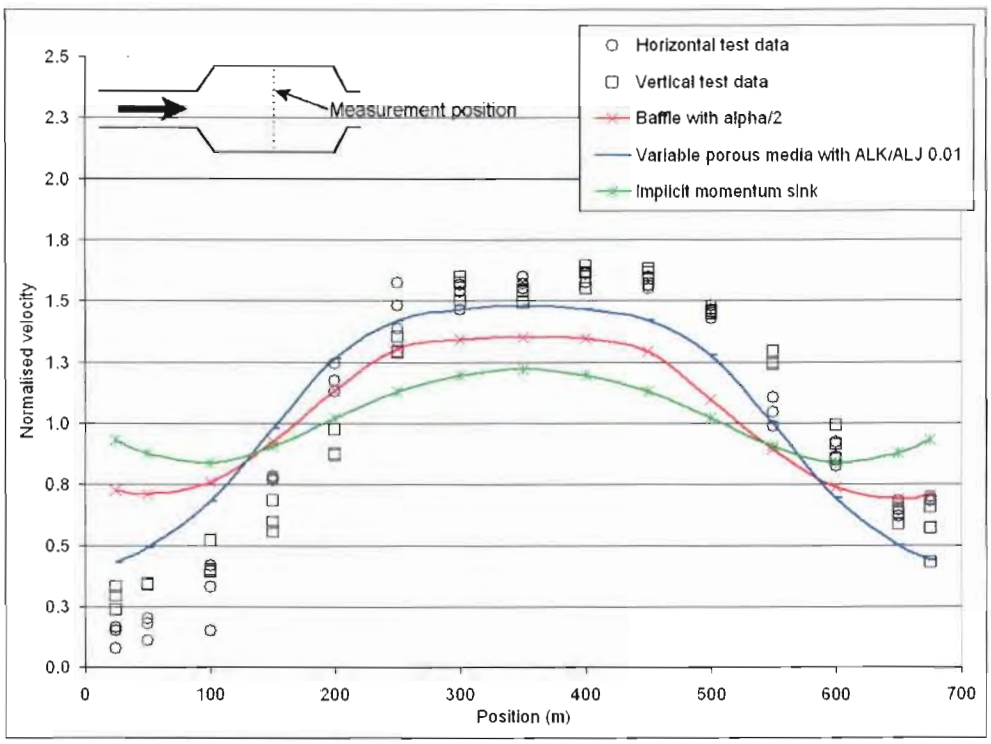

Figure 92: 60° diffuser central position with screen 5

7.4.9.2 Pressure drop prediction

Again the predicted pressure drop is under estimated between 7 and 11 percent.

Table 18: Pressure drop comparison with the 60° diffuser screen 5 (Pa)

		CFD pressure drop (Pa)	Pressure drop comparison	Measured Total Pressure Drop
1	Variable porous media with ALJ/ALK 0.01	146.62	-10.60%	164.0
2	Baffle with alpha divided by 2	152.44	-7.05%	
3	Implicit momentum sink	148.64	-9.36%	

7.4.10 120° Diffuser: Screen One (50 percent FAR, 0.5mm thickness)

With the 120° diffuser, the expansion of the diffuser is more abrupt than with the 60° diffuser. It was found in Chapter 5 that the flow separates from the walls if no screens are used in the diffuser resulting in an abrupt change in the flow profile. This section shows the measured flow profiles with the different screens in position and also presents the predicted CFD results with the different screen modelling approaches.

7.4.10.1 Comparison of flow profiles

From Figure 93 it can be seen that the momentum sink and porous baffle approaches do not predict the flow profile very well with an over estimation of the flow acceleration near the walls.

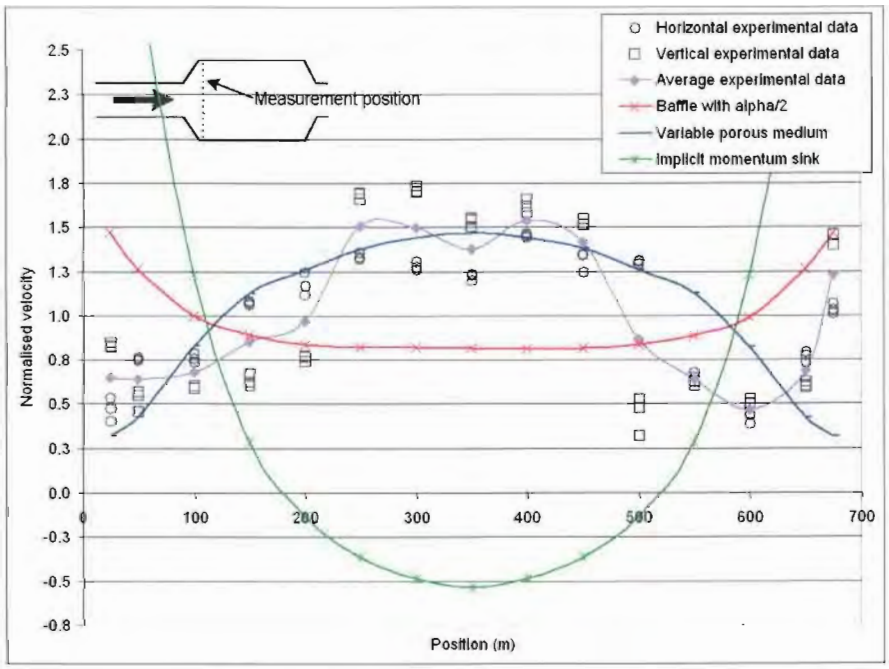

Figure 93: 120° diffuser frontal position with screen 1

In this instance, it was found that the variable porous medium approach shows a reasonably good correlation with the empirical data.

7.4.10.2 Pressure drop prediction

The variable porous medium approach under-predicted the total pressure drop by only 13.3 percent. Coupled with the good prediction of the flow profile, this approach shows a very good representation of the flow conditions downstream of the screen. The other approaches showed an under-prediction of 34 and 18.6 percent respectively.

Table 19: Pressure drop comparison with the 120° diffuser screen 1 (Pa)

		CFD pressure drop (Pa)	Pressure drop comparison	Measured Total Pressure Drop
1	Variable porous media with ALJ/ALK 0.01	201.61	-13.29%	232.52
2	Baffle with alpha divided by 2	153.37	-34.04%	
3	Implicit momentum sink	189.22	-18.62%	

7.4.11 120° Diffuser: Screen Two (50 percent FAR, 6mm thickness)

7.4.11.1 Comparison of flow profiles

It was found that the variable porous medium approach again shows the best prediction of the flow profile as shown in Figure 94.

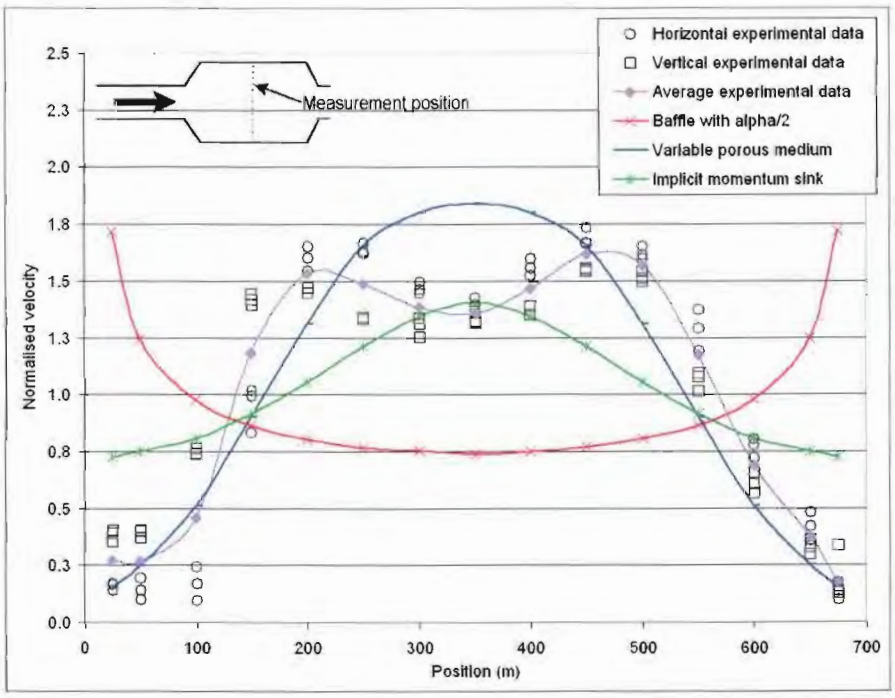

Figure 94: 120° diffuser central position with screen 2

This approach did however not predict the reduction of the flow in the centre of the duct. It can be seen that the momentum sink approach underestimated the large variation of the flow near the walls compared to the flow in the centre. The porous baffle approach showed a very poor prediction of the flow profile. This simulation was repeated with the ratio between ALI and ALJ/ALK set to 1, but it was found that the solution algorithm diverged. Even with the solution algorithm highly under relaxed it still diverged.

7.4.11.2 Pressure drop prediction

From Table 20 it can be seen that the variable porous medium approach over predicted the total pressure drop by 17.7 percent. This is still considered to be a reasonably good representation of the flow conditions downstream from the screen. The other approaches showed a poor prediction of the total pressure drop.

Table 20: Pressure drop comparison with the 120° diffuser screen 2 (Pa)

		CFD pressure drop (Pa)	Pressure drop comparison	Measured Total Pressure Drop
1	Variable porous media with ALJ/ALK 0.01	288.58	17.66%	245.27
2	Baffle with alpha divided by 2	153.23	-37.53%	
3	Implicit momentum sink	359.63	46.63%	

7.4.12 120° Diffuser: Screen Three (50 percent FAR, 0.5mm, 71mm Pitch)

7.4.12.1 Comparison of flow profiles

In this instance, it was found that the porous baffle approach showed the best prediction of the flow profile with the momentum sink approach over estimating the acceleration of the flow near the walls.

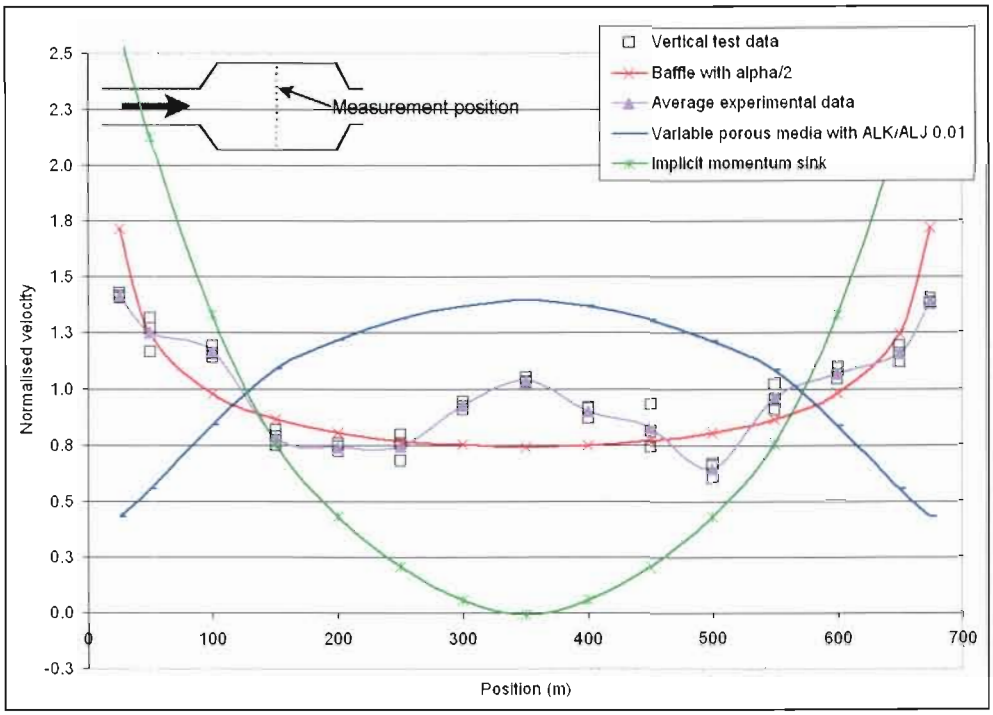

Figure 95: 120° diffuser central position with screen 3

7.4.12.2 Pressure drop prediction

Although the porous baffle approach showed a good correlation with the empirical flow profile, the total pressure drop was underestimated by 46.2 percent, which is considered a poor prediction. The other approaches also under predicted the pressure drop.

Table 21: Pressure drop comparison with the 120° diffuser screen 3 (Pa)

		CFD pressure drop (Pa)	Pressure drop comparison	Measured Total Pressure Drop
1	Variable porous media with ALJ/ALK 0.01	195.21	-31.27%	284.03
2	Baffle with alpha divided by 2	152.93	-46.16%	
3	Implicit momentum sink	178.89	-37.02%	

7.4.13 120° Diffuser: Screen Four (30 percent FAR, high resistance screen)

7.4.13.1 Comparison of flow profiles

It was found that both the momentum sink and porous baffle approaches highly over estimated the acceleration of the flow near the walls of the diffuser as shown in Figure

96. The best prediction of the flow profile was achieved by the variable porous medium approach although the acceleration of the flow near the walls were not accurately predicted. In an attempt to reduce the over prediction of the flow near the walls with the momentum sink approach, this simulation was repeated with the ratio between the perpendicular and transverse resistance factors set to 1. It was found that this change had no influence on the results.

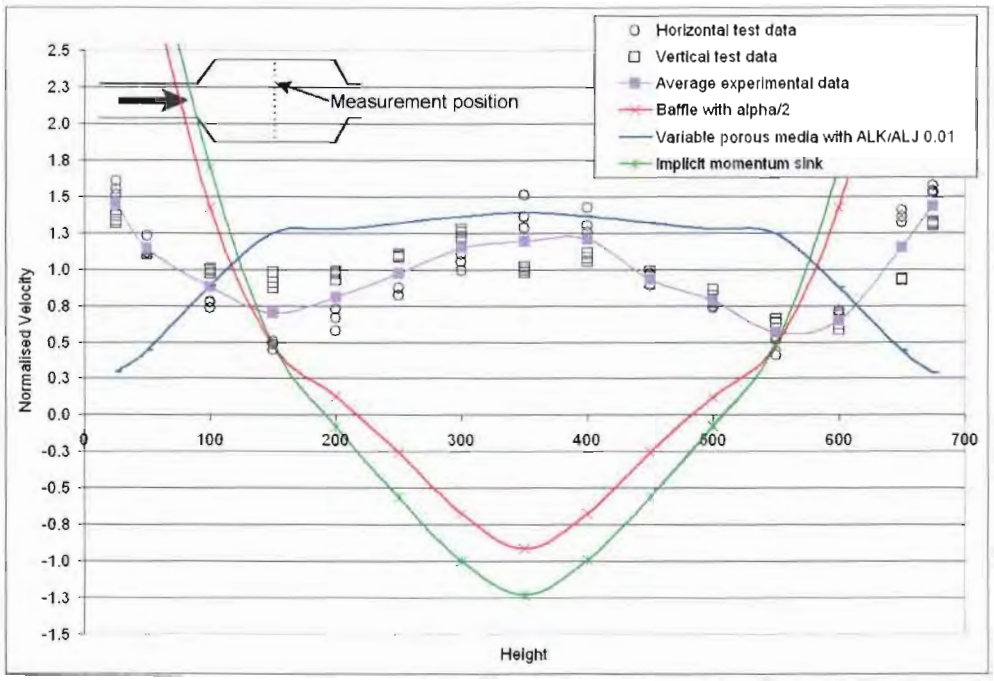

Figure 96: 120° diffuser central position with screen 4

7.4.13.2 Pressure drop prediction

Although the total pressure drop predicted by the different momentum sink approaches showed a correlation within 2 percent from the empirical value, the poor prediction of the flow profile makes this approach unacceptable.

Table 22: Pressure drop comparison with the 120° diffuser screen 4 (Pa)

		CFD pressure drop (Pa)	Pressure drop comparison	Measured Total Pressure Drop
1	Variable porous media with ALJ/ALK 0.01	318.44	-18.49%	390.67
2	Baffle with alpha divided by 2	222.73	-42.99%	
3	Implicit momentum sink	384.78	-1.51%	
4	Implicit momentum sink with ALJ/ALK 1	384.78	-1.51%	

The variable porous medium showed an under prediction of 18.5 percent and combined with the relatively good correlation achieved with the flow profile in the central region, it shows the best results for this screen although the comparison is still not satisfactory.

7.4.14 120° Diffuser: Screen Five (70 percent FAR, low resistance screen)

7.4.14.1 Comparison of flow profiles

It was found that the variable porous medium approach showed an excellent correlation with the empirical data as shown in Figure 97. Both the other approaches under predicted the higher flow in the centre of the diffuser section.

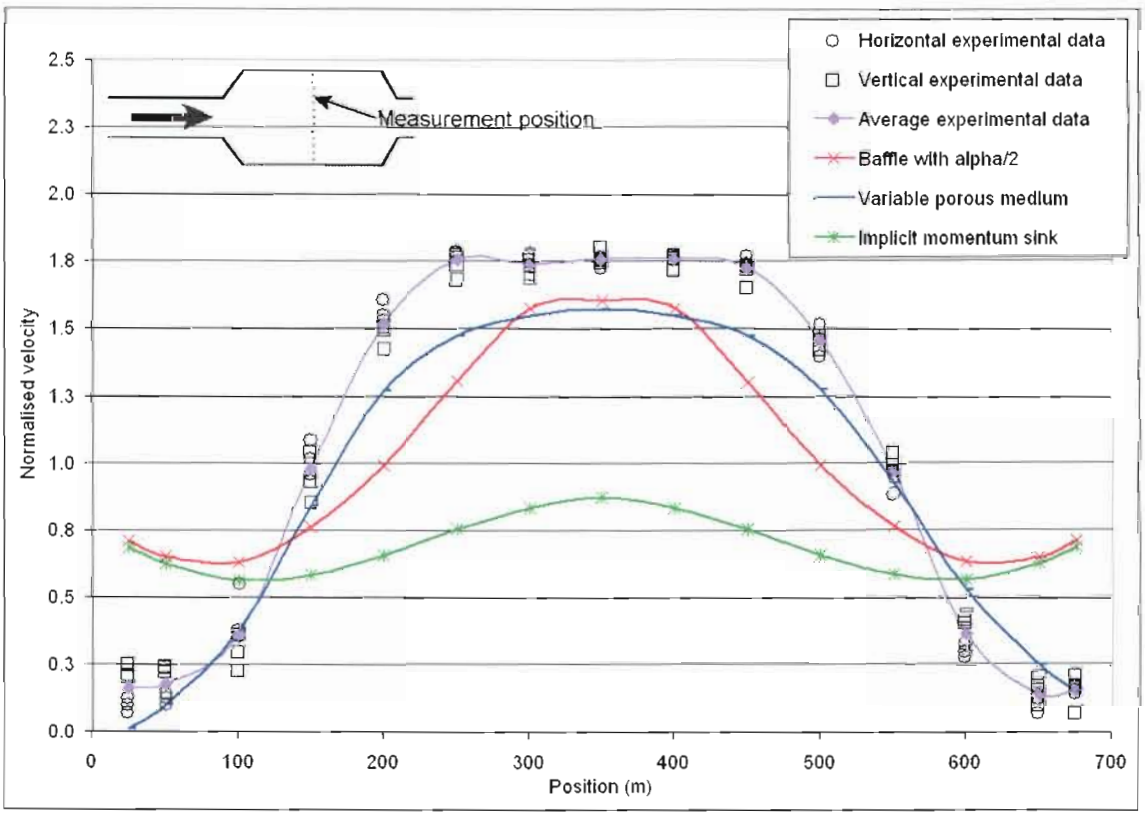

Figure 97: 120° diffuser central position with screen 5

7.4.14.2 Pressure drop prediction

Table 23 shows that all three approaches under predicted the pressure drop by a margin ranging between 30 and 35 percent.

Table 23: Pressure drop comparison with the 120° diffuser screen 5 (Pa)

		CFD pressure drop (Pa)	Pressure drop comparison	Measured Total Pressure Drop
1	Variable porous media with ALJ/ALK 0.01	151.32	-30.33%	217.19
2	Baffle with alpha divided by 2	140.52	-35.30%	
3	Implicit momentum sink	142.98	-34.17%	

7.4.15 Grid (mesh) independence

Although grid independence was discussed in Chapter 5, a new grid was generated for this chapter and therefore it was required to again ensure grid independence. Independence of the numerical mesh should be investigated with finer and coarser grids. It is not very easy to reduce the number of cells in a given flow domain without recreating the complete model. A simple method to test a coarser screen is to run the simulation with a first order discretisation scheme (e.g. UD) instead of the higher order MARS scheme that was used for all the simulations. In order to test a finer grid, the model shown in Figure 79 was refined in all three cell based directions (2*2*2) resulting in a mesh that is eight times finer. With such a refinement, it is important to ensure that y+ values are still within the allowable limits. Since the boundary cells were refined twice, the y+ values were reduced from approximately 100 to 50, which is still above the lower limit of 30. The total number of cells after this refinement was approximately 1.2 million cells. Considering the small section of duct simulated by this model, this is considered to be an extremely fine mesh for this application.

Results with the MARS discretisation scheme revealed a peculiar unsteady flow pattern as shown in Figure 98. These tests were repeated with the UD discretisation scheme on the fine mesh and it was found that the unsteady flow pattern disappeared. The results obtained with the refined model and the MARS scheme may be due to the extremely high level of refinement coupled to the highly turbulent nature of the flow downstream of the diffuser. Due to the sensitive nature of information regarding the MARS scheme, very little is known about the characteristics of the scheme. It is believed however that the unstable behaviour may be due to un-boundedness introduced by the downstream component of the MARS scheme, being a higher order discretisation scheme.

It was found that this model was very unstable and would not converge further than 1e-2. This can be contributed to the fact that the instability of the recirculation zones in the diffuser is better simulated by the fine mesh. With the coarser mesh, numerical diffusion smoothes out these instabilities resulting in a more stable solution algorithm. From the results shown in Figure 98 it can be seen that the results obtained show a highly irregular flow pattern, which is considered to be unphysical. A more stable solution algorithm may be achieved if the solution algorithm is highly under relaxed. Based on this flow pattern, it was thought however that results will not show an improved correlation with the physical data. It can therefore be concluded that the refinement of the numerical model is optimal and that further refinement will most likely not result in a significant improvement in the predicted results.

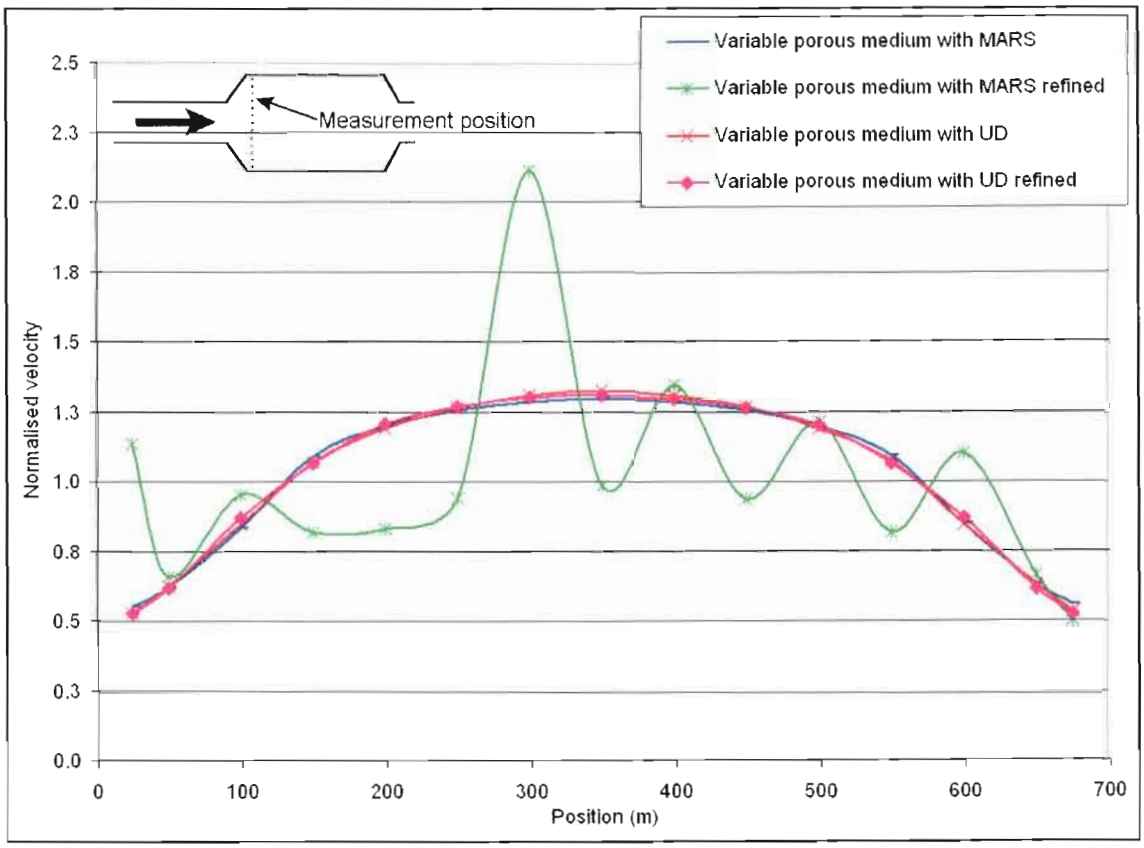

Figure 98: Grid independence study results

7.5 Summary

7.5.1 Preparation and development

The first part of this chapter focused on the preparation and development work that were conducted before the CFD simulations of the screens could commence. This

section discussed the user coding that was developed and the programming methodology that was adopted. All user coding that was developed for this study are presented in ANNEXURE E.

A study was conducted into the convergence behaviour of the diffuser type Star-CD model with the porous medium approach included in the model. The following conclusions were made from this study:

- It was found that the lowest residual values were obtained with the solution algorithm convergence set to 0.5, 0.2, 0.5.
- The instability in the simulation algorithms was significantly reduced with the removal of the atmospheric pressure boundary. The best results were achieved with a fixed mass flow inlet boundary coupled with a standard outlet boundary that is removed far enough away from the diffuser section not to have inflow at this outflow boundary due to the recirculation zone behind the diffuser.
- It was found that the refinement of the mesh immediately upstream and downstream of the screen resulted in a more stable solution algorithm. It is recommended that at least four cells should be refined to a similar thickness as the screen cells.
- It was also found that the refinement of the cells in the region of the diffuser expansion resulted in a better and more stable solution algorithm of the flow separation in the diffuser.
- It was found that the ratio between the perpendicular and transverse resistance factors could not be lower than 0.01 for the solution algorithm to remain stable.
- Finally, it was found that the thickness of the porous medium in the perpendicular direction should not be thinner than the screen thickness.

The first section of this chapter also discussed the different possible approaches to the problem of defining a variable resistance to simulate the flow across a screen in a diffuser and finally commented on the limitations that are applicable for the coding.

7.5.2 Discussion of results

The second part of this chapter presented the results that were obtained from the experimental and CFD studies and also discussed the correlation between the empirical data and the different CFD methodologies.

A number of different possible approaches were investigated with the first screen and it was concluded that the porous baffle approach with $\alpha=k/4$ showed a reasonably good correlation with empirical results while the best correlation was achieved by the momentum sink approach for the thin 50 percent FAR screen in the 60° diffuser. Furthermore, the total pressure drop was under predicted by a margin ranging between 10 and 25 percent with the cases that reached convergence. The following conclusions were made from these results:

- For the application in this study, the difference between the standard high Reynolds number k-ε turbulence model and the RNG turbulence model was negligible. This finding is consistent with results obtained where no screens were included in the diffusers. It should however be noted that the RNG turbulence model is a derivative of the k-ε model. It is therefore recommended that the influence of turbulence models should be investigated with later versions of Star-CD when higher order turbulence models become available.
- It was found that the influence of the turbulent intensity (user setting for the porous medium approach) is negligible.
- It was found that the variable porous medium approach showed better results than the conventional porous medium approach.
- Furthermore, it was found that the porous baffle approach where $\alpha=k/4$ showed a better correlation with the empirical data than the conventional approach (where $\alpha=k/2$).
- The introduction of a momentum sink in the Navier Stokes equations introduced an instability in the code that required severe under-relaxation of the solution algorithm (i.e. 0.3, 0.1, 0.3).
- It was also found that the explicit momentum sink approach resulted in an unphysical solution of the flow field with the solution algorithm diverging after 2300 iterations.
- Even with the low relaxation values, it was found that the implicit approach converged after 1000 iterations and that the predicted flow field and pressure drop showed a very good correlation with the empirical data.

From the results of the first screen (50 percent FAR with 0.5mm thickness), the following recommendations were made for the remainder of the simulations:

- The standard k-ε high Reynolds number turbulence model was recommended.

- All further simulations should be conducted with the ratio between the perpendicular (ALI) and transverse resistance coefficients (ALK/ALJ) set to 0.01.
- Since the turbulent intensity setting for the porous media did not have a significant influence on the results, it is recommended that all further simulations be conducted with the default value of 0.1

Based on the above discussion, it was decided to choose a solution method that showed the best results from each of the three approaches, i.e. porous baffles, porous media and momentum sinks. The following simulations were therefore included for the remainder of the screens:

- Porous baffle with $\alpha=k/4$.
- Variable resistance porous media with ALJ and ALK set to 0.01 of ALI.
- Implicit momentum sink approach with the correction factor to compensate for the under-prediction of the momentum sink term.

Results with the thicker screen (12 times the thickness of screen 1) did unfortunately not show a very good correlation with the empirical data. The poor prediction of the flow field downstream of the screen was contributed to fact that the coding could not accurately compensate for the change in flow direction through the thicker screen. It was believed that the definition of the variable resistance factor would accurately capture this phenomenon. However, the requirement to impose limits on these resistance factors resulted in a limited application of this approach. Further research would be required to optimise the implementation of limits to ensure the accurate solution of the flow through screens with larger thickness.

It can therefore be concluded that although the variable resistance approach does compensate for a change in screen thickness, it still does not accurately predict the pressure drop or flow profile across a thicker screen. It did however show an improvement from the conventional porous medium and porous baffle approaches. Further research would however be required to improve on this approach especially for screens with larger thickness. Thin screens are defined as having a ratio between lattice size and thickness exceeding a value of 10.

Furthermore, it was found that none of the CFD results predicted the flow profile very well for the very high resistance screen (i.e. 30 percent FAR). The momentum sink approach showed the best prediction, although the higher flow near the walls were over estimated. Further research would be required to improve on the predicted CFD results with higher resistance screens.

In general, it can be concluded that at least one of the three approaches tested in this study showed a reasonably good prediction of the flow field downstream of the screen for *thin* screens with FAR's exceeding 50 percent. It was found that the total pressure drop was under predicted by an average value of approximately 25 percent for these screens. For screens with larger thickness or higher resistance (i.e. 30 percent FAR), it was found that the CFD models did not predict the flow profile or pressure drop very well. It was however concluded that the newly developed approaches did show an improvement to the conventional methods used.

The experimental procedures focused on the flow distribution downstream of the screen. Based on results from this study, it was recognised however that the flow distribution between the start of the diffuser and the screen has a major influence on the distribution downstream of the screen. To improve the accuracy of numerical models, it would be required to improve the experimental procedures in order to accurately measure the flow profiles just upstream of the screen and compare this empirical data with results from the numerical methods.

Although a single numerical approach could not be found that accurately predicted the flow profile for all screens tested, results from this study serves as a foundation for further research into this field.

The following chapter summarises the conclusions based on the research and development that is presented by this study and also discusses the contribution made and practical applicability of the research performed. Recommendations are also made on possible future work and further research required.

CHAPTER 8: CONCLUSIONS AND RECOMMENDATIONS

8.1 Summary

Chapter 1 provided an overview of the problem statement and the relevant background pertaining to the physical area of application. The problem statement was discussed in detail referring in short to the literature that was most relevant to the background and definition of the problem statement. The importance of this research was outlined and the delimitations applicable to this study were listed.

Chapter 2 presented an in depth discussion into the literature survey conducted for this study. This discussion investigated the relevance of previous studies, the applicability to this study and also commented on the methodologies that were adopted from the relevant literature. Although flow through screens has been well researched and documented, it was found that the notion of variable resistance coefficients was only investigated by Hoffmann in recent years (2002). No literature could be found on the use of momentum sink terms for the simulation of flow through screens.

Chapter 3 investigated the feasibility of modelling screens in detail and the practical implications of detailed modelling. In this discussion, it was shown why it is necessary to devise mathematical models to simulate screens in a diffuser rather than modelling screens in detail. It was concluded that the modelling of screens in detail is not economically viable hence the need to develop and test mathematical models.

Chapter 4 discussed the design, construction and commissioning of a low speed wind tunnel. This discussion included the test setup and test procedures, correlation of empirical data with literature and dynamic similarity of the wind tunnel. It was shown that empirical data obtained from this wind tunnel compared very well with results from the literature. Furthermore, it was shown that these results were repeatable and the experimental error was calculated to be less than 3 percent for flows with a Reynolds number exceeding $1*10^5$. For flows with a lower Reynolds number, the error was calculated to be approximately 9 percent. Since all the experimental data was obtained

with flows higher than a Reynolds number of $1*10^5$, it was concluded that the error of 3 percent is acceptable.

Chapter 5 investigated the modelling of flow separation in wide-angle diffusers if no screens are used to distribute the flow. The discussion first focussed on the detail of the CFD model used for this study and then elaborated on the modelling approach adopted. The sensitivity of the results to mesh refinement was investigated and the application of modelling assumptions was discussed. The remainder of this chapter focused on the influence of numerical assumptions (i.e. turbulence models, numerical discretisation schemes and localised cell refinement) on the accurate prediction of the separation and re-attachment of the flow for different diffuser angles.

Chapter 6 presented a detailed discussion on the mathematical and numerical methodology that was proposed as the solution to the definition of variable resistances through screens. The discussion also included an introduction on writing and compiling the user defined functions that formed part of the hypothesis.

Chapter 7 was divided into two main sections with the first discussing the preparation and development that was required before the CFD simulations could commence. The second part presented the empirical and numerical results obtained and investigated the correlation between these results. Results showed that no single model could accurately predict the flow profiles for all the screens included in this study.

8.2 Conclusions

It was the objective of this research to investigate advanced methodologies for the mathematical simulation of screens in wide-angle diffusers and to find possible solutions for the implementation of variable resistance coefficients. The feasibility of modelling screens in detail was investigated and it was found that this approach would not be economically viable and that it is therefore required to develop mathematical models that would accurately predict the flow conditions down stream from a screen in a diffuser.

In order to achieve this objective, it was firstly required to construct and commission a low speed wind tunnel to obtain experimental data that could not be found in literature.

Based on a correlation to literature, it was concluded that results from this experimental facility were accurate to within 3 percent at Reynolds numbers exceeding $1*10^5$ and that results were repeatable to a very high standard of 98.9 percent. The most significant conclusion was that experimental testing is not easily accomplished and that even with a relatively simple geometry such as the one used in this study, small imperfections, such as alignment of components, can result in significant errors in measurement.

From the literature study, it was found that experimental data on flow through wide-angle diffusers is very limited and therefore it was required to digress from the original aim of this study in order to investigate the modelling techniques that would be required to accurately simulate flow through wide-angle diffusers with no screens to distribute the flow. Results from this study were used for the remainder of the CFD simulations.

From the study into the influence of numerical modelling parameters on the flow through wide-angle diffusers it was concluded that the discretisation scheme had a significantly larger influence on the results than the turbulence model used. It should however be noted that the turbulence models included in the version of Star-CD used in this study (i.e. version 3.15 for Windows) are all derivatives of the standard k-ε model. It was proposed that the higher order MARS discretisation scheme should be used together with the standard k-ε model.

Through the literature survey, it was found that three possible methods could be used to simulate screens, i.e. porous baffles (planar resistances), porous media or negative momentum source terms. No literature could be found on the momentum source term approach and it was required to conduct further study into the theory and application of momentum source terms specifically relating to this application.

The following conclusions were made regarding the accurate prediction of the flow distribution downstream of the screen:

- It was found that none of the CFD results predicted the flow profile very well for the very high resistance screen (i.e. 30 percent FAR). The momentum sink approach showed the best prediction, although the higher flow near the walls were over

estimated. Further research would be required to improve on the predicted CFD results with higher resistance screens.

- With the 120° diffuser, only the variable porous medium approach showed similar trends to the experimental data although it failed to predict the flow profile precisely.
- Results showed that no single model could accurately predict the flow profiles for all the screens included in this study.
- The porous baffle approach showed an improved prediction of the flow field downstream of the screen for *thin* screens with FAR's exceeding 50 percent when compared to conventional methods. Thin screens are defined as having a ratio between lattice size and thickness exceeding a value of 10. For screens with increased thickness or higher resistance (i.e. 30 percent FAR), it was found that the CFD models did not predict the flow profile or pressure drop very well.
- It was found that the influence of screen thickness could not yet be simulated accurately since numerical results for the thicker screen did not compare very well with the experimental data. It was found that the variable porous medium approach showed the best correlation with both the 60° and 120° screens.
- The variable porous medium approach also showed very good correlation with the experimental data for the 70 percent FAR screens with both the 60° and 120° screens.

It was found that the total pressure drop was under-estimated by an average value of approximately 25 percent for screens with a FAR exceeding 50 percent. The pressure drop was severely underestimated for high resistance (30 percent FAR) screens reporting errors of up to 45 percent.

The experimental procedures focused on the flow distribution downstream of the screen. Due to the geometry of the diffuser it was found that the flow is very unstable in the region between the start of the diffuser and the screen. This is the result of unsteady flow separation in this region. With the uncertainty of the flow direction in this area, specialised measuring equipment would be required to gain a better understanding of the flow through this region. Using this experimental data for correlation, it would be required to investigate the prediction of the flow through this region by different turbulence models.

It can be concluded that this study achieved the objective of investigating advanced methodologies for the simulation of flow through screens in wide-angle diffusers. Furthermore it succeeded in finding possible solutions for the modelling of these screens, however with limited success. From the comparison with experimental data, it is clear that further research would be required to improve on the models developed during this study. It is recommended that higher order turbulence models should be investigated for the modelling of the flow through the diffuser with- and without screens in place. Results from this study also provided a better understanding of the behaviour of the flow through these diffusers with- and without screens in place. Higher order closure models (like Reynolds stress) would probably be required to gain a better understanding of the flow pattern. The k-ε model and its derivatives will by nature fail to predict such flows successfully, since they all assume isotropic turbulence.

This study also investigated additional methodologies (referring to the different momentum sink approaches) that were not included in the original scope in order to gain a better understanding of the problem and to supply alternative methods.

8.3 Research contribution

Based on the outcome of this study the following research contributions were made:

(i) During the experimental phase of this project, various measuring and flow visualisation techniques were investigated. This research can be used to simplify experimental studies where similar results are investigated.

(ii) Since literature on modelling techniques in wide angle diffusers was very limited, it was required to conduct a study into the behaviour of flow through diffusers where no screens are included in order to determine the influence of modelling parameters such as turbulence models and discretisation schemes. Based on this research, certain conclusions were made (see paragraph 8.2) on the influence of turbulence models and discretisation schemes that may be applicable to other areas of flow research where abrupt expansion of the flow is simulated.

(iii) Results from the study conducted into the convergence behaviour of the solution algorithm when simulating wide-angle diffusers can be used to achieve more stable solutions of any relevant CFD application.

(iv) The investigation into momentum source terms can be used as the basis for further research into the simulation of screens. This research can also be used in all applications where the momentum source approach is required as an alternative when the porous medium approach does not comply with the limitations imposed by the specific CFD code being used.

8.4 Practical use and applicability of this research

Although a single numerical approach could not be found that accurately predicted the flow profile for all screens tested, results from this study can serve as a foundation for further research into this field. It is believed that the proposed methods can be optimised to accurately predict the flow conditions downstream from all screens through further research

Both the porous baffle and variable porous medium approaches showed improved results (when compared to conventional methods) for screens with a lower resistance (i.e. exceeding 50 percent FAR) and screens where the ratio between the screen thickness and the lattice size does not exceed 10 percent.

Measured pressure drops and flow profiles can be used in industry and as correlation for future studies.

8.5 Recommendations for further research

The following recommendations are made:

- Flow profiles were not measured directly in front of the screen and it is recommended that a study be conducted to investigate the flow profiles between the inlet to the diffuser and the screen. This is required to investigate the flow patterns in this region and to compare experimental data with numerical data using different turbulence models and discretisation schemes. It should however be noted that it could potentially prove problematic to measure this flow profile due to the uncertainty of the flow angle. A different approach than the pitot static tube would therefore be required.
- Where the screens were placed in the centre of the diffuser for this study, it is recommended that these tests be expanded to also include screens at the end

(largest part) and front (smallest part) of the diffuser. Further research should also investigate other locations in the inlet cone. The objective should be to develop a fairly universal model.

- Further research should investigate other types of screens, e.g. round wire meshes and expanded metal screens.
- This study focused only on steady state simulations. Due to the unsteady nature of the flow through the diffusers, it is recommended that transient simulations should also be conducted.
- All the turbulence models tested in this study are derivatives of the standard k-ε model. It is recommended that the influence of the latest turbulence models such as v2f is tested. Furthermore, it is advised that higher order turbulence models such as Reynolds Stress or even LES be investigated. This is recommended for cases with and without the screen in place in the diffuser.
- Due to time constraints, this study only included screens that represented the upper and lower spectrum of a certain parameter, e.g. the thickness was tested at 0.5mm and 6mm (12 times difference). It is recommended that intermediate values should also be tested to investigate the trend of results.
- Similarly, only two diffusers (i.e. a 60° and a 120° diffuser) were included in this study. It is recommended that these tests should be repeated with a 90° diffuser as well.
- Further research would be required to improve the variable resistance approach for screens with a larger thickness.
- Further research would be required to improve the predicted CFD results for screens with higher resistance.
- It is also recommended that the UDF's developed in this study be tested in a different CFD code.

☆ ☆ ☆ ☆ ☆ ☆ ☆ ☆ ☆ ☆

BIBLIOGRAPHY

ADAPCO 2002. ADAPCO ONLINE PUBLICATION: Turbulence modelling, 11 April 2002. [Available on Internet:] http://www.adapco-online.com/feature_arts/turbulence/turb.html

AIRFLOW DEVELOPMENTS LIMITED. Pitot static tube. Leaflet No. AI 133/984.

ANDERSON, D.C., TANNEHILL, J.C., PLETCHER, R.H., 1984. *Computational fluid mechanics and heat transfer.* Hemisphere Publishing Corporation: ISBN: 0-89116-471-5.

APPARATEBAU ROTHEMüHLE. 1999. *General Sales and Marketing brochure.*

BLEVINS, R.D. 1984. *Applied Fluid Dynamics Handbook.* New-York: Van Nostrand Reinhold Company Inc.

BOSCH, F.J. 1993. *Particulate Emission Control Technology evaluation and database*, Eskom Report No TRR/P93/034, July 1993.

BRUNDRETT, E. 1993. Prediction of Pressure Drop for Incompressible Flow Through Screens. *Journal of Fluids Engineering*, vol. 115, pp. 239-242.

BUDOFF, M. and ZORUMSKI, W.E. 1971. Flow resistance of perforated plates in tangential flows. *NASA Technical Memorandum*, No. X-2361, p. 1-11.

CRAIG, K. J., VENTER, P.J., DE KOCK, D. J. AND SNYMAN, J.A., 1998. Optimisation of structured grid spacing parameters for separated flow simulation using mathematical optimisation. *Journal of Wind Engineering and Industrial Aerodynamics*, 80 (1999), p. 221-231.

ECKERT, B. and PFLUGER, F. 1941. The resistance coefficient of commercial round wire grids. *Luftfahrtforschung*, vol. 18, no. 4, pp. 1-11.

ELDER, J.W. 1959. Steady flow through non-uniform gauzes of arbitrary shape. *Journal of Fluid Mechanics*, 5:355-363.

FERZIGER, J. H. AND PERIĆ, M. 2002. *Computational methods for fluid dynamics*. 3rd revised edition. Springer: Berlin, Germany.

FLUENT INC. Version 6.1 2003, *Users guide*, Section 6.19.

FRIED, E. AND IDELCHIK, I.E. 1989, *Flow resistance: A design guide for Engineers*, United States of America: Hemisphere Publishing Corporation, ISBN-89116-435-9.

GIBSON, D. 1992. *Boiler Erosion*. Eskom Technology Research and Investigations, Report reference: TRR/P92/118.

GIBSON, D., SCHMITZ, W. 1999. *Electrostatic Dust Precipitator Skew Gas Flow Technology reduces Particulate Emissions*, *In* INT-PEC International Power and energy conference, Monash University Gibsland, Australia 1999.

GIBSON, D. 2002. *A summary of the cold air velocity distribution investigations conducted within units 1, 2 and 6 Boilers at Matimba Power Station*, Eskom Report No TRR/P93/070, August 2002.

GIECK, K. and GIECK, R. 1990. *Technical Formulae*. 7th Ed. Gieckverlag Germering: West-Germany.

HOFFMANN, J. 2002. *Porosity models for expanded metal screens*, Eskom Research Report RES/RR/01/14809, August 2002.

HOLMAN, J.P. 1978. *Experimental methods for engineers*. 5th Ed. Singapore: McGraw-Hill, ISBN 0-07-029601-4.

HOLMAN, J.P. 1989. *Heat Transfer*. SI Metric Edition. Adapted by Dr. P.N. Rao, Singapore: Mc Graw-Hill.

HORVATH, A.L. 1975. *Physical Properties of Inorganic Compounds (SI Units)*. London: Edward Arnold Ltd.

IACCARINO, G, 2000. *Prediction of the turbulent flow in a diffuser with commercial CFD codes*, Centre for turbulence research, Annual Research briefs 2000.

IDELCHIK, I.E. 1986. *Handbook of Hydraulic Resistance*. 2nd Ed. Translated by E. Fried, Washington.

IDELCHIK, I.E. 1996. *Handbook of Hydraulic Resistance*. 3rd Ed. Translated by G.R. Malyavskaya, A. V. Luikov Heat and Mass Transfer Institute, Minsk. Published in the United States of America: Begell house, Inc., ISBN 1-56700-074-6.

JANSE VAN RENSBURG, J. J. 1997. *A comparison between experimental and numerical modelling of flow through screens*. M. Dip. Tech. Dissertation. Pretoria: Technikon Pretoria.

JAPIKSE, D., BAINES, N.C., 1998. *Diffuser design technology*, United States of America: Concepts ETI, Inc.

KOO, J.K., JAMES, DAVID.F. 1973. Fluid flow around and through screens. *Journal of Fluid Mechanics*, vol. 60, part 3, p. 513-538.

LAURENCE, D.R., URIBE, J. C., UTYUZHNIKOV, S.V. 2003. A robust formulation of the v^2-f model.

LIVESEY, J.L., LAWS, E.M. 1972. Simulation of Velocity Profiles by Shaped Gauze Screens. *AIAA Journal*, vol. 11, no. 2, p. 184-188.

LIVESEY, J.L., LAWS, E.M. 1973. Flow through non-uniform gauze screens. *Journal of Fluid Mechanics*, 59: 737-743.

LIVESEY, J.L., LAWS, E.M. 1978. Flow through screens. *AIAA Journal*, vol. 11, no. 2, p. 184-188.

MANGLIK, R., WHITE, F. M. 1999. *Fluid Flow Data book.* General Electric Company. United States of America: Genium Publishing Corporation, ISBN 0-931690-02-1.

Mc CARTHY, J.H. 1964. *Steady flow past non-uniform wire grids.* Hydrodynamics Laboratory, David Taylor model basin, Washington.

MOORE, C.A., KLINE, S.J. 1958. *Some effects of vanes and of turbulence in two-dimensional wide-angle subsonic diffusers.* National Advisory Committee for Aeronautics (NACA), Technical note No. 4080.

MILLER, D.S. 1978. *Internal Flow Systems.* BHRA Fluid Engineering Series, BHRA Fluid Engineering, vol. 5.

NAUDIN, J.L. September 26th 1999. *The Coanda effect.* [Available on Internet:] http://www.jnaudin.free.fr/html/coanda.htm

NIEMAND, H.J., 2003. *A methodology for estimating uncertainty and sensitivity in thermal-fluid simulations.* M-Tech dissertation. Vaal Triangle Technikon: Vanderbijl Park, South Africa.

PATANKAR, S.V., 1980. *Numerical Heat Transfer and Fluid Flow.* Series in Computational Methods in Mechanics and Thermal Sciences. W.J. Minkowycz and E.M. Sparrow. Editors. Hemisphere publishing corporation: United States of America. ISBN: 0-89116-522-3.

PINKER, R.A., HERBERT, M.V. 1967. Pressure loss associated with compressible flow through square-mesh wire gauzes. *Journal of Mechanical Engineering*, Sci. 9:11-23.

PLINT, M.A., BÖSWIRTH, L. 1978. *Fluid mechanics: A laboratory course.* London and High Wycombe: Charles Griffin & Company.

RAASK, E. April 23 1969. *Tube erosion by ash impaction.* Wear - Elsvier Sequoia S.A., Lausanne, Central Electricity Research Laboratories, Leatherland, Surrey, Great Britain.

RASKIN, J. 1994. *Coanda effect: Understanding why wings work.* [Available on Internet:]
http://humane.sourceforge.net/published/coanda_effect.html

SAHIN, B., WARD-SMITH, A.J. 1991. Flow control by perforated plates using a blanking technique in wide-angle diffusers employed in practical electrostatic precipitator systems. *Journal of Wind Engineering and Industrial Aerodynamics.* 37: 269-284. Amsterdam (Netherlands): Elsevier Science Publishers B.V.

SCHMITZ, W., PRETORIUS, L., VAN NIEKERK, A. AND LALLA, T. J. 1998. *Modelling of screens within industrial flow applications. In* Proceedings of the 2nd South African Conference on Applied Mechanics (SACAM). 13-15 January, 1998. Vol. 2, pp. 865-875.

SCHMITZ, W., PRETORIUS, L. January 2004. *Performance modelling of electrostatic precipitators using CFD. In* Proceedings of the 4th South African conference on Applied Mechanics (SACAM), Paper 55.

SCHUBAUER, G.B. and SPANGENBERG, W.G. 1948. *Effect of screens in wide-angle diffusers.* National Advisory Committee for Aeronautics (NACA), Technical note No. 1610.

SCHUBAUER, G.B., SPANGENBERG, W.G. and KLEBANOFF, P.S. 1950. *Aerodynamic characteristics of damping screens.* National Advisory Committee for Aeronautics (NACA), N.A.C.A. Technical note No. 2001.

SIMONSEN, J.P., NIELSEN, N.F., SORENSEN, N.N., LIND, L. 1998. *Numerical simulation of screens in Electrostatic Precipitator inlets. In* Proceedings of the 7th International Conference on Electrostatic Precipitators (ICESP VII), Kyongju, Korea: pp: 702-709.

STAR-CD *Methodology manual*, Version 3.15, 2001. Methodology pp 1.1-10.2, Computational Dynamics LTD, Latemer Road, London, United Kingdom.

STAR-CD *User guide*, Version 3.15, 2001. Computational Dynamics LTD, Latemer Road, London, United Kingdom.

TAYLOR, G.I. and DAVIES, R.M. 1944. *The aerodynamics of Porous Sheets*. Reports and Memoranda, No. 2237.

TILLY, G.P. 1979. Erosion caused by Impact of Solid Particles. *Treatise on materials science and technology*, Vol 13, Transport and Road Research Laboratory, Crowthorne, Berkshire England.

TURNER, J. T. 1969. A computational method for the flow through non-uniform gauzes: the general two-dimensional case. *Journal of Fluid Mechanics*, Vol. 36, part 2: 367-383.

VAIVADS, R.H., GAUTHEIR, J.E.D., LEMIEUX, G. AND SPRINGFORD, D., 1998. *CFD simulation of the RMC wind tunnel*, BIB196, Department of Mechanical Engineering, Royal Military College of Canada, Kingston, Ontario, K7K 7B4.

VERSTEEG, H.K., MALALASEKERA, W., 1995. *An Introduction to Computational Fluid Dynamics The Finite Volume Method*. Malaysia: Longman Group Ltd. ISBN: 0-582-21884-5.

WHITE, Frank M. 1988. *Fluid Mechanics*. 2nd Ed. Singapore: Mc. Graw-Hill.

WHITE, Frank M. 1991. *Viscous Fluid Flow*. 2nd Ed. Singapore: Mc. Graw-Hill.

ANNEXURE A : THREE-DIMENSIONAL FLOW PROFILES

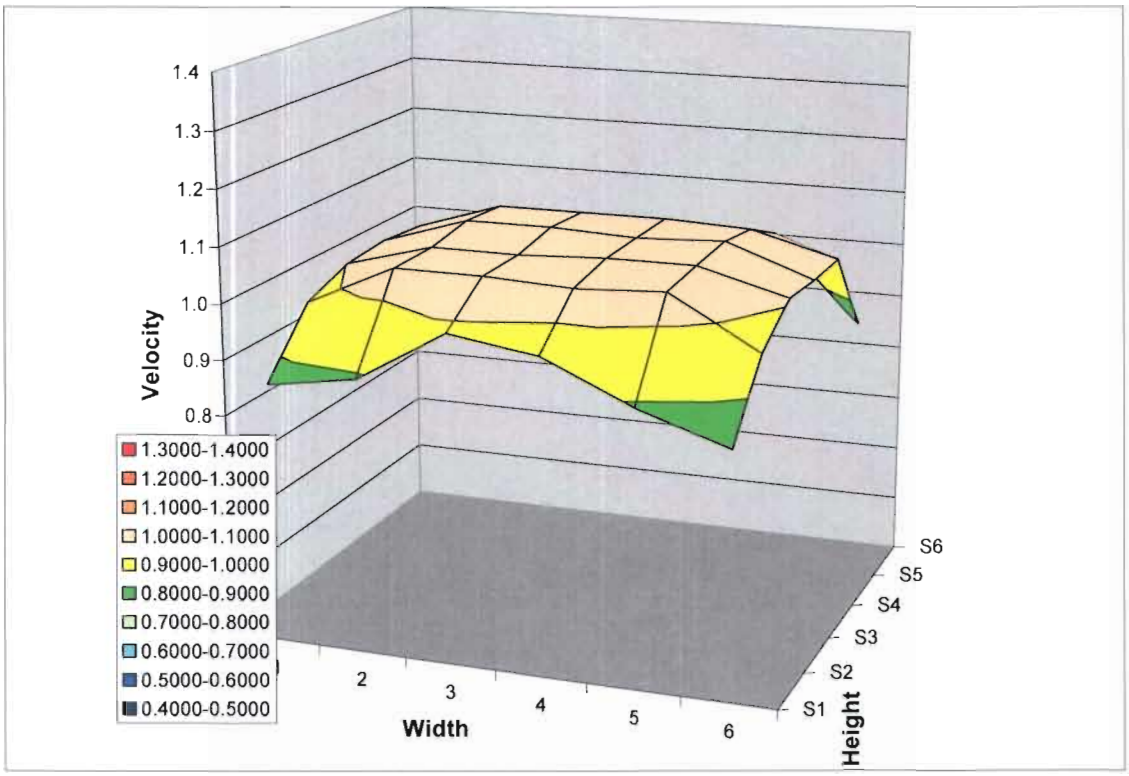

Figure 99: Normalised measured low velocity distribution (±3.7m/s)

Note: The figures in this section represent the three-dimensional flow profiles as discussed in paragraph 4.5.

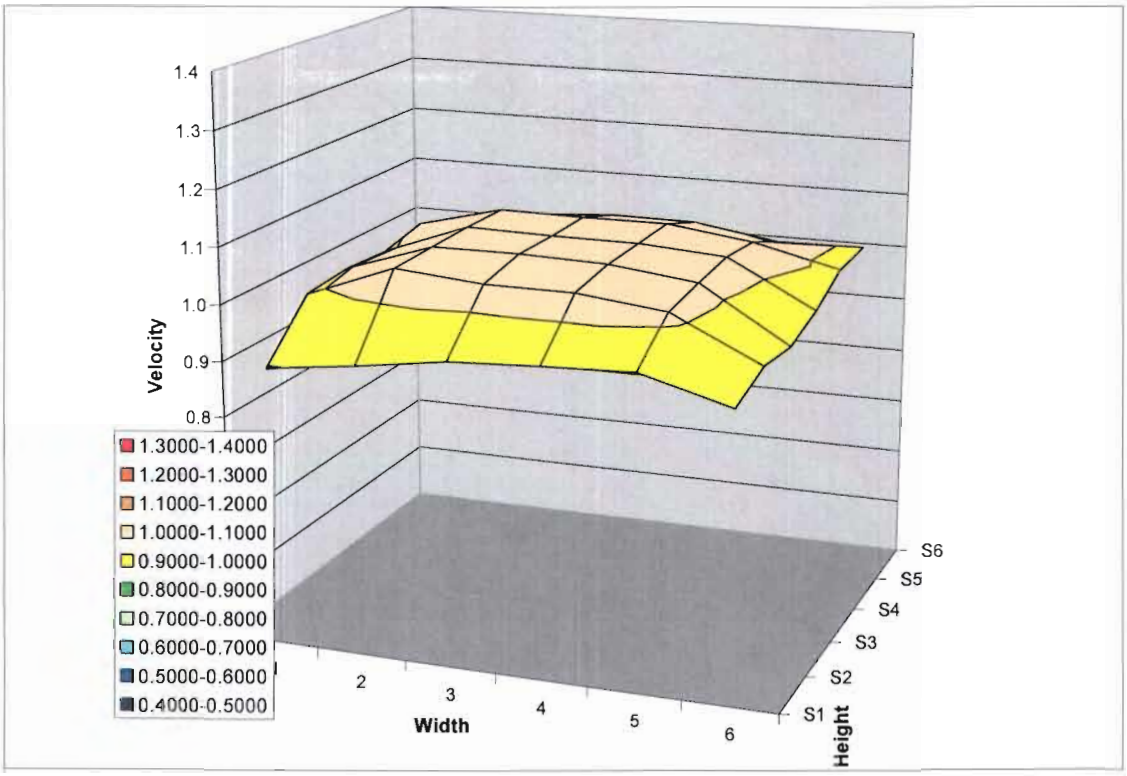

Figure 100: Normalised measured mid velocity distribution (±8.9m/s)

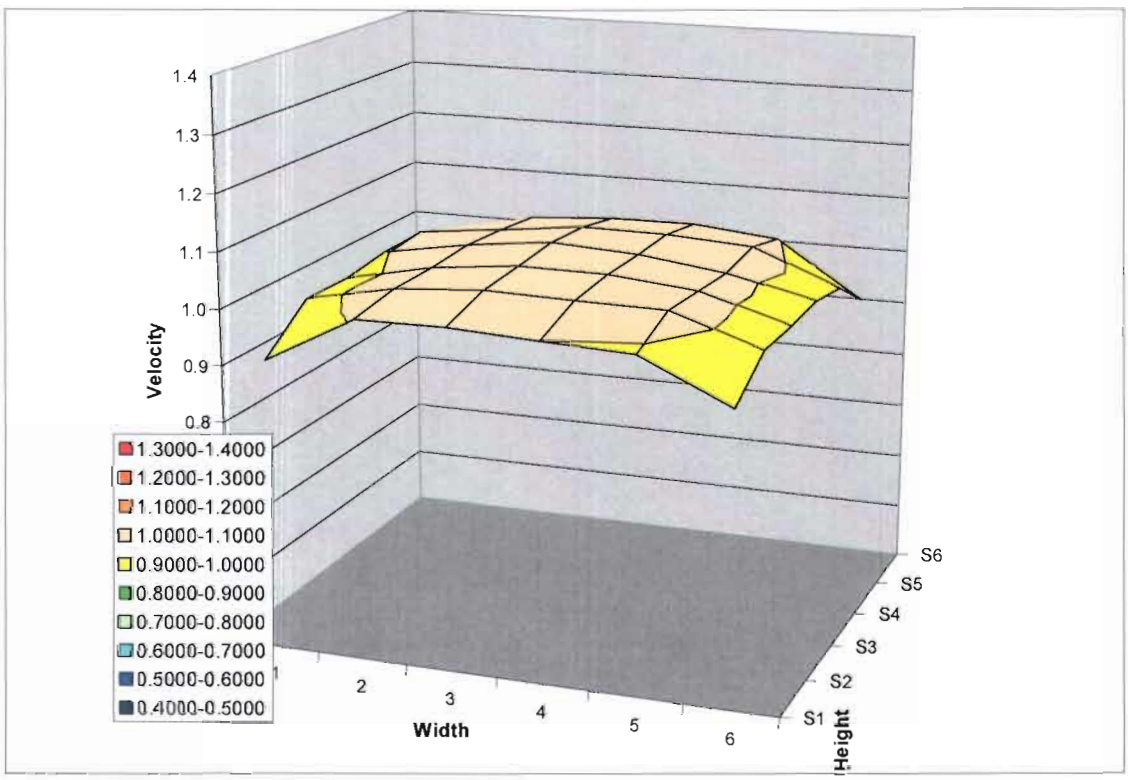

Figure 101: Normalised measured high velocity distribution (±22.6m/s)

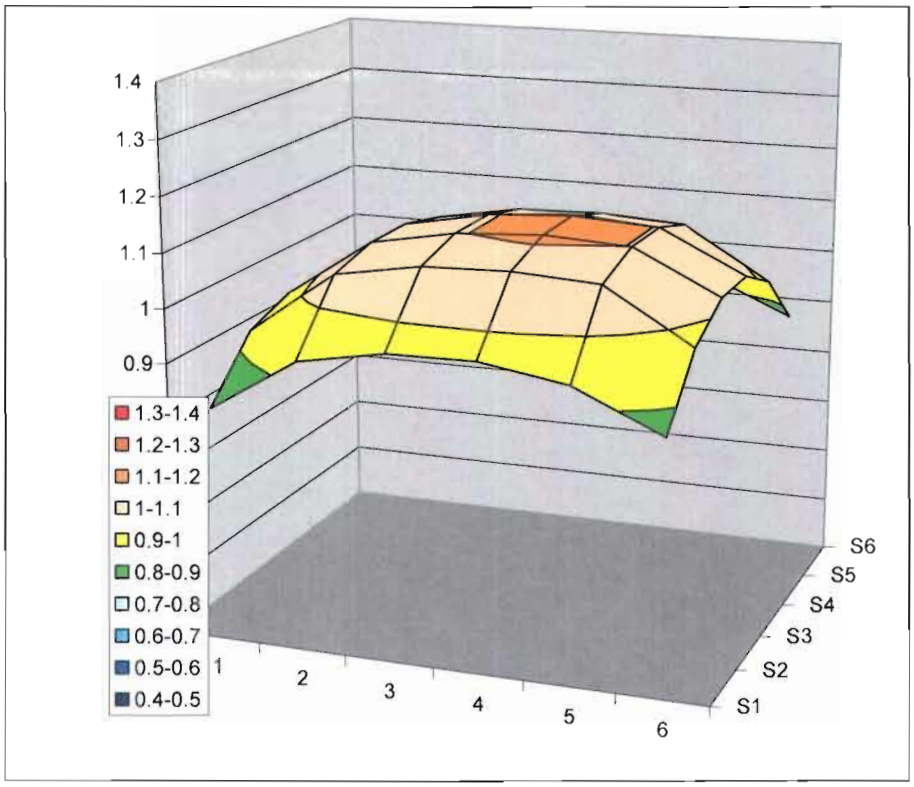

Figure 102: Normalised velocity distribution at 3.7m/s predicted by the CFD model

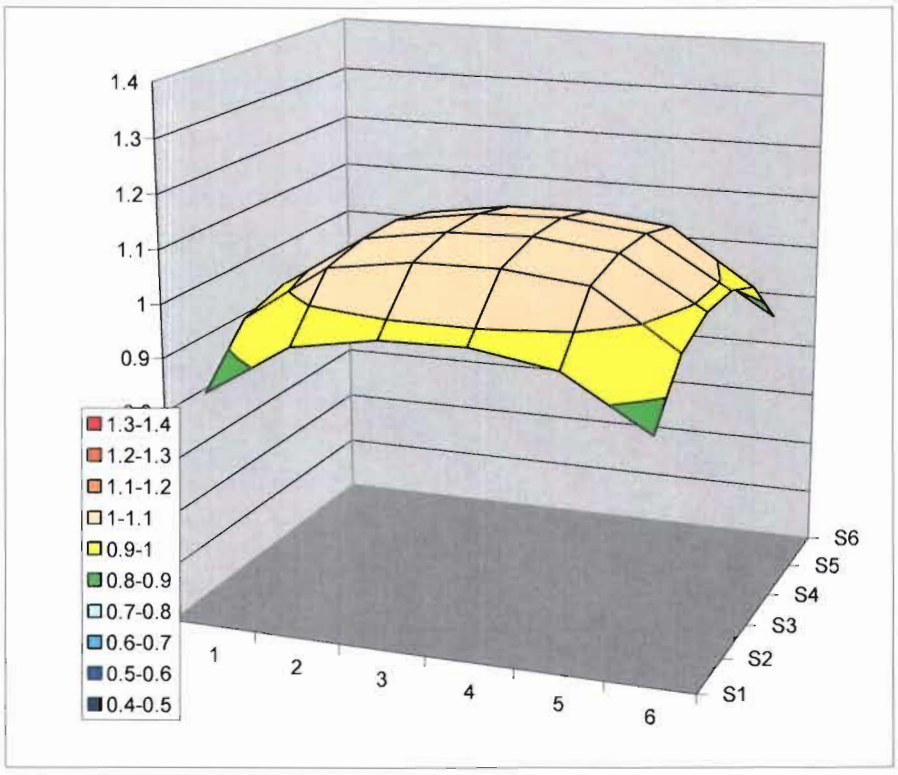

Figure 103: Normalised velocity distribution at 8.9m/s predicted by the CFD model

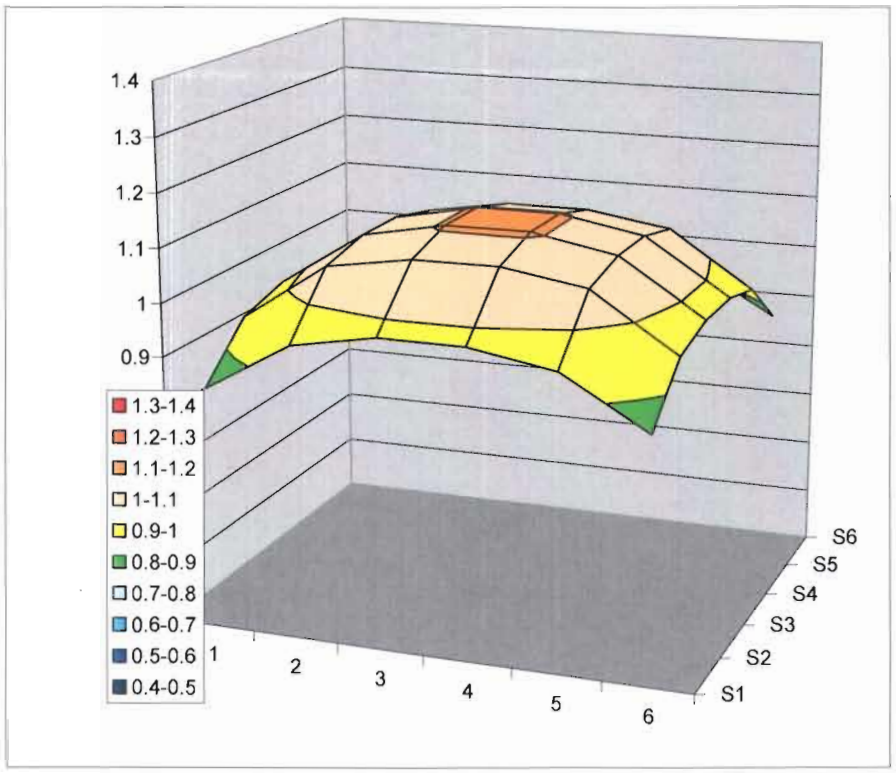

Figure 104: Normalised velocity distribution at 8.9m/s predicted by the CFD model

ANNEXURE B : INSTRUMENTATION CALIBRATION CERTIFICATES

AIRFLOW

SPECIALISTS IN AIR MOVEMENT TECHNOLOGY

CERTIFICATE OF CALIBRATION

INSTRUMENT PVM 100

SERIAL No. 113790

SPECIFICATION TP155-2

CERTIFICATE NUMBER IL113790P

DATE CERTIFIED [illegible]

PART NUMBER J71967801

This Certificate is issued in accordance with QCS 023 "Standard Conditions of Acceptance for Calibration" as currently published by Airflow Developments Ltd.

The measurements were correct at the time of calibration.

Metric Pa.			Imperial ins.wg		
Range	Instr. Reading	True Reading	Range	Instr. Reading	True Reading
0 - +3500	3500	3500	0 - +14	14.051	14.051
0 - +3500	1756	1750	0 - +14	7.050	7.026
0 - +3500	875	875	0 - +14	3.513	3.513
0 - -3500	-877	-875	0 - -14	-3.521	-3.513
0 - -3500	-1752	-1750	0 - -14	-7.034	-7.026
0 - -3500	-3500	-3500	0 - -14	-14.051	-14.051

Calibration temperature 20.9°C/ 69.6°F Barometric pressure 999.3mb./ 29.5"Hg.

This is to certify that the above item has been calibrated in accordance with our Specification and conforms to our published accuracy.

All measured parameters are traceable to BMT Fluid Mechanics Ltd or to National Standards where applicable - see overleaf for reference standards traceability.

It is recommended that this instrument should be re-calibrated annually.

CALIBRATED BY T.P.

The uncertainty of the applied pressure is estimated not to exceed ± (0.02% of reading + 0.04Pa. + instrument resolution). The uncertainties are for a confidence probability of not less than 95%.

Figure 105: Certificate calibration for Airflow PVM100 instrument

HJR
MICROPTIC TM
BK 89/32363/23

METROLOGY SERVICES
METROLOGIESE DIENSTE

P/N31230
Wonderboompoort, 0033
☎ (012) 335-4187
335-6663
335-6664
Fax: (012) 335-6665

SPECIALIZING IN MEASURING, CALIBRATING SYSTEMS, REPAIRS & SALES
SPESIALISEER IN MEET, KALIBRASIESISTEME, HERSTEL EN VERKOPE

METROLOGY REPORT 03-3717

CALIBRATED FOR : MONITORING & CONTROL LABORATORIES

CALIBRATION ITEM : WET & DRY BULB HYGROMETER

SERIAL NO : XM784

CALIBRATION METHOD : BY COMPARISON

REFERENCE STANDARD : HOBO 7232.WH52 (SABS)

TEMPERATURE : 20 °C ± 1 °C HUMIDITY : 40-60 %

UNCERTAINTY OF MEASUREMENT FOR CONFIDENCE LEVEL OF APPROXIMATELY 95 % (FACTOR K=2) = ± 1 °C & ± 10 % RH

CALIBRATION DATE : 24/11/2003

RECOMMENDED EXPIRY DATE : 24/11/2004

ALL MEASUREMENTS TRACEABLE TO NATIONAL OR INTERNATIONAL STANDARDS.

RESULTS

DRY BULB:

ACTUAL	UUT
0,2	0
10,1	10
20,3	20
25,1	25
50,1	50

HUMIDITY: DIFFERENCE BETWEEN DRY BULB & WET BULB WORKS OUT TO BE WITHIN 3 % RH AT DIFFERENT TEMPERATURES.

ALL MEASUREMENTS CORRECT AT 20 °C.

TECHNICAL SIGNATORY: P.J. MYNHARDT
APPROVED BY:

PJM/edp-REF03961
PAGE 1 OF 1

WE INVITE ALL OUR CLIENTS TO OFFER COMMENTS, SUGGESTIONS OR ANY COMPLAINTS ON OUR SERVICES.

Figure 106: Certificate of calibration for Hygrometer

SANAS

ACCREDITED LABORATORY

TSI

Technology Services International

TECHNOLOGY SERVICES INTERNATIONAL

SANAS ACCREDITED CALIBRATION LABORATORY No 205

PRESSURE METROLOGY

CERTIFICATE OF CALIBRATION

Date of issue 09-04-2003

Certificate number 0303P5084-4

Head of Laboratory

M Matt

The accuracy of all measurements is traceable to the national measuring standards.

The values in this certificate are correct at the time of calibration. Subsequently the accuracy will depend on such factors as the care executed in handling and use of the device, and the frequency of use. Recalibration should be performed after the period so chosen to ensure that the instrument's accuracy remains within the desired limits.

This certificate is issued in accordance with the conditions of the accreditation granted by the South African National Accreditation System (SANAS). It is a correct record of the measurements made. This certificate may not be reproduced other than in full except with prior written approval of the issuing laboratory.
In the event of a mistake by TSI in calibration/certification work performed for the applicant, any legal liability arising therefrom shall be limited to the cost of recalibration and or certification, but the applicant indemnifies TSI against any consequential or other loss.

SANAS is a signatory to the Multilateral Agreement of the European co-operation for Accreditation (EA) and to the Mutual Recognition Agreements with the Republic of China (CNLA), Australia (NATA), and New Zealand (IANZ) for the mutual recognition of equivalence of calibration and test certificates.

Lower Germiston Road Private Bag 40175 Cleveland 2022 Gauteng South Africa
Telephone +27 11 629 5111 Facsimile +27 11 629-5229 Web Address www.TSI-SA.com

Figure 107: Certificate of calibration for MEDM500 pressure manometer – Page 1

SANAS
ACCREDITED LABORATORY

TECHNOLOGY SERVICES INTERNATIONAL
Private Bag 40175
Cleveland, 2022 Tel. (011) 629-5016

TSI
Technology Services International

CERTIFICATE OF CALIBRATION

Certificate Number	:	**0303P5084-4**
Calibration of a	:	**Digital Pressure Indicator**
Manufacturer & Type	:	**Airflow MEDM 500**
Serial Number	:	**063721**
Calibrated for	:	**TSI**
Procedure Number	:	**53-130-00**
Date of Calibration	:	**09-04-2003**
Date of Issue	:	**09-04-2003**
Laboratory Environment	:	**21,1 °C**
Reference Standards	:	**205-S-01 Ruska 6200 PPG S/N 39478**

Reference Pressure (Pa)	Indication (Pa)		Correction (Pa)	
	Rising	Falling	Rising	Falling
0	0	0	0	0
100	100	100	0	0
200	201	201	-1	-1
300	303	303	-3	-3
400	402	402	-2	-2
500	505	505	-5	-5

Uncertainty of calibration: ± 20.1 Pa
The reported uncertainty is based on a standard uncertainty multiplied by a coverage factor of k=2, which unless specifically stated otherwise, provides a confidence level of 95%.

Comments:

Calibrated by : M Sekonya

Head of Laboratory

Lower Germiston Road Private Bag 40175 Cleveland 2022 Gauteng South Africa
Telephone +27 11 629 5111 Facsimile +27 11 629-5229 Web Address www.TSI-SA.com

Figure 108: Certificate of calibration for MEDM500 pressure manometer – Page 2

ANNEXURE C : PSYCHROMETRIC CHART

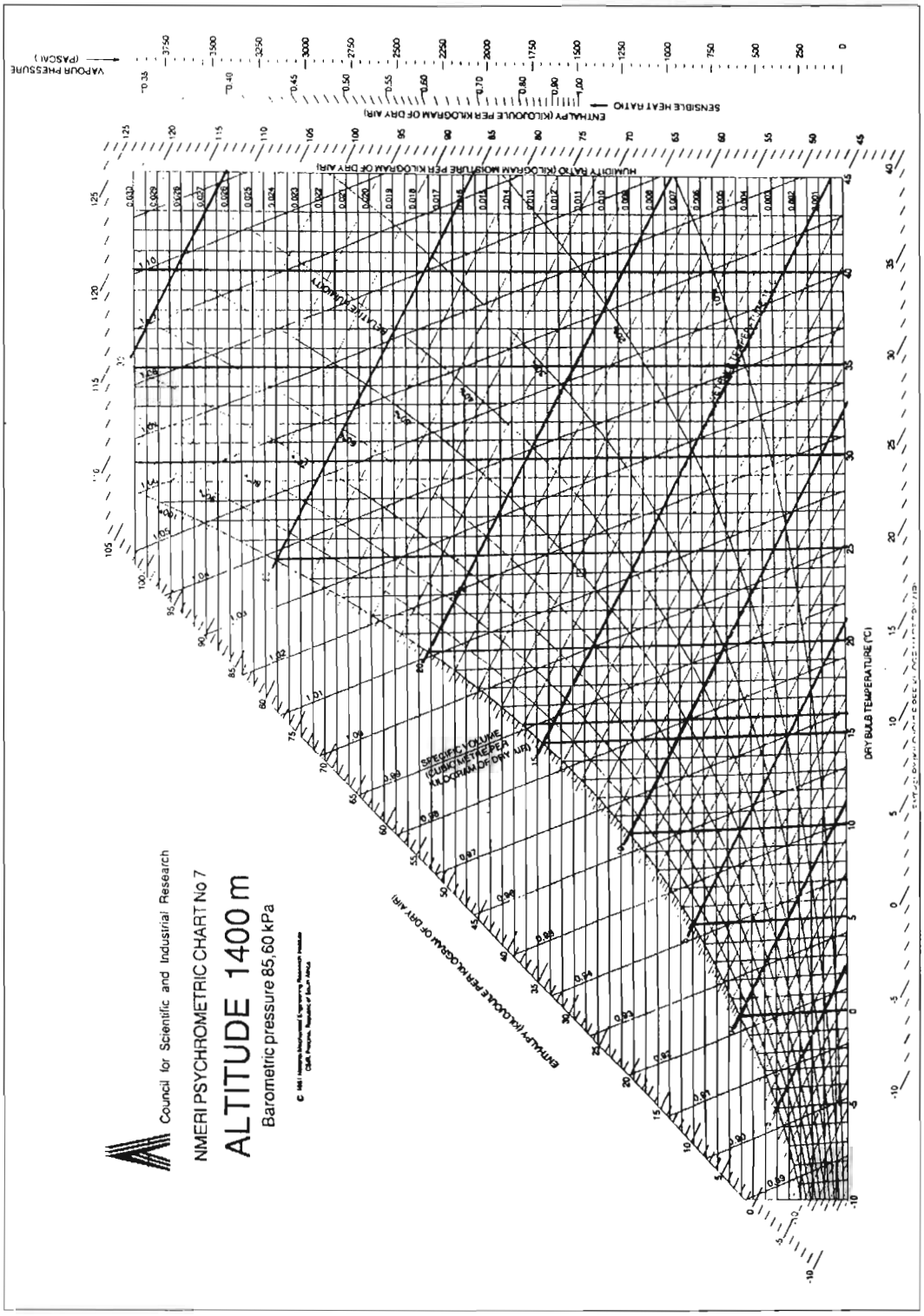

Figure 109: Psychrometric chart for the altitude of 1400m above sea level

ANNEXURE D: UNCERTAINTY CALCULATION

Calculating the uncertainty of a high velocity reading (± 22m/s)

To calculate the expected uncertainty, an example of a typical test case is used where:

B = 85 kPa atmospheric pressure (850 mbar).

T = 20 °C Gas temperature (293 K).

P_s = -67 Pa Relative duct static pressure.

P_v = 250 Pa Dynamic pressure

The nominal value of the velocity is:

$$v = 1.291\left[\frac{1000}{850} * \frac{293}{289} * \frac{100000}{100000-67} * 250\right]^{\frac{1}{2}} = 22.301 m/s$$

(8.1)

At this velocity, the Reynolds number is $3.73*10^5$. The uncertainty of this value is calculated by applying equation (4.9). The values of the various partial differential equations are:

$$\frac{\partial v}{\partial B} = \frac{1}{2} * 1.291\left[\frac{1000}{850} * \frac{293}{289} * \frac{100000}{100000-67} * 250\right]^{-\frac{1}{2}} * \left[\frac{-1000}{850^2} * \frac{293}{289} * \frac{100000}{100000-67} * 250\right]$$

$$\frac{\partial v}{\partial B} = -13.118 * 10^{-3}$$

(8.2)

$$\frac{\partial v}{\partial T} = \frac{1}{2} * 1.291\left[\frac{1000}{850} * \frac{293}{289} * \frac{100000}{100000-67} * 250\right]^{-\frac{1}{2}} * \left[\frac{1000}{850} * \frac{1}{289} * \frac{100000}{100000-67} * 250\right]$$

$$\frac{\partial v}{\partial T} = 38.171 * 10^{-3}$$

(8.3)

$$\frac{\partial v}{\partial Pv} = \frac{1}{2} * 1.291 \left[\frac{1000}{850} * \frac{293}{289} * \frac{100000}{100000 - 67} * 250 \right]^{-\frac{1}{2}} * \left[\frac{1000}{850} * \frac{293}{289} * \frac{100000}{100000 - 67} * 1 \right]$$

$$\frac{\partial v}{\partial Pv} = 44.601 * 10^{-3}$$

(8.4)

$$\frac{\partial v}{\partial Ps} = \frac{1}{2} * 1.291 \left[\frac{1000}{850} * \frac{293}{289} * \frac{100000}{100000 - 67} * 250 \right]^{-\frac{1}{2}} * \left[\frac{1000}{850} * \frac{293}{289} * \frac{-100000}{(100000 - 67)^2} * 250 \right]$$

$$\frac{\partial v}{\partial Ps} = -0.1116 * 10^{-3}$$

(8.5)

The uncertainty values of these terms are:

w_B = Uncertainty of ±5 percent = 850*0.05 = 42.5

w_T = Gas temperature with an uncertainty of ±1 °C = 1 °C

w_{Ps} = Duct static pressure with an uncertainty not exceeding ±(0.028 percent of reading + 0.04 Pa + Instrument resolution (1 Pa))
= 0.00028*67+0.04+1 = 1.05876

w_{Pv} = Dynamic pressure with an uncertainty not exceeding ±(0.028 percent of reading + 0.04 Pa + Instrument resolution (1 Pa))
= 0.00028*250+0.04+1= 1.11

The uncertainty of the velocity measurement can be calculated by replacing these values in equation (4.9):

$$w_v = \left[\begin{array}{l} (42.5)^2 * \left(-13.118 * 10^{-3}\right)^2 + (1)^2 * \left(38.171 * 10^{-3}\right)^2 + \\ (1.05876)^2 * \left(-0.1116 * 10^{-3}\right)^2 + (1.11)^2 * \left(44.601 * 10^{-3}\right)^2 \end{array} \right]^{\frac{1}{2}}$$

$$w_v = 0.561 \quad m/s \quad or \quad 2.516 \quad \%$$

(8.6)

Calculating the uncertainty of a mid velocity reading (±9.2m/s)

Due to the fact that the uncertainty of the digital pressure manometer is not just a percentage of the displayed reading, but includes the instrument resolution, it is required to also calculate the uncertainty if the velocity is reduced to approximately 9.2m/s.

B = 85 kPa atmospheric pressure (850 mbar).

T = 20 °C Gas temperature (293 K).

P_s = -40 Pa Relative duct static pressure.

P_v = 42.7 Pa Dynamic pressure

The nominal value of the velocity is:

$$v = 1.291\left[\frac{1000}{850} * \frac{293}{289} * \frac{100000}{100000-40} * 42.7\right]^{\frac{1}{2}} = 9.215 m/s$$

(8.7)

At this velocity, the Reynolds number is $1.5*10^5$. The uncertainty of this value is calculated by applying equation (4.9). The values of the various partial differential equations are:

$$\frac{\partial v}{\partial B} = \frac{1}{2} * 1.291\left[\frac{1000}{850} * \frac{293}{289} * \frac{100000}{100000-40} * 42.7\right]^{-\frac{1}{2}} * \left[\frac{-1000}{850^2} * \frac{293}{289} * \frac{100000}{100000-40} * 42.7\right]$$

$$\frac{\partial v}{\partial B} = -5.421 * 10^{-3}$$

(8.8)

$$\frac{\partial v}{\partial T} = \frac{1}{2} * 1.291\left[\frac{1000}{850} * \frac{293}{289} * \frac{100000}{100000-40} * 42.7\right]^{-\frac{1}{2}} * \left[\frac{1000}{850} * \frac{1}{289} * \frac{100000}{100000-40} * 42.7\right]$$

$$\frac{\partial v}{\partial T} = 15.726 * 10^{-3}$$

(8.9)

$$\frac{\partial v}{\partial Pv} = \frac{1}{2} * 1.291 \left[\frac{1000}{850} * \frac{293}{289} * \frac{100000}{100000 - 40} * 42.7 \right]^{-\frac{1}{2}} * \left[\frac{1000}{850} * \frac{293}{289} * \frac{100000}{100000 - 40} * 1 \right]$$

$$\frac{\partial v}{\partial Pv} = 107.91 * 10^{-3}$$

(8.10)

$$\frac{\partial v}{\partial Ps} = \frac{1}{2} * 1.291 \left[\frac{1000}{850} * \frac{293}{289} * \frac{100000}{100000 - 40} * 42.7 \right]^{-\frac{1}{2}} * \left[\frac{1000}{850} * \frac{293}{289} * \frac{-100000}{(100000 - 40)^2} * 42.7 \right]$$

$$\frac{\partial v}{\partial Ps} = -46.0942 * 10^{-6}$$

(8.11)

The uncertainty values of these terms are:

w_B = Uncertainty of ±5 percent = 850*0.05 = 42.5 mbar

w_T = Gas temperature with an uncertainty of ±1 °C = 1 °C

w_{Ps} = Duct static pressure with an uncertainty not exceeding ±(0.028 percent of reading + 0.04 Pa + Instrument resolution)
= 0.00028*40+0.04+1 = 1.0512 Pa

w_{Pv} = Dynamic pressure with an uncertainty not exceeding ±(0.028 percent of reading + 0.04 Pa + Instrument resolution)
= 0.00028*42.7+0.04+1= 1.052 Pa

The uncertainty of the velocity measurement can be calculated by replacing these values in equation (4.9):

$$w_v = \left[\begin{array}{l} (42.5)^2 * \left(-5.421 * 10^{-3}\right)^2 + (1)^2 * \left(15.726 * 10^{-3}\right)^2 + \\ (1.0512)^2 * \left(46.094 * 10^{-6}\right)^2 + (1.052)^2 * \left(107.91 * 10^{-3}\right)^2 \end{array} \right]^{\frac{1}{2}}$$

$$w_v = 0.25732 \quad m/s \quad or \quad 2.792 \quad \%$$

(8.12)

Calculating the uncertainty of a low velocity reading (±3.5m/s)

Due to the fact that the uncertainty of the digital pressure manometer is not just a percentage of the displayed reading, but includes the instrument resolution, it is required to also calculate the uncertainty if the velocity is reduced to approximately 3.5m/s.

B = 85 kPa atmospheric pressure (850 mbar).

T = 20 °C Gas temperature (293 K).

P_s = -7 Pa Relative duct static pressure.

P_v = 6.3 Pa Dynamic pressure

The nominal value of the velocity is:

$$v = 1.291\left[\frac{1000}{850} * \frac{293}{289} * \frac{100000}{100000-7} * 6.3\right]^{\frac{1}{2}} = 3.54 m/s$$

(8.13)

At this velocity, the Reynolds number is $5.4*10^4$. The uncertainty of this value is calculated by applying equation (4.9). The values of the various partial differential equations are:

$$\frac{\partial v}{\partial B} = \frac{1}{2} * 1.291\left[\frac{1000}{850} * \frac{293}{289} * \frac{100000}{100000-7} * 6.3\right]^{-\frac{1}{2}} * \left[\frac{-1000}{850^2} * \frac{293}{289} * \frac{100000}{100000-7} * 6.3\right]$$

$$\frac{\partial v}{\partial B} = -2.0818 * 10^{-3}$$

(8.14)

$$\frac{\partial v}{\partial T} = \frac{1}{2} * 1.291\left[\frac{1000}{850} * \frac{293}{289} * \frac{100000}{100000-7} * 6.3\right]^{-\frac{1}{2}} * \left[\frac{1000}{850} * \frac{1}{289} * \frac{100000}{100000-7} * 6.3\right]$$

$$\frac{\partial v}{\partial T} = 6.0393 * 10^{-3}$$

(8.15)

$$\frac{\partial v}{\partial Pv} = \frac{1}{2} * 1.291 \left[\frac{1000}{850} * \frac{293}{289} * \frac{100000}{100000-7} * 6.3 \right]^{-\frac{1}{2}} * \left[\frac{1000}{850} * \frac{293}{289} * \frac{100000}{100000-7} * 1 \right]$$

$$\frac{\partial v}{\partial Pv} = 280.877 * 10^{-3}$$

(8.16)

$$\frac{\partial v}{\partial Ps} = \frac{1}{2} * 1.291 \left[\frac{1000}{850} * \frac{293}{289} * \frac{100000}{100000-7} * 6.3 \right]^{-\frac{1}{2}} * \left[\frac{1000}{850} * \frac{293}{289} * \frac{-100000}{(100000-7)^2} * 6.3 \right]$$

$$\frac{\partial v}{\partial Ps} = -17.697 * 10^{-6}$$

(8.17)

The uncertainty value of these terms are:

w_B = Uncertainty of ±5 percent = 850*0.05 = 42.5 mbar

w_T = Gas temperature with an uncertainty of ±1°C = 1°C

w_{Ps} = Duct static pressure with an uncertainty not exceeding ±(0.028 percent of reading + 0.04 Pa + Instrument resolution)
= 0.00028*7+0.04+1 = 1.04196 Pa

w_{Pv} = Dynamic pressure with an uncertainty not exceeding ±(0.028 percent of reading + 0.04 Pa + Instrument resolution)
= 0.00028*6.3+0.04+1= 1.04176 Pa

The uncertainty of the velocity measurement can be calculated by replacing these values in equation (4.9):

$$w_v = \left[\begin{array}{l} (42.5)^2 * \left(-2.0818 * 10^{-3}\right)^2 + (1)^2 * \left(6.0393 * 10^{-3}\right)^2 + \\ (1.04196)^2 * \left(-17.697 * 10^{-6}\right)^2 + (1.04176)^2 * \left(280.877 * 10^{-3}\right)^2 \end{array} \right]^{\frac{1}{2}}$$

$$w_v = 0.30575 \quad m/s \quad or \quad 8.64\%$$

(8.18)

Comparison of resistance coefficient (K)

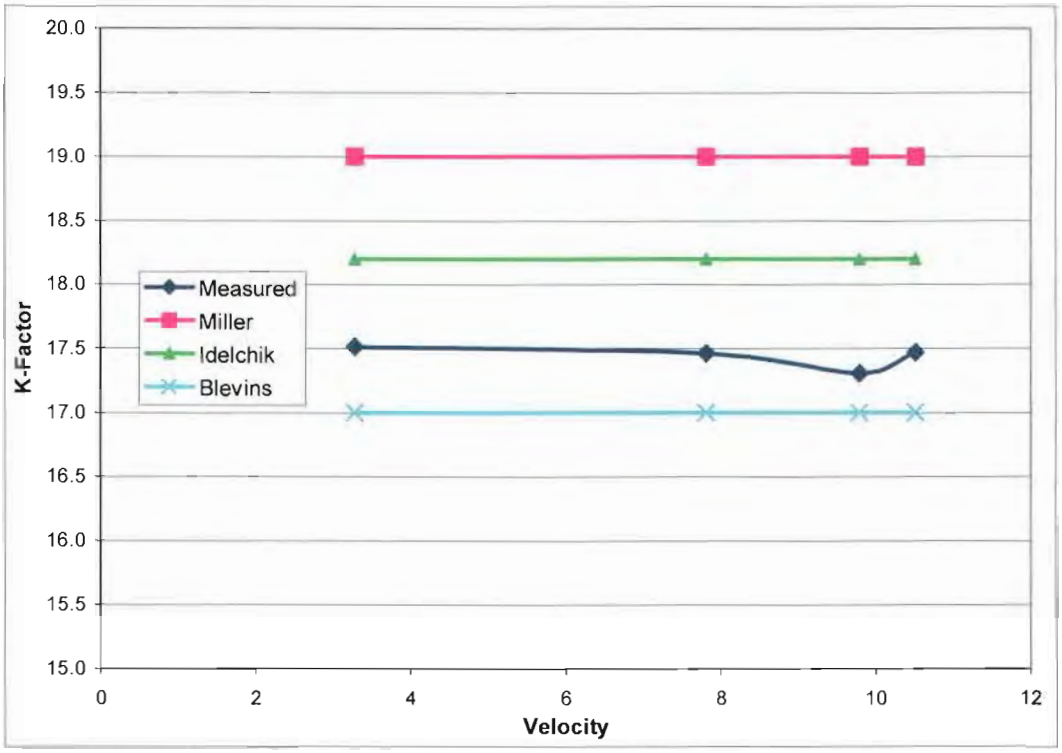

Figure 110: 30 percent FAR screen resistance comparison

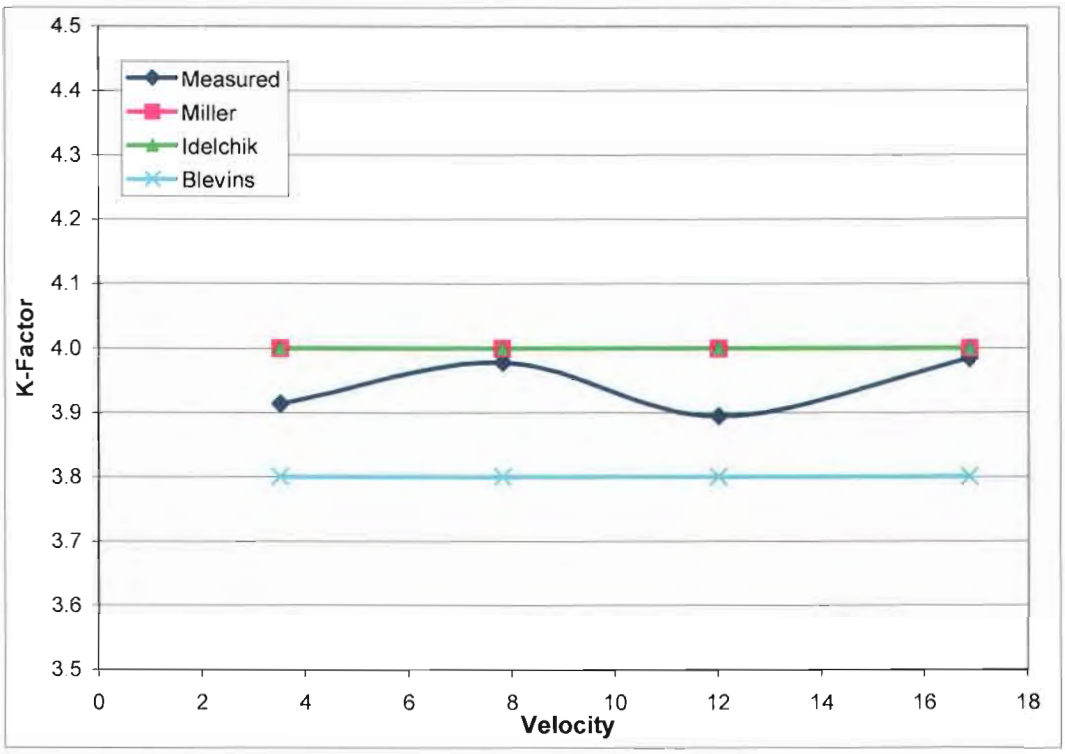

Figure 111: 50 percent FAR screen resistance comparison

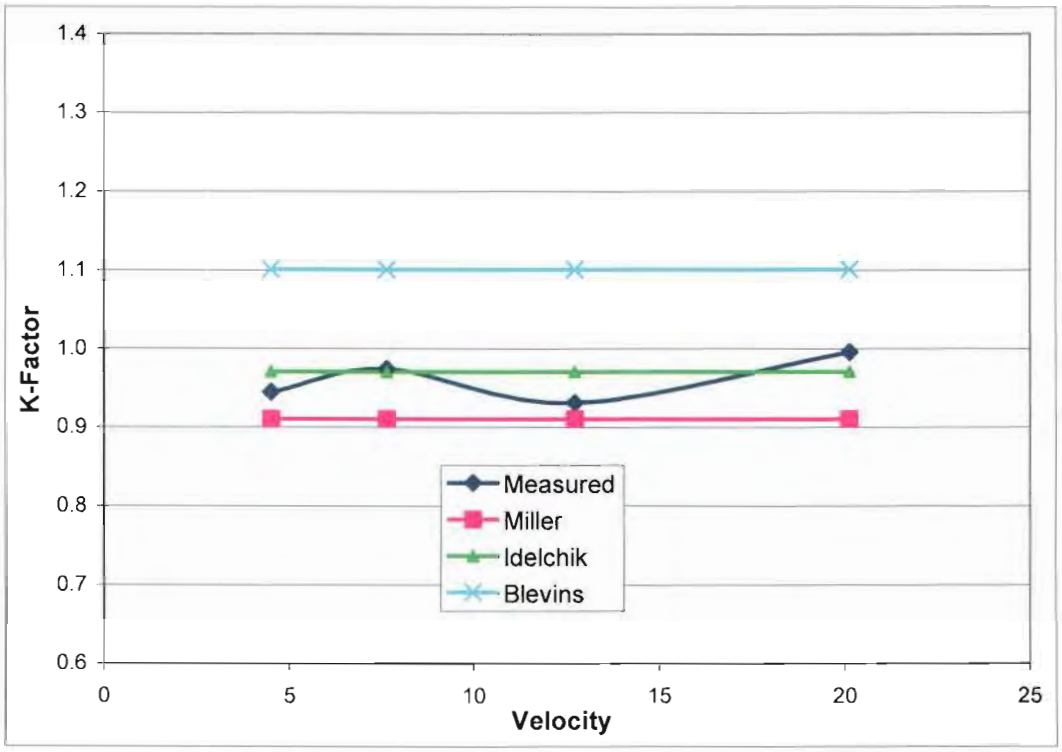

Figure 112: 70 percent FAR screen resistance comparison

Repeatability of results

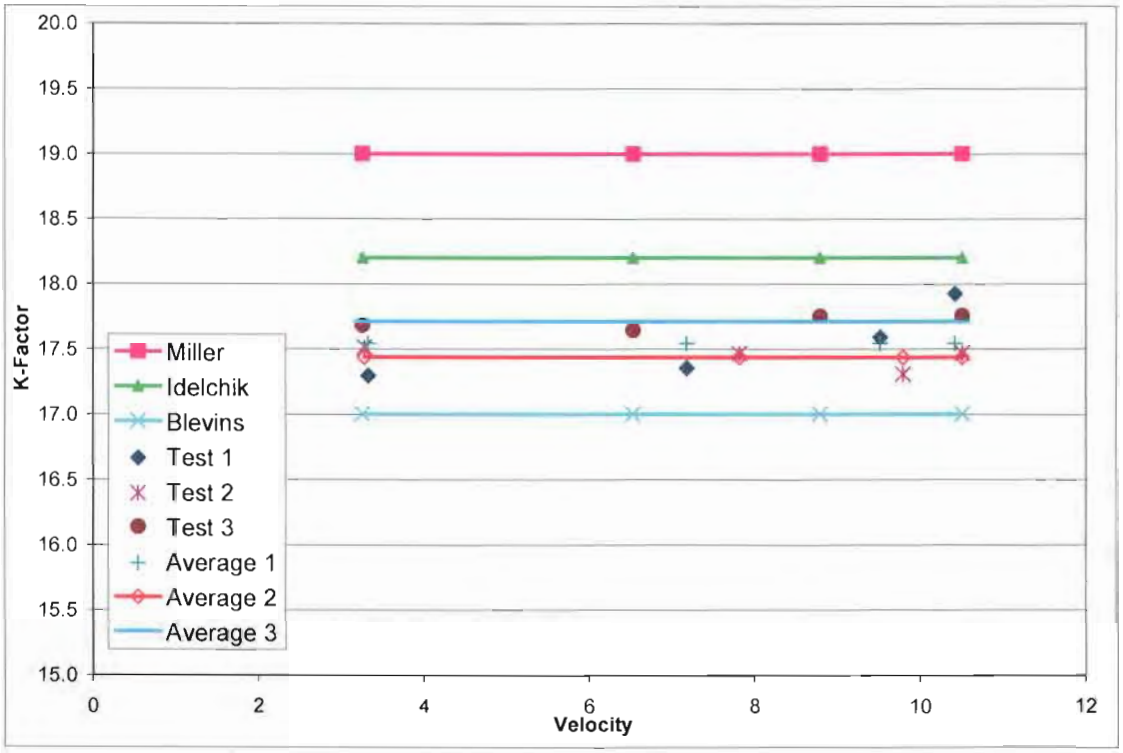

Figure 113: Repeatability test for 30 percent FAR screen

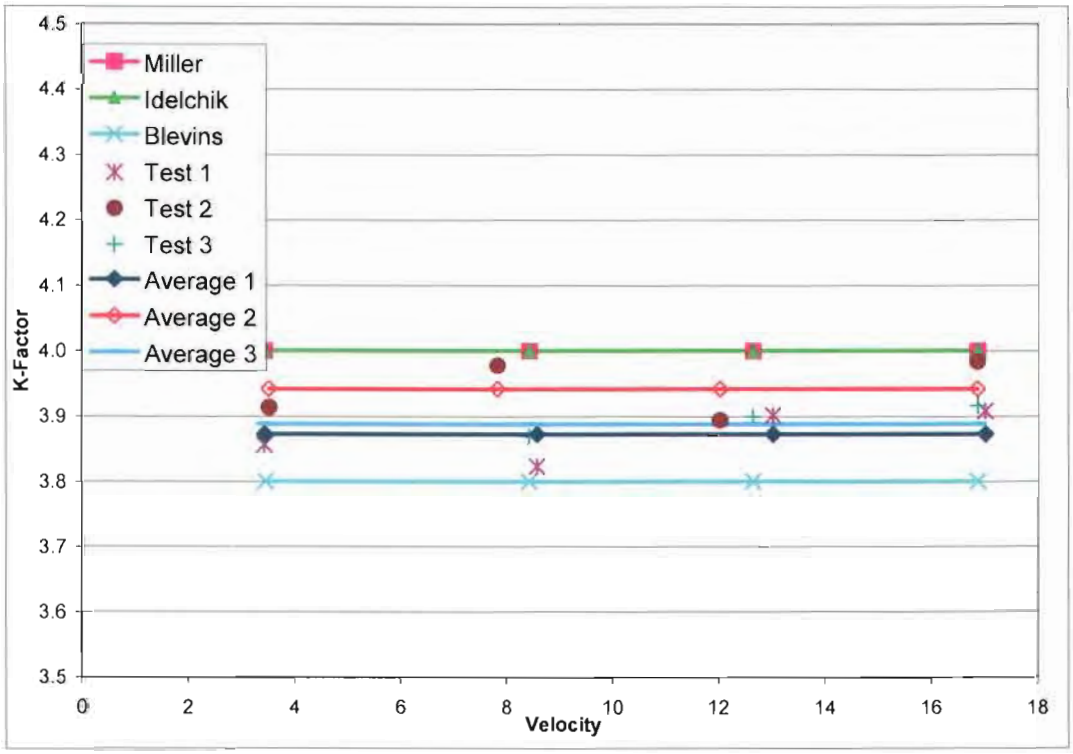

Figure 114: Repeatability test for 50 percent FAR screen

ANNEXURE E : USER DEFINED FUNCTIONS

ANNEXURE E.1 : INPUT DATA ASSIGNMENT FILE

Filename: inpdata.inc

```
C_____
C_____ Input data assignment _____
C_____
C_____ Section 1: Screen definition _____
C_____
C_____ Screen thickness _____
      ST = 0.0005
C_____ Hole size in Y-direction _____
      HSY = 0.0154
C_____ Hole size in Z-direction _____
      HZS = HSY
C_____ Hole pitch in Y-direction _____
      HPY = 0.0217
C_____ Hole pitch in Z-direction _____
      HPZ = HPY
C_____ Lattice size in Y-direction _____
      SLY = 0.0063
C_____ Lattice size in Z-direction _____
      SLZ = SLY
C_____
C_____ Section 2: Code specific variables _____
C_____
C_____ Porous medium thickness _____
      SP = 0.0005
C_____ Ratio between alpha and beta _____
      BA = 0.0001
C_____ Define relaxation factor _____
C__Note: This ratio indicates the weight of the old velocity value
C__in the calculation of the new velocity
      RELAO = 0.9
C_____ Cell number offset for neighbours _____
      IOFF = 5444
C_____ First Cell type number _____
      ICTY = 14
C_____ Monitoring Cell number _____
      MONC = 117070
      MON2 = 116272
      MON3 = 119566
C_____ Porosity ID _____
      IPID = 1
C_____ Inititalisation velocity _____
      AINI = 1.0
C_____ Iteration to write info _____
      ITWR = 55
C_____ Correction factor _____
      CORF = 1.0
C_____ Define lower limit of FAR _____
      DLL = 0.05
C_____ Define upper limit of FAR _____
      DUL = 0.95
C_____ Define ratio between ALI and ALJ/ALK _____
      RIJ = 0.001
C_____
```

ANNEXURE E.2 : ADDITIONAL COMMON BLOCK DEFINITION FILE

Filename: cblocks.inc

```
!_____ Additional common blocks required _____________

      COMMON/DCO2/ PP(-NBMAX:NCMAX),VIS(-NBMAX:NCMAX),
     & UU(3,-NBMAX:NCTMAX),TEE(-NBMAX:NCMAX),EDD(-NBMAX:NCMAX),
     & TT(-NBMAX:NCTMAX,1+NSC),DENS(-NBMAX:NCTMAX),
     & CPP(-NBMAX:NCTMAX)

      COMMON /DCO5/ LQ(6,NCTMAX)

      COMMON /RC01/ INL(NCTMAX),UNL(3,NCTMAX),INB(NCTMAX),
     & UNB(3,NCTMAX),INC(NCTMAX),UNC(3,NCTMAX)

      COMMON /RC02/ UOLA(3,NCTMAX),UOLB(3,NCTMAX),
     & UOLC(3,NCTMAX)

      COMMON /SC02/ SCL1(NCTMAX),SCL2(NCTMAX),SCL3(NCTMAX),
     & SCL4(NCTMAX),SCL5(NCTMAX),SCL6(NCTMAX)
```

ANNEXURE E.3 : DEFINITION OF THE CELL NEIGHBOUR LISTS

```
C***********************************************************************
      SUBROUTINE POSDAT(KEY,VOL,U,TE,ED,T,P,VIST,DEN,CP,VISM,CON,
     *  F,ICLMAP,ICTID,RESOR,VF,FORCB,IRN,PREFM,LEVEL)
C     Post-process data
C***********************************************************************
C-----------------------------------------------------------------------*
C     STAR RELEASE 3.150                                                *
C-----------------------------------------------------------------------*
      INCLUDE 'comdb.inc'
      INCLUDE '../parm.inc'

      COMMON/USR001/INTFLG(100)
      DIMENSION KEY(-NBMAX:NCTMAX),VOL(NCTMAX),U(3,-NBMAX:NCMAX),
     * TE(-NBMAX:NCMAX),ED(-NBMAX:NCMAX),T(-NBMAX:NCTMAX,1+NSC),
     * P(-NBMAX:NCMAX),VIST(-NBMAX:NCMAX),DEN(-NBMAX:NCTMAX),
     * CP(-NBMAX:NCTMAX),VISM(-NBMAX:NCMAX),CON(-NBMXCU:NCMXCU),
     * F(3,-NBMAX:NCMAX),ICLMAP(NCTMAX),ICTID(NCTMAX),
     * RESOR(63,-100:100),VF(NCDMXU),
     * FORCB(3,NWLMX),IRN(NWLMX)

      DOUBLE PRECISION P
      DIMENSION PREFM(4)

      INCLUDE 'usrdat.inc'
C
C     Extra internal STAR Common Blocks
C
      COMMON /MAINU/ junk1,NBP23,NWLBT,NNODE,NREG,NBCT0F,NBCYCF,NFLU,
     *    NSOL,
     *    NBEAM,NTRAD,MAXCNO,NBC01,NBC012,NB(6),NTB(6),NBCUT0,NBCUT1,
     *    NBCUT2,NBCUT3,NBCUTS,NBCUT,NBPH,NINL(6),
     *    NOUT(6),NPRB(6),NBNCST,NBNCEN,NSCL,NEMB1,NEMB2,junk2,ITERSO,
     *    ITERSN,ITERNO,NRIT
C     COMMON /DCO5/ LQ(6,NCTMAX)
      COMMON /C06013/ LX(1)
      COMMON /INDMP1/ NDIR(-3:3),NDINAB(6)
      COMMON /INDMP2/ NDIN(6)
      COMMON /C06005/ LCU(2,NCUTMX)
      COMMON /C06006/ ICU(2,NCUTMX)
      COMMON /C1C003/ IBLMAP(4)
      COMMON /DCO21/ CX(3,-NBMAX:NCTMAX)
      COMMON /DCO31R/ DUMMY(NBN1MX:NBN2MX),SB(3,NBN1MX:NCUTMX+1)
      COMMON /DCO14/S(3,3,-NBMAX:NCTMAX)

C_____________________________________________________________________
C_____________________ Additional common blocks ____________________
C_____________________________________________________________________

      INCLUDE 'cblocks.inc'
C_____________________________________________________________________
C_____________________ USER Input data _____________________
C_____________________________________________________________________

      INCLUDE 'inpdata.inc'
C
C     End of Extra internal STAR Common Blocks
C
C-----------------------------------------------------------------------

      IF(LEVEL.EQ.1) RETURN
```

```
C    loop through structured cells
     DO IC1 = 1 , NCTMAX
        ICT1 = ICTID(IC1)
        IP1 = ICLMAP(IC1)
            IOF2 = IOFF * 2
            IOF3 = IOFF * 3

C          IF(ICT1.EQ.CTYP) THEN
C           IF(ITER.EQ.1) PRINT *,'IOFFset1= ',IOFF
C           PRINT *,'IOFFset1= ',IOFF
C           PRINT *,'IOFFset2= ',IOF2
C           PRINT *,'IOFFset3= ',IOF3
C          ENDIF
C_____ SETUP 1ST NEIGHBOUR LIST _____

          IC2 = IC1 - IOFF
          IP2 = ICLMAP(IC2)
              INL(IC1) = IC2
              UNL(1,IC1) = U(1,IC2)
              UNL(2,IC1) = U(2,IC2)
              UNL(3,IC1) = U(3,IC2)
              TNL = INL(IC1)
C_____ SETUP 2ND NEIGHBOUR LIST _____

          IC2B = IC1 - IOF2
          IP2B = ICLMAP(IC2B)
              INB(IC1) = IC2B
              UNB(1,IC1) = U(1,IC2B)
              UNB(2,IC1) = U(2,IC2B)
              UNB(3,IC1) = U(3,IC2B)
              TNLB = INB(IC1)
C_____ SETUP 3RD NEIGHBOUR LIST _____

          IC2C = IC1 - IOF3
          IP2C = ICLMAP(IC2C)
              INC(IC1) = IC2C
              UNC(1,IC1) = U(1,IC2C)
              UNC(2,IC1) = U(2,IC2C)
              UNC(3,IC1) = U(3,IC2C)
              TNLC = INC(IC1)

C          IF(ICT1.EQ.CTYP) THEN
C            PRINT *,'IP1= ',IP1,' IP2= ',IP2
C            PRINT *,'IP2B= ',IP2B,' IP2C= ',IP2C
C            PRINT *,'TEST NL= ',TNL
C            PRINT *,'TEST NLB= ',TNLB
C            PRINT *,'TEST NLC= ',TNLC
C          ENDIF

C           IF(IP.EQ.INMA)
C            PRINT *,'IP1= ',IP1,' IP2= ',IP2
C            PRINT *,'IP2B= ',IP2B,' IP2C= ',IP2C
C            PRINT *,'TEST NL= ',TNL
C            PRINT *,'TEST NLB= ',TNLB
C            PRINT *,'TEST NLC= ',TNLC
C          ENDIF
      ENDDO
C    end of loop through structured cells
     RETURN
     END
C
```

ANNEXURE E.4 : INLET BOUNDARY PROFILE IMPLEMENTATION FILE

```
C***********************************************************************
      SUBROUTINE BCDEFI(SCALAR,U,V,W,TE,ED,T,DEN,TURINT)
C     Boundary conditions at inlets
C***********************************************************************
C-----------------------------------------------------------------------*
C     STAR RELEASE 3.150                                                *
C-----------------------------------------------------------------------*
      INCLUDE 'comdb.inc'
      INCLUDE '../parm.inc'

      COMMON/USR001/INTFLG(100)

      DIMENSION SCALAR(50)
      LOGICAL TURINT
      INCLUDE 'usrdat.inc'
      DIMENSION SCALC(50)
      EQUIVALENCE( UDAT12(001), ICTID )
      EQUIVALENCE( UDAT04(002), DENC )
      EQUIVALENCE( UDAT04(003), EDC )
      EQUIVALENCE( UDAT02(005), PR )
      EQUIVALENCE( UDAT04(005), PRC )
      EQUIVALENCE( UDAT04(009), SCALC(01) )
      EQUIVALENCE( UDAT04(007), TC )
      EQUIVALENCE( UDAT04(008), TEC )
      EQUIVALENCE( UDAT04(059), UC )
      EQUIVALENCE( UDAT04(060), VC )
      EQUIVALENCE( UDAT04(061), WC )
      EQUIVALENCE( UDAT04(064), UCL )
      EQUIVALENCE( UDAT04(065), VCL )
      EQUIVALENCE( UDAT04(066), WCL )
      EQUIVALENCE( UDAT02(070), X )
      EQUIVALENCE( UDAT02(071), Y )
      EQUIVALENCE( UDAT02(072), Z )
C_____________________________________________________________________
C_____________________ Additional common blocks ____________________
C_____________________________________________________________________

      INCLUDE 'cblocks.inc'
C_____________________________________________________________________
C_____________________ USER Input data _____________________
C_____________________________________________________________________

      INCLUDE 'inpdata.inc'
C-----------------------------------------------------------------------
C
C     This subroutine enables the user to specify INLET boundary
C     conditions for U,V,W,TE,ED,T and SCALAR.
C
C     Set TURINT=.TRUE.   if turbulence intensity and length scale are
C                         specified as TE and ED respectively
C     Set TURINT=.FALSE.  if k and epsilon are specified as TE and
C                         ED respectively
C
C     ** Parameters to be returned to STAR: U,V,W,TE,ED,T,
C                                  SCALAR, DEN, TURINT
C
C     NB U,V and W are in the local coordinate-system of the
C     inlet boundary.
C
C-----------------------------------------------------------------------
```

```
C
C     Sample coding: To specify inlet values for region 1
C
C      IF(IREG.EQ.1) THEN
C        TURINT=.FALSE.
C        U=
C        V=
C        W=
C        TE=
C        ED=
C        T=
C        SCALAR(1)=
C        DEN=
C      ENDIF
C-----------------------------------------------------------------------

      IF(IREG.EQ.1) THEN

C_____ Define input values

            AIV = -15.6827
        V=0.0
        W=0.0
        TE=3.689206
        ED=38.811464
        T=294.15
        SCALAR(1)=0.0
        DEN=1.000

C_____ Calculate U
            VCF = 1.017683
C_____ Define curve fit

            Y2 = Y*Y
            Y3 = Y*Y*Y
            Y4 = Y*Y*Y*Y

            Z2 = Z*Z
            Z3 = Z*Z*Z
            Z4 = Z*Z*Z*Z
            AA = -204.0193622
            BB = 122.4116173
            CC = -27.52188034
            DD = 2.748041322
            EE = 0.920200329

        TURINT=.FALSE.
            YCF = (AA*Y4)+(BB*Y3)+(CC*Y2)+(DD*Y)+EE
            ZCF = (AA*Z4)+(BB*Z3)+(CC*Z2)+(DD*Z)+EE
            ZCF = ZCF / 1.023
            U = AIV * YCF * ZCF * VCF

C       IF(IBP.EQ.4015) THEN
C          PRINT *,'YCF= ',YCF,' ZCF= ',ZCF
C          PRINT *,'U= ',U,' Y= ',Y,' Z= ',Z
C          PRINT *,'V= ',V,' W= ',W,' TE= ',TE
C          PRINT *,'T= ',T,' DEN= ',DEN
C       ENDIF
      ENDIF
       RETURN
      END
C
```

ANNEXURE E.5 : DEFINITION OF THE SCALAR VALUES

```
C*************************************************************************
      SUBROUTINE SCALFN(PHI)
C     Species-scalar function
C*************************************************************************
C-------------------------------------------------------------------------*
C     STAR RELEASE 3.150                                                  *
C-------------------------------------------------------------------------*
      INCLUDE 'comdb.inc'
      INCLUDE '../parm.inc'

      COMMON/USR001/INTFLG(100)

      INCLUDE 'usrdat.inc'
      DIMENSION SCALAR(50), HFORM(50)
      EQUIVALENCE( UDAT12(001), ICTID )
      EQUIVALENCE( UDAT03(001), CON )
      EQUIVALENCE( UDAT03(009), DUDX )
      EQUIVALENCE( UDAT03(010), DVDX )
      EQUIVALENCE( UDAT03(011), DWDX )
      EQUIVALENCE( UDAT03(012), DUDY )
      EQUIVALENCE( UDAT03(013), DVDY )
      EQUIVALENCE( UDAT03(014), DWDY )
      EQUIVALENCE( UDAT03(015), DUDZ )
      EQUIVALENCE( UDAT03(016), DVDZ )
      EQUIVALENCE( UDAT03(017), DWDZ )
      EQUIVALENCE( UDAT04(001), CP )
      EQUIVALENCE( UDAT04(002), DEN )
      EQUIVALENCE( UDAT04(003), ED )
      EQUIVALENCE( UDAT04(006), P )
      EQUIVALENCE( UDAT04(008), TE )
      EQUIVALENCE( UDAT04(009), SCALAR(01) )
      EQUIVALENCE( UDAT04(059), U )
      EQUIVALENCE( UDAT04(060), V )
      EQUIVALENCE( UDAT04(061), W )
      EQUIVALENCE( UDAT04(062), VISM )
      EQUIVALENCE( UDAT04(063), VIST )
      EQUIVALENCE( UDAT04(007), T )
      EQUIVALENCE( UDAT04(067), X )
      EQUIVALENCE( UDAT04(068), Y )
      EQUIVALENCE( UDAT04(069), Z )
      EQUIVALENCE( UDAT09(001), IS )
      EQUIVALENCE( UDAT10(101), HFORM(01) )

C_____________________________________________________________________
C_____________________ Additional common blocks ____________________
C_____________________________________________________________________

      INCLUDE 'cblocks.inc'
C_____________________________________________________________________
C_____________________ USER Input data _____________________
C_____________________________________________________________________

      INCLUDE 'inpdata.inc'

C-----------------------------------------------------------------------
C
C     This subroutine enables the user to specify SCALAR(IS) in an
C     arbitrary manner, instead of solving the corresponding transport
C     equation.
C
```

```
C    ** Parameter to be returned to STAR: PHI
C
C-------------------------------------------------------------------------

          ICT2 = ICTY + 1
          ICT3 = ICTY + 2

          IF(ICTID.EQ.ICTY.OR.ICTID.EQ.ICT2.OR.ICTID.EQ.ICT3) THEN
           IF (IS.EQ.1) THEN
            PHI = SCL1(IP)
           ENDIF

           IF (IS.EQ.2) THEN
            PHI = SCL2(IP)
           ENDIF

           IF (IS.EQ.3) THEN
            PHI = SCL3(IP)
           ENDIF

           IF (IS.EQ.4) THEN
            PHI = SCL4(IP)
           ENDIF

           IF (IS.EQ.5) THEN
            PHI = SCL5(IP)
           ENDIF

           IF (IS.EQ.6) THEN
            PHI = SCL6(IP)
           ENDIF

          ENDIF

    RETURN
    END
C
```

ANNEXURE E.6 : VARIABLE RESISTANCE: POROUS MEDIUM APPROACH

```
C***********************************************************************
      SUBROUTINE POROS1(ALI,ALJ,ALK,BTI,BTJ,BTK,POROS)
C     Permeability
C***********************************************************************
C-----------------------------------------------------------------------*
C     STAR RELEASE 3.150                                                *
C-----------------------------------------------------------------------*
      INCLUDE 'comdb.inc'
      INCLUDE '../parm.inc'

      COMMON/USR001/INTFLG(100)

      INCLUDE 'usrdat.inc'
      DIMENSION SCALAR(50)
      EQUIVALENCE( UDAT12(001), ICTID )
      EQUIVALENCE( UDAT04(001), CP )
      EQUIVALENCE( UDAT04(002), DEN )
      EQUIVALENCE( UDAT04(005), PR )
      EQUIVALENCE( UDAT04(009), SCALAR(01) )
      EQUIVALENCE( UDAT04(059), U )
      EQUIVALENCE( UDAT04(060), V )
      EQUIVALENCE( UDAT04(061), W )
      EQUIVALENCE( UDAT04(064), UL )
      EQUIVALENCE( UDAT04(065), VL )
      EQUIVALENCE( UDAT04(066), WL )
      EQUIVALENCE( UDAT04(062), VISM )
      EQUIVALENCE( UDAT04(063), VIST )
      EQUIVALENCE( UDAT04(007), T )
      EQUIVALENCE( UDAT04(067), X )
      EQUIVALENCE( UDAT04(068), Y )
      EQUIVALENCE( UDAT04(069), Z )
      EQUIVALENCE( UDAT04(070), XL )
      EQUIVALENCE( UDAT04(071), YL )
      EQUIVALENCE( UDAT04(072), ZL )

C_____________________________________________________________________
C_____________________ Additional common blocks ____________________
C_____________________________________________________________________
      INCLUDE 'cblocks.inc'
C_____________________________________________________________________
C_____________________ USER Input data _____________________________
C_____________________________________________________________________
      INCLUDE 'inpdata.inc'
C-----------------------------------------------------------------------
C
C     This subroutine enables the user to specify permeability coeffici-
C     ents ALI,ALJ,ALK,BTI,BTJ,BTK and POROS in an arbitrary manner.
C
C     ** Parameters to be returned to STAR: ALI,ALJ,ALK,BTI,BTJ,BTK,POROS
C
C-----------------------------------------------------------------------
C_____________________________________________________________________
C_____________________ Define relaxation factor ____________________
C_____________________________________________________________________
C          RELAO = 0.5
           RELAN = 1 - RELAO
C          INIT = 5
C_____________________________________________________________________
C_____________________ Test Input data assignment __________________
C_____________________________________________________________________
```

```
          IOF2 = IOFF * 2
          IOF3 = IOFF * 3
          INMA = MONC
          INMB = INMA + IOFF
          INMC = INMA + IOF2
          ICTB = ICTY + 1
          ICTC = ICTY + 2

          IF(ITER.EQ.1) THEN
        IF (IP.EQ.INMA) PRINT *,'Porosity ID= ',IPID,'ICTY= ',ICTY
        IF (IP.EQ.INMA) PRINT *,'ICTB= ',ICTB,'ICTC ',ICTC
        IF (IP.EQ.INMA) PRINT *,'INMA= ',INMA,'INMB= ',INMB
        IF (IP.EQ.INMA) PRINT *,'INMC= ',INMC
        IF (IP.EQ.INMA) PRINT *,'OFFSET 1= ',IOFF,'OFFSET 2= ',IOF2
        IF (IP.EQ.INMA) PRINT *,'OFFSET 3= ',IOF3
        IF (IP.EQ.INMA) PRINT *,'ST= ',ST,' HSY= ',HSY,' HZS=',HZS
        IF (IP.EQ.INMA) PRINT *,'HPY= ',HPY,' HPZ= ',HPZ,' SLY=',SLY
        IF (IP.EQ.INMA) PRINT *,'SLZ= ',SLZ,' SP= ',SP,' BA=',BA
        IF (IP.EQ.INMA) PRINT *,'SLZ= ',SLZ,' SP= ',SP,' BA=',BA
        IF (IP.EQ.INMA) PRINT *,'Ratio between alphas= ',RIJ
          ENDIF
C         IF(ITER.EQ.1) THEN
C        IF (IP.EQ.INMA) PRINT *,'UL= ',UL,' VL= ',VL,' WL=',WL,
C         ENDIF
C_____________________________________________________________________
C_____________ Start of neighbour velocity calculation _____________
    IF(NPPOR.EQ.IPID) THEN
C_____________________ Initialise velocities _____________________
          IF(ITER.LE.1) THEN

           UN = AINI
           VN = AINI
           WN = AINI

           IF(IP.EQ.INMA) PRINT *,'UN=',UN,'VN=',VN,'WN=',WN

           UOLA(1,INL(IP)) = UN
           UOLA(2,INL(IP)) = VN
           UOLA(3,INL(IP)) = WN

           UOLB(1,INL(IP)) = UN
           UOLB(2,INL(IP)) = VN
           UOLB(3,INL(IP)) = WN

           UOLC(1,INL(IP)) = UN
           UOLC(2,INL(IP)) = VN
           UOLC(3,INL(IP)) = WN

           UTA = UOLA(1,INL(IP))
           VTA = UOLA(2,INL(IP))
           WTA = UOLA(3,INL(IP))

           UTB = UOLB(1,INL(IP))
           VTB = UOLB(2,INL(IP))
           WTB = UOLB(3,INL(IP))

           UTC = UOLC(1,INL(IP))
           VTC = UOLC(2,INL(IP))
           WTC = UOLC(3,INL(IP))

C____ PRINT TO TEST
C         IF(IP.EQ.INMA) PRINT *,'INMA',INMA
C         IF(IP.EQ.INMA) PRINT *,'UTA',UTA,'VTA=',VTA,'WTA=',WTA
```

```
C          IF(IP.EQ.INMB) PRINT *,'INMB',INMB
C          IF(IP.EQ.INMB) PRINT *,'UTB',UTB,'VTB=',VTB,'WTB=',WTB
C          IF(IP.EQ.INMC) PRINT *,'INMC',INMC
C          IF(IP.EQ.INMC) PRINT *,'UTC',UTC,'VTC=',VTC,'WTC=',WTC

          ENDIF
C         ELSE IF(ITER.GE.2) THEN
C_______IF(ITER.LE.1)

C          PRINT *,'ELSE',UN,'VN2=',VN,'WN2=',WN

C_____ Start of neighbouring cell data _____
C_____ retrieval _____
C_____ 1st row of cells _____
          IF(ITER.GT.1) THEN

          IF(ICTID.EQ.ICTY) THEN
           JNL = INL(IP)
           UN = UNL(1,INL(IP))
           VN = UNL(2,INL(IP))
           WN = UNL(3,INL(IP))

C          IF(IP.EQ.INMA) PRINT *,'IP=',IP,'JNL=',JNL
C          IF(IP.EQ.INMA) PRINT *,'UN2=',UN,'VN2=',VN,'WN2=',WN

C__ Underrelax resistance calculation _

           UNEW = UN
           VNEW = VN
           WNEW = WN

           UO = UOLA(1,INL(IP))
           VO = UOLA(2,INL(IP))
           WO = UOLA(3,INL(IP))

C          IF(IP.EQ.INMA) PRINT *,'UO-PR=',UO,'VO-PR=',VO,'WO-PR=',WO

           UN = (UNEW*RELAN)+(UO*RELAO)
           VN = (VNEW*RELAN)+(VO*RELAO)
           WN = (WNEW*RELAN)+(WO*RELAO)

C          IF(IP.EQ.INMA) PRINT *,'UN-RE=',UN,'VN-RE=',VN,'WN-RE=',WN

           UOLA(1,INL(IP)) = UN
           UOLA(2,INL(IP)) = VN
           UOLA(3,INL(IP)) = WN

           UO = UN
           VO = VN
           WO = WN

           UN = ABS(UN)
           VN = ABS(VN)
           WN = ABS(WN)

C          IF(IP.EQ.INMA) PRINT *,'UO-PA=',UO,'VO-PA=',VO,'WO-PA=',WO
C          IF(IP.EQ.INMA) PRINT *,'UNA=',UNA,'VNA=',VNA,'WNA=',WNA
C          IF(IP.EQ.INMA) PRINT *,'TEST LOOP A'

C         ELSE IF(ICTID.EQ.ICTB) THEN
          ENDIF
C___ End of: 1st row of cells _____
```

```
C_____ 2nd row of cells _____
      IF(ICTID.EQ.ICTB) THEN

            JNL = INB(IP)
            UN = UOLA(1,INB(IP))
            VN = UOLA(2,INB(IP))
            WN = UOLA(3,INB(IP))

            UN = ABS(UN)
            VN = ABS(VN)
            WN = ABS(WN)

C           PRINT *,'Check'
C           IF(IP.EQ.INMB) PRINT *,'Check'
C           IF(IP.EQ.INMB) PRINT *,'IP=',IP,'JNL=',JNL,'NB=',INMB
C           IF(IP.EQ.INMB) PRINT *,'UN2=',UN,'VN2=',VN,'WN2=',WN

          ENDIF
C___ End of: 2nd row of cells _____
C_____ 3rd row of cells _____
      IF(ICTID.EQ.ICTC) THEN

            JNL = INC(IP)
            UN = UOLA(1,INC(IP))
            VN = UOLA(2,INC(IP))
            WN = UOLA(3,INC(IP))

            UN = ABS(UN)
            VN = ABS(VN)
            WN = ABS(WN)
C           PRINT *,'Check'
C           IF(IP.EQ.INMC) PRINT *,'IP=',IP,'JNL=',JNL,'NC=',INMC
C           IF(IP.EQ.INMC) PRINT *,'UN3=',UN,'VN3=',VN,'WN3=',WN
          ENDIF
C___ End of: 3rd row of cells _____
     ENDIF
C___ IF(ITER.GE.1)
C___ End of neighbour velocity calculation _____

C_____ Calculate angle of incidence in XY plane _____

          THETA = ATAN(VN/UN)
          PI = 3.141593
C         IF(ITER.EQ.1) THEN
C        IF (IP.EQ.INMA) PRINT *,'THETA= ',THETA,' PI= ',PI
C         ENDIF

C_____ Convert angle to degrees _____
          TRD = THETA*180/PI
          TR = THETA
C_____ Calculate angle of incidence in XZ plane _____
          PHI = ATAN(WN/UN)
C_____ Convert angle to degrees _____
          PRD = PHI*180/PI
          PR = PHI
C         IF(ITER.EQ.1) THEN
C        IF (IP.EQ.INMA) PRINT *,'TRD= ',TRD
C        IF (IP.EQ.INMA) PRINT *,' PR= ',PR,'PRD= ',PRD
C         ENDIF

C_____ Define limits for the angle of incidence _____

c_____rad
```

```
          AMNR = ATAN(ST/HSY)
c_______DEG
          AMNA = AMNA/PI*180
c_______rad
          DALM = 90*PI/180
          DRL = (DALM-AMNR)*0.95
c_______DEG
          DAL = DRL/PI*180

      IF (IP.EQ.INMA) PRINT *,'Min mesh ratio= ',AMNR
      IF (IP.EQ.INMA) PRINT *,'Minimum angle (deg)= ',DALM
      IF (IP.EQ.INMA) PRINT *,'Angle limit (deg)= ',DAL
      IF (IP.EQ.INMA) PRINT *,'Angle limit (rad)= ',DRL

      IF (TR.GE.DRL) PRINT *,'Angle limited= ',TR,'at cell',IP

          IF (TR.GE.DRL) THEN
           TR = DRL
          ENDIF

      IF (PR.GE.DRL) PRINT *,'Angle limited= ',PR,'at cell',IP
          IF (PR.GE.DRL) THEN
           PR = DRL
          ENDIF

C_____________________ Calculate FAR _____________ _____ _____
          FAR1 = (HSY*COS(TR))-(ST*SIN(TR))
          FAR2 = (HZS*COS(PR))-(ST*SIN(PR))
          FAR3 = (HSY*COS(TR))+(SLY*COS(TR))
          FAR4 = (HZS*COS(PR))+(SLZ*COS(PR))

          FAR = (FAR1*FAR2)/(FAR3*FAR4)

C_____________ Define FAR limits _____________
          IF (FAR.LE.DLL) PRINT *,'FAR low limit at cell=',IP
          IF (FAR.LE.DLL) THEN
            FAR = DLL
          ENDIF

          IF (FAR.GE.DUL) PRINT *,'FAR high limit at cell=',IP
          IF (FAR.GE.DUL) THEN
            FAR = DUL
          ENDIF

          SCALAR(1) = FAR
          SCL1(IP) = FAR

C         IF (IP.EQ.INMA) PRINT *,'DLL= ',DLL,
C         IF (IP.EQ.INMA) PRINT *,'DUL= ',DUL,
        IF (IP.EQ.INMA) PRINT *,'NA=',INMA,'FAR= ',FAR,
        IF (IP.EQ.INMB) PRINT *,'NB=',INMB,'FAR= ',FAR,

C         IF(ITER.EQ.1) THEN
C         IF (IP.EQ.INMA) PRINT *,'FAR= ',FAR,
C         ENDIF
C_____________ Calculate variable resistance coefficient _____
          AA = -4444.8297
          BB = 13200.9818
          CC = -15548.5414
          DD = 9129.9442
          EE = -2705.0564
          FF = 331.5113
```

```
        RC = AA*FAR**5+BB*FAR**4+CC*FAR**3+DD*FAR**2+EE*FAR+FF
        RC = ABS(RC)
        SCALAR(2) = RC
        SCL2(IP) = RC

C       IF(ITER.EQ.1) THEN
      IF (IP.EQ.INMA) PRINT *,'NA=',INMA,'K-Factor-A= ',RC
      IF (IP.EQ.INMB) PRINT *,'NB=',INMB,'K-Factor-B= ',RC
      IF (IP.EQ.INMC) PRINT *,'NC=',INMC,'K-Factor-C= ',RC
C       ENDIF

C___ Calculate Velocity vector _____________
        VMAG=SQRT(UN*UN+VN*VN+WN*WN)
C       VCOR = VMAG/ABS(UN)
C        IF (IP.EQ.INMA) PRINT *,'VMAG= ',VMAG,'UN= ',UN
C        IF (IP.EQ.INMA) PRINT *,'Vel Correction factor= ',VCOR

C_____________ Calculate variable value of alpha (Unit length) __
        ALU = RC*DEN/2

C_____ Calculate thickness of porous medium as a function of _____
C__________ the angle of incidence in three dimensions ___________

C       DTP=SQRT(DTY**2+(DTZ*(SIN(PR))**2)

        DRAT=VMAG/UN
        DTP=SP*DRAT

        SCALAR(6) = DTP
        SCL6(IP) = DTP

        IF (IP.EQ.INMA) PRINT *,'SP=',SP
        IF (IP.EQ.INMA) PRINT *,'TR=',TRD,'PR=',PRD,'DTP=',DTP
        IF (IP.EQ.MON2) PRINT *,'TR-corner=',TRD,'PR=',PRD,'DTP=',DTP
        IF (IP.EQ.MON3) PRINT *,'TR-centre=',TRD,'PR=',PRD,'DTP=',DTP

C_____________ Define limits for PM length _____________________

        IF (DTP.LE.SP) THEN
      PRINT *,'PM length low limit',DTP,'at cell',IP
        DTP=SP
        ENDIF

        DTYL=SP/(COS(DRL))
        DTPL=SQRT(DTYL**2+(WN*DRAT)**2)
        DTPL=15.9

        IF (DTP.GE.DTPL) THEN
      PRINT *,'PM length high limit',DTP,'at cell',IP
        DTP=DTPL
        ENDIF

C_____________ Calculate variable value of alpha (True length) __
C       AL = (ALU/SP)*CORF*VCOR
        AL = (ALU/DTP)*CORF
        BE = AL*BA
        ALI=AL
        SCALAR(3) = ALI
        SCL3(IP) = ALI
C       ALJ=AL
C       ALK=AL
        ALJ = RIJ * AL
        ALK = RIJ * AL
```

```
C         ARAT = HSY / ST
C         ALJ = AL / ARAT
C         ALK = AL / ARAT

          BTI=BE
          BTJ=BE
          BTK=BE

          SCALAR(4) = ALJ
          SCL4(IP) = ALJ

          SCALAR(5) = ALK
          SCL5(IP) = ALK

C__________ Print data for testing _________

          IF(ITER.EQ.1) THEN
        IF (IP.EQ.INMA) PRINT *,'Alpha= ',AL,'Beta= ',BE
        IF (IP.EQ.INMA) PRINT *,'ALI=',ALI,'ALJ=',ALJ,'ALK=',ALK
        IF (IP.EQ.INMA) PRINT *,'BTI=',BTI,'BTJ=',BTJ,'BTK=',BTK
          ENDIF

C___ Calculate theoretical dP _______________

C         DP=SP*((AL*VMAG*VMAG)+(BE*VMAG))
C         IF(ITER.EQ.1) THEN
C           IF (IP.EQ.INMA) PRINT *,'Vel vector= ',VMAG,'dP= ',DP,
C         ENDIF

C___ Testing _______

C         INMA=232
C         IF (IP.EQ.INMA) PRINT *,'Alpha= ',AL,' Beta= ',BE,'DP=',DP,
C         IF (IP.EQ.INMA) PRINT *,'Den= ',DEN,'UN=',UN,'VN',VN,'WN',WN,
C         IF (IP.EQ.INMA) PRINT *,'Vel vector= ',VMAG,'Cell= ',INMA,
C         IF (IP.EQ.INMA) PRINT *,'Vel vector= ',VMAG,'dP= ',DP,

C____ Test at later iterations ________
        IF(ITER.EQ.ITWR) THEN
        IF (IP.EQ.INMA) PRINT *,'UN= ',UN,' VN= ',VN,' WN=',WN,
        IF (IP.EQ.INMA) PRINT *,'THETA= ',THETA,' PI= ',PI,
        IF (IP.EQ.INMA) PRINT *,'TRD= ',TRD,
        IF (IP.EQ.INMA) PRINT *,'PR= ',PR,'PRD= ',PRD,
        IF (IP.EQ.INMA) PRINT *,'FAR= ',FAR,
        IF (IP.EQ.INMA) PRINT *,'K-Factor= ',RC,
        IF (IP.EQ.INMA) PRINT *,'Alpha= ',AL,'Beta= ',BE,
        IF (IP.EQ.INMA) PRINT *,'ALI=',ALI,'ALJ=',ALJ,'ALK=',ALK,
        IF (IP.EQ.INMA) PRINT *,'BTI=',BTI,'BTJ=',BTJ,'BTK=',BTK,
            IF (IP.EQ.INMA) PRINT *,'Vel vector= ',VMAG,'dP= ',DP,
C           IF (IP.EQ.INMA) PRINT *,'Correction factor= ',CORF
C           IF (IP.EQ.INMA) PRINT *,'Vel Correction factor= ',VCOR
            IF (IP.EQ.INMA) PRINT *,'Scalar 1= ',SCALAR(1)
            IF (IP.EQ.INMA) PRINT *,'Scalar 2= ',SCALAR(2)
          ENDIF
      ENDIF
C     IF(NPPOR.EQ.PID)
      RETURN
      END
C
```

ANNEXURE E.7 : IMPLICIT IMPLEMENTATION OF THE MOMENTUM SINK TERM: TEST CASE

```
C***********************************************************************
      SUBROUTINE SORMOM(S1U,S2U,S1V,S2V,S1W,S2W,POROS)
C     Source-term for momentum
C***********************************************************************
C-----------------------------------------------------------------------*
C     STAR VERSION 3.20.000                                             *
C-----------------------------------------------------------------------*
      INCLUDE 'comdb.inc'
       COMMON/USR001/INTFLG(100)
       INCLUDE 'usrdat.inc'
      DIMENSION SCALAR(50)
      EQUIVALENCE( UDAT12(001), ICTID )
      EQUIVALENCE( UDAT03(001), CON )
      EQUIVALENCE( UDAT03(006), G1 )
      EQUIVALENCE( UDAT03(007), G2 )
      EQUIVALENCE( UDAT03(008), G3 )
      EQUIVALENCE( UDAT03(019), VOLP )
      EQUIVALENCE( UDAT04(001), CP )
      EQUIVALENCE( UDAT04(002), DEN )
      EQUIVALENCE( UDAT04(003), ED )
      EQUIVALENCE( UDAT04(005), PR )
      EQUIVALENCE( UDAT04(008), TE )
      EQUIVALENCE( UDAT04(009), SCALAR(01) )
      EQUIVALENCE( UDAT04(059), U )
      EQUIVALENCE( UDAT04(060), V )
      EQUIVALENCE( UDAT04(061), W )
      EQUIVALENCE( UDAT04(062), VISM )
      EQUIVALENCE( UDAT04(063), VIST )
      EQUIVALENCE( UDAT04(007), T )
      EQUIVALENCE( UDAT04(067), X )
      EQUIVALENCE( UDAT04(068), Y )
      EQUIVALENCE( UDAT04(069), Z )
C-----------------------------------------------------------------------
C
C     This subroutine enables the user to specify the momentum source
C     term (per unit volume) in linearised form:
C
C        Source in x direction = S1U-S2U*U, (N/m3)
C        Source in y direction = S1V-S2V*V, (N/m3)
C        Source in z direction = S1W-S2W*W, (N/m3)
C
C     in an arbitrary manner.
C
C     ** Parameters to be returned to STAR:  S1U,S2U,S1V,S2V,S1W,S2W,
C                                   POROS
C-----------------------------------------------------------------------
C     Sample coding: Body forces due to rotation around the z-axis
C
C      OMEGA=100.
C      S1U=DEN*X*OMEGA**2
C      S1V=DEN*Y*OMEGA**2
C-----------------------------------------------------------------------C
      if (ictid.eq.4) then
C       vmag=(u**2+v**2+w**2)**.5
      s1u=0
      s2u=10*u
      s1v=0
      s2v=10*v
```

```
      s1w=0
      s2w=10*w
      endif
      RETURN
      END
C
```

ANNEXURE E.8 : EXPLICIT IMPLEMENTATION OF THE MOMENTUM SINK TERM: TEST CASE

```
C*************************************************************************
      SUBROUTINE SORMOM(S1U,S2U,S1V,S2V,S1W,S2W,POROS)
C     Source-term for momentum
C*************************************************************************
C-------------------------------------------------------------------------*
C     STAR VERSION 3.20.000                                               *
C-------------------------------------------------------------------------*
      INCLUDE 'comdb.inc'
      COMMON/USR001/INTFLG(100)
      INCLUDE 'usrdat.inc'
      DIMENSION SCALAR(50)
      EQUIVALENCE( UDAT12(001), ICTID )
      EQUIVALENCE( UDAT03(001), CON )
      EQUIVALENCE( UDAT03(006), G1 )
      EQUIVALENCE( UDAT03(007), G2 )
      EQUIVALENCE( UDAT03(008), G3 )
      EQUIVALENCE( UDAT03(019), VOLP )
      EQUIVALENCE( UDAT04(001), CP )
      EQUIVALENCE( UDAT04(002), DEN )
      EQUIVALENCE( UDAT04(003), ED )
      EQUIVALENCE( UDAT04(005), PR )
      EQUIVALENCE( UDAT04(008), TE )
      EQUIVALENCE( UDAT04(009), SCALAR(01) )
      EQUIVALENCE( UDAT04(059), U )
      EQUIVALENCE( UDAT04(060), V )
      EQUIVALENCE( UDAT04(061), W )
      EQUIVALENCE( UDAT04(062), VISM )
      EQUIVALENCE( UDAT04(063), VIST )
      EQUIVALENCE( UDAT04(007), T )
      EQUIVALENCE( UDAT04(067), X )
      EQUIVALENCE( UDAT04(068), Y )
      EQUIVALENCE( UDAT04(069), Z )
C-------------------------------------------------------------------------

      if (ictid.eq.4) then
      vmag=(u**2+v**2+w**2)**.5
      s1u=-10*5*5
      s2u=0
      s1v=-10*v
      s2v=0
      s1w=-10*w
      s2w=0
      endif
      RETURN
      END
C
```

ANNEXURE E.9 : IMPLICIT IMPLEMENTATION OF THE MOMENTUM SINK TERM WITH A CORRECTION FACTOR: TEST CASE

```
C**********************************************************************
      SUBROUTINE SORMOM(S1U,S2U,S1V,S2V,S1W,S2W,POROS)
C     Source-term for momentum
C**********************************************************************
C----------------------------------------------------------------------*
C     STAR VERSION 3.20.000                                            *
C----------------------------------------------------------------------*
      INCLUDE 'comdb.inc'
      COMMON/USR001/INTFLG(100)
      INCLUDE 'usrdat.inc'
      DIMENSION SCALAR(50)
      EQUIVALENCE( UDAT12(001), ICTID )
      EQUIVALENCE( UDAT03(001), CON )
      EQUIVALENCE( UDAT03(006), G1 )
      EQUIVALENCE( UDAT03(007), G2 )
      EQUIVALENCE( UDAT03(008), G3 )
      EQUIVALENCE( UDAT03(019), VOLP )
      EQUIVALENCE( UDAT04(001), CP )
      EQUIVALENCE( UDAT04(002), DEN )
      EQUIVALENCE( UDAT04(003), ED )
      EQUIVALENCE( UDAT04(005), PR )
      EQUIVALENCE( UDAT04(008), TE )
      EQUIVALENCE( UDAT04(009), SCALAR(01) )
      EQUIVALENCE( UDAT04(059), U )
      EQUIVALENCE( UDAT04(060), V )
      EQUIVALENCE( UDAT04(061), W )
      EQUIVALENCE( UDAT04(062), VISM )
      EQUIVALENCE( UDAT04(063), VIST )
      EQUIVALENCE( UDAT04(007), T )
      EQUIVALENCE( UDAT04(067), X )
      EQUIVALENCE( UDAT04(068), Y )
      EQUIVALENCE( UDAT04(069), Z )
C-----------------------------------------------------------------------C
      if (ictid.eq.4) then
      vmag=(u**2+v**2+w**2)**.5
      cf=5/u
      s1u=0.0
      s2u=10*5*cf
      s1v=0.0
      s2v=0.0
      s1w=0.0
      s2w=0.0
      endif
      RETURN
      END
C
```

ANNEXURE E.10 : EXPLICIT IMPLEMENTATION OF THE MOMENTUM SINK TERM: FULL DIFFUSER MODEL

```
C***********************************************************************
      SUBROUTINE SORMOM(S1U,S2U,S1V,S2V,S1W,S2W,POROS)
C     Source-term for momentum
C***********************************************************************
C-----------------------------------------------------------------------*
C     STAR RELEASE 3.150                                                *
C-----------------------------------------------------------------------*
      INCLUDE 'comdb.inc'
      INCLUDE '../parm.inc'

      COMMON/USR001/INTFLG(100)

      INCLUDE 'usrdat.inc'
      DIMENSION SCALAR(50)
      EQUIVALENCE( UDAT12(001), ICTID )
      EQUIVALENCE( UDAT03(001), CON )
      EQUIVALENCE( UDAT03(006), G1 )
      EQUIVALENCE( UDAT03(007), G2 )
      EQUIVALENCE( UDAT03(008), G3 )
      EQUIVALENCE( UDAT03(019), VOLP )
      EQUIVALENCE( UDAT04(001), CP )
      EQUIVALENCE( UDAT04(002), DEN )
      EQUIVALENCE( UDAT04(003), ED )
      EQUIVALENCE( UDAT04(005), PR )
      EQUIVALENCE( UDAT04(008), TE )
      EQUIVALENCE( UDAT04(009), SCALAR(01) )
      EQUIVALENCE( UDAT04(059), U )
      EQUIVALENCE( UDAT04(060), V )
      EQUIVALENCE( UDAT04(061), W )
      EQUIVALENCE( UDAT04(062), VISM )
      EQUIVALENCE( UDAT04(063), VIST )
      EQUIVALENCE( UDAT04(007), T )
      EQUIVALENCE( UDAT04(067), X )
      EQUIVALENCE( UDAT04(068), Y )
      EQUIVALENCE( UDAT04(069), Z )
C_____________________________________________________________________
C_____________________ Additional common blocks ____________________
C_____________________________________________________________________

      INCLUDE 'cblocks.inc'

C_____________________________________________________________________
C_____________________ USER Input data _____________________________
C_____________________________________________________________________

      INCLUDE 'inpdata.inc'
C-----------------------------------------------------------------------
C     This subroutine enables the user to specify the momentum source
C     term (per unit volume) in linearised form:
C
C        Source in x direction = S1U-S2U*U, (N/m3)
C        Source in y direction = S1V-S2V*V, (N/m3)
C        Source in z direction = S1W-S2W*W, (N/m3)
C
C     in an arbitray manner.
C
C     ** Parameters to be returned to STAR:  S1U,S2U,S1V,S2V,S1W,S2W,
C                                            POROS
```

```
C
C-----------------------------------------------------------------------
C
C     Sample coding: Body forces due to rotation around the z-axis
C
C      OMEGA=100.
C      S1U=DEN*X*OMEGA**2
C      S1V=DEN*Y*OMEGA**2
C-----------------------------------------------------------------------C

C_____________________________________________________________________
C_____________________ Define relaxation factor ______________________
C_____________________________________________________________________

C          RELAO = 0.5
           RELAN = 1 - RELAO
C          INIT = 5

C_____________________________________________________________________
C_____________________ Test Input data assignment ____________________
C_____________________________________________________________________

           IOF2 = IOFF * 2
           IOF3 = IOFF * 3
           INMA = MONC
           INMB = INMA + IOFF
           INMC = INMA + IOF2
           ICTB = ICTY + 1
           ICTC = ICTY + 2

           IF(ITER.EQ.1) THEN
         IF (IP.EQ.INMA) PRINT *,'Porosity ID= ',IPID,'ICTY= ',ICTY
         IF (IP.EQ.INMA) PRINT *,'ICTB= ',ICTB,'ICTC ',ICTC
         IF (IP.EQ.INMA) PRINT *,'INMA= ',INMA,'INMB= ',INMB
         IF (IP.EQ.INMA) PRINT *,'INMC= ',INMC
         IF (IP.EQ.INMA) PRINT *,'OFFSET 1= ',IOFF,'OFFSET 2= ',IOF2
         IF (IP.EQ.INMA) PRINT *,'OFFSET 3= ',IOF3
         IF (IP.EQ.INMA) PRINT *,'ST= ',ST,' HSY= ',HSY,' HZS=',HZS
         IF (IP.EQ.INMA) PRINT *,'HPY= ',HPY,' HPZ= ',HPZ,' SLY=',SLY
         IF (IP.EQ.INMA) PRINT *,'SLZ= ',SLZ,' SP= ',SP,' BA=',BA
         IF (IP.EQ.INMA) PRINT *,'SLZ= ',SLZ,' SP= ',SP,' BA=',BA
         IF (IP.EQ.INMA) PRINT *,'Ratio between alphas= ',RIJ
           ENDIF

C          IF(ITER.EQ.1) THEN
C         IF (IP.EQ.INMA) PRINT *,'UL= ',UL,' VL= ',VL,' WL=',WL,
C          ENDIF

C_____________________________________________________________________

C_____________ Start of neighbour velocity calculation _____________
      IF(ICTID.EQ.ICTY.OR.ICTID.EQ.ICTB.OR.ICTID.EQ.ICTC) THEN

C_____________________ Initialise velocities ________________________
           IF(ITER.LE.1) THEN

            UN = AINI
            VN = AINI
            WN = AINI

           IF(IP.EQ.INMA) PRINT *,'UN=',UN,'VN=',VN,'WN=',WN

            UOLA(1,INL(IP)) = UN
```

```
            UOLA(2,INL(IP)) = VN
            UOLA(3,INL(IP)) = WN

            UOLB(1,INL(IP)) = UN
            UOLB(2,INL(IP)) = VN
            UOLB(3,INL(IP)) = WN

            UOLC(1,INL(IP)) = UN
            UOLC(2,INL(IP)) = VN
            UOLC(3,INL(IP)) = WN

            UTA = UOLA(1,INL(IP))
            VTA = UOLA(2,INL(IP))
            WTA = UOLA(3,INL(IP))

            UTB = UOLB(1,INL(IP))
            VTB = UOLB(2,INL(IP))
            WTB = UOLB(3,INL(IP))

            UTC = UOLC(1,INL(IP))
            VTC = UOLC(2,INL(IP))
            WTC = UOLC(3,INL(IP))

C____ PRINT TO TEST
C           IF(IP.EQ.INMA) PRINT *,'INMA',INMA
C           IF(IP.EQ.INMA) PRINT *,'UTA',UTA,'VTA=',VTA,'WTA=',WTA
C           IF(IP.EQ.INMB) PRINT *,'INMB',INMB
C           IF(IP.EQ.INMB) PRINT *,'UTB',UTB,'VTB=',VTB,'WTB=',WTB
C           IF(IP.EQ.INMC) PRINT *,'INMC',INMC
C           IF(IP.EQ.INMC) PRINT *,'UTC',UTC,'VTC=',VTC,'WTC=',WTC

          ENDIF
C         ELSE IF(ITER.GE.2) THEN
C_______IF(ITER.LE.1)

C           PRINT *,'ELSE',UN,'VN2=',VN,'WN2=',WN

C_____ Start of neighbouring cell data ____
C_____ retrieval _____

C_____ 1st row of cells _____
          IF(ITER.GT.1) THEN

       IF(ICTID.EQ.ICTY) THEN

            JNL = INL(IP)
            UN = UNL(1,INL(IP))
            VN = UNL(2,INL(IP))
            WN = UNL(3,INL(IP))

C           IF(IP.EQ.INMA) PRINT *,'IP=',IP,'JNL=',JNL
C           IF(IP.EQ.INMA) PRINT *,'UN2=',UN,'VN2=',VN,'WN2=',WN

C__ Underrelax resistance calculation _

            UNEW = UN
            VNEW = VN
            WNEW = WN

            UO = UOLA(1,INL(IP))
            VO = UOLA(2,INL(IP))
            WO = UOLA(3,INL(IP))
```

```
C         IF(IP.EQ.INMA) PRINT *,'UO-PR=',UO,'VO-PR=',VO,'WO-PR=',WO

          UN = (UNEW*RELAN)+(UO*RELAO)
          VN = (VNEW*RELAN)+(VO*RELAO)
          WN = (WNEW*RELAN)+(WO*RELAO)

C         IF(IP.EQ.INMA) PRINT *,'UN-RE=',UN,'VN-RE=',VN,'WN-RE=',WN

          UOLA(1,INL(IP)) = UN
          UOLA(2,INL(IP)) = VN
          UOLA(3,INL(IP)) = WN

          UO = UN
          VO = VN
          WO = WN

          UN = ABS(UN)
          VN = ABS(VN)
          WN = ABS(WN)

C         IF(IP.EQ.INMA) PRINT *,'UO-PA=',UO,'VO-PA=',VO,'WO-PA=',WO
C         IF(IP.EQ.INMA) PRINT *,'UNA=',UNA,'VNA=',VNA,'WNA=',WNA
C         IF(IP.EQ.INMA) PRINT *,'TEST LOOP A'

C        ELSE IF(ICTID.EQ.ICTB) THEN
         ENDIF
C___ End of: 1st row of cells _____

C_____________________ 2nd row of cells _____________
     IF(ICTID.EQ.ICTB) THEN

          JNL = INB(IP)
          UN = UOLA(1,INB(IP))
          VN = UOLA(2,INB(IP))
          WN = UOLA(3,INB(IP))

          UN = ABS(UN)
          VN = ABS(VN)
          WN = ABS(WN)

C         PRINT *,'Check'
C         IF(IP.EQ.INMB) PRINT *,'Check'
C         IF(IP.EQ.INMB) PRINT *,'IP=',IP,'JNL=',JNL,'NB=',INMB
C         IF(IP.EQ.INMB) PRINT *,'UN2=',UN,'VN2=',VN,'WN2=',WN

         ENDIF
C___ End of: 2nd row of cells _____

C_____________________ 3rd row of cells _____________
     IF(ICTID.EQ.ICTC) THEN

          JNL = INC(IP)
          UN = UOLA(1,INC(IP))
          VN = UOLA(2,INC(IP))
          WN = UOLA(3,INC(IP))

          UN = ABS(UN)
          VN = ABS(VN)
          WN = ABS(WN)

C         PRINT *,'Check'
C         IF(IP.EQ.INMC) PRINT *,'IP=',IP,'JNL=',JNL,'NC=',INMC
C         IF(IP.EQ.INMC) PRINT *,'UN3=',UN,'VN3=',VN,'WN3=',WN
```

```
          ENDIF
C___ End of: 3rd row of cells _____

      ENDIF
C___ IF(ITER.GE.1)

C___ End of neighbour velocity calculation _____

C_____ Calculate angle of incidence in XY plane _____

          THETA = ATAN(VN/UN)
          PI = 3.141593

C         IF(ITER.EQ.1) THEN
C        IF (IP.EQ.INMA) PRINT *,'THETA= ',THETA,' PI= ',PI
C         ENDIF

C_____ Convert angle to degrees _____

          TRD = THETA*180/PI
          TR = THETA

C_____ Calculate angle of incidence in XZ plane _____

          PHI = ATAN(WN/UN)

C_____ Convert angle to degrees _____

          PRD = PHI*180/PI
          PR = PHI

C         IF(ITER.EQ.1) THEN
C        IF (IP.EQ.INMA) PRINT *,'TRD= ',TRD
C        IF (IP.EQ.INMA) PRINT *,' PR= ',PR,'PRD= ',PRD
C         ENDIF

C_____ Define limits for the angle of incidence _____

c_____rad
          AMNR = ATAN(ST/HSY)
c_____DEG
          AMNA = AMNA/PI*180
c_____rad
          DALM = 90*PI/180
          DRL = (DALM-AMNR)*0.95
c_____DEG
          DAL = DRL/PI*180

      IF (IP.EQ.INMA) PRINT *,'Min mesh ratio= ',AMNR
      IF (IP.EQ.INMA) PRINT *,'Minimum angle (deg)= ',DALM
      IF (IP.EQ.INMA) PRINT *,'Angle limit (deg)= ',DAL
      IF (IP.EQ.INMA) PRINT *,'Angle limit (rad)= ',DRL

      IF (TR.GE.DRL) PRINT *,'Angle limited= ',TR,'at cell',IP

          IF (TR.GE.DRL) THEN
           TR = DRL
          ENDIF

      IF (PR.GE.DRL) PRINT *,'Angle limited= ',PR,'at cell',IP

          IF (PR.GE.DRL) THEN
```

```
          PR = DRL
         ENDIF

C_____ Calculate FAR _____

         FAR1 = (HSY*COS(TR))-(ST*SIN(TR))
         FAR2 = (HZS*COS(PR))-(ST*SIN(PR))
         FAR3 = (HSY*COS(TR))+(SLY*COS(TR))
         FAR4 = (HZS*COS(PR))+(SLZ*COS(PR))

         FAR = (FAR1*FAR2)/(FAR3*FAR4)

!_____ Define FAR _____

         IF (FAR.LE.DLL) PRINT *,'FAR low limit at cell=',IP

         IF (FAR.LE.DLL) THEN
           FAR = DLL
         ENDIF

         IF (FAR.GE.DUL) PRINT *,'FAR high limit at cell=',IP

         IF (FAR.GE.DUL) THEN
           FAR = DUL
         ENDIF

         SCALAR(1) = FAR
         SCL1(IP) = FAR
C        IF (IP.EQ.INMA) PRINT *,'DLL= ',DLL,
C        IF (IP.EQ.INMA) PRINT *,'DUL= ',DUL,
       IF (IP.EQ.INMA) PRINT *,'NA=',INMA,'FAR= ',FAR,
       IF (IP.EQ.INMB) PRINT *,'NB=',INMB,'FAR= ',FAR,

C        IF(ITER.EQ.1) THEN
C        IF (IP.EQ.INMA) PRINT *,'FAR= ',FAR,
C        ENDIF

C_____ Calculate variable resistance coefficient _____

         AA = -4444.8297
         BB = 13200.9818
         CC = -15548.5414
         DD = 9129.9442
         EE = -2705.0564
         FF = 331.5113

         RC = AA*FAR**5+BB*FAR**4+CC*FAR**3+DD*FAR**2+EE*FAR+FF
         RC = ABS(RC)

         SCALAR(2) = RC
         SCL2(IP) = RC

C        IF(ITER.EQ.1) THEN
       IF (IP.EQ.INMA) PRINT *,'NA=',INMA,'K-Factor-A= ',RC
       IF (IP.EQ.INMB) PRINT *,'NB=',INMB,'K-Factor-B= ',RC
       IF (IP.EQ.INMC) PRINT *,'NC=',INMC,'K-Factor-C= ',RC
C        ENDIF

C___ Calculate Velocity vector _____

         VMAG=SQRT(UN*UN+VN*VN+WN*WN)

C        VCOR = VMAG/ABS(UN)
```

```
C          IF (IP.EQ.INMA) PRINT *,'VMAG= ',VMAG,'UN= ',UN
C          IF (IP.EQ.INMA) PRINT *,'Vel Correction factor= ',VCOR

C_____ Calculate variable value of alpha (Unit length) __

          ALU = RC*DEN/2

C_____ Calculate thickness of porous medium as a function of _____
C_____ the angle of incidence in three dimensions _____

C         DTP=SQRT(DTY**2+(DTZ*(SIN(PR))**2)

          DRAT=VMAG/UN
          DTP=SP*DRAT

          SCALAR(6) = DTP
          SCL6(IP) = DTP

          IF (IP.EQ.INMA) PRINT *,'SP=',SP
          IF (IP.EQ.INMA) PRINT *,'TR=',TRD,'PR=',PRD,'DTP=',DTP
          IF (IP.EQ.MON2) PRINT *,'TR-corner=',TRD,'PR=',PRD,'DTP=',DTP
          IF (IP.EQ.MON3) PRINT *,'TR-centre=',TRD,'PR=',PRD,'DTP=',DTP

C_____ Define limits for PM length _____

          IF (DTP.LE.SP) THEN
       PRINT *,'PM length low limit',DTP,'at cell',IP
          DTP=SP
          ENDIF

          DTYL=SP/(COS(DRL))
          DTPL=SQRT(DTYL**2+(WN*DRAT)**2)
          DTPL=15.9
          IF (DTP.GE.DTPL) THEN
       PRINT *,'PM length high limit',DTP,'at cell',IP
          DTP=DTPL
          ENDIF

C_____ Calculate variable value of alpha (True length) __

C         AL = (ALU/SP)*CORF*VCOR
          AL = (ALU/DTP)*CORF

          BE = AL*BA

          ALI=AL

          SCALAR(3) = ALI
          SCL3(IP) = ALI

C         ALJ=AL
C         ALK=AL
          ALJ = RIJ * AL

          SCALAR(4) = ALJ
          SCL4(IP) = ALJ

          ALK = RIJ * AL

          SCALAR(5) = ALK
          SCL5(IP) = ALK

C         ARAT = HSY / ST
```

```
C         ALJ = AL / ARAT
C         ALK = AL / ARAT

          BTI=BE
          BTJ=BE
          BTK=BE

          IF(ITER.EQ.1) THEN
        IF (IP.EQ.INMA) PRINT *,'Alpha= ',AL,'Beta= ',BE,
        IF (IP.EQ.INMA) PRINT *,'ALI=',ALI,'ALJ=',ALJ,'ALK=',ALK,
        IF (IP.EQ.INMA) PRINT *,'BTI=',BTI,'BTJ=',BTJ,'BTK=',BTK,
          ENDIF

C___ Calculate theoretical dP _____________

C         DP=SP*((AL*VMAG*VMAG)+(BE*VMAG))

C         IF(ITER.EQ.1) THEN
C           IF (IP.EQ.INMA) PRINT *,'Vel vector= ',VMAG,'dP= ',DP,
C         ENDIF

C___ Testing ______

C         INMA=232
C         IF (IP.EQ.INMA) PRINT *,'Alpha= ',AL,' Beta= ',BE,'DP=',DP,
C         IF (IP.EQ.INMA) PRINT *,'Den= ',DEN,'UN=',UN,'VN',VN,'WN',WN,
C         IF (IP.EQ.INMA) PRINT *,'Vel vector= ',VMAG,'Cell= ',INMA,
C         IF (IP.EQ.INMA) PRINT *,'Vel vector= ',VMAG,'dP= ',DP,

C_____ Define momentum sink __________

      s1u=-AL*VMAG*VMAG
      s2u=0.0
      s1v=0.0
      s2v=0.0
      s1w=0.0
      s2w=0.0

          IF (IP.EQ.INMA) PRINT *,'S1U= ',s1u,' S2U= ',s2u

C____ Test at later iterations _______
          IF(ITER.EQ.ITWR) THEN
        IF (IP.EQ.INMA) PRINT *,'UN= ',UN,' VN= ',VN,' WN=',WN,
        IF (IP.EQ.INMA) PRINT *,'THETA= ',THETA,' PI= ',PI,
        IF (IP.EQ.INMA) PRINT *,'TRD= ',TRD,
        IF (IP.EQ.INMA) PRINT *,'PR= ',PR,'PRD= ',PRD,
        IF (IP.EQ.INMA) PRINT *,'FAR= ',FAR,
        IF (IP.EQ.INMA) PRINT *,'K-Factor= ',RC,
        IF (IP.EQ.INMA) PRINT *,'Alpha= ',AL,'Beta= ',BE,
        IF (IP.EQ.INMA) PRINT *,'ALI=',ALI,'ALJ=',ALJ,'ALK=',ALK,
        IF (IP.EQ.INMA) PRINT *,'BTI=',BTI,'BTJ=',BTJ,'BTK=',BTK,
            IF (IP.EQ.INMA) PRINT *,'Vel vector= ',VMAG,'dP= ',DP,
C           IF (IP.EQ.INMA) PRINT *,'Correction factor= ',CORF
C           IF (IP.EQ.INMA) PRINT *,'Vel Correction factor= ',VCOR
            IF (IP.EQ.INMA) PRINT *,'Scalar 1= ',SCALAR(1)
            IF (IP.EQ.INMA) PRINT *,'Scalar 2= ',SCALAR(2)
          ENDIF
      ENDIF
C     IF(NPPOR.EQ.PID)
      RETURN
      END
C
```

ANNEXURE E.11 : IMPLICIT IMPLEMENTATION OF THE MOMENTUM SINK TERM WITH A CORRECTION FACTOR: FULL DIFFUSER MODEL

The definition of the neighbour cell lists and calculation of the resistance factor is the same for the implicit and explicit approach as shown in the previous section. The only difference is the definition of the momentum sink term where S2 is defined instead of S1:

```
>>>
C_____ Define momentum sink _____________

C__Calculate velocity magnitude of neighbour cells
        VMAG=SQRT(UN*UN+VN*VN+WN*WN)

C__Calculate velocity magnitude of local cells
        VMGL=SQRT(U*U+V*V+W*W)

        CF=VMAG/VMGL

      s1u=0.0
      s2u=AL*VMAG*CF
      s1v=0.0
      s2v=0.0
      s1w=0.0
      s2w=0.0

        IF (IP.EQ.INMA) PRINT *,'Correction factor= ',CF
        IF (IP.EQ.INMA) PRINT *,'S1U= ',s1u,' S2U= ',s2u
        IF (IP.EQ.INMA) PRINT *,'VMAG= ',VMAG,' VMGL= ',VMGL
>>>
```

ANNEXURE F : ADDITIONAL COMPARITIVE RESULTS

ANNEXURE F.1 : Flow through diffusers

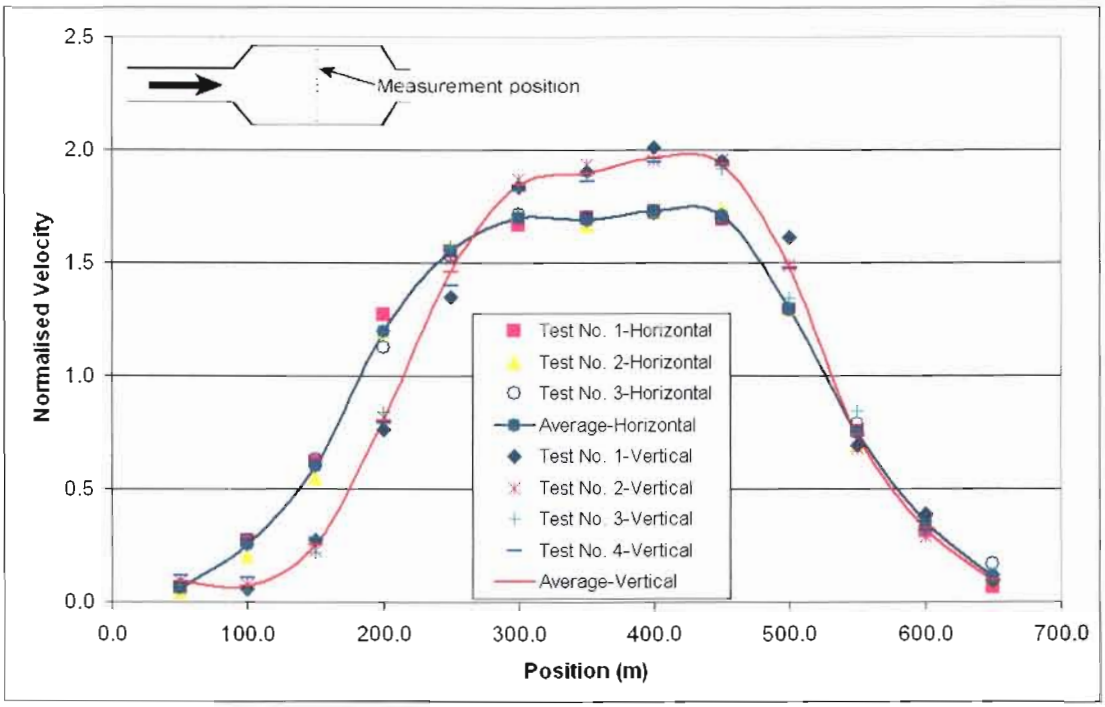

Figure 115: Normalised flow distribution in the centre of the 120° diffuser

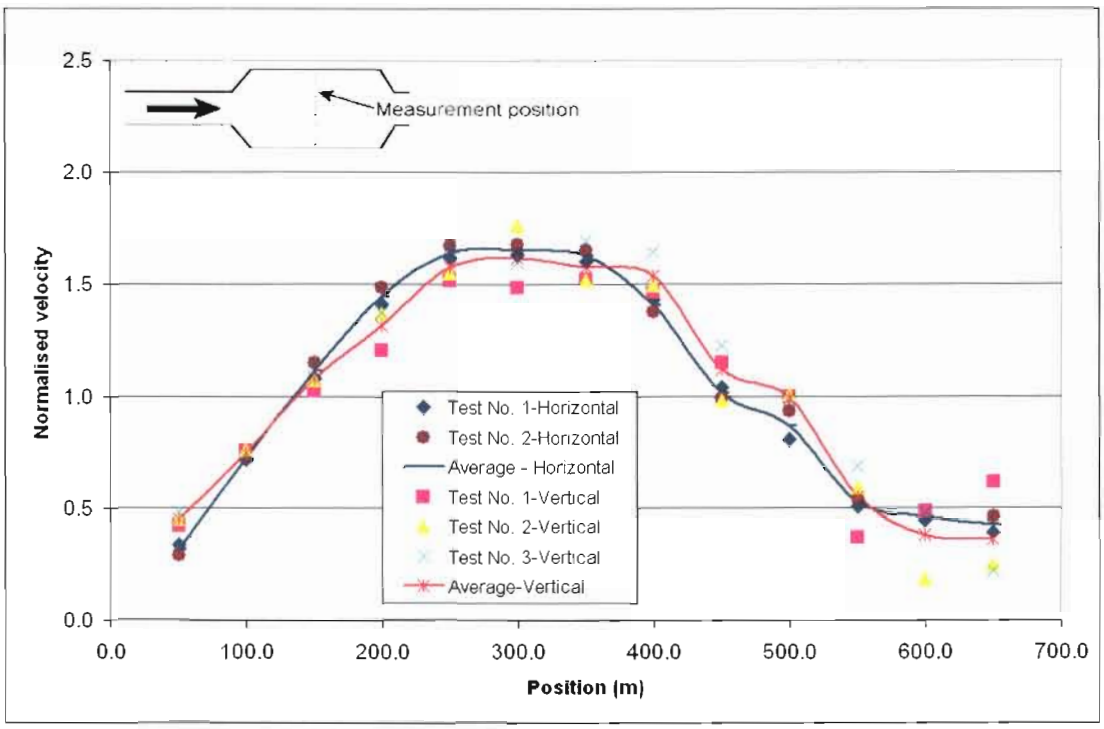

Figure 116: Normalised flow distribution in the centre of the 60° diffuser

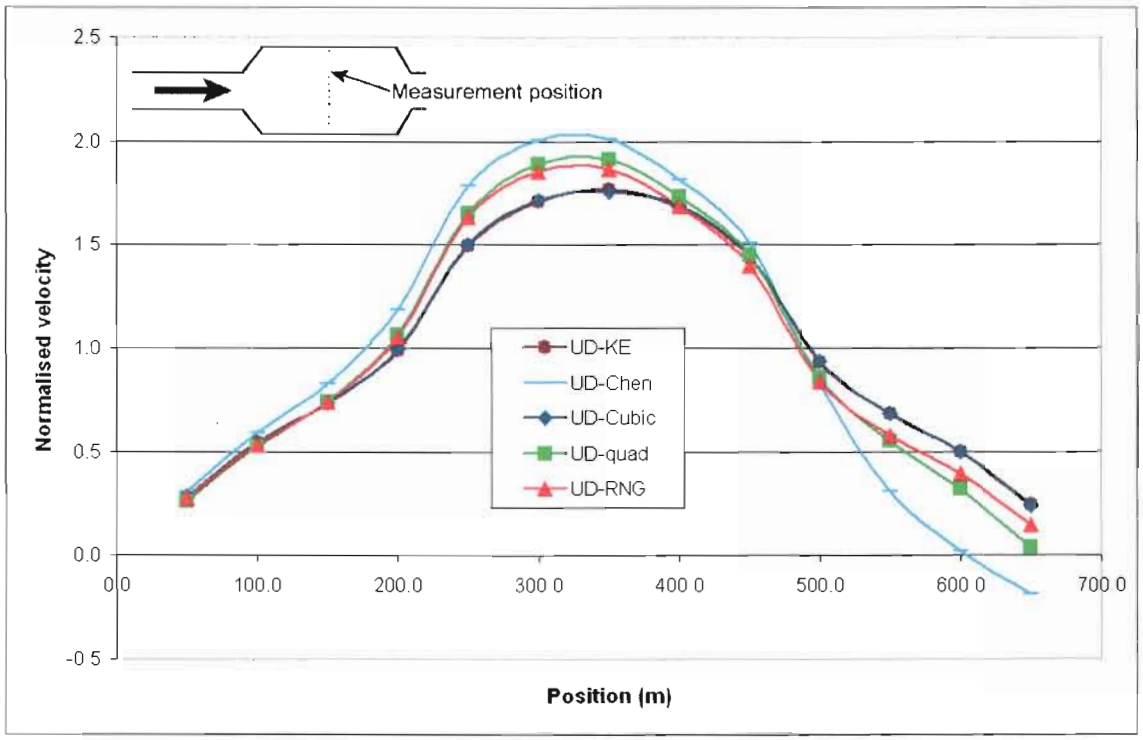

Figure 117: Testing different turbulence models on the 120° diffuser central position

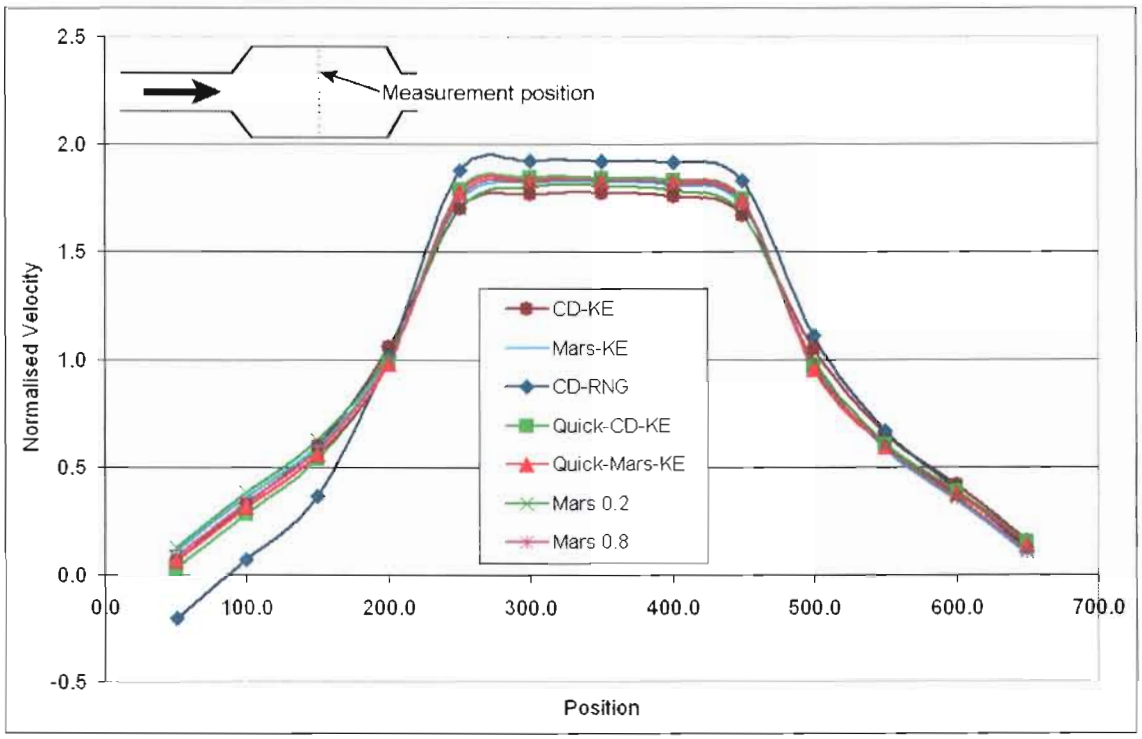

Figure 118: Testing discretisation schemes on the 120° diffuser central position

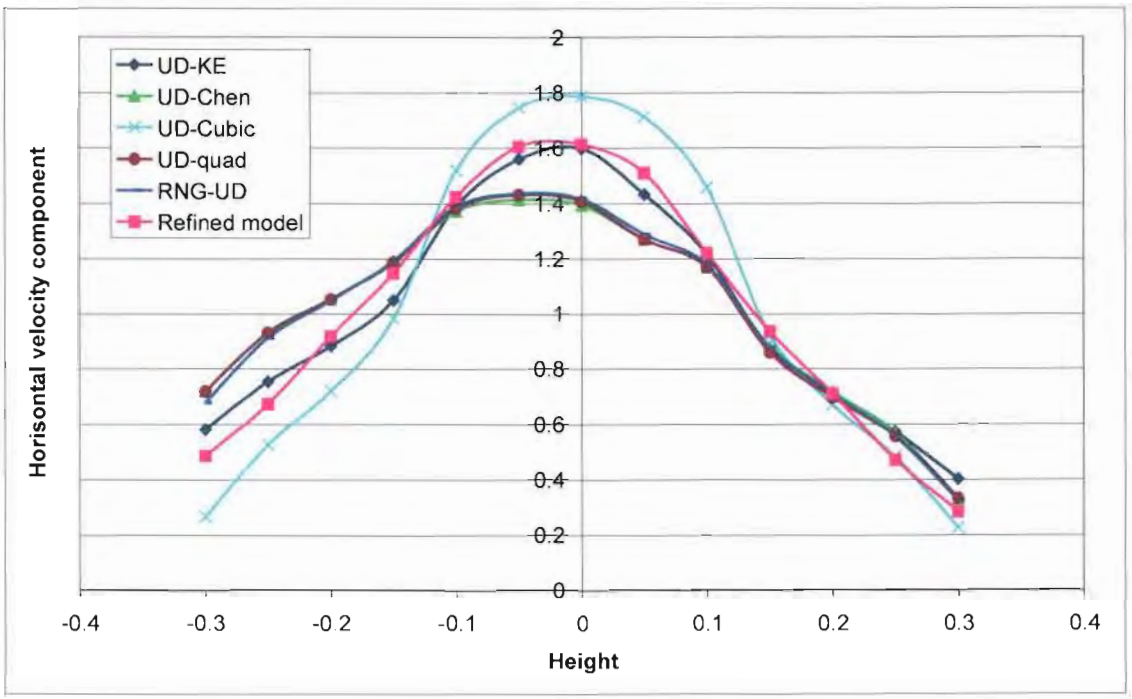

Figure 119: Testing different turbulence models on the 60° diffuser central position

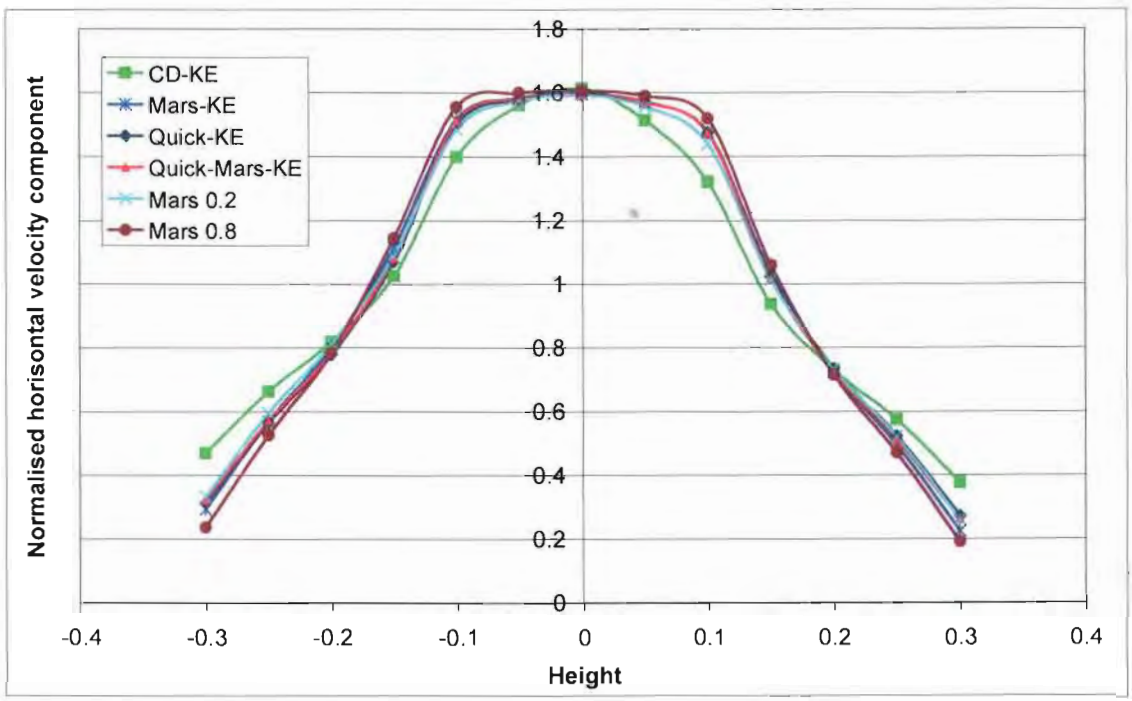

Figure 120: Testing discretisation schemes on the 60° diffuser front position

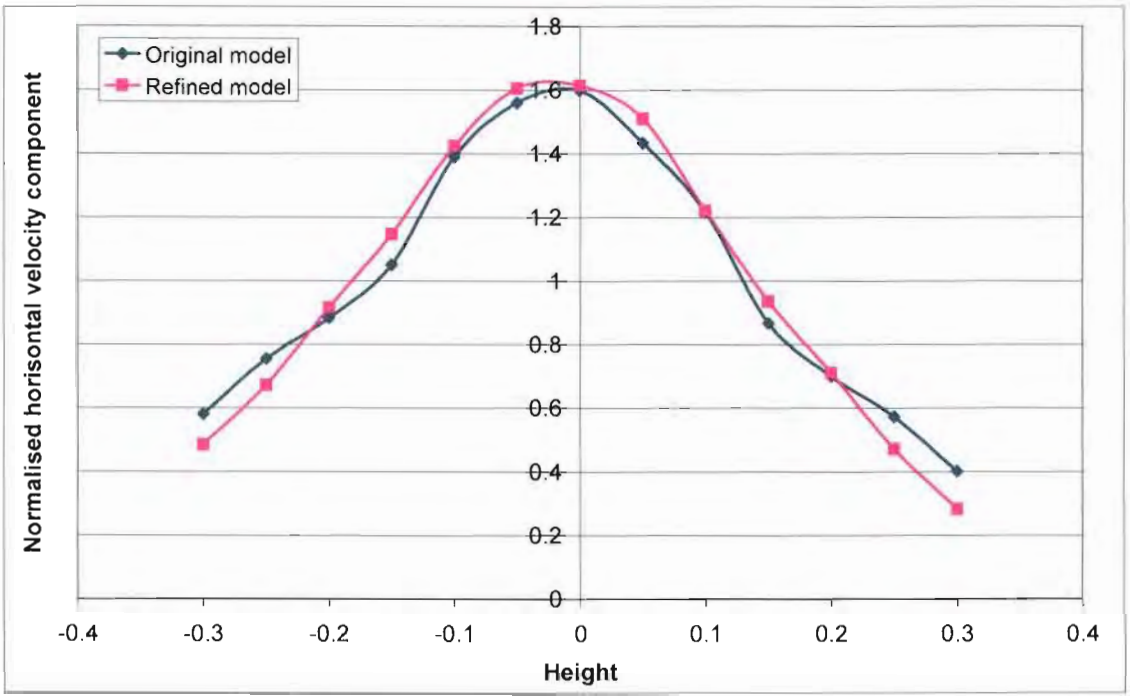

Figure 121: The influence of cell refinement on the flow distribution in the centre

ANNEXURE F.2 60° Diffuser with screens

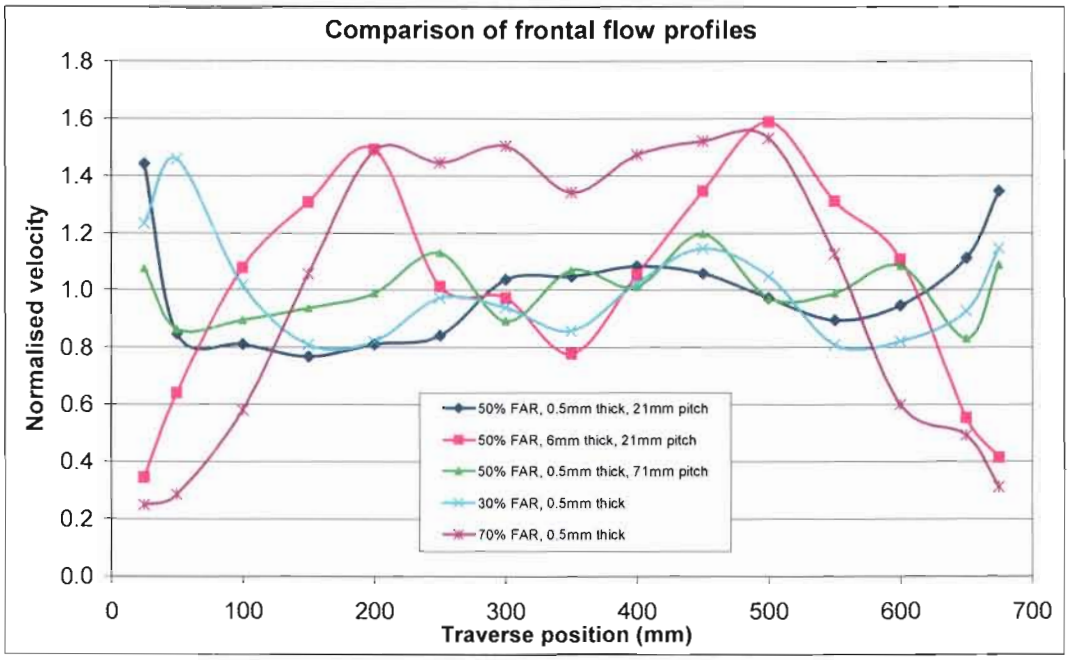

Figure 122: Comparison of averaged profiles in the frontal diffuser position

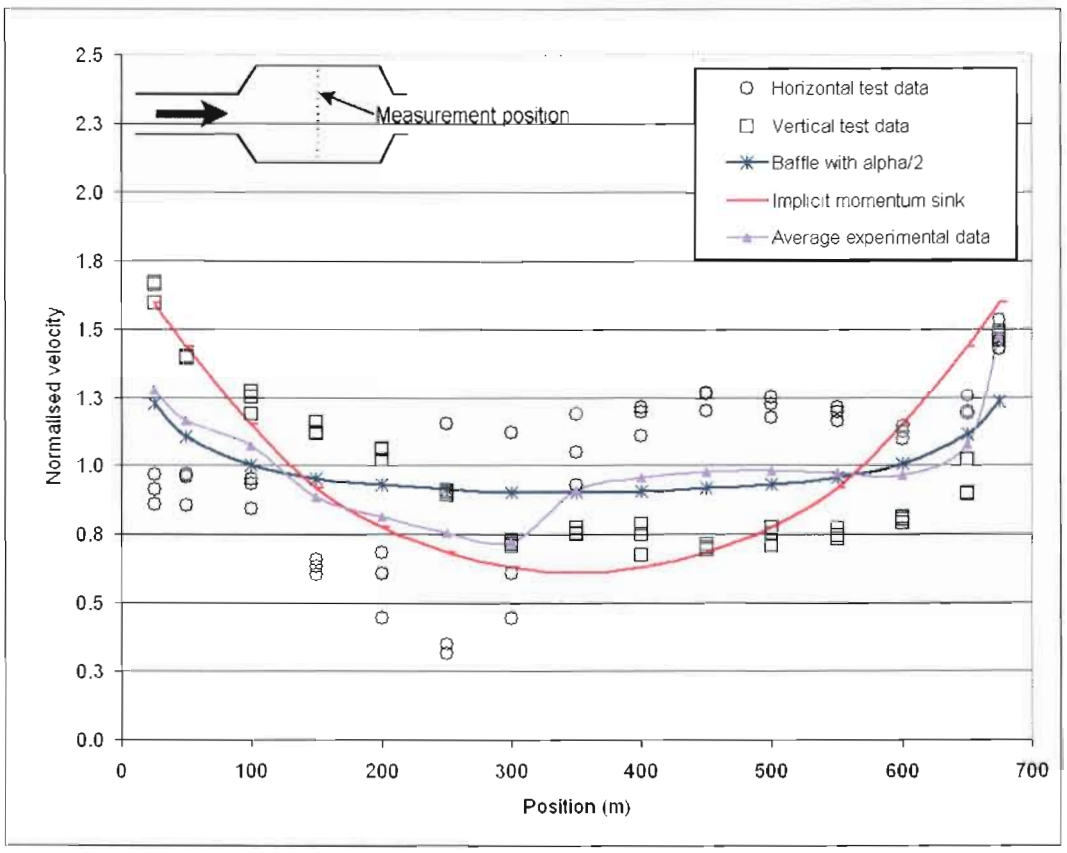

Figure 123: Implicit momentum sink results (central duct position): Screen 1

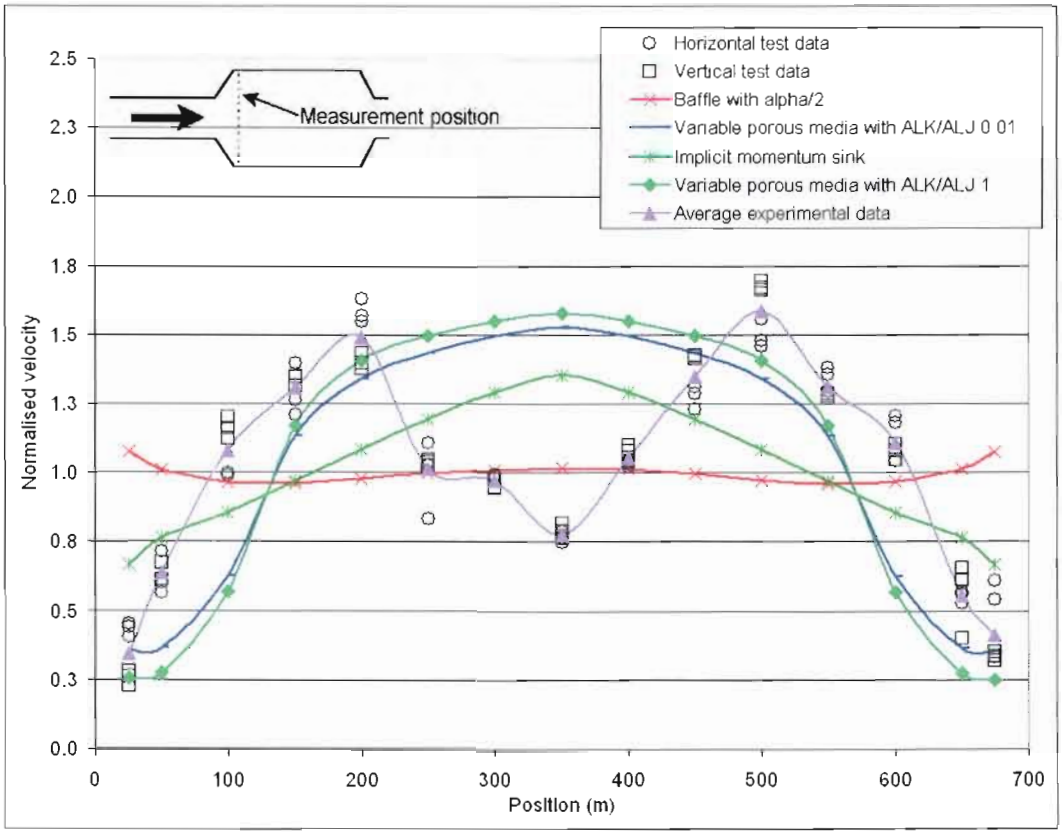

Figure 124: 60° diffuser frontal position with screen 2

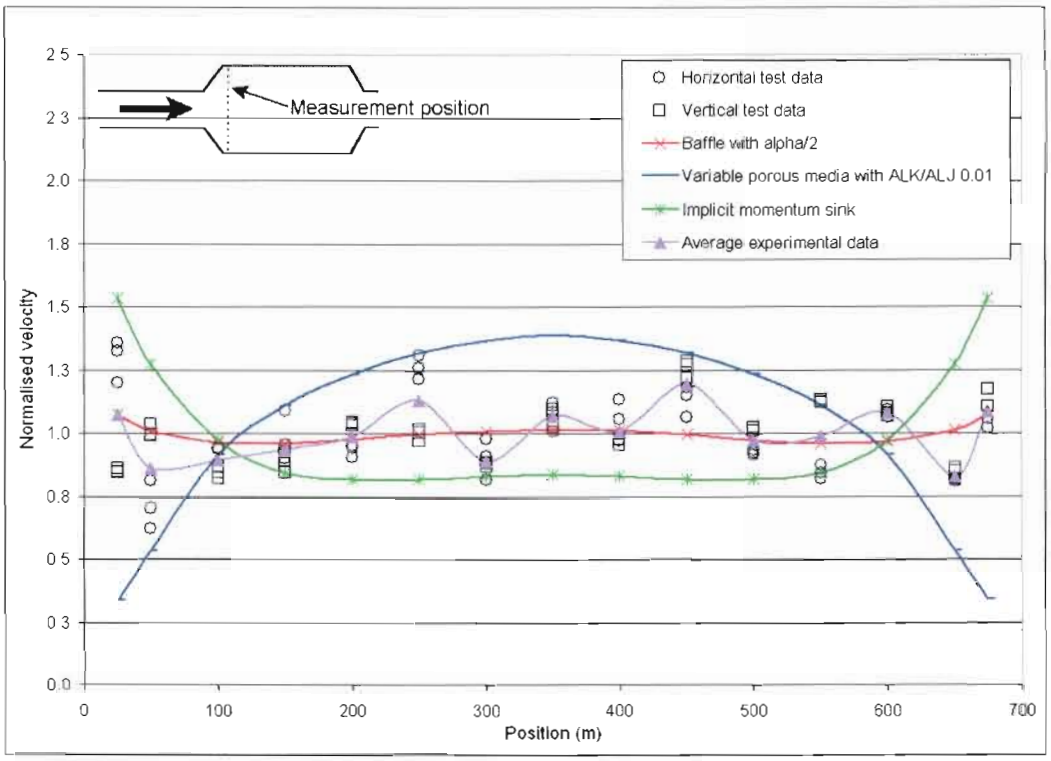

Figure 125: 60° diffuser frontal position with screen 3

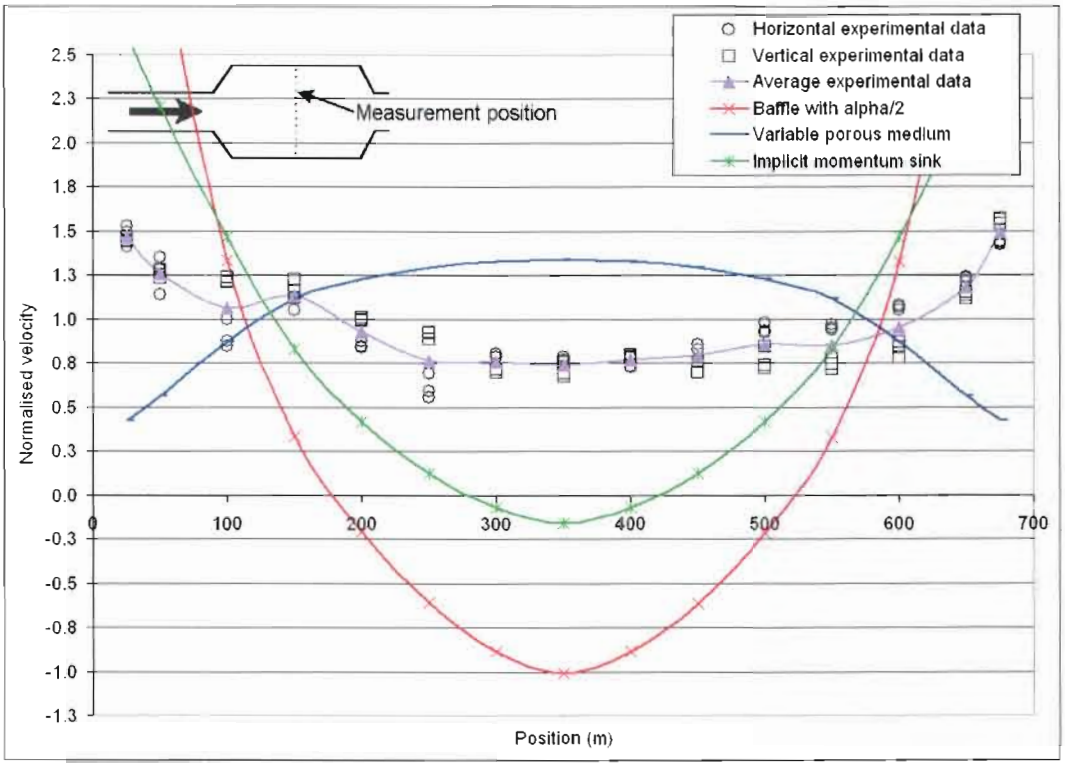

Figure 126: 60° diffuser central position with screen 4

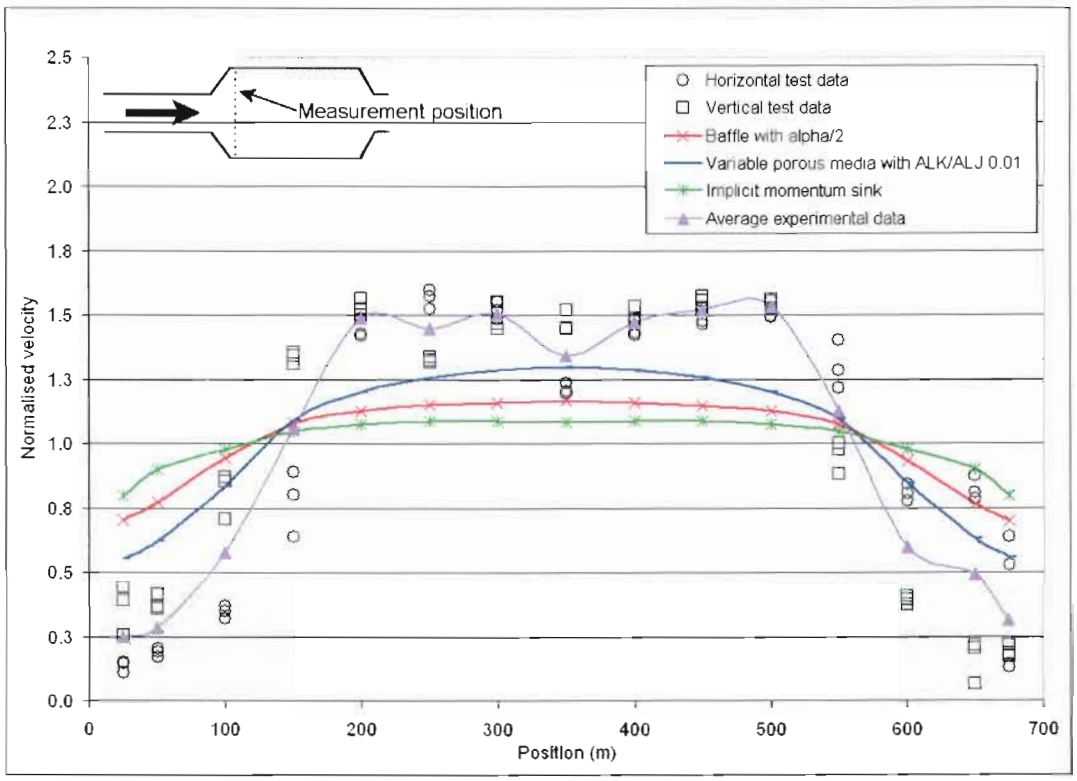

Figure 127: 60° diffuser frontal position with screen 5

ANNEXURE F.3 : 120° Diffuser with screens

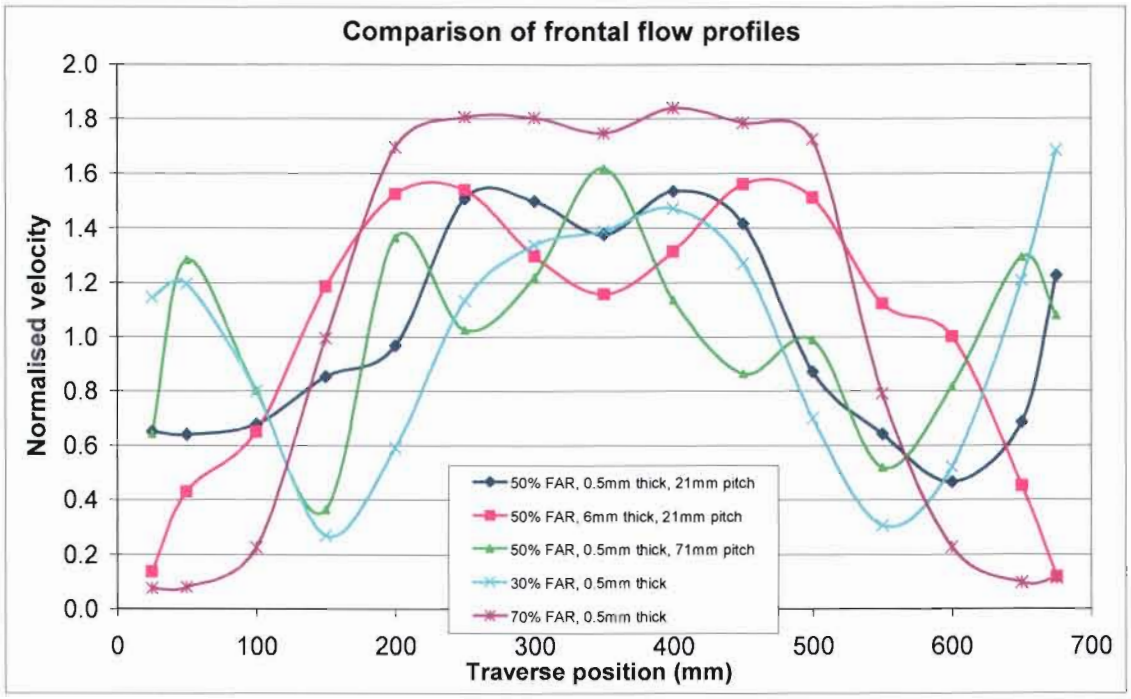

Figure 128: Comparison of averaged profiles in the frontal diffuser position

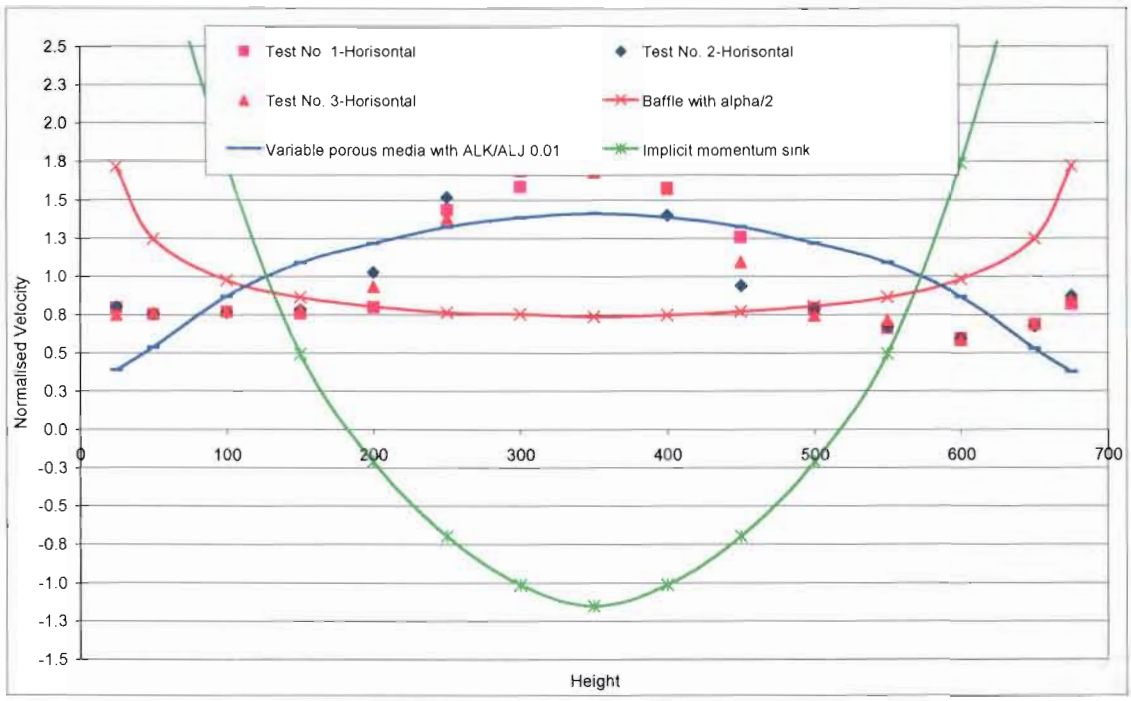

Figure 129: 120° diffuser frontal position with screen 1

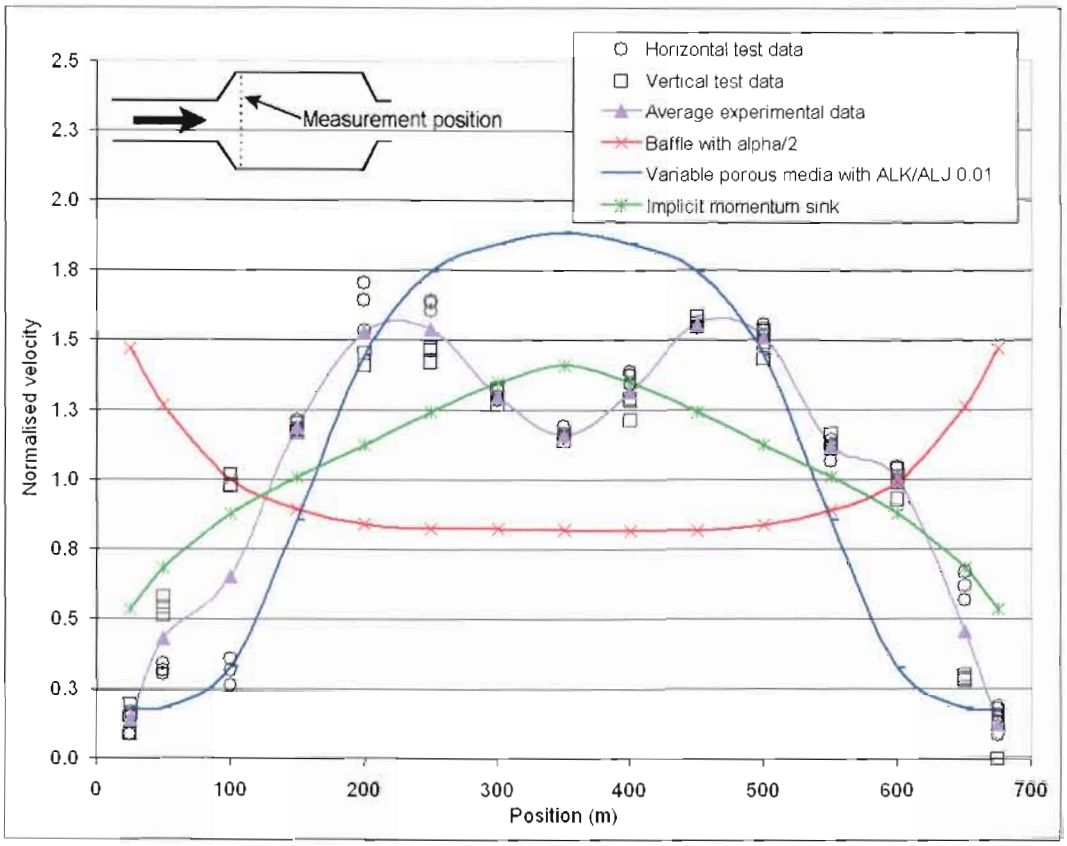

Figure 130: 120° diffuser frontal position with screen 2

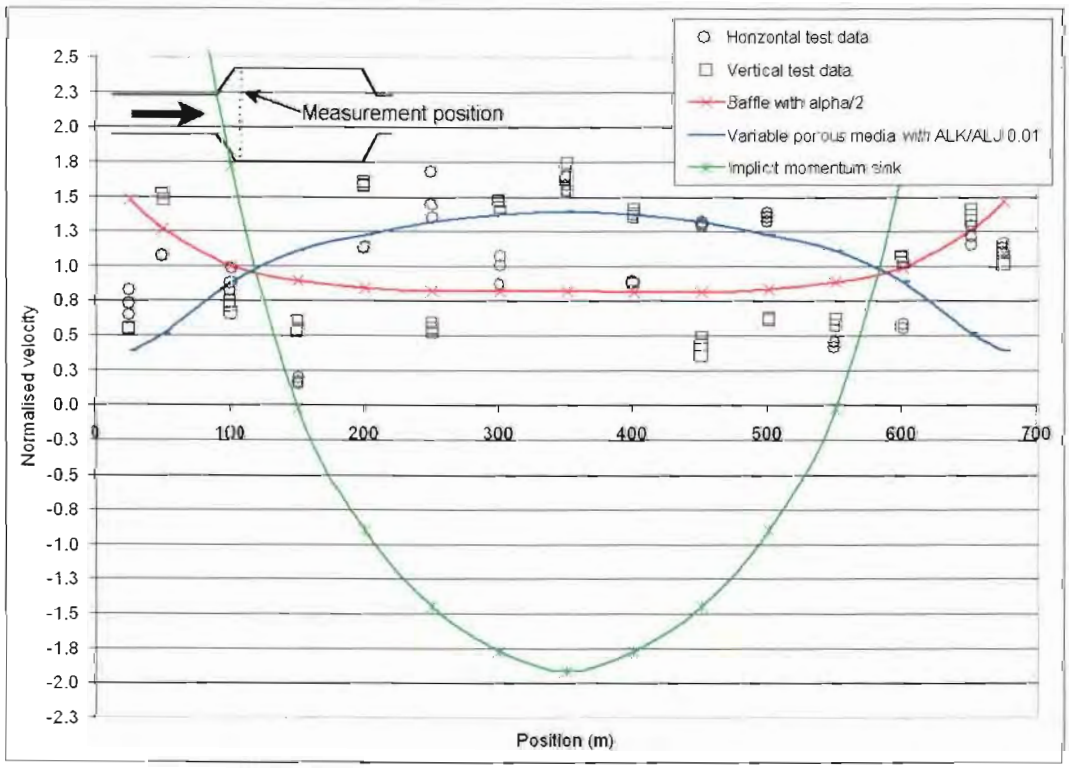

Figure 131: 120° diffuser frontal position with screen 3

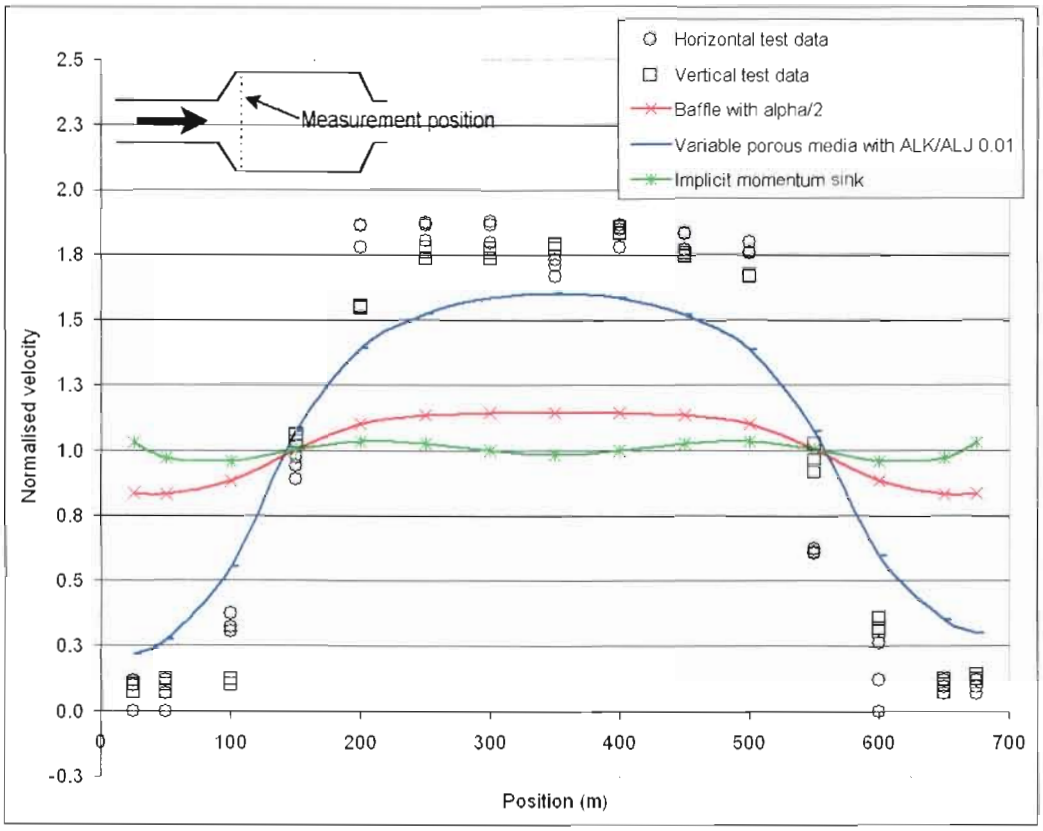

Figure 132: 120° diffuser frontal position with screen 5

ANNEXURE G : SPREADSHEET TO TEST THE EQUATIONS BEFORE STARTING WITH THE CODING

Calculating the variable resistance factor - Screen 1													
50% FAR, 21.7mm pitch, 0.5mm thickness													
Screen width	0.5	mm	t	Test Perpendicular FAR						Coefficients of 5th order polynomial			
Hole size	15.4	mm	a, b										
Hole pitch	21.7	mm		Perp FAR		50.3642%				a	-4444.8		
Lattice size	6.3	mm	v, w							b	13201		
Average approach velocity	15.5	m/s								c	-15549		
Approximate density	1	kg/m^3								d	9129.94		
Length of porous media	0.0005	m								e	-2705.1		
Ratio of beta to alpha	1.00E-04									f	331.511		

Angle of incidence: Two-dimensional				Variable resistance coefficient							
Angle in X-direction (degrees)	Angle in X direction (radians)	Angle in Y direction (degrees)	Angle in Y direction (radians)	Variable FAR	Variable resistance factor	Predicted pressure drop (Pa)	Variable value of alpha (Unit length)	Variable value of alpha (True length)	Variable value of Beta (True length)	Pressure drop calculated by Star	Percentage difference
0	0	0	0.000	0.504	3.971	477.066	1.986	3971.410	0.397	477.069	0.000
0	0	1	0.017	0.503	3.978	477.912	1.989	3978.454	0.398	477.915	0.000
0	0	5	0.087	0.502	4.007	481.317	2.003	4006.797	0.401	481.320	0.000

0	0	10	0.175	0.501	4.043	485.659	2.021	4042.943	0.404	485.662	0.000
0	0	15	0.262	0.499	4.080	490.164	2.040	4080.452	0.408	490.167	0.000
0	0	20	0.349	0.498	4.120	494.917	2.060	4120.018	0.412	494.920	0.000
0	0	25	0.436	0.496	4.162	500.018	2.081	4162.482	0.416	500.021	0.000
0	0	30	0.524	0.494	4.209	505.596	2.104	4208.913	0.421	505.599	0.000
0	0	35	0.611	0.492	4.261	511.820	2.130	4260.726	0.426	511.823	0.000
0	0	40	0.698	0.490	4.320	518.926	2.160	4319.879	0.432	518.929	0.000
0	0	45	0.785	0.487	4.389	527.253	2.195	4389.204	0.439	527.257	0.000
0	0	50	0.873	0.484	4.473	537.318	2.236	4472.993	0.447	537.322	0.000
0	0	55	0.960	0.480	4.578	549.949	2.289	4578.143	0.458	549.953	0.000
0	0	60	1.047	0.475	4.717	566.576	2.358	4716.553	0.472	566.580	0.000
0	0	65	1.134	0.469	4.911	589.910	2.455	4910.801	0.491	589.914	0.000
0	0	70	1.222	0.459	5.210	625.845	2.605	5209.948	0.521	625.849	0.000
0	0	75	1.309	0.443	5.746	690.243	2.873	5746.039	0.575	690.247	0.000
0	0	80	1.396	0.411	7.049	846.806	3.525	7049.373	0.705	846.811	0.000
0	0	85	1.484	0.317	15.283	-	7.642	15283.323	1.528	1835.921	0.000
0	0	90	1.571	-	-	-	-	-	-	-	-

Angle of incidence: Three-dimensional				Variable resistance coefficient							
Angle in X-direction (degrees)	Angle in X direction (radians)	Angle in Y direction (degrees)	Angle in Y direction (radians)	Variable FAR	Variable resistance factor	Predicted pressure drop	Variable value of alpha (Unit length)	Variable value of alpha (True length)	Variable value of Beta (True length)	Pressure drop calculated by Star	Percentage difference
0	0.000	0	0.000	0.504	3.971	477.066	1.986	3971.410	0.397	477.069	0.000
1	0.017	1	0.017	0.503	3.986	478.758	1.993	3985.502	0.399	478.761	0.000
5	0.087	5	0.087	0.501	4.042	485.580	2.021	4042.291	0.404	485.583	0.000
10	0.175	10	0.175	0.498	4.115	494.305	2.057	4114.924	0.411	494.308	0.000
15	0.262	15	0.262	0.495	4.191	503.391	2.095	4190.561	0.419	503.394	0.000
20	0.349	20	0.349	0.492	4.271	513.013	2.135	4270.661	0.427	513.017	0.000
25	0.436	25	0.436	0.489	4.357	523.387	2.179	4357.021	0.436	523.390	0.000
30	0.524	30	0.524	0.485	4.452	534.791	2.226	4451.950	0.445	534.794	0.000
35	0.611	35	0.611	0.481	4.559	547.598	2.279	4558.566	0.456	547.601	0.000
40	0.698	40	0.698	0.477	4.681	562.336	2.341	4681.255	0.468	562.339	0.000
45	0.785	45	0.785	0.471	4.827	579.783	2.413	4826.500	0.483	579.787	0.000
50	0.873	50	0.873	0.465	5.004	601.155	2.502	5004.412	0.500	601.159	0.000
55	0.960	55	0.960	0.458	5.232	628.474	2.616	5231.836	0.523	628.478	0.000
60	1.047	60	1.047	0.449	5.539	665.412	2.770	5539.326	0.554	665.416	0.000
65	1.134	65	1.134	0.436	5.989	719.440	2.995	5989.094	0.599	719.445	0.000
70	1.222	70	1.222	0.418	6.731	808.563	3.366	6731.014	0.673	808.568	0.000
75	1.309	75	1.309	0.389	8.235	989.285	4.118	8235.465	0.824	989.292	0.000

80	1.396	80	1.396	0.335	12.849	-	6.425	12849.460	1.285	1543.551	0.000
85	1.484	85	1.484	0.199	51.442	-	25.721	51442.027	5.144	6179.513	0.000
90	1.571	90	1.571	-	-	-	-	-	-	-	-